5-2014

Efficient Processes for Power Generation and Energy Storage

Easa Ismail Al-musleh
Purdue University

PURDUE UNIVERSITY
GRADUATE SCHOOL
Thesis/Dissertation Acceptance

This is to certify that the thesis/dissertation prepared

By Easa Ismail Al-musleh

Entitled
Efficient Processes for Power Generation and Energy Storage

For the degree of Doctor of Philosophy

Is approved by the final examining committee:

Prof. Rakesh Agrawal

Prof. Gintaras Reklaitis

Prof. Joseph Pekny

Prof. Mohit Tawarmalani

To the best of my knowledge and as understood by the student in the *Thesis/Dissertation Agreement. Publication Delay, and Certification/Disclaimer (Graduate School Form 32)*, this thesis/dissertation adheres to the provisions of Purdue University's "Policy on Integrity in Research" and the use of copyrighted material.

Prof. Rakesh Agrawal

Approved by Major Professor(s): _____

_____

Approved by: Prof. Michael Harris 04/23/2014

Head of the Department Graduate Program Date

EFFICIENT PROCESSES FOR POWER GENERATION AND ENERGY STORAGE

A Dissertation

Submitted to the Faculty

of

Purdue University

by

Easa I. Al-musleh

In Partial Fulfillment of the

Requirements for the Degree

of

Doctor of Philosophy

May 2014

Purdue University

West Lafayette, Indiana

Dedicated to my country (Qatar) and my family

ACKNOWLEDGMENTS

First and foremost praise belongs to Allah, the One who has blessed me in my entire affair. Without His help nothing could have been accomplished. Next I am grateful to my country, the state of Qatar, and Qatar University for providing me with such valuable opportunity to pursue my higher education in the United States.

It is a pleasure to sincerely thank my main advisor, Prof. Rakesh Agrawal, for his patience, valuable feedback and knowledge during my masters and PhD degrees. Also, I would like to covey my gratitude to my wife for the support she provided me throughout my life. Her support has contributed to all my success. Back home I would like to express my grateful thanks to my respected teachers: Prof. Hassan Alfadala, Saudi Binladin Group; Mr. Cesar Wazen, Qatar University; Prof. Dr. Ramazan Kahraman, Qatar University; Prof. Faried Ben Yahya, Qatar University; Mohamad Hassan AlKabbi, Qatar Foundation; for their constant encouragement, guidance and support. Lastly, I am heartily thankful to my beloved parents, sisters and friends for their support, warm prayers and simply just giving me the strength throughout the program.

TABLE OF CONTENTS

Page

LIST OF TABLES

Table Page

LIST OF FIGURES

Figure Page

SYMBOLS

AF	SOFC pressure adjustment factor
C_p^{RGas}	Regeneration gas constant pressure heat capacity
C_p^{Vessel}	Vessel constant pressure heat capacity
C_p^{Water}	Water constant pressure heat capacity
D	Vessel diameter
EX_C	Carbon fuel exergy content per mole of carbon
$EX_{H\rightarrow C}$	Exergy stored in the carbon fuel relative to hydrogen exergy during the carbon fuel synthesis step
EX_i *or* EX_j	Exergy of a stream=$H_i - T_o S_i$
EX_V	Carbon fuel exergy content per unit fuel volume under storage temperature and pressure
F	Faradays constant, 96,485 Columb/mol electrons (Columb = Ampere times second)
G_i	For carbon fuel exergy calculations: Gibbs free energy per mole of fuel i. For Solid Oxide Fuel Cell and Solid Oxide Electrolysis Cell modeling:Gibbs free energy of a stream
h	Vessel height (m)=$h_B + 1.5$
h_B	Adsorbent bed height
H_i	Enthalpy of a stream
$\Delta H_{Desorption}$	Water heat of desorption
$\Delta H_{Dissociation}$	Heat of dissociation reaction at operating temperature and pressure
I_{Stack}	SOFC/SOEC electrical current

LHV_{LNG}	Liquefied Natural Gas Lower Heating Value
$m_{Adsorbent}$	Adsorbent mass
m_s^{Feed}	Steam feed molar flow rate
m_{o_2}	Molar flow rate of oxygen across the electrolyte
m_{RGas}	Mass flow of the regeneration gas
m_{so_2}	Stoichiometric oxygen molar flow rate
m_{water}	Mass of adsorbed water
m_{Vessel}	Vessel mass
n	Number of electors transferred as a result of the electrochemical reaction
N_{Cell}	Number of fuel cells in the SOFC/SOEC
P_o	Ambient pressure= 1.01325bar
ΔP	Pressure drop
q_g	Actual gas (i.e. gas to be dehydrated) volumetric flow rate
$Q_{Adsorber}$	Heat essential to regenerate the adsorber
$Q_{Cathode}$	SOFC heat absorbed by the air following in the fuel cell cathode
$Q_{Dissociation}$	Heat required by the steam dissociation reaction in the cathode sides at the defined operating conditions
Q_{Net}	SOFC/SOEC net heat duty (positive: heat is required, negative: heat is produced)
$Q_{Reforming}$	SOFC heat required to carry out the reforming reactions
S_i	Entropy of a stream
t	Vessel thickness
t_R	Length of the regeneration cycle
$T_{Initial}$	Initial temperature of the adsorber prior the regeneration
T_o	Ambient temperature=298K (25^o)
T_{Out}	Temperature of the regeneration gas leaving the adsorber under regeneration
T_{Sat}	Water saturation temperature at the regeneration pressure

U_f	SOFC fuel utilization (i.e. conversion)
U_s	SOEC steam utilization (i.e. conversion)
v_g	Superficial gas (i.e. gas to be dehydrated) velocity
V_{LNG}	LNG traded volume in 2011 at 15^{o}C and 1.01 bar
V	SOFC/SOEC voltage
V_{TN}	SOEC thermal-neutral voltage
W_{Actual}	SOFC/SOEC Direct Current electrical power
W_{Cold}^{rev}	Reversible power from the evaporation of refrigerated liquid
W_{Losses}	SOFC/SOEC electrical power losses as a result of activation polarization, diffusion polarization, and ohmic losses
$W_{Max.}^{LNG}$	Exergy (or maximum power) from vaporizing LNG
$W_{Min.}^{CO_2CL}$	Exergy (or minimum power) for capturing and liquefying carbon dioxide
$W_{Min.}^{Carbondioxide}$	Exergy (or maximum power) from vaporizing carbon dioxide
$W_{Min}^{Methane}$	Exergy (or minimum power) for purifying and liquefying methane
x	Adsorbent capacity
λ	Mole of hydrogen required to synthesis one mole of the carbon fuel
λ_f	SOFC molar rate of fuel conversion
ρ_g	Gas (i.e. gas to be dehydrated) density
ρ_B	Adsorbent bulk density
ρ_{LNG}	Liquefied Natural Gas density at 15^{o}C and 1.01bar
μ	gas (i.e. gas to be dehydrated) viscosity
η^{rev}	Reversible efficiency of a heat engine

ABBREVIATIONS

AC	Alternating current
ASU	Air Separation Unit
C-	Column
CC	Combined Cycle
CAES	Compressed Air Energy Storage
CCS	Carbon Capture and Sequestration
CO_2CL	Carbon dioxide Capture and Liquefaction
CW	Cooling Water
DC	Direct current
DEA	Diethanolamine
E-	Heat exchanger
ERPP	Electrochemical Refrigeration Power Plant
FT	Fischer tropsch
g	gas
G	Gaseous
GHG	Green House Gases
Gj	Giga joules
GM-C	Gaseous Methane-Cycle
GW	Giga Watt
GWh	Giga Watt hour
HRSG	Heat Recovery Steam Generator
HP	High Pressure
ID	Identification

IP	Intermediate pressure
J-T (or JT)	Joule Thomson
K-	Compressor
kmol	Kilo mole
kW	Kilo Watt
kWh	Kilo Watt hour
l	Liquid
L	Liquid
LHV	Lower Heating Value
Li-ion	Lithium-ion
LM-C	Liquid Methane-Cycle
LNG	Liquefied Natural Gas
LP	Low Pressure
Max.	Maximum
MEA	Monoethanolamine
Min.	Minimum
Mj	Mega joules
Mo-C	Methanol-Cycle
MoCC	Methanol Combined Cycle
mol	Mole
MoW-C	Methanol Water-Cycle
MR	Mixed Refrigerant
MW	Mega Watt
MWh	Mega Watt hour
NG	Natural Gas
NGCC	Natural Gas Combined Cycle
oxy-fuel	fuel combustion using oxygen
P-	Pump
PHEV	Plug-In Hybrids Vehicles

PHS	Pumped Hydroelectric Storage
PEM	Proton exchange membrane fuel cells
PSRK	Predictive Redlich-Kwong-Soave equation of state
R	Regeneration
R-	Reactor
RWGS	Reverse Water Gas Shift
SA	Sustainably Available
SOEC	Solid Oxide Electrolysis Cell
SOFC	Solid Oxide Fuel Cell
SQP	Successive Quadratic Programming
STC	Steam to Carbon Ratio
Syngas	Synthesis gas
T-	Turbine
TES	Thermal Energy Storage
TWh	Tera Watt hour
US	United State
USA	United State America
V-	Vessesl
W	Watt
WGS	Water Gas Shift

ABSTRACT

Al-musleh, Easa I. Ph.D., Purdue University, May 2014. Efficient processes for power generation and energy storage. Major Professor: Rakesh Agrawal.

Finite fossil fuels reserves and unprecedented carbon dioxide levels warrant the need for efficient energy utilization and/or carbon free energy sources. This dissertation addresses the aforementioned issue and provides two solutions. 1) An efficient Natural Gas (NG) based Solid Oxide Fuel Cell (SOFC) power plant equipped with near 100% carbon dioxide capture. The power plant uses a unique refrigeration based process to capture and liquefy carbon dioxide from the SOFC exhaust. Here, carbon dioxide is captured and condensed at different pressure levels by contacting the gas stream with liquid carbon dioxide reflux generated at higher pressure. The uncondensed gas mixture, comprising of relatively high purity unconverted fuel, is recycled to the SOFC and found to boost up the power generation of the SOFC by 22%, when compared to a stand alone SOFC. If Liquefied Natural Gas (LNG) is available at the plant gate, then the refrigeration available from its evaporation is used for carbon dioxide Capture and Liquefaction (CO_2CL). If NG is utilized, then a Mixed Refrigerant (MR) vapor compression cycle is utilized for CO_2CL. Alternatively, the necessary refrigeration can be supplied by evaporating the captured liquid carbon dioxide at a lower pressure, which is then compressed to supercritical pressures for pipeline transportation. From rigorous simulations, the power generation efficiency of the proposed processes is found to be 70-76% on a lower heating value (LHV) basis. The benefit of the proposed designs is evident from the similar efficiency (73%) achieved by a conventional SOFC-Gas Turbine power plant without carbon dioxide capture. The refrigeration based process that capture and liquefy carbon dioxide is also found to be applicable for capturing and liquefying carbon dioxide from flue gases other than

SOFC. An oxygen based Natural Gas Combined Cycle (oxy-fuel NGCC) process is developed and tested to implement the above mentioned capture process. The power generation efficiency here is estimated to be near 49% with almost 98% liquid carbon dioxide recovery. 2) Efficient means of using intermittent renewable energy such as solar for baseload applications with dense large-scale energy storage. Unique carbon recirculation cycles are developed for this purpose. Here, during the period of renewable energy availability, a suitable carbon molecule is synthesized from the stored liquid carbon dioxide and then stored in a liquid state. Subsequently, when renewable energy is unavailable, the carbon molecule is oxidized to deliver electricity and carbon dioxide is recovered and liquefied for storage. Eexergy based metrics are introduced to systematically identify candidate carbon molecules for the cycle. Such a search provides us the trade-off between the exergy stored per carbon atom, exergy used to synthesize the molecule and the exergy stored per unit volume. While no carbon molecule simultaneously has the most favorable values for all three metrics, favorable candidates identified include methane, methanol, propane, ethane and dimethyl ether. For cases where the molecule to be stored is gaseous under ambient conditions, we suggest synergistic integration between liquefaction and boilup of this gas and that of recirculating carbon dioxide. This unique feature allows for minimizing the energy penalty associated with the recovery, purification and liquefaction of carbon dioxide and storage of carbon molecules. Using process simulations we show that these cycles have a potential to provide GWh of electricity corresponding to an overall energy storage efficiency of 53-58% at much reduced storage volumes compared to other options.

CHAPTER 1. INTRODUCTION

1.1 Motivation and objective

Fossil fuels have played an enormous role in improving the human race quality of life. Almost all kind of activities carried out by humans involve burning coal, oil, and/or Natural Gas (NG). Currently, around 86 % of the world utilized energy is sourced from fossil resources [1]. Such energy sources; however, are finite and there will be a time at which it will not be possible or difficult to get access to them. For example, oil production is expected to peak in 10 to 50 years [2]. On the other hand, it is estimated that if the US will use its proven coal reserves to produce transportation liquid fuels, using a conventional process, to satisfy the domestic transportation sector requirements, then this coal will last for around 89 years [3].

Another major issue with fossil fuels is Greenhouse Gas (GHG) emissions . Concerns over the role of GHG emissions in affecting climate change have prompted widespread research and development efforts into reducing future emissions from stationary and distributed sources [4, 5]. As of 2010, plants producing heat and electricity from the combustion of fossil fuels like coal and NG accounted for 41% of global carbon dioxide emissions [6, 7]. One option towards reducing future carbon dioxide emissions from electrical power generation is implementing carbon-free renewable energy sources like solar, wind etc. The global installed generation capacity of solar and wind power grew by 73% (29 GW) and 20% (41 GW) in 2011 [8]. Overall, the global installed generation capacity of non-hydroelectric renewable power grew by 77 GW in 2011 [9], due to a combination of several factors including favorable government policies and substantial cost reductions. However, in the absence of an effective energy storage options, the intermittent nature of the energy source currently limits

the use of renewable power generation to peak shaving rather than baseload applications. For exmple, among the known energy storage methods, current batteries are known for their high storage efficiency (75 to 94 %) [10]. However, their currently low energy densities (less than 2 GJ/m3) [10, 11] and short cycle life (e.g. near 2500 for sodium-sulfur batteries) [11], make them impractical for storing GWh levels of electricity. For example, the most mature commercially available sodium-sulfur batteries, are typically installed to store electrical energy amounts at the MWh level, with a current world wide deployment of 270 MW [11, 12]. Use of hydrogen either as a cryogenic liquid or compressed gas results in low energy storage efficiencies typically near 20-30% [13] (see section 6.6). Use of thermophysical materials like molten salts to store thermal energy, which is subsequently transformed to electrical power via a steam Rankine cycle, is associated with low energy density (less than 3 GJ/m3) and a storage efficiency that is constrained by the cycle thermodynamics (typically less than 30%) [14–16]. For example, the Andasol solar power station in Spain, one of the largest plants using molten salt, has a storage capacity of 1.1 GWh of deliverable electricity (or 150 MW for 7.5 hours) [14]. On the other hand, compressed air and pumped hydroelectric storage, despite their relatively high energy efficiencies and large scale energy storage capability (greater than 3 GWh) [11], are constrained by the need for suitable geological and geographic locations respectively [4].

Alternative approaches for reducing carbon dioxide emissions from baseload power generation rely on using fossil fuels more efficiently with or without carbon dioxide Capture and Sequestration (CCS) [5, 17]. Implementing CCS for electric power generation involves capturing 80-90% of the carbon dioxide in the exhaust gas from the power plant, compressing it to supercritical conditions (for pipeline transportation), and subsequently storing it in a suitable geological location [18]. The energy input for these steps comes at the expense of about 9-15% reductions in the efficiency of converting primary energy to electricity [1,17,19]. If ships, road or rail tankers are utilized for carbon dioxide transportation, then carbon dioxide needs to be maintained as a low pressure subambient liquid [20], which may require additional electricity in-

put due to the need for a refrigeration cycle (for carbon dioxide liquefaction prior its shipping). Currently, the focus of CCS deployment efforts has been towards power plants using coal rather than NG [17]. This is because a coal power plant has roughly double the carbon dioxide emissions when compared to the same size state-of-art Natural Gas Combined Cycle (NGCC) power plant [17]. The recent increased interest in developing shale gas reserves, notably in the US, points to the possibility of increased use of NGCC power plants for electricity generation [21]. For example, the share of total US electricity generation from NG has increased from near 21% in 2008 to almost 25% in 2011 [22]. However, despite using the lower GHG emitting NGCC power plants, it is estimated that CCS technologies would be necessary to achieve 50-80% GHG emissions reduction compared to the present levels [7, 17].

This dissertation proposes solutions for the above-mentioned problems (i.e. effective energy storage and penalty of implementing CCS). All of these solutions make use of available proven technologies that are commercially available. As shown in Figure 1.1, the dissertation is made of seven chapters. Chapter 2 presents new process designs developed for efficient electrical power generation from NG and methanol with near 100% carbon dioxide capture. On the other hand, chapter 3 presents a new concept for energy storage that enable continuous baseload electrical power supply from an intermittently available renewable energy source such as solar, wind, etc. Detailed process designs that make use of the concept proposed in chapter 3 (Liquid Methane-Cycle, Gaseous Methane-Cycle, Methanol-Cycle, and Methanol Water-Cycle) are presented with detailed discussions in chapter 4. Chapter 5 shows the possible flexibility of the proposed concept of chapter 3 for baseload synthetic natural gas and liquid fuels continuous supply (again from intermittently renewable energy sources). Elaboration on the details of the modeling, optimization, and simulation approaches adopted in this work, is given in chapter 6. Finally, chapter 7 summarizes the conclusions of this dissertation.

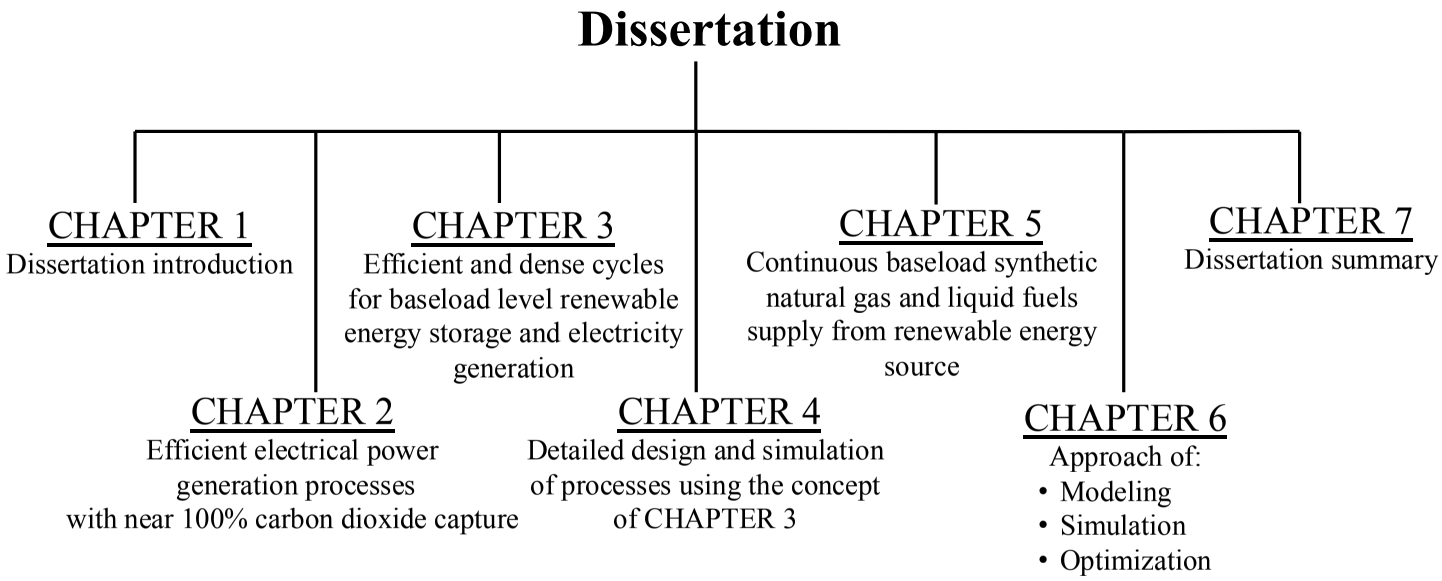

Figure 1.1. Dissertation structure

CHAPTER 2. EFFICIENT POWER GENERATION PROCESSES WITH NEAR 100% CARBON DIOXIDE CAPTURE

2.1 Introduction

Carbon dioxide capture processes are classified into the following categories: 1) Post-combustion capture, 2) Pre-combustion capture, 3) Oxygen-fuel combustion (oxy-fuel) capture, 4) and chemical looping combustion. Each may be applied in power and heat generation plants. In post-combustion capture, the fuel is first oxidized with air and carbon dioxide, generated from the oxidation, is subsequently recovered. For carbon dioxide recovery, processes based on absorption systems utilizing chemical solvents (i.e. solvents react with carbon dioxide) such as Monoethanolamine (MEA), diethanolamine (DEA), and hindered amine are usually deployed [23]. Here, the flue gas (i.e. stream leaving the combustion unit) is contacted with the solvent, in an absorption column, to selectively absorb the carbon dioxide by chemical reaction. The solvent plus carbon dioxide leave the bottom of the absorber to be regenerated, typically in a distillation column, for reuse in the absorption step. Carbon dioxide leaving the top of the regenerator is then compressed and/or liquefied for transportation.

In pre-combustion capture the fuel is first decarbonized in a process consisting of a fuel reforming step (or gasification for solid fuels such as coal, biomass, residue oil) followed by a Water Gas Shift (WGS) step. In the reforming section, the fuel is converted into a synthesis gas (syngas) rich in hydrogen and carbon monoxide, using reforming practices such as steam reforming, partial oxidation, or auto thermal reforming [24]. The carbon monoxide is reacted with steam in the WGS reactor to produce carbon dioxide and additional hydrogen [25]. Carbon dioxide is removed us-

ing absorption technology similar to those used in postcombustion capture. However, physical solvents, such as methanol or mixtures of dimethyl ethers of polyethylene glycol, are preferred. For relatively high carbon dioxide concentration flue gas, such as the case in pre-combustion capture, physical solvents offer carbon dioxide capture with reduced circulation rate in the absorber; thus, reducing the equipment sizes and energy consumption during the solvent regeneration [26]. While the carbon dioxide solvent mixture leaves the bottom of the absorber, the purified hydrogen rich stream leaves the top of the absorber for energy generation (via combustion) with water as the main byproduct.

Oxy-fuel capture processes involve combusting the fuel with an enriched oxygen stream supplied from an Air Separation Unit (ASU). This approach produces a flue gas rich in carbon dioxide and water with impurities such as nitrogen and argon (depending on the purity of the oxygen supplied from the ASU). To avoid excessive temperature in the combustion unit, portion of the carbon dioxide rich flue gas is recycled back, after byproduct water condensation, to the combustion unit. The remaining carbon dioxide is processed in a purification unit to remove the inerts sourced from the ASU. Another approach for controlling the combustion temperature is to recycle the combustion byproduct water, after condensation to remove carbon dioxide, to the combustion unit. Here, energy expensive gaseous carbon dioxide recycle compression is replaced with a less energy intensive water recycle pumping [27].

In chemical looping combustion, the fuel combustion is carried out indirectly in which two reactors are involved, reducer and oxidizer. Fuel and metal oxide particles (e.g. nickel oxide) are fed into the reducer causing the reduction of metal oxide into metal with water and carbon dioxide as byproducts. The metal, which is readily separable from the carbon dioxide/steam mixture, is fed into the oxidizer. In the oxidizer, the metal particles are oxidized into metal oxide, for recycle into the reducer reactor, using air. The oxygen depleted air, carrying portion of the oxidation heat, leaves the oxidizer for power generation in gas turbine/steam turbine Combined Cycle (CC) [28].

For NG based power plant, post-combustion using hindered amine solvent is associated with a power generation efficiency near 50% (based on LHV) with carbon dioxide recovery of 85-90%. Using pre-combustion approach, in which NG is reformed using partial oxidation approach, result in near similar power generation efficiency and carbon dioxide recovery. Improving the carbon dioxide recovery to near 97% is achievable with oxy-fuel combustion; but, with lower power generation efficiency of 44.7% [1,29]. Last but not least, chemical looping calculated efficiency is in the range 45-50% [1,27].

This dissertation presents process designs for high efficiency electrical power generation along with carbon dioxide Capture and Liquefaction (CO_2CL) from NG, available either as Liquefied Natural Gas (LNG) or compressed gas from a pipeline. The process, referred as the Electrochemical Refrigeration Power Plant (ERPP), is based on an integrated steam reforming-Solid Oxide Fuel Cell (SOFC) system followed by a unique process for CO_2CL. The ERPP is capable of achieving near100% carbon dioxide capture and liquefaction while attaining a power generation efficiency of 70.4-76.0%. Here, power generation efficiency is defined as the ratio of the net electrical energy output of the plant to the primary energy input of the feed fuel based on its LHV. When compared to a SOFC plant that does not capture carbon dioxide, the CO_2CL section in our process enable the plant to have nearly zero carbon dioxide emissions with an energy penalty less than 2 %. The following sections describe the different ERPP designs and their simulation via Aspen Plus^{TM} [30]. This is followed by a summary of the key results, sensitivity analysis, and comparison with other NG power plant designs.

2.2 Electrochemical Refrigeration Power Plant (ERPP)

The concept of the ERPP is shown in Figure 2.1. If NG is available as LNG, it is first evaporated and then fed to an integrated steam reforming-SOFC system for electrical power generation. The exhaust from the SOFC anode, composed primarily

of the oxidation products carbon dioxide and water (80-90 mo%), is processed for CO_2CL using the cold refrigeration released from the evaporating LNG and a small amount of additional electricity. If NG is available from a pipeline, then a portion of the generated electrical power is utilized to supply the refrigeration needs of the CO_2CL process. In both cases, the process of CO_2CL is the same and consists of two rectifying columns operating at different pressures. In each column, carbon dioxide is captured, purified, and liquefied by refluxing the SOFC exhaust gas (raising up in the column) with liquid carbon dioxide condensed at high pressure.

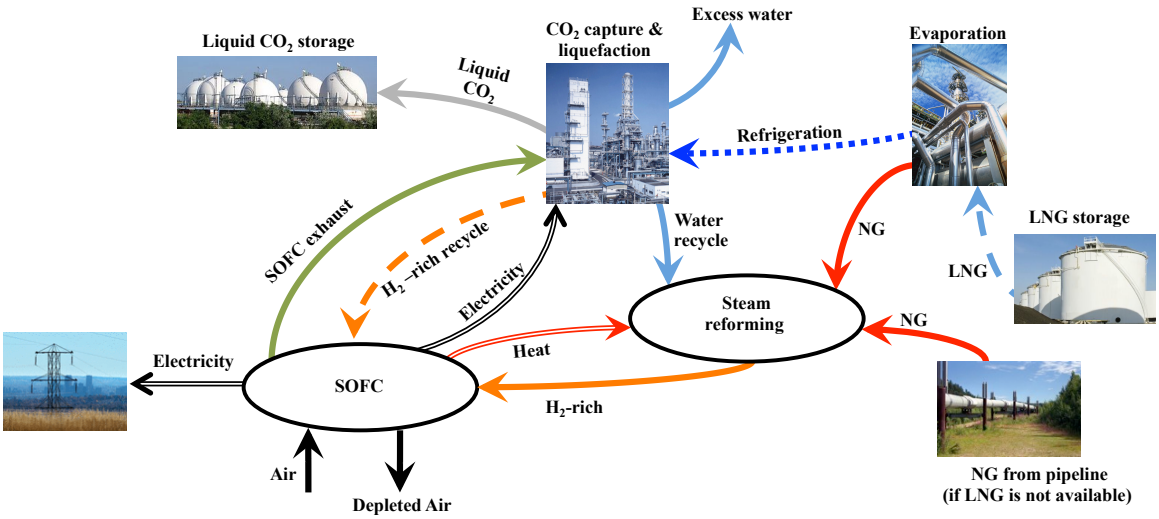

Figure 2.1. A conceptual sketch of the ERPP. SOFC = Solid Oxide Fuel Cell. LNG = Liquefied Natural Gas.

A SOFC (which runs on a synthesis gas) exhaust contains unconverted hydrogen and carbon monoxide in amounts that depend on the extent of fuel utilization (i.e. operating current) [31, 32]. A suggested process to capture carbon dioxide from the SOFC exhaust stream is first convert carbon monoxide to hydrogen via a high-

temperature and then a low-temperature WGS reaction, followed by the carbon dioxide capture through a Selexol^{TM} process [33]. The purified hydrogen rich stream leaving the Selexol^{TM} process is then combusted for additional power generation [33]. Although such a design leads to high power generation efficiency from NG (69% LHV according to [33]), the carbon dioxide recovery is generally limited to 90%. It has also been proposed to use two SOFC devices in series, the first one produces electrical power and the second acts as an afterburner that achieves near 95% combustion with negligible power generation (see Figure 2.7) [33, 34]. Here, the system benefits from fuel combustion using pure oxygen; thus, avoids carbon dioxide dilution. The reported process efficiency at carbon dioxide recovery near 90% is around 68%, which is 5% lower than a process that does not capture carbon dioxide, see section 2.6.

To achieves close to 100% carbon dioxide recovery, it is suggested to combust the SOFC exhaust with a pure oxygen stream supplied from an ASU. This leads to a power generation efficiency of near 63% LHV basis [35], a 10% penalty when compared to a process that does not capture carbon dioxide (see section 2.6). While using enriched oxygen stream, instead of pure oxygen, could reduce the power demand of the ASU, it may not necessarily improve the process efficiency. This is because the flue gas leaving the combustion unit will need to be purified from its associated inserts (i.e. nitrogen, argon, excess oxygen, sourced from the ASU) to obtain the required carbon dioxide sequestration purity [36]. This will typically involve the use of a cryogenic based process, that will add an extra capital and energy penalty to the overall system. A trade off between carbon dioxide purification and ASU powers is presented in [37] for carbon dioxide capture from a furnace exhaust combusting fuel with enriched oxygen. Also it worth mentioning that, in addition to the use of capital and energy expensive ASU, the relatively low composition of hydrogen and carbon monoxide (i.e. low LHV) in the SOFC anode exhaust (at the current corresponding to maximum SOFC efficiency) could necessitate the use of expensive catalytic combustion [38].

The proposed ERPP design, through the use of a novel refrigeration-based process for CO_2CL, can achieve nearly 100% carbon dioxide capture with a purity of

99.6 mole %. This means that all the unconverted fuel (i.e. hydrogen and carbon monoxide) is recovered at high purity (near 12 mole% carbon dioxide) and is available for recycle to the SOFC anode. The recycle stream is found to achieve nearly 22% increase in the SOFC power output compared to a standalone SOFC operation. Thus, achieving high efficiency with zero carbon dioxide emission. All these benefits are accomplished without using expensive catalytic combustion, ASU, additional SOFC, or gas purification process.

Depending on the storage site (or end user) location, the transportation of carbon dioxide may either require supercritical compression for pipeline transportation, or liquefaction for sea, road or rail transportation. The ERPP design produces low pressure liquid carbon dioxide, which can be readily shipped [18, 20, 39]. The use of LNG is among the preferred methods for shipping large quantities of NG over long distances. In 2011, the world wide LNG imports was estimated to be near 331 billion standard m^3 (at 15^oC and 1 bar) [8], which is equivalent to 6.61×10^5 TWh of LHV energy (see equation 2.1). However, liquefaction of NG is energy intensive, typically resulting near 6% of the feed NG being consumed for the process [18, 39]. Around about 0.2 kWh of compression energy is needed to produce one standard m^3 of LNG using a propane-mixed refrigerant vapor compression cycle [40]. By considering LNG rather than NG as feed to the ERPP, the design enables the recovery of a portion of the energy invested in the upstream NG liquefaction process. Previous works have addressed the recovery of LNG refrigeration for nitrogen liquefaction, power generation, and carbon dioxide liquefaction [18, 39, 41–45]. In one example configuration for carbon dioxide liquefaction, the LNG is first evaporated and then split for pipeline NG supply and power generation using oxygen combustion (oxygen supplied from ASU) [41, 42]. Subsequently, carbon dioxide produced from the power generation is liquefied using all of the available LNG refrigeration. In contrast, the ERPP design relies on a unique CO_2CL configuration that captures and liquefies 100% of the generated carbon dioxide using the refrigeration from the LNG feed to the power plant along with a small amount of the generated electric power.

$$
\begin{aligned}
Traded\ LNG\ LHV\ energy &= \rho_{LNG} \times LHV_{LNG} \times V_{LNG} \times \frac{1}{1000} \\
&= 0.771 \times 49.1 \times 330.8 \times 10^9 \\
&= 1.252 \times 10^{10} GJ
\end{aligned}
$$

Where,

ρ_{LNG}: the LNG density at 15^{o}C and 1.01bar, kg/m^3

LHV_{LNG}: LNG LHV, MJ/kg

V_{LNG}: LNG traded in 2011 at 15^{o}C and 1.01 bar, m^3.

$\frac{1}{1000}$: Mj to Gj conversion factor, GJ/MJ

The ERPP design also benefits from the use of SOFC systems versus combustion-based power generation systems like NGCC [31, 32, 46, 47]. The SOFC, producing electricity in a single electrochemical conversion step, reduces the fuel chemical exergy losses associated with multistep systems, such as combustion-based methods [46, 47]. SOFC also avoids direct mixing between the fuel and air, instead allowing for oxygen from the cathode (air feed) to diffuse as an oxygen ion to the anode (fuel feed) for oxidation [46, 47]. This means that the anode exhaust is not diluted with nitrogen (or other diluents), which makes the subsequent carbon dioxide capture less energy intensive relative to the NGCC plant using air.

2.3 Design and simulation of the ERPP

A detailed configuration of the ERPP design, with LNG as feed, is shown in Figures 2.2 and 2.3. Aspen Plus^{TM} is used to rigorously simulate the process using the PSRK thermodynamic property method and steam tables (see appendix A for stream data). The process is designed for a net power output of near 158 MW, with details of the simulation basis shown in chapter 6. The modeling of the SOFC is adopted from the relevant references shown in [31,32] and implemented in Aspen Plus^{TM} using Aspen Calculator tool [30]. Here, the oxidation reactions in the SOFC are modeled to be at chemical equilibrium. The model also include experimentally derived relations

(from [31, 32]) for electrochemical losses due to anode/cathode activation/diffusion polarization, electrolyte resistance, and interconnectors resistance. Since the adopted model in [31, 32] is based on atmospheric SOFC operation, the model is corrected to include the effect of pressure by adding to the calculated voltage a pressure adjustment factor obtained from [48]. The ERPP design consists of the three steps of power generation and heat recovery, carbon dioxide compression and dehydration, and CO_2CL. Detailed descriptions of each of these steps are provided below.

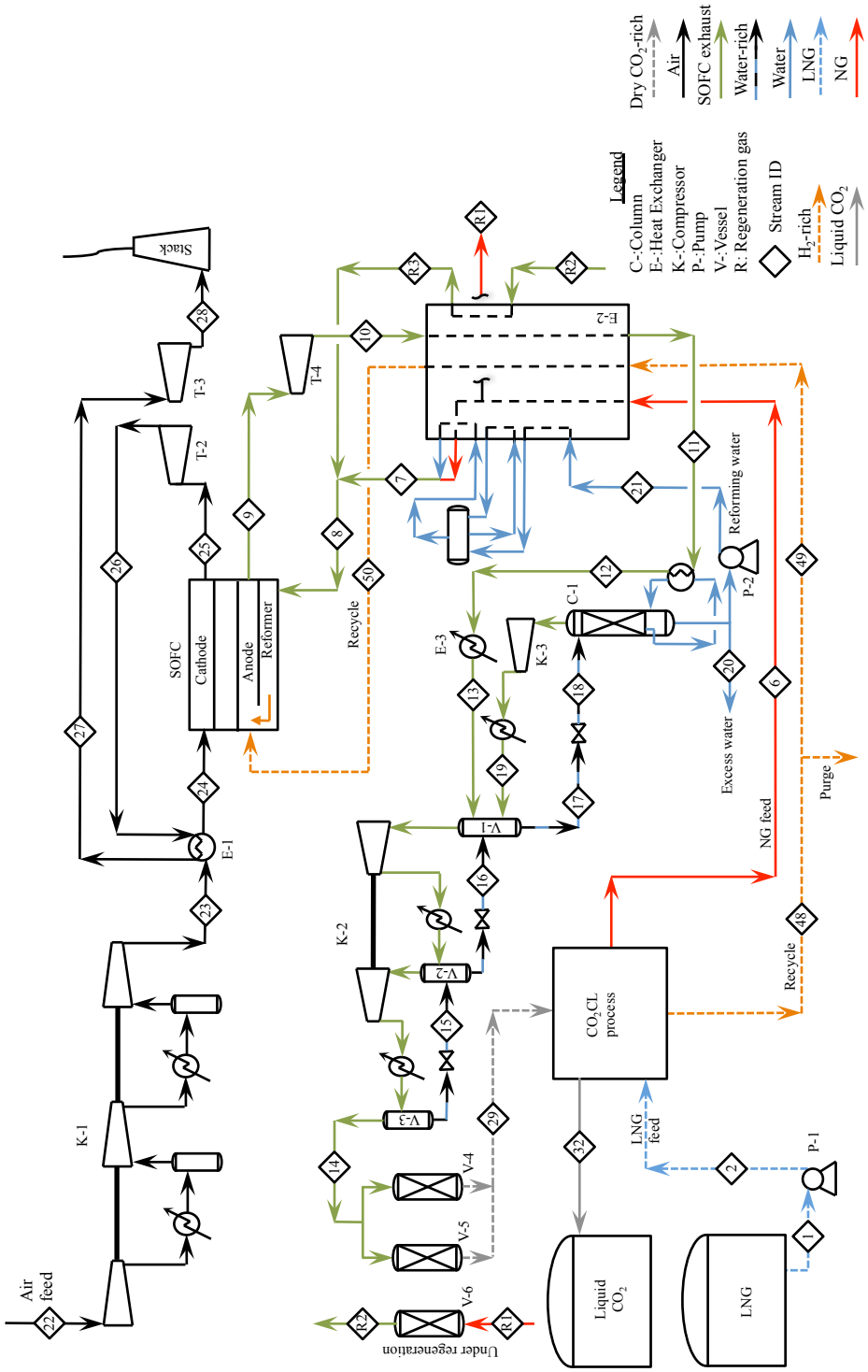

Figure 2.2. A detailed flowsheet for the ERPP concept of Figure 2.1 capturing near 100% carbon dioxide.For CO_2CL flowsheet see Figure 2.3.

2.3.1 Power generation and heat recovery

Since the direct use of NG in the SOFC causes carbon deposition, the NG feed needs to be converted to hydrogen-rich syngas [49]. In the process of Figure 2.2, NG is steam reformed internally (but separated from the anode) by soaking up the SOFC waste heat. This heat integration is a unique feature of SOFC systems [24, 46]. The steam reforming reactions are modeled using chemical equilibrium at the reformer operating conditions. Referring to Figure 2.2, the stored LNG is first evaporated and its refrigeration is utilized for CO_2CL (discussed in section 2.3.3). The vaporized NG (i.e. stream 6) is then heated up to 680^{o}C in heat exchanger E-2, mixed with 10 bar superheated steam (at 680^{o}C) sourced from reboiled column C-1, and then fed to the SOFC reforming section. Before reaching 680^{o}C, a portion of the NG leaves heat exchanger E-2 via stream R1 at 310^{o}C to regenerate the molecular sieve adsorber V-6 (see section 2.3.2). NG plus desorbed water leave the regenerating adsorber V-6 via stream R2 to be heated up to 680^{o}C in E-2 and finally mixed with stream 7 for NG steam reforming. In heat exchanger E-2, heat is supplied by cooling the exhaust stream from turbine T-4 (i.e. stream 10), where the turbine discharge pressure is adjusted to achieve a minimum temperature approach of 28^{o}C (design basis) in the heat exchanger. Increasing the temperature of the SOFC improves the efficiency of SOFC power generation and increases the conversion of NG to syngas [24, 50]. Therefore, we have chosen to operate the SOFC at 950^{o}C, which is close to the maximum limit of 1,000^{o}C. The reformer is operated at 922^{o}C to maintain a minimum temperature approach for heat exchange of 28^{o}C (design basis). Further, increasing the SOFC operating pressure improves power generation efficiency by reducing the heat dissipation due to the aforementioned electrochemical losses. Here, we set the SOFC pressure to be 10 bar, close to the maximum allowable pressure for existing commercial systems [48]. The generated syngas is fed to the SOFC anode to be electrochemically oxidized at 950^{o}C and 10 bar according to the following reactions.

$$H_2 + O^{2-} \rightarrow H_2O + 2e^- \tag{2.1}$$

$$CO + O^{2-} \rightarrow CO_2 + 2e^- \tag{2.2}$$

The fuel utilization in the SOFC is defined as the percent syngas conversion via the oxidation reactions 2.1-2.2. In agreement with the current corresponding to the maximum power generation efficiency of the ERPP (see section 2.4.2), the fuel utilization is set to near 80%. This means that the amount of oxygen consumed by reactions 2.1-2.2 is near 80% of the stoichiometric requirement. The oxygen needed for the fuel oxidation is provided by compressed and heated air stream 24 fed to the cathode side of the SOFC. Stream 24, at 680^{o}C and 10 bar, is produced from feed air stream 22 via multistage intercooled air compressor K-1 followed by heat exchanger E-1. At the SOFC cathode, oxygen ions are generated via reaction 2.3 and diffuse through the yttria-stabilised zirconia electrolyte to the anode side for fuel oxidation [31, 32]. For the chosen fuel utilization of 80%, excess air (equal to 1.07 times the oxidation stoichiometry requirement) is fed to the SOFC cathode to absorb the SOFC waste heat (of near 23 MW) that is in excess of the steam reforming heat requirements (of near 70 MW). Depleted air stream 25 leaves the cathode side of the SOFC to be expanded in turbine T-2, partially cooled to 180^{o}C against inlet air stream 23 in heat exchanger E-1, and finally expanded to 1.1 bar in turbine T-3. Similar to turbine T-4, the discharge pressure of turbine T-2 is set to achieve a minimum temperature approach of 28^{o}C in heat exchanger E-1.

$$O_2 + 4e^- \rightarrow 2O^{2-} \tag{2.3}$$

2.3.2 Carbon dioxide compression and dehydration

Dehydration of carbon dioxide prior to storage and transportation is essential for the following reasons. 1) Storage of carbon dioxide at low pressure requires subambient cooling that may freeze water, if not removed. Freezing of a component in a stream could block pipelines and heat exchanger passages that would disrupt normal process operation. 2) When contacted with water, carbon dioxide tends to form carbonic acid (see reaction 2.4), which tends to corrode typical storage and pipeline

materials of construction (e.g. carbon steel). The stream containing carbon dioxide needs to be dehydrated to the extent such that the water dew point (i.e. the temperature at which water starts to condenses) is below the storage temperature of carbon dioxide, which is -52^{o}C in this study. This extent of dehydration can be achieved using molecular sieve adsorbers (V-4, V-5, and V-6 in Figure 2.2) [51].

$$H_2O + CO_2 \rightarrow H_2CO_3 \tag{2.4}$$

Referring to Figure 2.2, the SOFC anode exhaust, after its passage through heat exchanger E-2, stream 11, is fed to the reboiler of stripping column C-1 to provide the column with the heat duty (at 157^{o}C) necessary for boilup. Stream 12 leaving the reboiler, is then cooled to 43^{o}C in heat exchanger E-3 (using cooling water) to condense a portion of the water present in the stream. The uncondensed gases are separated from the condensed water in a vapor-liquid separator V-1 and compressed to 15 bar in the multistage intercooled compressor K-2. The compression of the SOFC exhaust via K-2 to 15 bar improves the power generation efficiency and per pass liquid carbon dioxide recovery in the downstream CO_2CL section (see sections 2.4.2 and 2.5). Compression also favors water condensation to produce a gaseous carbon dioxide-rich stream. This reduces the dehydration load (e.g. amount of water removal) on the downstream molecular sieve adsorbers (i.e. V-4, V-5, and V-6). As the gaseous stream is compressed in K-2, condensed water plus small amounts of dissolved gases (i.e. hydrogen, nitrogen, carbon monoxide, carbon dioxide) leaving the interstage coolers are separated via vapor-liquid separators V-2 and V-3. The water-rich liquid separated in V-3 is pressure reduced from 15 bar to 12 bar and then fed to the upstream separator V-2. This enables the partial recovery of the dissolved gases in the liquid leaving separator V-3 at intermediate pressure of 12 bar, thereby avoiding low-pressure recompression work. Similarly, the water-rich liquid leaving V-2 is pressure reduced from 12 bar to 9 bar to further separate the dissolved gases in separator V-1. Lastly, the collected water-rich liquid leaving separator V-1 (stream 17 near 99.8 mo% water) is pressure reduced from 9 bar to 2 bar and fed to stripping

column C-1. Column C-1 strips stream 18 of the remaining dissolved gases. The stripped gases are sent to separator V-1 via compressor K-3.

The carbon dioxide-rich gas, stream 14, leaving separator V-3 is sent to the molecular sieve adsorbers, V-4 and V-5, to reduce the stream water dew point (by water removal) to -60^{o}C. While two adsorbers dehydrate gas stream 14, a fully water saturated adsorber (in this case V-6) goes through regeneration by means of hot NG stream (stream R1). When the regeneration is completed, the adsorber is brought online for dehydration of carbon dioxide stream 14 and the another water saturated adsorber goes through regeneration.

2.3.3 Carbon dioxide Capture and Liquefaction (CO_2CL)

The dry carbon dioxide-rich gas stream 29 leaving the molecular sieve adsorbers is fed to the CO_2CL section, described in Figure 2.3. Almost 85 mole % per pass of the feed gaseous carbon dioxide is recovered and stored as liquid carbon dioxide at a purity of near 99.6 mole %, at -52^{o}C and 10 bar. The remaining carbon dioxide is recycled via stream 48 to the SOFC and contains near 12 mole % carbon dioxide. Such high recovery and purity are achieved using three separation stages, represented by C-2, C-3, and V-7, and the vaporizing LNG provides a good portion of the refrigeration required by the process. In the first separation stage, stream 29 is cooled to a temperature of 0^{o}C and then its pressure is reduced to 10 bar (stream 31). This pressure reduction further cools the stream to -3^{o}C using the Joule-Thomson (J-T) effect. In an alternative configuration, the J-T valve may be replaced with a turbine device to achieve greater cooling by power generation (see section 2.5). The vapor portion of the cooled stream leaving the J-T valve is then refluxed in rectifying column C-2 with liquid carbon dioxide-rich stream (near 98 mole% carbon dioxide) sourced from rectifying column C-3. This produces a 99.6 mol% carbon dioxide stream 32 from the bottom of C-2. The uncondensed gases, stream 33, leave column C-2 for refrigeration recovery in heat exchangers E-5 and E-4. Stream 34 leaving exchanger E-4,

completes the first separation stage and is then compressed to a pressure of 34 bar via compressor K-4. The compressed gas, stream 35, is fed to the second separation stage where it is cooled via heat exchangers E-4 and E-5 to 1^{o}C. The cooled stream 36 is then fed at the bottom of the rectifying column C-3 and the rising vapor is refluxed with stream 42 (containing near 92 mole % carbon dioxide) sourced from vapor-liquid separator V-7. The uncondensed gas, stream 38, leaving column C-3, is fed to E-5 and E-4 to recover refrigeration, producing stream 39 which completes the second separation stage. Stream 39 is recompressed in compressor K-5 to pressure of 100 bar for the last separation stage. Stream 40 is partially condensed by cooling via E-4, E-5, E-6, and E-7 to -53^{o}C. The uncondensed gases are separated in vapor-liquid separator V-7 to produce stream 43, which is heated via E-6, E-5 and E-4 and then expanded in turbine T-5. The discharge pressure of turbine T-5 is limited to ensure that the discharge temperature of stream 45 should be greater than -55^{o}C. This temperature limit is necessary to avoid the undesirable carbon dioxide freezing conditions. Stream 45 is fed to E-6, E-5 and E-4 for refrigeration recovery. Leaving heat exchanger E-4, stream 46 is further expanded in turbine T-6 to around 10 bar. The turbine discharge stream 47 is fed to heat exchanger E-4 for refrigeration recovery before being recycled to the SOFC as stream 48.

The LNG sourced from the storage tank (at -160^{o}C and 1.3 bar) is pumped to a pressure of 100 bar via pump P-1 and fed to E-7, E-6, E-5, and E-4 to provide the primary process refrigeration needs. Stream 3, leaving heat exchanger E-4, is expanded in turbine T-1 to a pressure of near 40 bar, which cools down the NG from 35^{o}C to -24^{o}C. Any further pressure reduction will cause the heavier components in the NG stream (i.e. propane and nbutane) to condense in the turbine and is therefore avoided. Instead, a J-T valve is utilized to generate stream 5 at 11 bar and -46^{o}C. This stream is fed to E-6, E-5, and E-4 to provide the remaining process refrigeration, and leaves as stream 6 at 35^{o}C to the high temperature heat exchanger E-2.

The above CO_2CL operating conditions are identified using the optimization problem formulated in Table 2.1. Here, the compression power (K-2, K-4, K-5) is mini-

mized subject to heat exchangers minimum temperature approach $\geq 1.1^{o}$C, per pass liquid carbon dioxide recovery of $\geq$ 85 mole %, and liquid carbon dioxide purity $\geq$ 99.5 mole % using Aspen Plus^{TM} Successive Quadratic Programming (SQP) method. The optimization is carried out using multiple starting points for the various independent variables to ensure a good quality optimum solution. This is further supported by sensitivity analysis on the key process variables, presented in section 2.4.2.

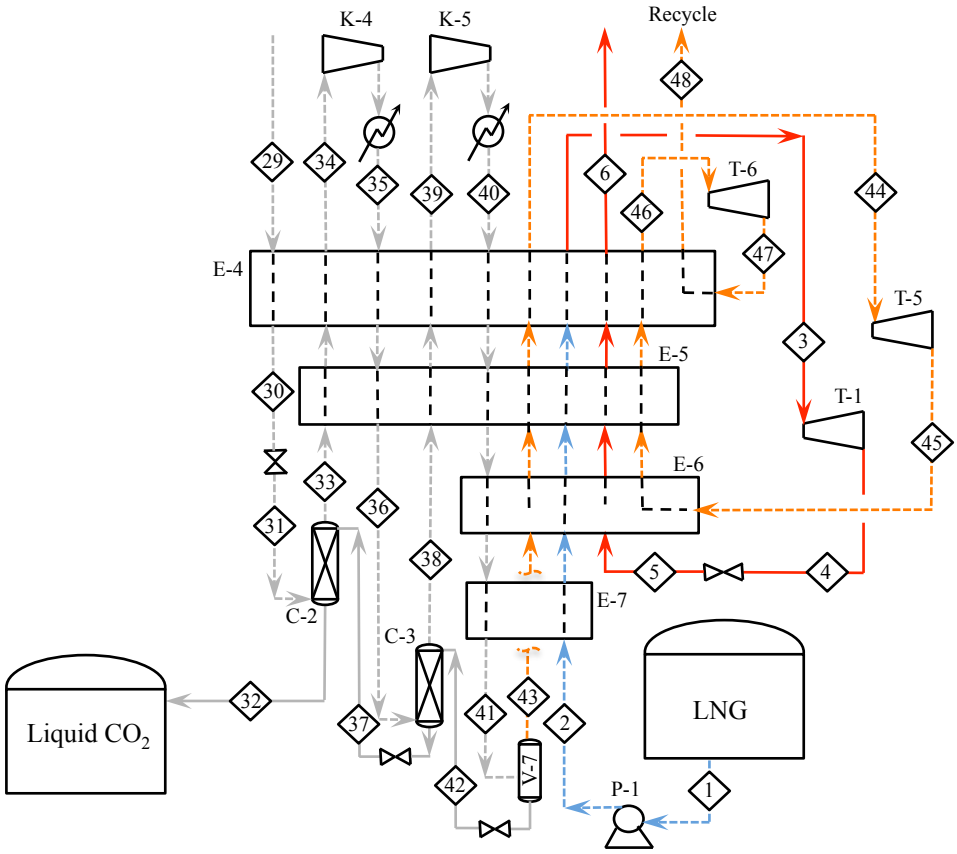

Figure 2.3. Detailed configuration of the CO_2CL section of the ERPP design of Figure 2.2. Stream data from modeling is available appendix A.

2.4 Results and discussion

2.4.1 Thermodynamic analysis

The presented ERPP design operates with an electrical power generation efficiency of 71.2% while achieving near 100% carbon dioxide capture. This efficiency is based on the process heat integration between the hot and cold streams, depicted by the composite curves of Figure 2.4. Here, cold streams below the temperature of the cooling water utility (at 32^{o}C) are not included. In addition, Figure 2.4 does not consider integration of the SOFC waste heat. Instead, the integrated steam reformer-SOFC system is modeled to operate adiabatically, with the SOFC waste heat soaked up for heating the air stream 24 (from 680^{o}C to 922^{o}C) and the NG reforming reactions (at 922^{o}C). According to Figure 2.4, the process is deemed to be heat sufficient, which implies that there is no need to burn a portion of the feed NG for heat supply. Figure 2.4 also suggests that a portion of the heat available from the hot streams (near 155^{o}C and below), rather being rejected to the cold utility, can be used for additional electrical power generation. The heat rejected to the cold utility translates into near 18.4 MW of exergy or 11.6% of the plant net power output (see Figure 2.5 for exergy composite curves). A portion of this exergy could be recovered by use of Rankine cycle with maximum temperature near 155^{o}C. At such relatively low temperatures, using an organic fluid such as propane instead of steam may be more suitable for the Rankine cycle [52]. Although we have not included such a cycle in our analysis, considering about 20% of the exergy of the rejected heat may be recovered as electricity, the power generation efficiency could increase from 71.2% to 72.8%. Alternatively, the rejected heat could be utilized to co-generate low pressure steam to be exported.

$$W_{Min.}^{CO_2CL} = EX_{32} + EX_{48} - EX_{29} \tag{2.5}$$

$$W_{Max.}^{LNG} = EX_1 - EX_6 \tag{2.6}$$

According to equation 2.5 the minimum power for capturing and liquefying carbon dioxide $W_{Min.}^{CO_2CL}$ is 1.7 MW (or 5.9 MJ/kmol liquid carbon dioxide stored). Here, EX_j refers to the rate of exergy flow associated with a stream j (see appendix A for

Table 2.1
Optimization problem formulation for CO_2CL section of the ERPP shown in Figure 2.3

Minimize	Compression power (K-2,4 and 5)
Subject to	Stream 32 CO_2 mole % ≥ 99.5 Per pass liquid CO_2 recovery ≥ 85 mole % E-4,5,6, and 7 minimum temperature approach ≥ 1.1 °C Stream 31 temperature ≥ -55 °C (if J-T is replaced by turbine)
Independent variables	(1) K-2 discharge pressure (10 to 100 bar) (2) K-4 discharge pressure (10 to 100 bar) (3) K-5 discharge pressure (10 to 100 bar) (4) Stream 30 temperature (43 to -55 °C) (5) Stream 36 temperature (43 to -55 °C) (6) Stream 41 temperature (43 to -55 °C)
Method	Aspen Plus SQP [14]

exergy of a stream). On the other hand, the rate at which exergy (i.e. maximum power) is available from vaporizing LNG $W_{Max.}^{LNG}$ is 2.8 MW (or 9.9 MJ/kmol liquid carbon dioxide stored). The difference between $W_{Min.}^{CO_2CL}$ and $W_{Max.}^{LNG}$ represents the maximum rate at which exergy may be available from the vaporizing LNG, and is equal to near 1.1 MW. In other words, for a thermodynamically reversible CO_2CL section, near 1.1 MW of power could be produced. However, the simulation results in Table 2.3 suggest that, in addition to the available LNG refrigeration, around 5.1 MW of compression power (W_{K-4}+W_{K-5}+W_{P-1}-W_{T-1}-W_{T-5}-W_{T-6} from Table 2.3) is required. This additional power requirement is a consequence of the process exergy losses (irreversibilities) originating from temperature differences, pressure drops, compressors/turbines inefficiencies, etc. For example, the process composite curves for the CO_2CL heat exchangers (E-4, E-5, E-6 and E-7 in Figure 2.3), shown in Figure 2.6, reveal large temperature differences (i.e. large irreversibilities) in the coldest section of the process (-52^{o}C to -153^{o}C). Such large temperature differences are contributed by the hot streams physical properties (i.e. heat capacities, latent heat, etc.) as well as carbon dioxide minimum temperature constraint. As mentioned before,

cooling of streams containing carbon dioxide is set to be not less than -55^{o}C to avoid the undesirable carbon dioxide freezing conditions.

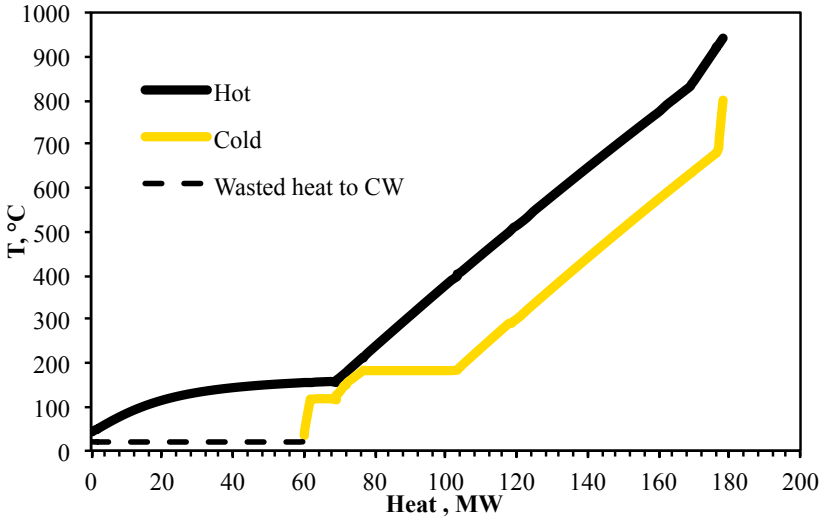

Figure 2.4. Process heat composite hot and cold curves for the ERPP design of Figure 2.2, including all process streams with a temperature greater than that of the available cold utility (32^{o}C).

2.4.2 Sensitivity analysis

Figure 2.7 shows the effect of the SOFC fuel utilization on the process power generation efficiency for different values of Steam to Carbon ratio (STC) used for NG reforming. For fixed STC, increasing the fuel utilization beyond 77% corresponds to decreasing power generation efficiency. The higher currents (i) associated with increased fuel utilization translate into a greater fraction of SOFC energy input lost as heat (losses scale as i^2). Even though a portion of the SOFC waste heat is recovered to produce power via air expansion, the cascading process energy losses (due to air compression and expansion) result in reduced work output and lower power generation efficiency. If the fuel utilization value is less than 77%, then the SOFC waste heat is observed to be insufficient to meet the heat requirements of the NG steam reforming.

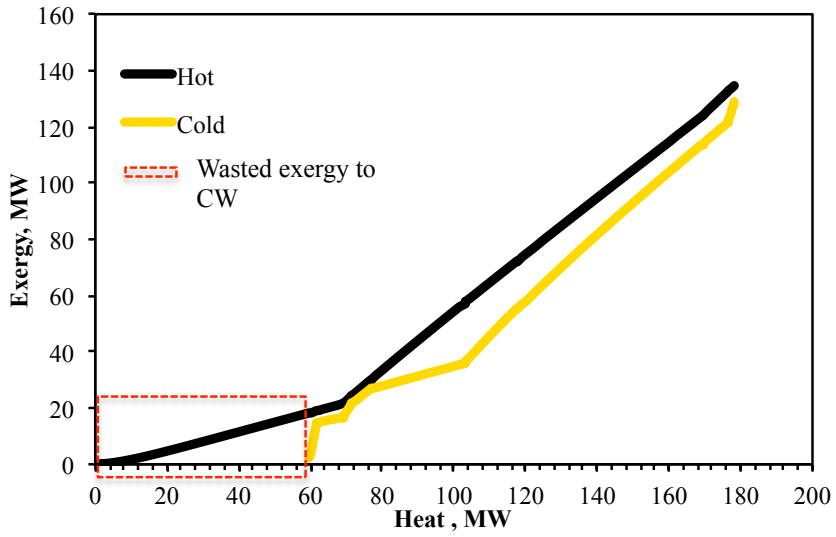

Figure 2.5. Process exergy composite hot and cold curves for the ERPP design of Figure 2.2, including all process streams with a temperature greater than that of the available cold utility (32^{o}C).

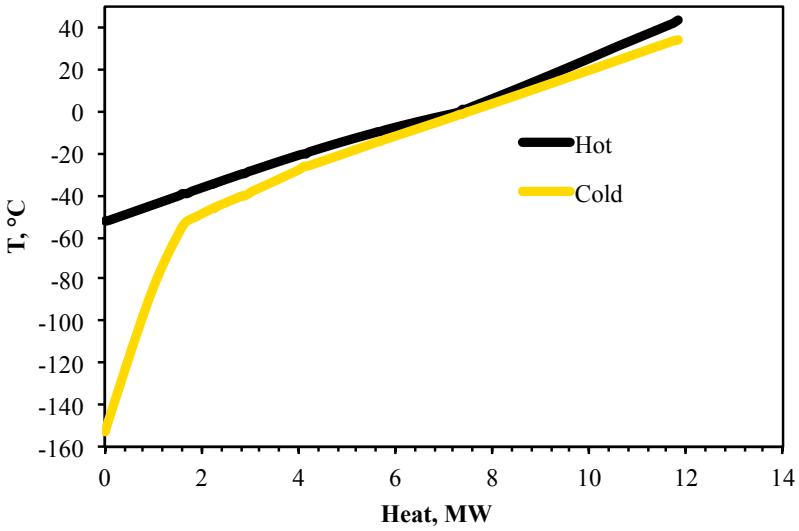

Figure 2.6. Heat Composite hot and cold curves of the heat exchangers E-4, E-5, E-6, and E-7 in the CO_2CL section of Figure 2.3.

In such a case, a portion of the NG needs to be combusted to supply the deficit heat required, which is not considered in this article. Also shown in Figure 2.7 is the improvement in power generation efficiency if the steam reformer can be operated at lower STC ratios. As the steam requirement is reduced, the turbine T-4 discharge pressure can be lowered to produce additional power without violating the minimum temperature approach in heat exchanger E-2. For instance, the maximum power generation efficiency of 76.0% is achievable at STC ratio of 1.5, which is close to the critical STC ratio for steam methane reforming [53]. Currently, this is made impractical due to the need for excess steam to suppress carbon formation during reforming [53].

The sensitivity of the power generation efficiency to the power needed for carbon dioxide compression and dehydration is represented in Figure 2.8. For all other process variables remaining constant, the maximum power generation efficiency is achieved for a compressor K-2 discharge pressure of 15 bar. Increasing the discharge pressure beyond 15 bar will allow for condensing additional water from stream 14 in Figure 2.2. This will reduce the regeneration energy penalty for the molecular sieve adsorbers (see Figure 2.9) at the expense of increasing the K-2 compressor power input. On the other hand, pressures below 15 bar will reduce K-2 compression power but will increase the regeneration energy requirements of the molecular sieve adsorbers. As a result greater fraction of the NG feed needs to be diverted via stream R1 to the adsorber being regenerated (see Figure 2.9). The overall effect of decreasing K-2 pressure below 15 bar is a reduction in the power generation efficiency. As shown in Figure 2.9, for a K-2 discharge pressure below 12 bar, the regeneration gas flow is identified to be more than the NG feed flow to the plant. Therefore, it is preferable to keep the K-2 discharge pressure to be higher than 12 bar.

The process power generation efficiency can also be improved by reducing the minimum temperature approach of the heat exchangers and SOFC. For example, for a STC ratio of 2.5, reducing the minimum temperature approach from 28^{o}C to 5^{o}C raises the power generation efficiency from 71.2% to 72.2% (see Figure 2.10).

Designing heat exchanger E-1 and E-2 to operate with lower minimum temperature approaches (i.e. lower than 28°C) will give the opportunity to further expand streams 9 and 25 in turbines T-4 and T-2, respectively. This will increase the net power output of the plant. However, it should be noted that reducing the minimum temperature approach would increase the heat transfer area and result in increased capital costs.

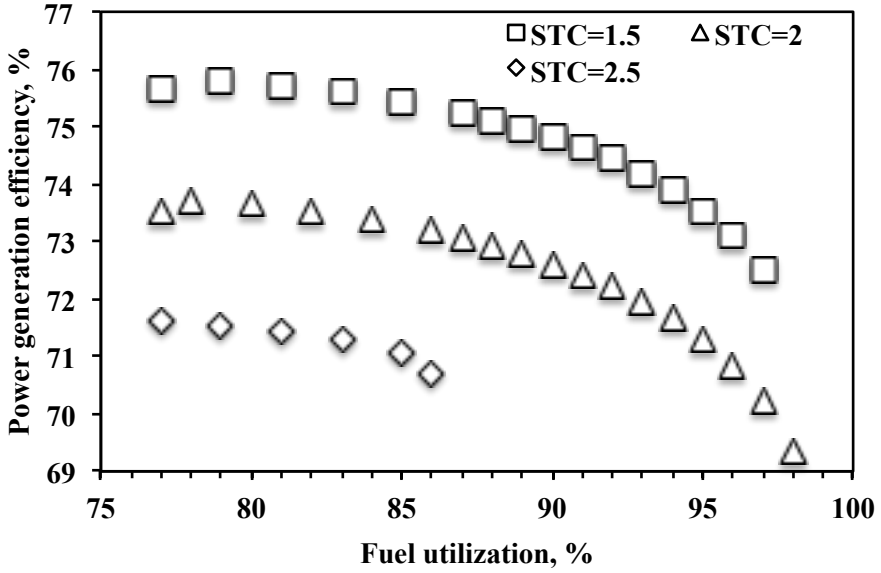

Figure 2.7. Impact of fuel utilization and NG reforming Steam To Carbon (STC) ratio on the power generation efficiency of the ERPP design of Figure 2.2.

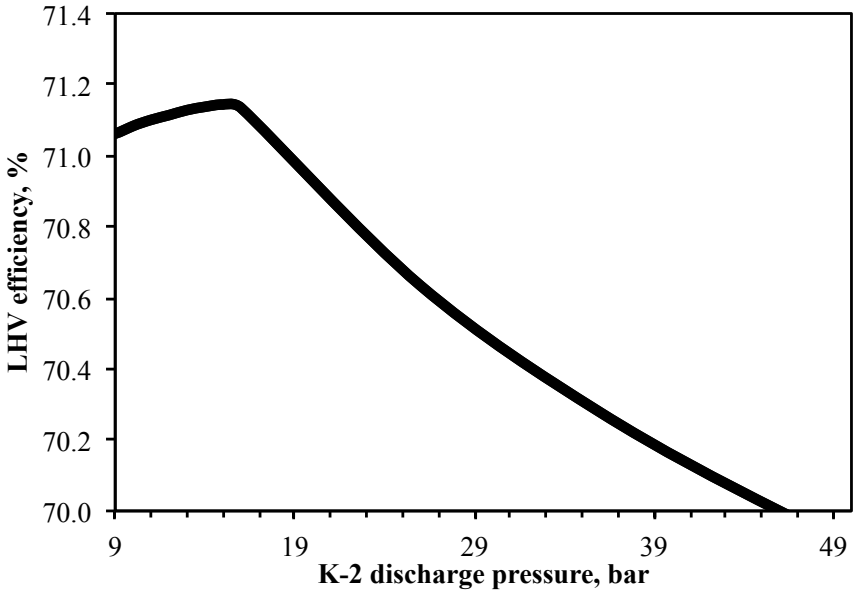

Figure 2.8. Impact of K-2 discharge pressure on the power generation efficiency of the ERPP design of Figure 2.2.

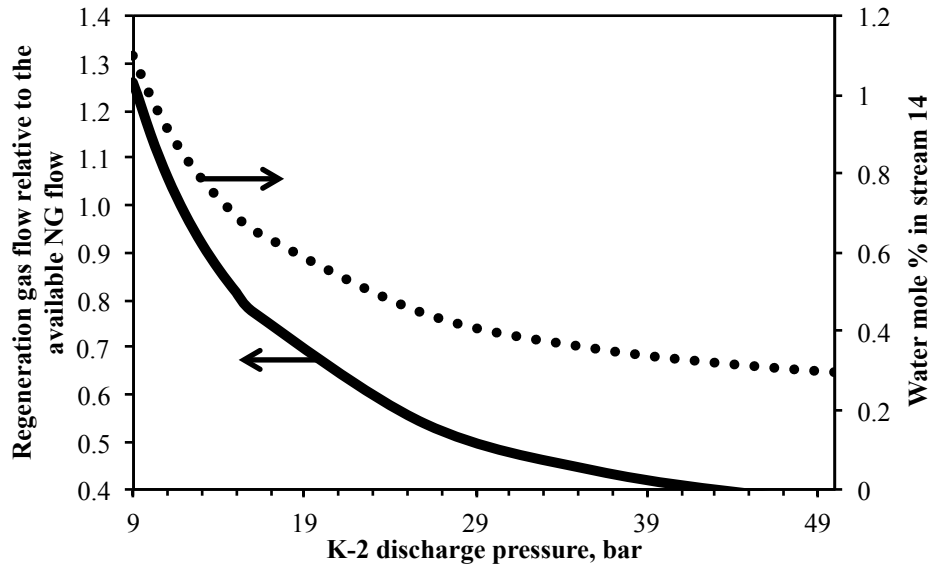

Figure 2.9. K-2 discharge pressure effect on the regeneration requirements of molecular sieve adsorber and stream 14 water content in Figure 2.2.

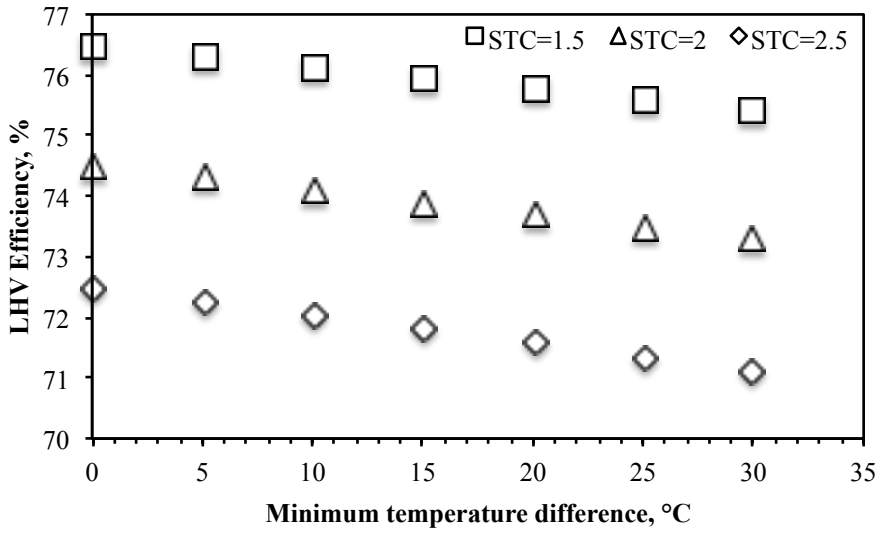

Figure 2.10. Variation of power generation efficiency against minimum temperature approach across the SOFC and heat exchangers E-1 and E-2 at different Steam To Carbon Ratios (STC) for NG reforming.

2.5 Alternative designs for carbon dioxide capture

While the CO_2CL section of Figure 2.3 is carried out using three separation stages, the process objective (i.e. carbon dioxide recovery and purity) can also be achieved using a configuration with two separation stages shown in Figure 2.11. However, as discussed below, a major drawback of such configuration is its higher compression power requirements relative to the three separation stages configuration of Figure 2.3. Further net power reduction is expected if one chooses to use four or more separation stages. Figure 2.12 presents the variation in input power requirement and carbon dioxide recovery for different values of feed pressures (i.e. K-A discharge pressure in Figure 2.11), second stage temperature (i.e. stream C temperature) and second stage pressure (i.e. K-B discharge pressure). The results of Figure 2.12 are generated using a standalone simulation of the CO_2CL process, carried out in isolation of the other components of the flowsheet of Figure 2.2. Here, the temperature of stream A is simultaneously varied to ensure that the minimum temperature approach (i.e. 1.1^oC) is not violated. As shown in Figure 2.12 for a fixed feed pressure, increasing the second stage pressure and decreasing the second stage temperature increases the per pass liquid carbon dioxide recovery as well as the net compression power required (for the compressors and turbines shown in Figure 2.11 . At the same time, for fixed second stage temperature and pressure, lowering the feed pressure reduces the net compression power (Figure 2.12(a) vs Figure 2.12(b)). However, a minimum limit of 15 bar is identified to be essential for maximizing the per pass liquid carbon dioxide recovery. For example, at a feed pressure of 13 bar (Figure 2.12(f)), the recovery is limited to near 80% at K-B pressure of 100 bar and stream C temperature of -45^oC. The temperature of stream C cannot be further reduced because it will result in violating the temperature approach in the heat exchanger. For feed pressures higher than 15 bar, the maximum per pass liquid carbon dioxide recovery of near 85% is achievable at K-B discharge pressure of 100 bar (Figure 2.12(b) and Figure 2.12(d)). While higher second stage pressures can improve liquid carbon dioxide recovery, the

maximum pressure of 100 bar is set in accordance with existing heat exchanger design limits.

For the CO_2CL configuration using three separation stages (Figure 2.3), the sensitivity of the relative net compression power input to the intermediate separation stage pressure (K-4 discharge pressure) and temperature (stream 36 temperature) is shown in Figure 2.13. Although the intermediate separation stage temperature and pressure impacts the process net compression power, the per pass liquid carbon dioxide recovery remains nearly constant at 85%. As seen in Figure 2.13, the minimum net compression power is achieved at an intermediate stage pressure and temperature of 30 bar and -25^{o}C, respectively.

As mentioned earlier, an alternative CO_2CL configuration to the one of Figure 2.3 would use a turbine device instead of a J-T valve for expanding stream 30 to 10 bar, resulting in stream 31 temperature of -32^{o}C. Such lower temperature (lower than the case of Figure 2.3) is a consequence of the power generation (i.e. enthalpy around the expander is not constant) associated with the turbine and leads to an improvement in the process efficiency from 71.2% to 71.7%. In this case, the optimal discharge pressure of the compressors K-2, K-3, and K-5 are estimated to be 18, 25, and 83 bar, respectively. Additionally, stream 29, 35, and 40 would need to be cooled to temperatures of -5^{o}C, -6^{o}C, and -51^{o}C, respectively.

Rather than LNG, if NG is available as a compressed gas from a pipeline (desulfurized and at 31 bar, 38^{o}C [54]) at the plant gate, then the CO_2CL section can be modified to either of the processes shown in Figure 2.14 or Figure 2.15. In both of these configurations, NG is expanded in turbine T-1 to 11 bar (SOFC pressure plus pressure drops), and then used in the CO_2CL section to recover the refrigeration available from expansion. In the process of Figure 2.14, liquid carbon dioxide (99.6 mol%) in stream 32 is pressure reduced to 6 bar (set to give a minimum temperature approach of 1.1^{o}C) and evaporated in the heat exchangers to provide the remaining process refrigeration. The carbon dioxide gas, stream A, is compressed in intercooled

multistage compressor K-6 to supercritical pressure of 100 bar, condensed, and finally pumped to 150 bar for pipeline transportation.

Instead of supercritical carbon dioxide, the alternative configuration of Figure 2.15 is proposed to produce low pressure liquid carbon dioxide. Here, a mixed refrigerant (MR) vapor compression cycle [40] is chosen to provide the process refrigeration requirements. In this case, compressor K-6 is used to compress the MR (optimal molar composition of 14% methane, 5% ethane, 1.2% propane, and 27% normal butane) to 19 bar which is subsequently cooled and condensed as it flows through heat exchangers E-4, E-5, and E-6. Leaving heat exchanger E-6, the high pressure liquid MR is reduced to 13 bar pressure and then rerouted via stream D to the heat exchangers to supply the process refrigeration. As seen in Table 2.3 use of the configurations of Figure 2.14 and Figure 2.15 in the developed ERPP results in power generation efficiencies of 70.5 and 70.4%, respectively. In both cases, the additional work required by the compressor K-6 is responsible for lowering the power generation efficiency below the efficiency of the ERPP using LNG. Heat exchangers composite curves and optimization approach are available in Figure 2.16, Figure 2.17, and Table 2.2, respectively. Detailed material and energy balance are available in appendix B and C.

Table 2.2
Optimization problem formulation for CO_2CL section of the process Figure 2.15

Minimize	K-6 power
Subject to	E-4,5,6, and 7 minimum temperature approach ≥ 1.1 °C
Independent variables	(1) K-6 discharge pressure (5 to 40 bar) (2) Stream C temperature (0 to -60 °C) (3) Stream D pressure (1.2 to 35 bar) (4) MR molar composition (methane: 0 to 1, ethane: 0 to 1, propane: 0 to 1, butane: 0 to 1) (5) Stream A flow rate (1,000 to 10,000 kmol/h)
Method	Aspen Plus SQP

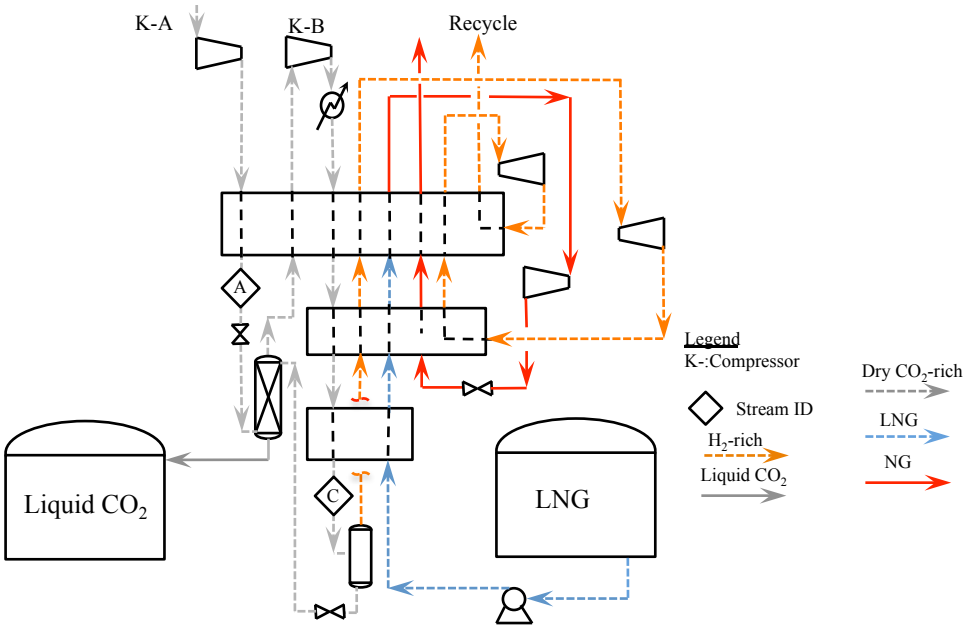

Figure 2.11. Alternative CO_2CL process configuration using two separation stages.

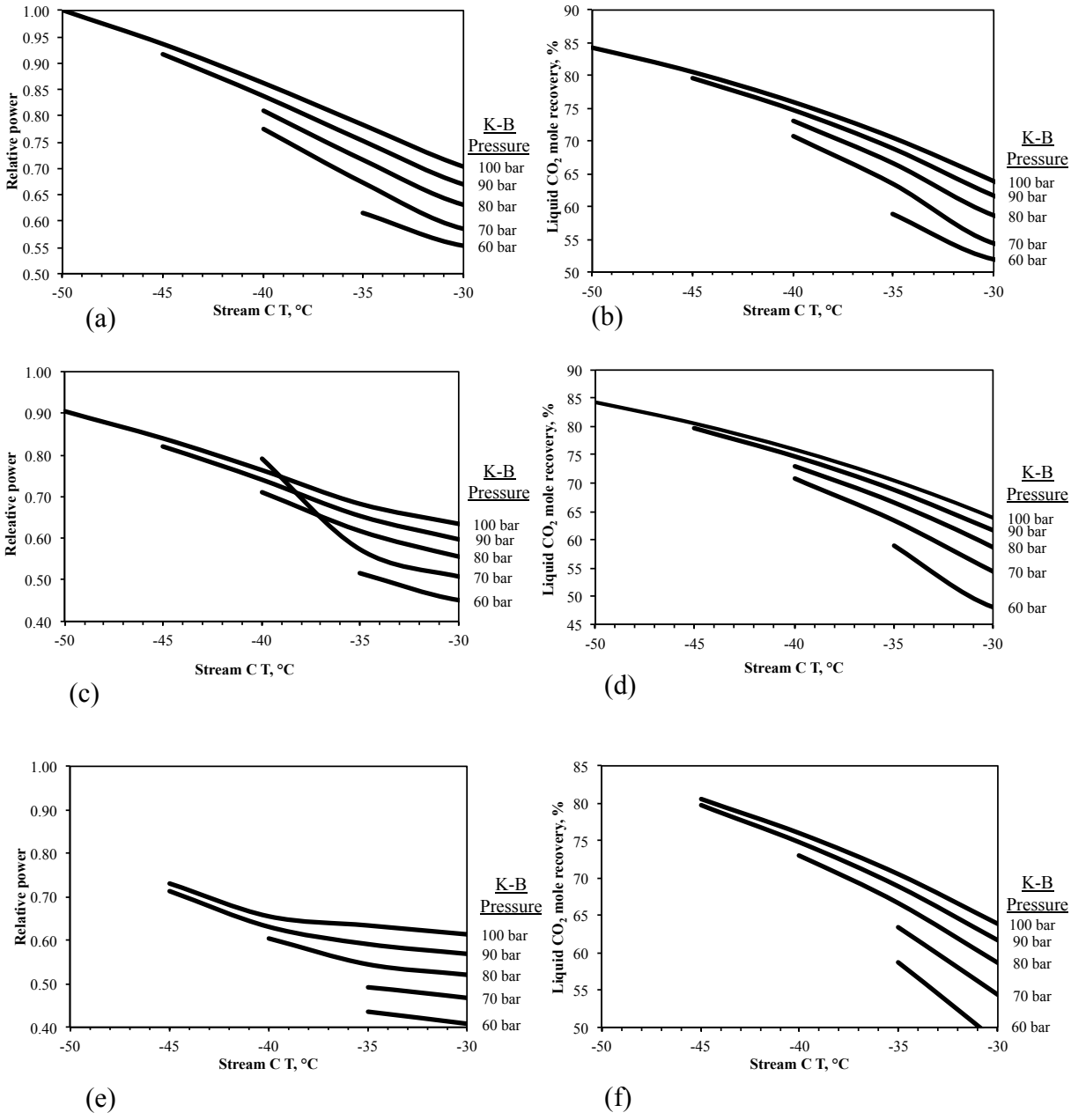

Figure 2.12. Characteristics of the CO_2CL configuration of Figure 2.11 for (a and b) K-A discharge pressure of 30 bar, (c and d) K-A discharge pressure of 20 bar, and (e and f) K-A discharge pressure of 13 bar. All the power values are relative to the maximum power for the case in (a).

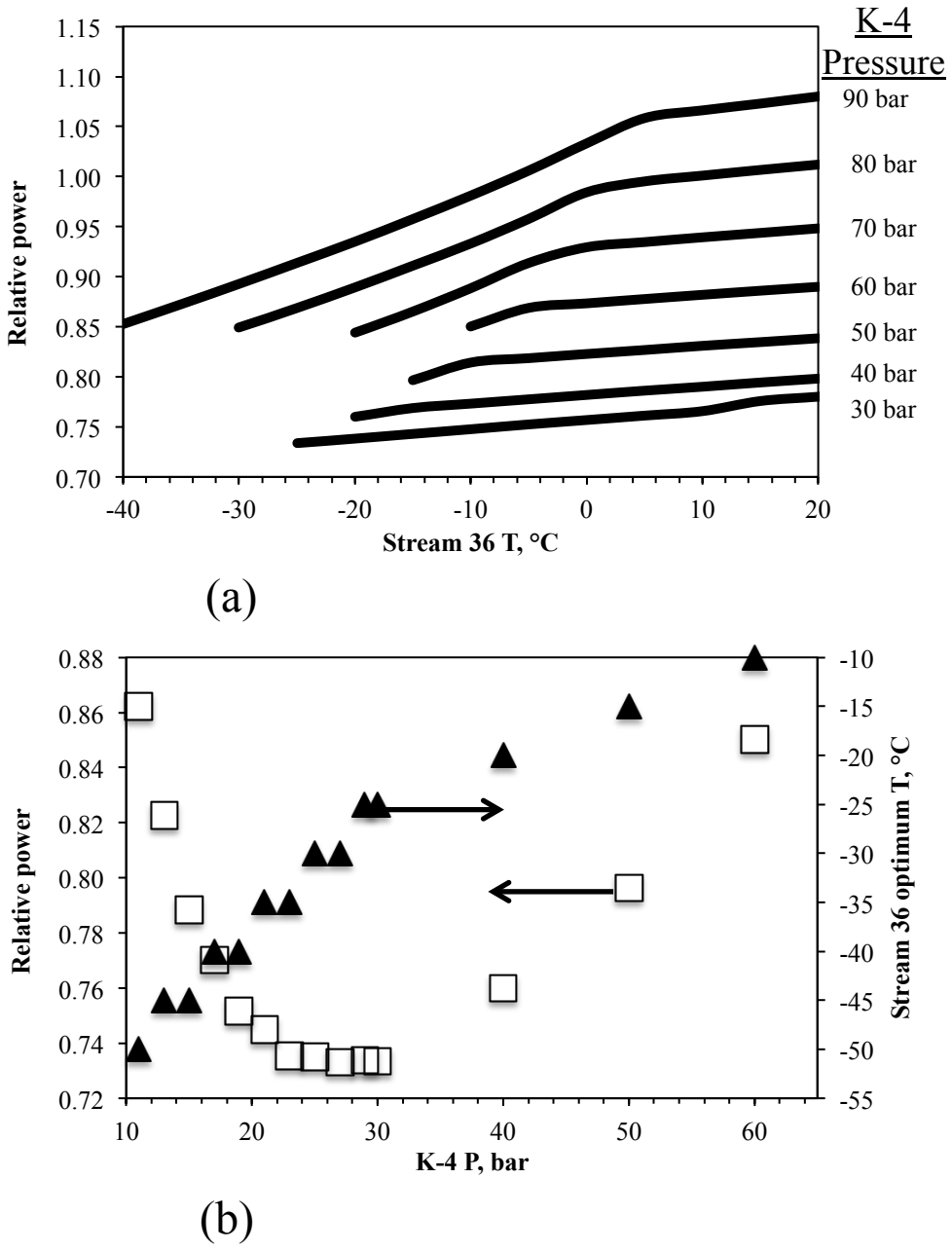

Figure 2.13. Characteristics of the CO_2CL process configuration using three separation stages (Figure 2.3). The power is relative to the maximum power for the case (a) in Figure 2.12.

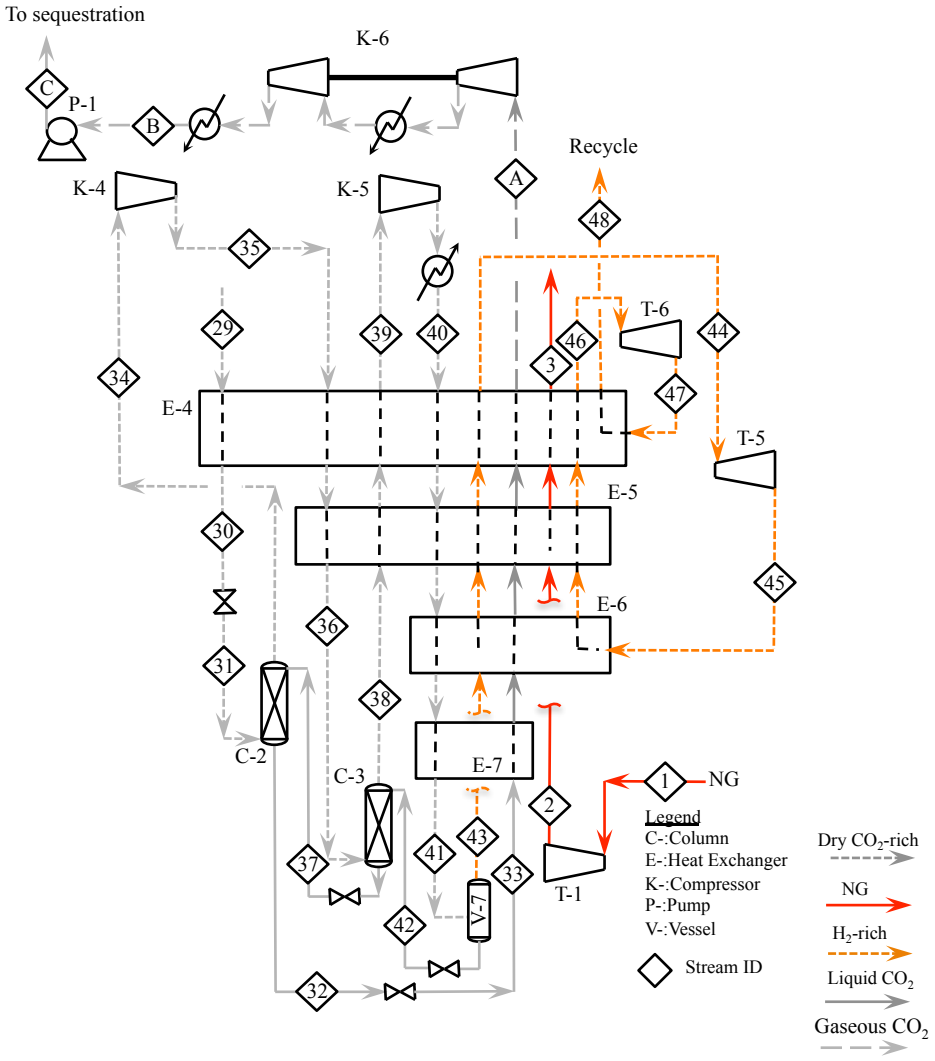

Figure 2.14. Alternative CO_2CL process configuration in which NG is available from a pipeline at the plant gate and the captured carbon dioxide is compressed to supercritical conditions for pipeline transportation. Stream data available in appendix B.

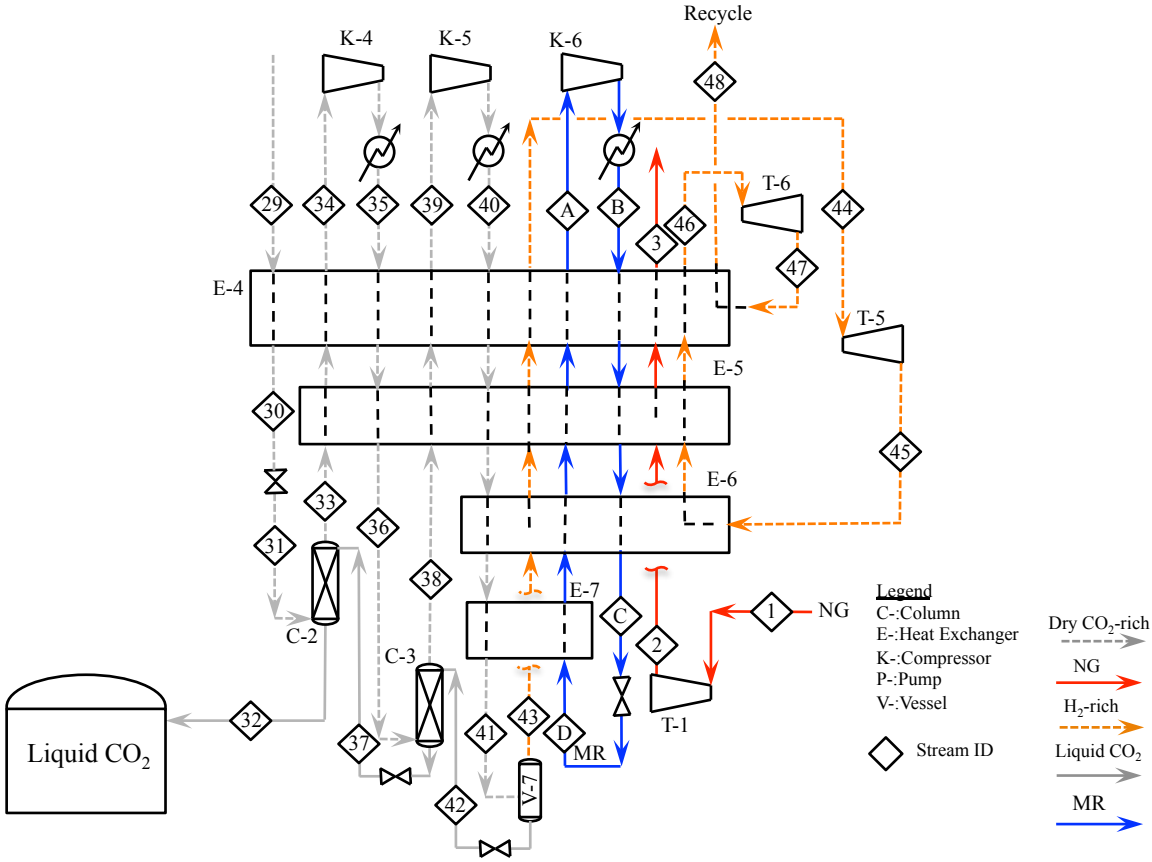

Figure 2.15. Alternative CO_2CL process configuration in which NG is available from a pipeline at the plant gate and the captured carbon dioxide is stored as a low pressure liquid. Stream data available in appendix C.

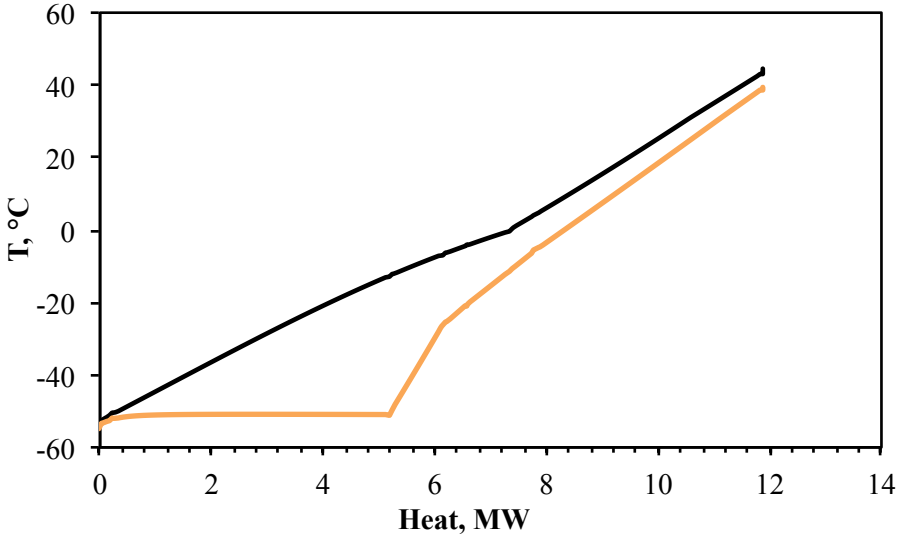

Figure 2.16. Hot and cold composite curves for the CO_2CL process producing supercritical carbon dioxide (Figure 2.14).

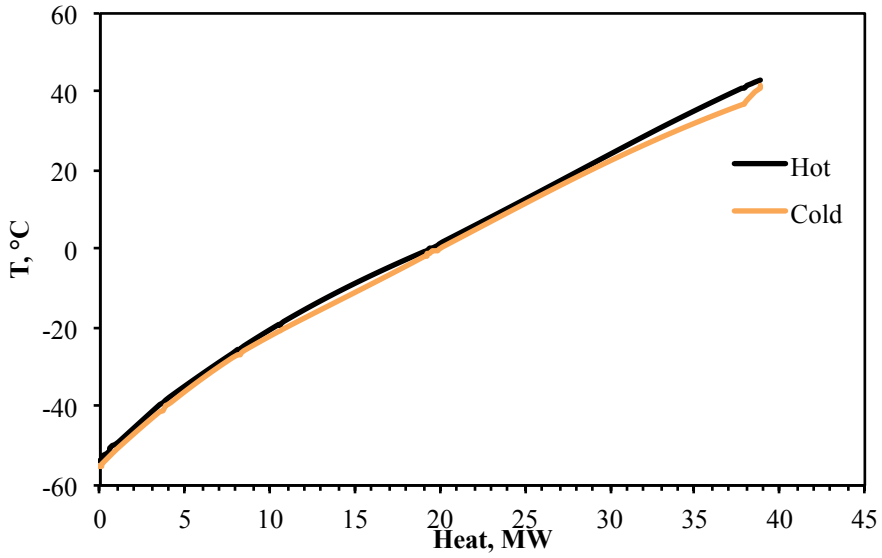

Figure 2.17. Hot and cold composite curves for the CO_2CL process using MR cycle (Figure 2.15).

2.6 ERPP vs conventional Solid Oxide Fuel Cell (SOFC) power plant

The conventional SOFC power generation plant [46], shown in Figure 2.18, is rigorously simulated to compare it with the developed ERPP designs. Here, the process does not capture carbon dioxide and the SOFC anode exhaust is combusted with the depleted air stream leaving the cathode side of the device. The combustion effluent gas is then expanded in turbine T-1 to a pressure of 3 bar, cooled by heat recovery in heat exchanger E-1 and E-2 to a temperature of 179^{o}C and 94^{o}C, respectively, and finally expanded to 1.1 bar in turbine T-2. Water is condensed for recycle to the SOFC reformer via pump P-2 and the carbon dioxide rich gas (stream 13) is discharged to the atmosphere. The process power generation efficiency of the plant is calculated to be 73.0%, which is slightly more efficient than the ERPP fed with LNG or NG as seen in Table 2.3. Also, notice the lower SOFC power output compared to the ERPP design. The difference is indicative of the additional power generated in the SOFC due to the recycle stream 48 in the ERPP design. It is interesting to note that the power penalty associated with the recovery and liquefaction of carbon dioxide is only 1.8% when compared with ERPP-LNG. This reflects the synergistic nature of the overall ERPP flowsheet.

The impact of the fuel utilization and turbine T-1 discharge pressure on the power generation efficiency of the conventional SOFC power plant (Figure 2.18) is shown in Figure 2.19. For each turbine T-1 discharge pressure, increasing the fuel utilization increases the power generation efficiency since a greater fraction of the net power is produced by the SOFC compared to the less efficient downstream combustion/turbine system. However, beyond a certain a fuel utilization (i.e. SOFC current), the heat dissipation from the SOFC becomes dominant, requiring increasing amounts of air feed for heat absorption. In such a case, the cascading energy losses associated with air compression, heating and expansion result in decreasing the power generation efficiency.

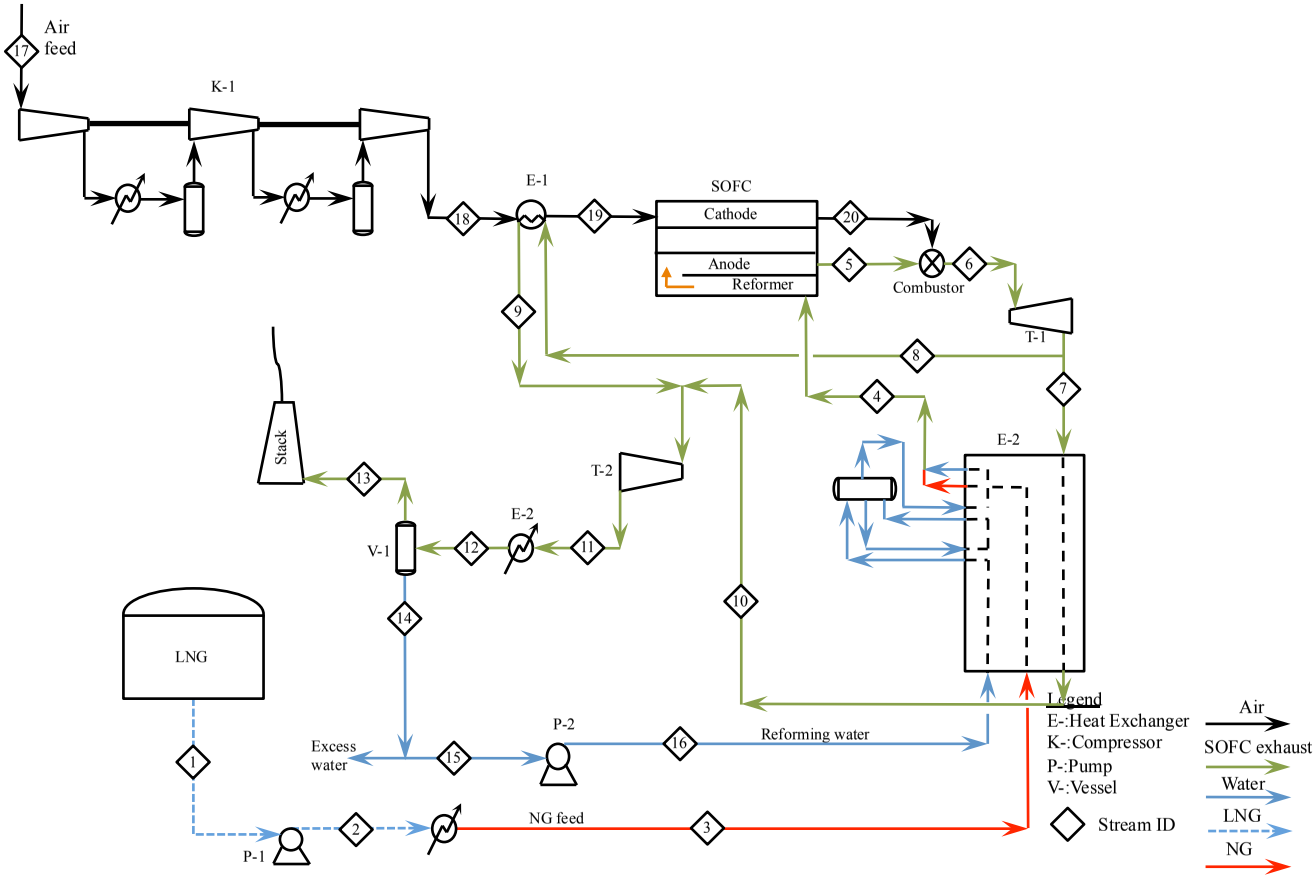

Figure 2.18. Conventional SOFC power plant without carbon dioxide capture. Unconverted hydrogen and carbon monoxide in SOFC exhaust gas is combusted in air for additional power generation. Stream data available in appendix D.

Table 2.3
Simulation results for the different ERPP designs as well as a comparable design for a conventional SOFC power plant using NG or LNG. The basis for all the power plant designs is a constant NG feed rate of 895 kmol/hr.

	ERPP-LNG	**ERPP-NG Supercritical CO_2**	**ERPP-NG Liquid CO_2**	**Conventional SOFC without CO_2 capture**
Compressors, MW				
K-1	27.42	27.42	27.42	26.12
K-2	1.41	1.41	1.41	-
K-3	0.02	0.02	0.02	-
K-4	3.89	2.68	3.98	-
K-5	3.05	3.08	3.09	-
K-6	-	2.89	1.76	-
Turbines, MW				
T-1	-0.35	-0.46	-0.46	-40.40
T-2	-6.81	-6.81	-6.81	-4.80
T-3	-9.99	-9.99	-9.99	-
T-4	-0.71	-0.71	-0.71	-
T-5	-1.06	-1.12	-1.15	-
T-6	-0.56	-0.51	-0.49	-
SOFC AC power, MW	-174.33	-174.33	-174.33	-142.81
Pumps, kW				
P-1	165.7	-	-	16.20
P-2	18.91	18.91	18.91	19.84
Net power output, MW	-157.83	-156.41	-156.28	-161.85
Feed LHV, MW		221.93		
Power generation efficiency, %	71.2	70.5	70.4	73.0

Negative values indicate power generation. Positive values indicate power consumption.

For each T-1 discharge pressure considered in Figure 2.19, there exists a value for the fuel utilization, exceeding which results in a minimum temperature approach (of 28^{o}C) violation in heat exchanger E-1. For example, in case the T-1 discharge pressure is equal to 4 bar, the minimum temperature approach in heat exchanger E-1 is violated for fuel utilization values greater than 92%. This is due to the increased air flow needed for the SOFC cooling. As T-1 discharge pressure is increased, more

heat is available in the turbine discharge stream. This also implies that the SOFC can be operated at higher fuel utilization without violating the minimum temperature approach in heat exchanger E-1. However, the overall effect of increasing T-1 discharge pressure is reduction in the power generation efficiency.

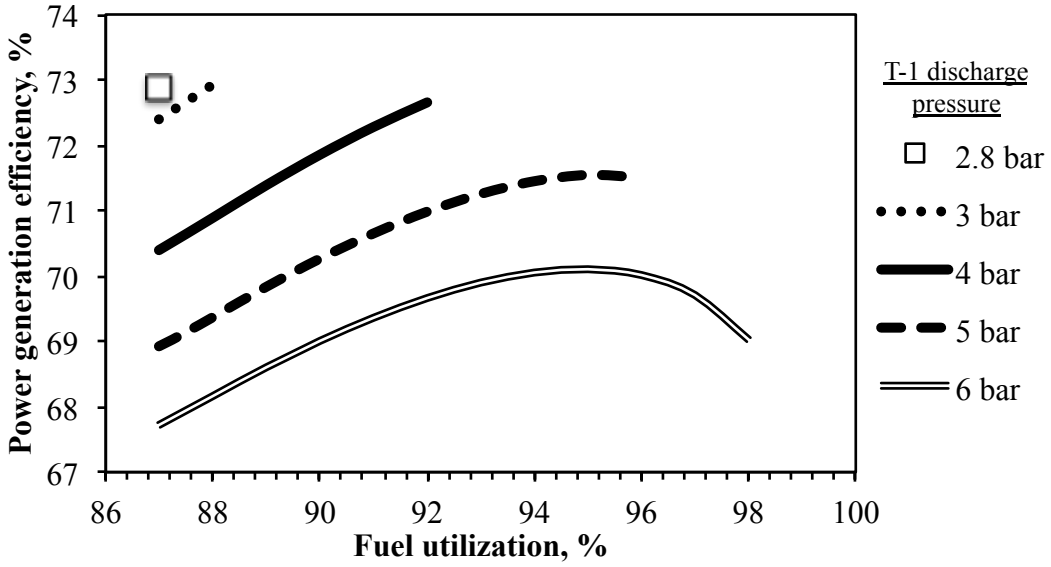

Figure 2.19. Effect of the SOFC fuel utilization and Turbine T-1 discharge pressure on the power generation efficiency of the process of Figure 2.18. Fuel utilization below 87% produces insufficient heat for steam reforming and is therefore not considered here. At each fuel utilization value, the flow of stream 7 is varied to maintain a minimum temperature approach of 28^{o}C in E-2 heat exchanger.

2.7 Methanol fueled ERPP

Methanol synthesis via renewable carbon dioxide and hydrogen, has been extensively discussed in the literature as a candidate energy carrier that can reduce the use of fossil fuel [13, 55]. The use of methanol in ERPP is; therefore, investigated. Detailed flowsheet and material and energy balances are presented in appendix E. The flowsheet is similar to the ERPP shown in Figures 2.2 and 2.15 with the fol-

lowing exceptions. 1) Methanol is used instead of (LNG). 2) The calculations show that expanding the SOFC exhaust, as in the case of the ERPP using LNG, results in violating the minimum temperature difference in the downstream heat exchanger E-1 (see Figure E.1 in appendix E). This may be related to the excess heat requirements to vaporize methanol (i.e. latent heat of vaporization) in the heat exchanger. Thus, the turbine is eliminated and the SOFC exhaust is directly fed into heat exchanger E-1. 3) Due to the lack of a refrigeration source, the MR based process shown in Figure 2.15 is used for the CO_2CL section without the NG feed.

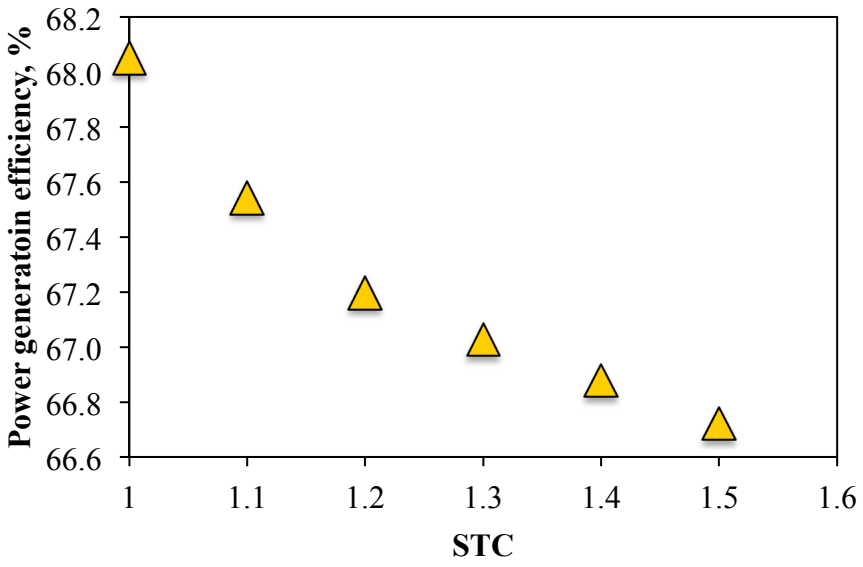

Figure 2.20. STC effect on the power generation efficiency of the methanol based ERPP shown in Figure E.1.

The simulation results reveal that the use of methanol in the ERPP gives a power generation efficiency of near 67% with LHV being calculated in which methanol is in the gas phase. If the liquid phase LHV is utilized, then the efficiency will increase to near 71%. The need to evaporate the 10 bar (SOFC pressure) methanol, which has a boiling point of 140^{o}C, and the lack of refrigeration source for CO_2CL are the main losses involved in the process. However, it worth mentioning that the reduced STC

(STC has to be slightly higher than 1) requirements for methanol reforming seems to be a key contributor to the relatively high efficiency of the process. Reducing the STC from the base case value of 1.3 to the stoichiometric steam requirements of 1, see Figure 2.20, can improve the power generation efficiency from 67% to 68% (with gaseous methanol LHV basis). However, slightly excess steam is needed to avoid any carbon deposition at the catalyst surface.

2.8 Efficient oxy-fuel Combined Cycle (CC)

Figure 2.21 shows a newly developed oxy-fuel NGCC that achieves 98 mole% liquid carbon dioxide recovery with relatively high efficiency. The process uses the same CO_2CL configuration deployed for the ERPP with LNG refrigeration being utilized to provide portion of the refrigeration need. Here, the process is developed, modeled, and simulated using Aspen Plus^{TM} for LNG feed similar to the one used in the ERPP. Detailed material and energy balances and design basis are presented in appendix F and chapter 6, respectively. The process of Figure 2.21 is different from previously discussed oxy-fuel NGCC [1, 27, 56] in terms of turbine exhaust heat utilization. In a typical configuration, the gas turbine exhaust is used to raise steam at multiple pressures in a HRSG for subsequent power generation in steam turbines [27]. While this approach helps in improving the power generation efficiency, it is associated with excessive exergy losses when applied for oxygen-based combustion. The reason is the high turbine exhaust temperature (in excess of 800^{o}C) relative to the maximum temperatures at which the steam turbines operate (near 550^{o}C). This implies big temperature differences (near 250^{o}C) in the HRSG; thus, excessive exergy losses. On the other hand, in an air based NGCC process (i.e. combustion is carried out using air), the gas turbine discharge temperature is near 600^{o}C [54]. Hence, the exergy losses in the HRSG are much lower than a cycle that uses oxygen-based combustion. The difference in exhaust temperature between these two cycles may be related to the physical properties of the turbine operating fluid (i.e. turbine inlet stream).

In particular, the fluid constant pressure heat capacity (C_p) and the change of the fluid volume with respect to temperature, see equation below, seems to be the two properties that control the turbine exhaust temperature.

$$dH = C_p dT + (V - T(\frac{\delta V}{\delta T})_p)dp \tag{2.7}$$

To overcome this, the process of Figure 2.21 uses the gas turbine exhaust (i.e. stream 9) to heat up the inlet NG (in stream 6) and oxygen/carbon dioxide mixture in stream 19. As revealed by the composite curves of heat exchanger E-1 and E-2, see Figure 2.22, this scheme of heat recovery results in near minimum temperature differences being achieved across most of the heat exchangers length. Consequently, exergy losses are minimized.

Referring to Figure 2.21, NG in stream 6, leaving CO_2CL section, is heated in heat exchanger E-2 to a temperature of 818^{o}C using portion of turbine T-2 exhaust stream (i.e. stream 11). The other portion of the exhaust is used to heats up the oxygen/carbon dioxide mixture in stream 19 (using heat exchanger E-1) to a temperature of 818^{o}C. NG, leaving heat exchanger E-2 (via stream 7), is combusted in the combustion chamber (using oxygen in stream 20) in which pressurized carbon dioxide acts as a diluent to maintain a maximum temperature of 1,328 ^{o}C (design basis) at the combustor outlet (i.e. stream 8). The discharge of the combustion chamber is then expanded in turbine T-2 to generate the needed electrical power. Turbine T-2 exhaust is cooled to 432^{o}C (stream 13 temperature) in heat exchanger E-1 and E-2, then utilized in the HRSG to raise steam at three pressures (4.9, 24.1, and 119.1 bar). The generated steam are used to produce additional electrical power in steam turbine T-3, T-4, and T-5.

Leaving the HRSG, the flue gas in stream 14 is cooled to 43^{o}C to condense the combustion byproduct water (by cooling in heat exchanger E-3 followed by E-4), which is then separated in vapor-liquid separator V-1. Part of the uncondensed gas, comprising of near 84mole% carbon dioxide and leaving separator V-1, is fed to multistage intercooled compressor K-5 while the other part (in stream 17) is recycled

to the combustor via compressor K-3. Compressor K-5 recovers water, condensed in heat exchanger E-5 and E-6, in a similar fashion to compressor K-2 in the ERPP (shown in Figure 2.2). Leaving the compression section (i.e. multistage intercooled compressor K-5), the compressed gas stream 22 is fed to molecular sieve adsorbers V-4 and V-5 for dehydration prior to the CO_2CL process (see section 2.3.2 for reason of dehydration). Similar to the adsorbers in the ERPP (see section 2.3.2), V-4 and V-5 are utilized for dehydrating stream 22 and the fully saturated adsorber V-6 is under regeneration. Regeneration here is carried out using portion of the feed NG (i.e. stream 6) withdrawn from heat exchanger E-2, via stream R1, at a temperature of 310^{o}C.

For oxygen generation, a conventional cryogenic ASU is used to supply the gaseous oxygen needed for combustion. The ASU consists of multistage intercooled air compression K-1, adsorbers V-8 and V-9, main heat exchangers E-13, air turbine T-9, high pressure column C-4, low pressure column C-5, and subcooler E-14. As in a typical cryogenic ASU configuration, column C-4 condenser is thermally linked to column C-5 reboiler such that the boiling oxygen in the bottom of the C-5 column supplies the refrigeration needed for condensing the nitrogen-rich stream utilized as a reflux for column C-4 and C-5. The pressure difference between column C-4 and C-5 ensures feasible temperature difference between the condensing nitrogen-rich reflux and boiling oxygen.

Referring to Figure 2.21, air in stream 51 is compressed (via multistage intercooled compressor K-1) to a pressure of near 5.8 bar then send to adsorbers V-8 and V-9. In the adsorbers, water and carbon dioxide are almost totally removed from the air stream to avoid the undesirable freezing conditions in the downstream equipment (see section 2.3.2 for explanation). The pressurized air stream leaving the adsorber is then cooled to -175^{o}C (close to the stream dew point) to be fed to the high pressure column C-4 operating at near 5 bar. Column C-4 is a rectifying column (i.e. a distillation column without a reboiler) producing enriched oxygen stream leaving the bottom of the column (i.e. stream 55) at a concentration of around 32 mole% . The enriched

oxygen in stream 55 is then pressure reduce to near 1.5 bar (via a J-T valve) for further purification in low pressure column C-5. At the top of column C-4, portion of the liquid nitrogen-rich stream (99.6 mole%), condensed in column C-4 condenser, is withdrawn via stream 60 for use as a reflux for column C-5. Prior refluxing, stream 60 is slightly subcooled in subcooler E-14 to be then pressure reduced to near 1.5 bar across the J-T valve. Subcooling is carried out to minimize the vapor generation across the downstream (i.e. downstream E-14) J-T valve. A relatively pure nitrogen (near 99.2 mole%) at a temperature of -192^{o}C leaves the top of column C-5 (via stream 57) to provide the refrigeration needed in heat exchanger E-14 and portion of the refrigeration required by the main heat exchanger E-13. On the other hand, gaseous 95 mole% oxygen is withdrawn from the bottom of column C-5 (i.e. stream 65) for refrigeration recovery in the main heat exchanger E-13. To compensate for any refrigeration loss from the ASU (via heat leaks), portion of the compressed air stream 63 is expanded in turbine T-9 and fed to column C-5.

The CO_2CL is similar to the process shown in Figure 2.3 but with an additional turbine T-8, see Figure 2.23. In the process of Figure 2.3, the uncondensed gases leaving vapor-liquid separator V-7 contains unconverted fuel (i.e. hydrogen and carbon monoxide) that are recycled to the SOFC. Thus, to avoid the use of a recycle compressor, turbine T-6 minimum outlet pressure is constrained by the SOFC pressure (i.e. close to 10 bar). However, in the process of Figure 2.23, the gas stream leaving vapor-liquid separator V-7 is eventually vented to the atmosphere (see Figure 2.21); thus, it is expanded to near atmospheric pressure using turbine T-8. This reduced pressure requires the use of the third turbine T-8, otherwise, turbine T-7 discharge temperature, if operated at close to atmospheric pressure, would drop to be less than -55^{o}C. Such low temperature is not desired because it may result in the undesirable carbon dioxide freezing condition.

For the simulation, the optimized operating conditions identified for the CO_2CL in the ERPP (see section 2.3.3) are used here in spite of the difference in the composition of the feed streams between the two flowsheets (ERPP containing SOFC unconverted

fuel and oxy-fuel NGCC containing atmospheric argon, oxygen, and nitrogen). Remarkably, the cooling curves (see Figure 2.6 and 2.24) were found to be very similar in shape implying that both are associated with nearly the same exergy losses. Thus, demonstrating the applicability of the developed CO_2CL process for different type of process technologies.

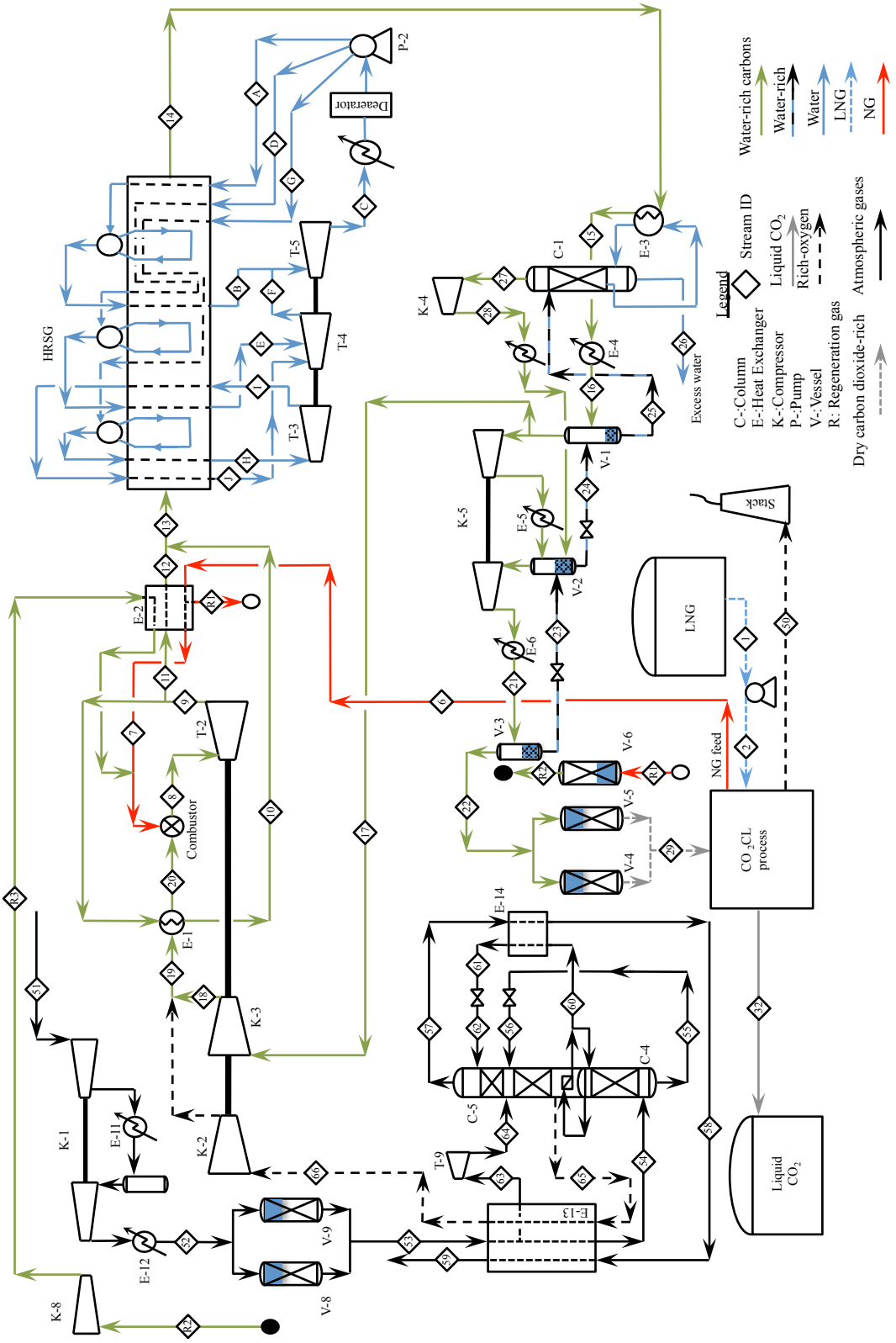

Figure 2.21. The developed oxy-fuel Natural Gas Combined Cycle (NGCC).

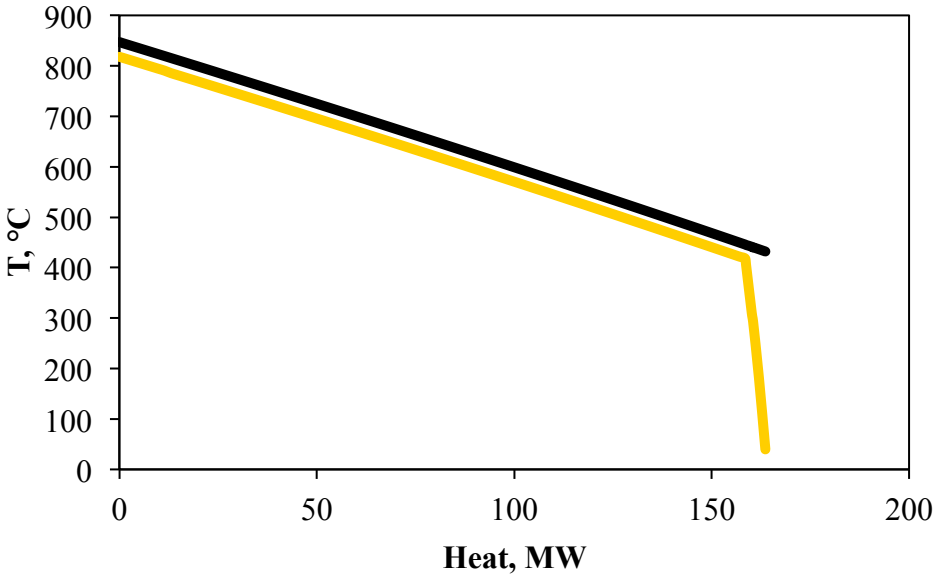

Figure 2.22. Composite hot and cold curves for heat exchanger E-1 and E-2 of the process of Figure 2.21.

2.8.1 Results and discussion

Key simulation results for the developed oxy-fuel NGCC are summarized in Table 2.4. In the cycle, the highest power consumers are the carbon dioxide recycle compressor K-3 followed by the ASU compressor K-1. Both K-1 and K-3 together consume near 55.3% of the total power generated from the turbines (i.e. near 236 MW). Overall, a net power of near 90 MW is generated with a power generation efficiency of near 40% in an LHV basis.

Figure 2.25 shows the impact of the pressure ratio across turbine T-2 on the power generation efficiency. As the pressure ratio is increased from 15 to 27, the power generation efficiency increases from near 38.8 to 40.2%. Beyond a pressure ratio of 27, the efficiency starts to decrease slightly. Increasing the pressure ratio implies that both compressors K-2 and K-3 power increases. However, for pressure ratios up to 27, turbine T-2 power output increases and results in an overall efficiency improvement. Beyond a pressure ratio of 27, the increase in compressors power seems to be more

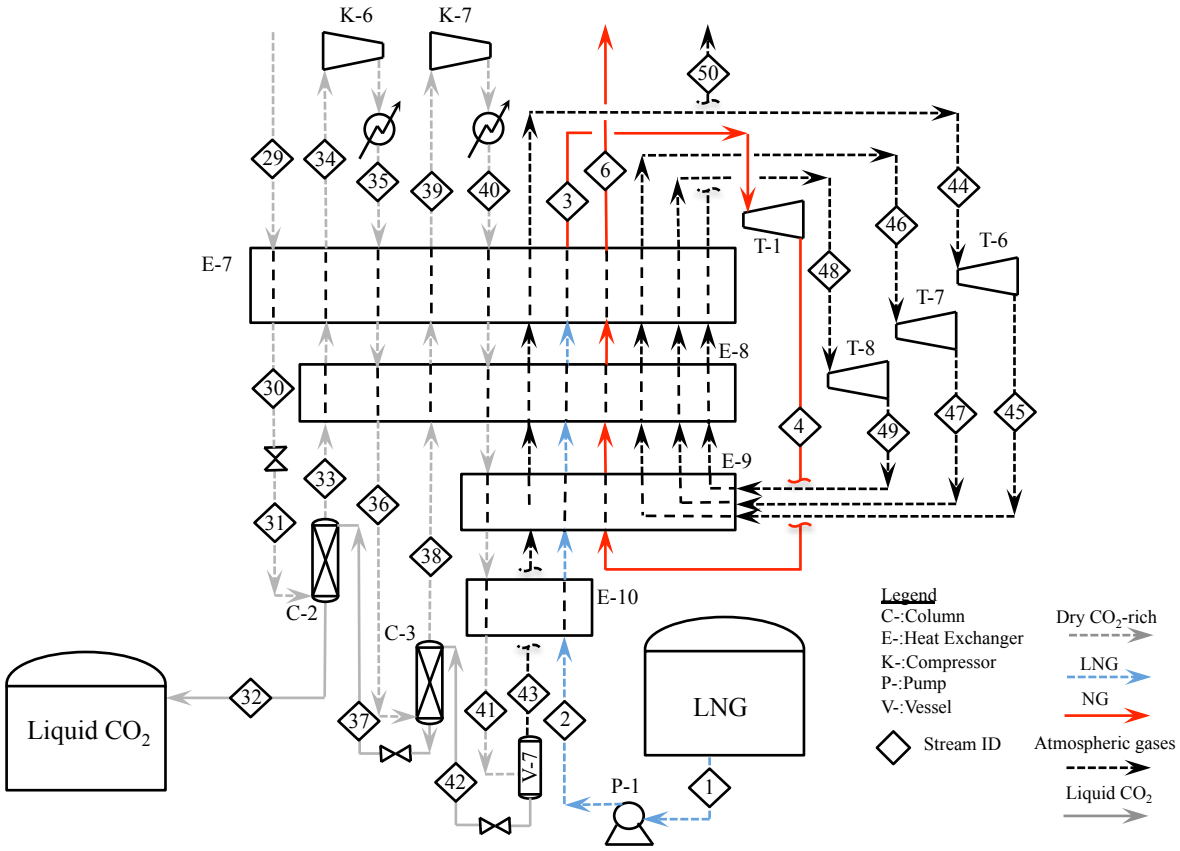

Figure 2.23. Carbon dioxide capture and liquefaction section of the developed oxy-fuel NGCC shown in Figure 2.21.

than that encountered in turbine T-2; hence, power generation efficiency starts to decrease. It also worth mentioning that turbine T-2 pressure ratio is increased by operating turbine T-1 with a higher discharge pressure. Now as T-1 discharge pressure is increased (i.e. increase in turbine T-2 pressure ratio), less refrigeration is extracted from stream 3; therefore, more power is consumed in the CO_2CL section. Thus, contribute to the reduction of the power generation efficiency.

Refereeing to the HRSG sensitivity analysis shown in Figure 2.26, increase in stream G (which is the high pressure steam) pressure, improves the cycle power generation efficiency for most of the investigated range of the other two steam pressures

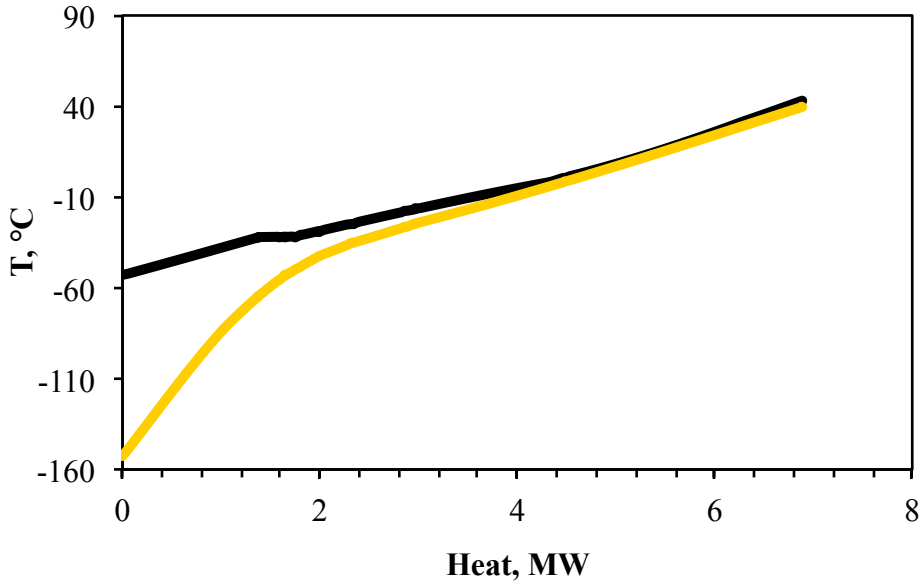

Figure 2.24. Heat Composite hot and cold curves of the heat exchangers E-7, E-8, E-9, and E-10 in the CO_2CL section of Figure 2.23.

Table 2.4
Key simulation results for the developed oxy-fuel NGCC.

Oxy-fuel			
Feed LHV=221.93 MW			
Compressors power, MW		Turbines power, MW	
K-1	19.86	T-1	-0.48
K-2	9.16	T-2	-203.83
K-3	110.65	T-3	-3.57
K-4	0.03	T-4	-9.91
K-5	3.50	T-5	-18.09
K-6	1.67	T-6	-0.07
K-7	1.59	T-7	-0.08
K-8	0.01	T-8	-0.08
		T-9	-2.23×10^{-5}
Net power, MW			
-89.64			
Power generation efficiency, %			
40.2			

Negative values indicate power generation, positive values indicate power consumption.

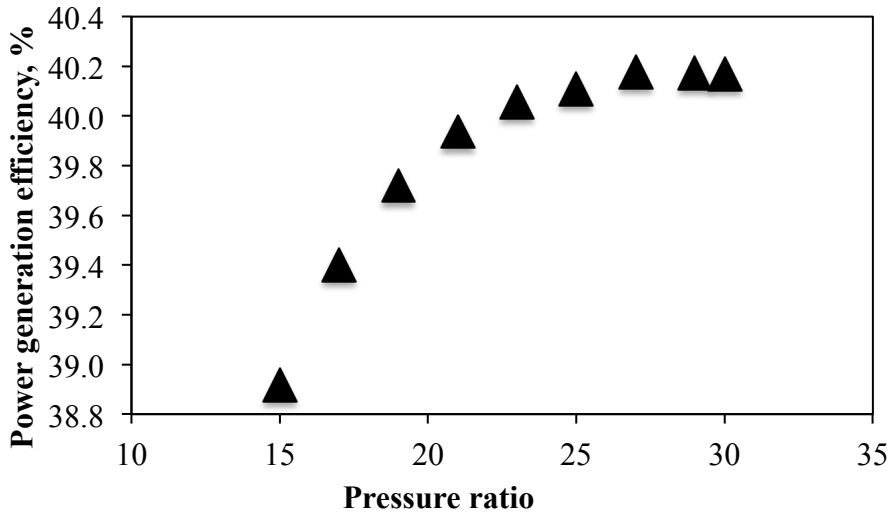

Figure 2.25. Impact of turbine T-2 pressure ratio on the power generation efficiency of the developed oxy-fuel NGCC process of Figure 2.21.

(i.e. stream A and D pressures). However, increasing stream A pressure, which is the low pressure steam, is not preferred. For example, at stream A pressure of 5.8, (see Figure 2.26 (a)) maximum efficiency of near 40.2% is reached at stream D pressure of around 25 bar. On the other hand, increasing stream A pressure from 5.8 to 10 bar, see Figure 2.26(b), will give a maximum power generation efficiency of near 39.9% at stream D pressure near 32 bar. In all the simulated cases of Figure 2.26, the flow rate of each steam (i.e. stream A, D, and G) is varied to ensures a minimum temperature difference of 28^{o}C at each location the steam starts its evaporation.

The developed oxy-fuel NGCC is also investigated with a more efficient ASU design and design specifications other than those found in chapter 6. For example, if the specification given by reference [27] are used along with an ASU specific power of 631 kj/kg oxygen [57], then the cycle power efficiency would increase from 40% to near 49%. The main difference between the design specifications reported in [27] and those presented in chapter 6 (which are used in all the processes discussed in this dissertation) are as follow: 1) lower temperatures approaches in the HRSG (10^{o}C vs 28^{o}C in this work), 2) higher steam turbine efficiency (89 to 92% vs 85% this work,

both in an isentropic basis), 3) lower ambient cooling temperature (30^{o}C vs 43^{o}C this work), 4) minimum steam turbine inlet pressure (4 bar vs 5 bar in this work), and 5) minimum steam turbine discharge pressure (0.04 bar vs 0.07 bar in this work).

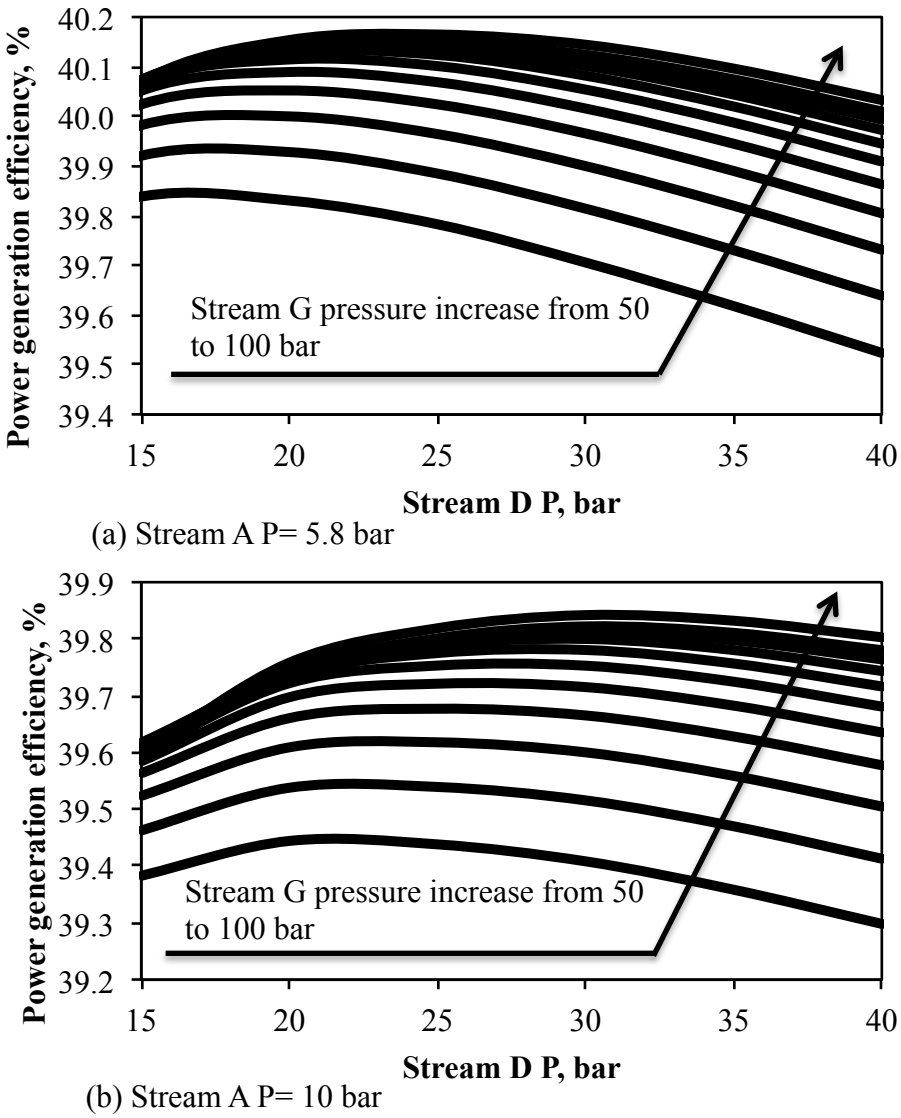

Figure 2.26. Impact of the HRSG steam pressures on the power generation efficiency of the developed oxy-fuel NGCC process of Figure 2.21. (a) Stream A P= 5.8 bar and (b) Stream A P=10 bar.

The developed flowsheet of Figure 2.21 is also investigated for methanol based fuel. However, due to the lack of refrigeration source, the MR based CO_2CL process of Figure 2.15 is utilized here with the addition of a third turbine, see section 2.8 for justification. The simulation of this oxy-fuel MoCC reveals a power generation efficiency of near 38.3% (in LHV basis with methanol in a gaseous state) with 98 mole% liquid carbon dioxide recovery. This is 1.7% less efficient than the oxy-fuel NGCC and may be attributed to the extra power needed to run the MR compressors used in the CO_2CL section of the cycle. Detailed flowsheets and material/energy balance are presented in appendix G. Using the specifications presented by [27] and the ASU process cited by [57], the MoCC power generation efficiency would increase to be near 47.3% with the same liquid carbon dioxide recovery.

2.9 Conclusion

The presented ERPP designs allow for efficient electrical power generation using LNG or NG, coupled with a novel process that achieves near 100% carbon dioxide capture. If LNG is to be utilized, then its evaporation step is integrated into the CO_2CL section. Here, captured carbon dioxide is stored as a low pressure liquid, thereby offering flexibility in storage and shipping. If NG is used, then an MR vapor compression cycle is deployed to capture and liquefy the carbon dioxide. Alternatively, if supercritical carbon dioxide is the preferred means of transportation, then the captured liquid carbon dioxide may be evaporated to supply the refrigeration need for its capture. This eliminates the need for an MR refrigeration cycle. In all of the above cases, the separated unconverted hydrogen and carbon monoxide are recycled to the SOFC. The calculations show that the recycle fuel-rich stream increases the SOFC power output by almost 22%. The design power generation efficiency, as identified by rigorous modeling and simulations, is in the range of 70.4 to 76.0% on LHV basis with near 100% carbon dioxide capture. When compared to a SOFC-Gas turbine plant that does not capture carbon dioxide, the ERPP achieves the benefit of nearly

zero carbon dioxide emissions with marginally (less than 2%) reduced energy penalty. The ERPP concept is also found to be a promising power generation method for methanol based fuel. Here, near 100% liquid carbon dioxide recovery is achieved with a power generation efficiency of almost 68%. The process capturing and liquefying carbon dioxide is also tested and found to be applicable for oxy-fuel combustion processes. Here, oxy-fuel NGCC and MoCC are developed and integrated with the carbon dioxide capture and liquefaction process. Simulations show that a liquid carbon dioxide recovery of near 98% is achievable with a power generation efficiency of 47 to 49%.

CHAPTER 3. EFFICIENT AND DENSE CYCLE FOR ENERGY STORAGE AND ELECTRICITY GENERATION

3.1 Introduction

The main challenge that faces the widespread adoption of renewable energy is its intermittent nature. Obviously, energy needs to be stored to overcome this challenge. However, the proposed and implemented storage systems seem to face two main technical issues. These are storage efficiency and storage volume. In this context, storage efficiency is the ratio of recoverable energy to stored energy. From economical view points, this efficiency definition address the system operating cost. On the other hand, storage volume partial addresses capital cost.

Energy storage methods are classified into two categories [58]:

1) Electricity storage

2) Thermal energy storage

Electricity storage may be carried out mechanically, chemically, or directly as electricity. On the other hand, thermal energy storage may be carried out by storing heat in a sensible heat, latent heat, sorption storage, or chemical forms.

3.1.1 Electricity storage

Pumped Hydroelectric Storage (PHS) is an example of electricity storage in a mechanical form. The idea here is to use electricity to pump water from a lower altitude reservoir to a higher altitude reservoir. When needed, electricity is generated by releasing the water from the upper reservoir to the lower reservoir to run water based turbine(s), located in between the two reservoirs. In such system, electricity is first converted to potential energy (i.e. water available at the high reservoir) which

is then recovered, when needed, as mechanical energy by running the turbine(s). Although it has a large storage capacity, PHS is a function of geographical sites that are limited in availability [58]. Depending on the equipment characteristics, used for PHS, the storage efficiency falls between 65 to 80% [59]. On the other hand, the capacity depends on the height of the waterfall and volume of the water. An example of a Mega-scale PHS Facility is the Grand Coulee project which has a capacity of 6,480 MW with a reservoir size of around 1.16×10^{10} m^3 [16].

Compressed Air Energy Storage (CAES) is another example of electricity storage in a mechanical form. Here, air is compressed and stored in underground caverns such as ancient salt mines and natural gas storage caves [12,16,59,60]. To reduce the air volume, the storage is carried out at high pressure (40 to 70 bar) near ambient temperature [59]. When electricity is needed, the stored air is extracted for fuel combustion in gas turbine(s). When compared to a stand alone combustion gas turbine systems [54], the fuel combustion with the stored high pressure air enhances the turbine power output; thus, improves the system efficiency. Taking into consideration the electricity generated from NG fuel, CAES storage efficiency can be as high as 82%. Without the fuel, storage efficiency is estimated to be near 66% [60].

At typical storage pressure and temperature, energy density of around 7.7 Mj/m^3 is achievable [16,59]. It is also to be noted that, as in the case of PHS, CAES requires suitable geographical sites; however, this constraint may be eliminated by storing air at a pressure of 20 to 100 bar in underground high pressure pipes. Here, volumetric energy density can be as high as 43.2 Mj/m^3 [59].

Storing electricity in batteries is an example of storing electricity in a chemical form. In batteries stored chemical energy is directly converted to electricity via a chemical reaction. If the battery is rechargeable (such as lead acid, nickel cadmium, Sodium sulfur (NaS), Lithium-ion (Li-ion), and metal air), then the chemical reaction can be reversed by supplying electricity; thus, storing electricity. Rechargeable batteries currently used in power systems application have storage efficiency in the range of 78 to 80% [61].

Due to their high energy density, Li-ion batteries are a very popular choice for the portable electronics industries with expectation that they will be the batteries that power the next generation of hybrid eclectic vehicles as well as Plug-In Hybrids Vehicles (PHEV) [10, 62]. In addition, they possess a lot of potential for future development and optimization [10, 58]. Example of Li-ion battery is the Swing 4400^{TM}, manufactured by Boston Power, with an estimated energy density of 1,511 Mj/m^3 [63]. On the other hand, the most mature and commercially available battery for grid application is the NaS battery with world wide deployment of around 270 MW [11, 12]. Typical energy density of around 1,321 Mj/m^3 is achievable with NaS [64].

3.1.2 Thermal Energy Storage (TES)

Thermal energy storage (TES) may be carried out in two forms: 1) storage of heat as sensible heat (sensible heat storage), and 2) storage of heat as latent heat (latent heat storage). For sensible heat storage, a heat source, typically solar energy, is used to heat up a storage media. When needed the stored heat in the storage media is used to generate high pressure, intermediate pressure, and/or low pressure steam that may be utilized as heat source or to run steam turbines to generate electricity [59, 65]. The use of molten salt, a mixture of 60% sodium nitrate ($NaNO_3$) and 40% potassium nitrate (KNO_3), as a storage media, with estimated energy density of near 756 Mj/m^3 [66], have been demonstrated in a number of projects [14]. Here, molten salt is pumped from a cold storage tank (at 290^{o}C) to be heated to 565^{o}C using concentrated solar energy. The heated mixture is then stored in hot storage tank to be used for steam generation during times at which the sun is not available [14, 59, 65]. For electrical power generation purposes, the storage efficiency depends on the power cycle efficiency. For steam Rankine cycle an efficiency of 34 % is achievable with steam maximum temperature and pressure of 535^{o}C and 100 bar, respectively [65, 67].

Another form of sensible heat storage is the use of refractory material heated to near 1,400^{o}C by electric resistances [59]. When energy is needed air is heated using

the refractory material then used in a power cycle, such as NGCC, to combust the fuel. Similar to CAES, the heated air enhances the power output of the cycle, when compared to a cycle operating with ambient temperature air. Energy density of such system is around 0.7 Mj/m^3 with storage efficiency of near 60% [59].

Latent heat storage uses constant temperature phase transition between liquid and solid to store energy in the form of heat. During storage time, the storage media will go through a phase change from solid to liquid; thus, storing heat in the form of latent heat of fusion. When energy is needed, the liquid phase is cooled down resulting in solidification of the storage media and the release of the latent heat of fusion. Sodium hydroxide is reported to be a good candidate for such application with an energy density of around 1,332 Mj/m^3 [59].

Sorption heat storage is similar to carrying on a reversible reaction [58]. During storage time, heat is used to carry on an endothermic reaction. Two products A and B are generated, separated, and stored separately. When energy is needed, the two products (i.e. A and B) are added together to carry on an exothermic reaction; thus, recovering the heat that was initially stored during the storage time. Examples of A/B components are $LiCL/H_2O$, $LiBr/H_2O$, $Zeolite/H_2O$, $Silica\ Gel/H_2O$ with energy densities of around 911, 648 to 1,116, 446, and 180 Mj/m^3, respectively.

3.1.3 Hydrogen storage

Hydrogen storage is an example of storing electricity, heat, or combination of electricity and heat in a chemical form. Such storage system involves generating hydrogen by supplying energy to a hydrogen atom containing species, such as water, methane, biomass, and coal. Water electrolysis, steam electrolysis, and water thermolysis are examples of processes generating hydrogen by supplying electricity, electricity and high temperature heat, and high temperature heat (greater than 3000^oC heat), respectively [68]. Methane reforming, biomass and coal gasification are other means

of hydrogen generation via supplying high temperature heat (greater thane 700^{o}C); however, are associated with generating carbon dioxide byproduct [1, 69].

Hydrogen may be stored using on of the following four methods, 1) gas storage, 2) liquid storage, and 3) geological storage [62]. Due to its low volumetric energy density, gaseous hydrogen storage requires high pressure compression, with pressure typically ranging between 350 to 700 bar [55]. For example, at 25^{o}C and 1.013 bar, hydrogen volumetric energy density is around 11.6 Mj/m^3; but at 25^{o}C and 700 bar, the volumetric energy density is near 5,423 Mj/m^3. While compressing hydrogen improves its volumetric energy density, the compression energy is equivalent to 10 to 15 % (depending on the storage pressure) of the energy content of hydrogen, making it an energy intensive system [55]. Liquid storage; on the other hand, makes hydrogen very energy dense with volumetric energy density of around 10,000 Mj/m^3 at its normal boiling point condition (i.e. -253^{o}C and 1.013 bar). Similar to compression, hydrogen liquefaction is energy intensive requiring expensive refrigeration energy. As a matter of fact, hydrogen is the second most difficult gas to liquefy after helium (boiling point of -269^{o}C) with about 30 to 40 % of its energy content is utilized for its liquefaction [55].

Geological hydrogen storage is being investigated and found to be technically feasible. Three geological hydrogen storage systems operate today and all utilize solution mined salt caverns. Research is also being conducted on using depleted NG reservoirs, aquifers, and geological formations similar to those used for CAES. Similar to PHS and CAES, geological hydrogen storage is function of geographical sites and unique locations are required [62].

3.1.4 Grid energy storage options

Grid energy storage may be classified into two categories: high power/rapid discharge application and energy management [62]. The high power/rapid discharge category is required for number of reasons, among them are grid stability, power quality, frequency regulation service (responding to random, rapid variations in de-

mand) and contingency reserves (rapidly responding to a generator or transmission failure). These require storage systems that respond rapidly for short periods, typically 1hr or less. Examples of storage system adequate for such applications are capacitors, superconductors, magnetic energy storage, flywheels, and batteries (ex. Li-ion and lead acid).

For the energy management category, which is the theme of this dissertation, the storage system respond speed is not an issue;however, the storage system needs to be adequate for dispatching electricity for extended periods (i.e. large volumes of stored energy). With this kind of category, electricity is stored during low demand or high availability of renewable energy and discharged from the storage system during high demand or low availability of renewable energy. Adequate systems for such applications are PHS, CAES, TES, batteries, and hydrogen.

3.2 Proposed solution for continuous baseload power supply from a renewable energy source

Energy storage at multiple time and energy scales remains an on-going challenge for transitioning from fossil fuels to intermittently available renewable energy sources as the dominant primary energy supply. The impact of energy storage technologies in enabling the use of renewable energy sources like solar, wind etc. for different end uses is illustrated from the magnitude of energy to be stored. For example, in the USA, on average, solar energy is available for only one-fifth of a twenty-four hour day [70]. This means for an average 100 MW power supply from solar energy, one needs to store enough energy to supply near 2 GWh of electricity for a twenty four hour cycle. This motivates the need to identify methods for storing GWh levels of energy in a reasonable volume which can also be subsequently delivered at a high efficiency. Here, a GWh-level electrical energy storage system that is dense, energy efficient and makes use of carbon fuels and their existing infrastructure is proposed.

As mentioned above, among the known energy storage methods, current batteries are known for their high storage efficiency. However, their currently low energy densities (less than 2 GJ/m^3) and short cycle life (e.g. near 2500 for NaS batteries) [11], make them impractical for storing GWh levels of electricity. Use of hydrogen either as a cryogenic liquid or compressed gas results in low energy storage efficiencies [13]. Use of thermophysical materials like molten salts to store thermal energy, which is subsequently transformed to electrical power via a steam Rankine cycle, is associated with low energy density and storage efficiency. On the other hand, CAES and PHS, despite their relatively high energy efficiencies and large scale energy storage capability [11], are constrained by the need for suitable geological and geographic locations respectively [4].

Carbon fuels (such as alkanes, alcohols, ethers, etc.) offer an attractive storage solution owing to their high volumetric energy density (e.g. gasoline is near 32 GJ/m^3), efficient conversion to electricity (50 to 70%) [46], and the well-established technology and infrastructure available for their utilization [68, 71]. Candidate fuel molecules suggested for energy storage applications include gaseous methane [71–73], methanol [13, 55], dimethyl ether [55, 73], and diesel [3]. However, the long-term use of such fuels for energy storage is contingent on our ability to synthesize them from renewable carbon and hydrogen sources. While hydrogen can be generated from water, the use of atmospheric carbon dioxide or biomass as possible renewable carbon source in such an open loop fashion is quite challenging [3, 68, 74]. For example, carbon dioxide extraction from the atmosphere, or even from industrial exhausts, is an energy intensive process, which could substantially impact the storage efficiency [71, 75]. On the other hand, growing biomass on agricultural land for energy use is generally constrained by the available arable land as well as other environmental issues [16, 76]. Only the Sustainably Available (SA) biomass comprising of crop residues and perennial grasses grown on marginal lands are readily available for energy production [77, 78]. However, the specific availability of the limited SA biomass for energy storage is uncertain mainly due to its anticipated competitive use for syn-

thesizing chemicals as well as liquid fuels for transportation [79]. Previous works have suggested closed loop storage cycles where the carbon dioxide formed during power generation is recirculated within the process [72, 80, 81]. This is consistent with the cyclical nature of energy storage and warrants further analysis to identify efficient and dense storage cycles.

The storage of a carbon fuel could by itself be a challenging task. Fuels having relatively high energy content per carbon atom such as methane and ethane, exist as gases at ambient conditions. Thus, they need to be either stored as liquids (close to ambient pressure) or as high-pressure gases (at ambient temperature or lower). Although liquefaction of these carbon fuels significantly reduces the storage volume, it is associated with a relatively large refrigeration energy penalty that could adversely impact the storage efficiency. High-pressure gas storage, on the other hand, is associated with a lower energy penalty, but requires much larger volumes for storing the same quantity of energy compared to liquefaction. For example, consider a large-scale storage of natural gas. An LNG tank (-162^{o}C and near 1.1 bar) with a typical capacity of 100,000 m^3 [82], is estimated to have an energy storage capability of almost 585 GWh in terms of LHV (assuming NG is 100% methane). On the other hand, the state of the art compressed natural gas VOLANDS^{TM} storage tank (comprising of bundles of cylinders operating at sub-ambient temperature of near -30^{o}C and 125 bar) is available for a storage capacity of up to 64,000 m^3. This volume corresponds to a storage capability of almost 132 GWh on a LHV basis [83]. In the USA, close to 4 million m^3 of LNG, which is equivalent to close to 23 TWh (LHV), is stored for NG peak demand supply [84]. Thus, as evident from the current NG storage practices, the volumetric and related practical constraints of storing large quantities of compressed gas make it less favourable compared to liquefied gas storage.

3.2.1 Efficient and dense cycle for energy storage and electricity generation

This dissertation proposes a concept, shown in Figure 3.1, which achieves efficient and dense energy storage within a closed carbon recirculation system. The cycle transforms carbon atoms back and forth between liquid carbon dioxide and liquid carbon fuel to enable the storage and then delivery of GWh levels of electrical energy. When renewable energy becomes available, the stored liquid carbon dioxide is vaporized and reacted with hydrogen (provided by water dissociation), to synthesize a carbon fuel. The synthesized carbon fuel is liquefied and stored. This section of the process is referred in this dissertation as storage mode.

To meet the power demand in the absence of the renewable energy source, the stored carbon fuel is vaporized and oxidized. The oxidation by-product, carbon dioxide, goes through capture, Purification, and Liquefaction processes prior to storage. This part of the process is referred as the delivery mode. Although not essential, the water produced during the carbon fuel oxidation in the delivery mode is also stored for reuse during the storage mode to minimize the net cycle water consumption. The storage efficiency of the cycle is defined as the ratio of electricity recovered during the delivery mode to the electricity used during the storage mode. For the efficiency calculation, electricity used during the storage mode includes directly consumed electricity and any used heat accounted by converting it to exergy at the temperature of use. Exergy is used to account for the process heat input in the storage efficiency as it allows to differentiate between heat used at different temperatures.

Aside from the little make up carbon input, the proposed cycle eliminates the need for a carbon source. In addition, unlike the previously suggested approaches for energy storage [72, 81], the proposed approach is general and not restricted to any particular carbon fuel, power generation or hydrogen production technologies. Moreover, the proposal stores the carbon fuel and carbon dioxide as liquids, which lends itself to synergistic integration opportunities and energy efficiency benefits, as elaborated later.

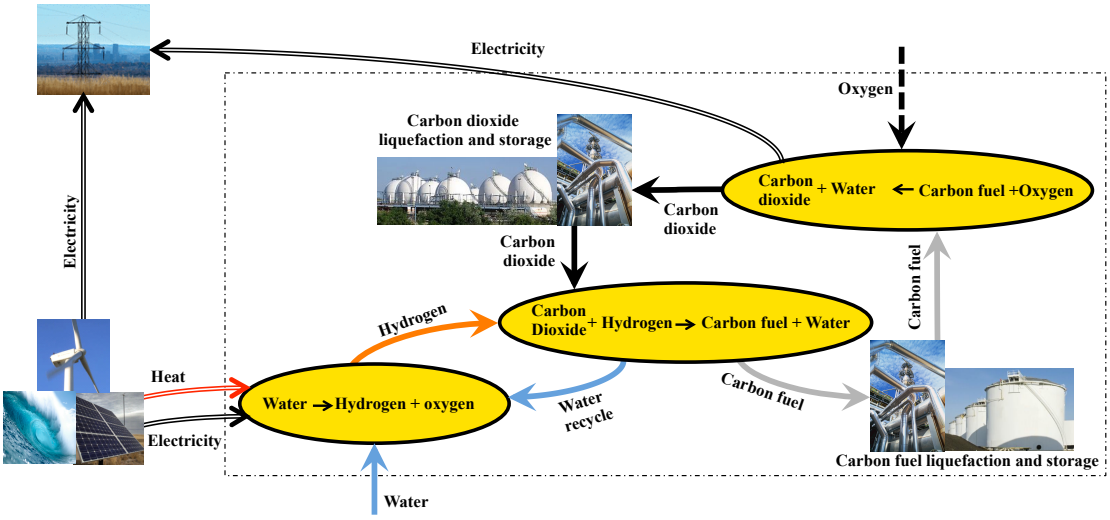

Figure 3.1. Schematic of the proposed storage and delivery concept.

CHAPTER 4. IMPLEMENTATION OF THE CYCLE CONCEPT

4.1 Fuel selection metrics

The selection of a carbon fuel for the proposed cycle given in Figure 4.1 impacts the overall storage efficiency and storage volume. Here, fuel selection metrics are suggested to systematically compare different carbon fuel candidates for the cycle of Figure 4.1 or any other energy storage strategies using carbon fuels. Based on these metrics, it is possible to identify favourable carbon fuel candidates, which can be further evaluated by conducting rigorous simulations or experimentation. The suggested metrics are: 1) EX_C: carbon fuel exergy content per mole of carbon, 2) $EX_{H\rightarrow C}$: exergy stored in the carbon fuel relative to hydrogen exergy during the carbon fuel synthesis step, 3) EX_V: carbon fuel exergy content per unit fuel volume under storage. The exergy of a fuel refers to the maximum reversible work that can be generated from it. It is calculated by applying the first and second law of thermodynamics at reversible conditions for the process shown in Figure 4.2. Ambient temperature (T_o) and pressure (P_o) were assumed to be 298 K (25^oC) and 1.013 bar, respectively. Applying the first and second law of thermodynamics gives:

$$EX_i = -\Delta G = G_i + G_{Air} - G_{Carbondioxide} - G_{Nitrogen} - G_{Water} \tag{4.1}$$

where;

EX_i: Fuel i exergy per mole of fuel

G_i: Gibbs free energy per mole of fuel i

G_{Air}, $G_{Carbondioxide}$, $G_{Nitrogen}$, and G_{Water}: Air, carbon dioxide, nitrogen, and water gibbs free energy per mole of fuel i.

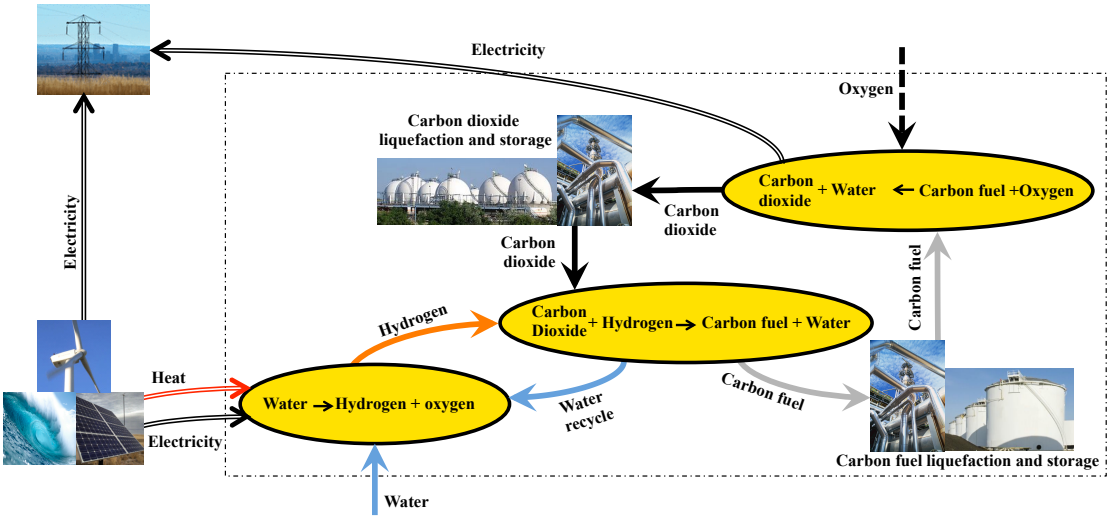

Figure 4.1. Schematic of the proposed storage and delivery concept.

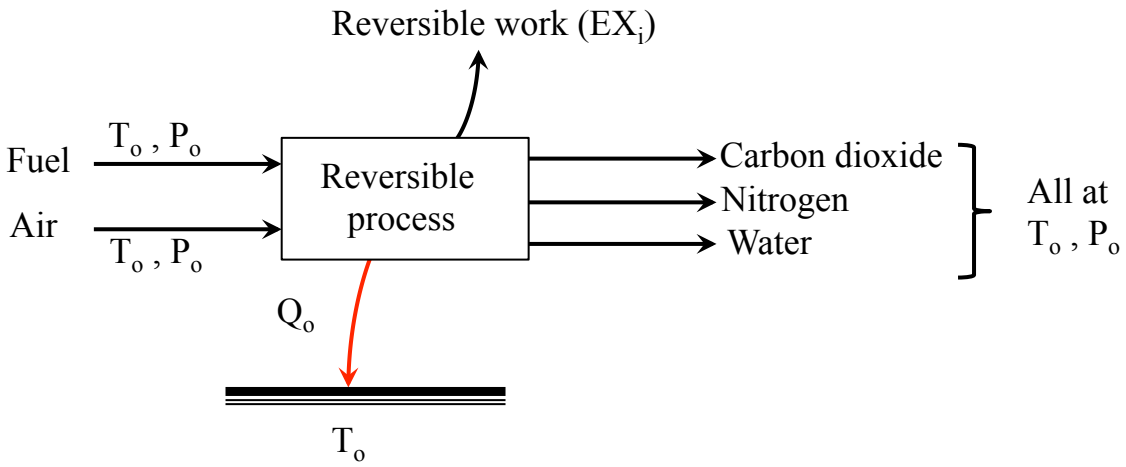

Figure 4.2. Representation of the reversible process used to calculate the fuel exergy. In case the fuel is hydrogen or ammonia, then the carbon dioxide stream is eliminated. If the fuel is carbon monoxide, then the water stream is eliminated.

For a carbon fuel, exergy per mole of carbon (EX_C) is calculated by dividing EX_i by the number of carbon atoms per mole of fuel. The fuel exergy per unit volume at

storage conditions (i.e. temperature and pressure) is calculated by multiplying EX_i by the fuel molar density at storage conditions. The molar densities are obtained using the PSRK thermodynamic package available in Aspen Plus^{TM} [30]. For fuels that are gases at 298K (25^oC) and 1.013bar, the molar densities are obtained at the gas normal boiling point of 1.013bar. On the other hand, for liquids molar densities are all obtained at 298K (25^oC) and 1.013bar. The exergy stored in the carbon fuel relative to the hydrogen exergy during the carbon fuel synthesis step, $EX_{H\rightarrow C}$:, is calculated as follows:

$$EX_{H\rightarrow C} = \frac{EX_i}{EX_{H_2}\lambda} \tag{4.2}$$

Where;

λ : is mole of hydrogen required to synthesis one mole of the carbon fuel.

In general, EX_C gives an indication of the moles of carbon atoms needed to store one unit (MJ) of exergy in the carbon fuel. Thus, choosing fuels with higher value of EX_C reduces the carbon demand for storing a unit of exergy. For the cycle of Figure 4.1, increasing EX_C reduces the carbon circulation between the two operation modes (i.e. storage and delivery modes). This translates into reduced energy penalties of carbon dioxide circulation (e.g. pressure drops, temperature differences, etc) and CO_2CL. $EX_{H\rightarrow C}$ indicates how much hydrogen exergy is wasted as heat of reaction during the carbon fuel synthesis step. The impact of this lost exergy can be minimized by recovering a portion of the heat of reaction as electrical power through steam generation. Alternatively, the heat of reaction may be utilized for heating process streams. However, such energy recovery mechanisms will only partially compensate for the hydrogen exergy that is lost due to increased hydrogen use. Therefore, choosing a fuel with higher values of $EX_{H\rightarrow C}$ may be beneficial and it could minimize the exergy (electricity) requirement for hydrogen production during the storage mode of the cycle. The third metric, EX_V, gives an indication of how much volume the fuel will occupy to store a unit amount of exergy. Fuels with higher values of EX_V will require lower storage volumes to meet a given energy demand. Table 4.1 lists different carbon fuels (alkanes, alkenes, alcohols, ethers, carboxylic acids, ketones, and aldehydes) of

Table 4.1
Comparison of candidate carbon fuels for energy storage.

Carbon fuel	EX_C (MJ/kmol C) (1,2,4)	Boiling point at 1 atm (K)(1)	$EX_{H \rightarrow C}$ (%)(1)	EX_V (GJ/m^3) (1,3)
Gases				
Methane	806	112	86	21
Ethane	723	185	88	25
Propane	692	231	89	26
Dimethyl ether	685	249	97	20
Ethene	657	169	93	26
Propene	643	225	92	27
Formaldeyde	523	255	112	14
Carbon monoxide	239	81	-	7
Non carbon options				
Hydrogen	234	21	-	9
Ammonia	335	240	95	11
Liquids				
Methanol	693	338	99	13
Ethanol	654	351	93	19
Iso-octane	652	399	89	27
Diethyl ether	651	308	93	22
Cetane	640	560	89	25
Acetone	572	329	92	18
Acetic Acid	433	391	93	10
Formic Acid	270	373	116	3

(1) Numbers rounded to nearest decimal for presentation.
(2) For non carbon fuels, EX_C unit is MJ/kmol fuel
(3) Gases: at 1 atm and normal boiling point. Liquids: at 1 atm and 298 K.
(4) Reference conditions for exergy calculations are 1 atm and 298 K

which some are gases and other are liquids at ambient conditions. Although, carbon monoxide and ammonia are highly toxic and hydrogen and ammonia are not carbon fuels, they are listed in the table for comparison. The initial conclusion that can be drawn from Table 4.1 is that there is no fuel that is superior in all the three proposed metrics. Gases, such as methane and ethane, are associated with higher values of EX_C

when compared to liquids such as iso-octane, ethanol and methanol. However, the high exergy content of these gases comes at the expense of lower values of $EX_{H\rightarrow C}$, particularly when compared against methanol. In general, carbon fuels that are gases at ambient conditions do not require energy intensive purification from the water produced during the carbon fuel synthesis step of the storage mode. However, this advantage is traded off with the corresponding energy requirements for purification (from the unconverted hydrogen and carbon dioxide) and liquefaction, also during the storage mode. Energy input for gaseous fuel purification is also expected to substantially increase for cases with lower carbon conversion per pass during the carbon fuel synthesis step. Nevertheless, gases such as methane and ethane, when liquefied, have comparable EX_V as liquids such as iso-octane, as shown in Table 4.1. In case of carbon fuels with values of $EX_{H\rightarrow C}$ greater than 100% (formic acid and formaldehyde), additional work input is necessary for the carbon fuel synthesis reaction to proceed to completion. In other words, the direct synthesis of formic acid and formaldehyde from carbon dioxide and hydrogen results in a positive Gibbs free energy change which makes their synthesis demanding [85]. Additionally, notice the much lower values of EX_C and EX_V for these two candidates compared to other fuels in Table 4.1. Therefore, we have not considered formic acid or formaldehyde as a feasible fuel candidate for the cycle of Figure 4.1.

Among the different classes of carbon fuels considered in Table 4.1, methane has the highest value of EX_C followed by ethane, methanol, propane, dimethyl ether and so on. Consequently, to the first approximation, if we assume that the EX_C to electricity conversion efficiencies are similar for all the fuels, methane use in the cycle will beneficially minimize the amount of carbon cycled to deliver a given amount of electrical power. Another interesting candidate in Table 4.1 is methanol, associated with the highest value of $EX_{H\rightarrow C}$ among all fuels and the highest value of EX_C compared to other liquids. Based on these observations, we have chosen to design and simulate detailed processes applying the concept of Figure 4.1 for methane (referred as Liquid Methane-Cycle or LM-C) and methanol (referred as Methanol-Cycle or Mo-C).

It is also worth mentioning that there exist catalysts for selectively synthesising these fuels from carbon dioxide and hydrogen [86, 87]. In addition, catalysts for methane synthesis can achieve near equilibrium conversion (per pass), which is in excess of 90% at 350^{o}C [87]. In these examples we have used solar energy (available for only one-fifth of a twenty-four hour) as an example of intermittently available renewable energy. However, the concepts are valid for any intermittently available energy source.

In addition to methane and methanol, there exist other options in Table 4.1, which warrant further evaluation, such as ethane, propane and dimethyl ether. All these fuels have lower energy penalty of liquefaction (as shown by their higher normal boiling points) and higher values of $EX_{H\rightarrow C}$ compared to methane. Incidentally, dimethyl ether has second highest value of $EX_{H\rightarrow C}$ in Table 4.1, while ethane and propane also have higher values of EX_V than methane. These fuels will be subject of future investigations.

4.2 Liquid Methane-Cycle (LM-C)

Figure 4.3 is a simplified schematic of the LM-C. During the energy storage mode, solar energy harnessed as heat and electricity is used for hydrogen production via high temperature steam electrolysis using a Solid Oxide Electrolysis Cell (SOEC) [68]. Gaseous hydrogen is then reacted with gaseous carbon dioxide according to the Sabatier reaction [87] to almost complete conversion, generating gaseous methane, water, and waste heat from the reaction at near 400^{o}C. The generated heat is recovered to evaporate and superheat the steam feed to the SOEC operating at 950^{o}C. Any additional heating needed to raise the temperature of the steam to 950^{o}C is supplied by concentrating the solar energy. After separating co-produced water by condensation and molecular sieve dehydration, the gaseous methane stream is purified and liquefied to be stored at a cryogenic temperature of near -172^{o}C and pressure of near 2 bar. Typically, achieving this low temperature of liquefaction for storage requires capital and energy intensive refrigeration systems, and may suggest

the use of high pressure gas storage instead. However, we propose integrating the carbon dioxide vaporization step into the methane liquefaction to reduce the need for the low temperature refrigeration. In this case, liquid carbon dioxide precools the methane to a temperature of near -45^{o}C during its evaporation step. The remaining cooling is carried out using Mixed Refrigerant (MR) refrigeration cycle [40], with the cycle compressors being driven by solar electricity. The MR refrigeration cycle is known to be among the most efficient refrigeration systems [40]. It is worth emphasizing that, due to the decreased load on the MR compressors, this synergy between liquid carbon dioxide and gaseous methane directly translates into capital cost savings. During the delivery mode when solar energy is unavailable, the stored methane energy is extracted by vaporizing liquid methane and oxidizing it via an integrated steam methane reformer SOFC unit to produce electricity [24, 46]. The carbon dioxide in the exhaust mixture leaving the SOFC goes through the CO_2CL process and is stored for reuse during the storage mode. Ordinarily, CO_2CL is an energy intensive process, which negatively impacts the process energy efficiency. Similar to the storage mode (and the ERPP of chapter 2), we propose integrating the methane vaporization step with the CO_2CL step thereby eliminating the need for a refrigeration cycle or other means of carbon capture. In this case, the energy penalty of liquefying methane during the storage mode (as measured by the electricity consumed by the MR compression) is partially recovered as cold refrigeration for carbon dioxide CO_2CL. The resulting CO_2CL process developed has the potential to be used for other carbon capture processes (see chapter 2). The proposed LM-C employing the synergistic liquefaction schemes described above is compared against a cycle using high pressure (205 bar) gaseous methane storage, referred as the Gaseous Methane-Cycle (GM-C).

In addition to the synergistic vaporization and liquefaction steps, the essential features of the proposed LM-C are the following. 1) The integration of the reforming process within the SOFC, a well-demonstrated technology [46], helps to recover an increased fraction of stored energy as electricity. Specifically, there is no need to combust a portion of the methane feed to provide the reforming heat because

the methane reforming process is carried out by soaking up the waste heat released during the operation of the SOFC [24,46]. 2) The SOFC anode exhaust is rich in carbon dioxide and water (1.6 mol% hydrogen, 0.5 mol% carbon monoxide, 17.9 mol% carbon dioxide and 80.0 mol% water), because the fuel is electrochemically oxidized using oxygen ions transported to the anode from the cathode side air feed. Hence, unlike conventional power plants, the exhaust is not diluted with nitrogen (or other diluents), thereby reducing the energy needed during subsequent CO_2CL. 3) Traditionally, SOFC power plants capturing carbon dioxide also consume unconverted carbon monoxide and hydrogen (generated during methane reforming) via enriched oxygen combustion downstream of the SOFC [33]. This generally requires expensive catalytic combustion [33, 38] as well as capital and energy intensive air separation unit. In contrast, the system here avoids combustion by utilizing liquid methane refrigeration to separate carbon dioxide and recycle high purity unconverted fuel (near 66 mole% hydrogen, 23 mole% carbon monoxide, and 11 mole % carbon dioxide) back to the SOFC unit, which further increases the SOFC power output. 4) The methane fuel fed to the SOFC, being free of sulfur and other corrosive materials allows for increased heat recovery of the SOFC exhaust without severe metallurgy impact (arising from condensing corrosive components). This enhanced heat recovery contributes to increased power output during the delivery mode. In addition, the capital and energy cost associated with fuel pre-treatment facilities are avoided. 5) During the storage mode, the operation of the SOFC unit may be reversed to operate it as SOEC for hydrogen production [68, 72]. This not only has a potential to save additional capital needed for hydrogen production, but more importantly, potential daily thermal cycling of the fuel cell stack is avoided. This will contribute to the smooth operation of the plant.

4.2.1 Design and simulation of the LM-C

The detailed process configuration of the storage mode of the proposed cycle (Figure 4.3) is shown in Figure 4.4 and Figure 4.5. The delivery mode process config-

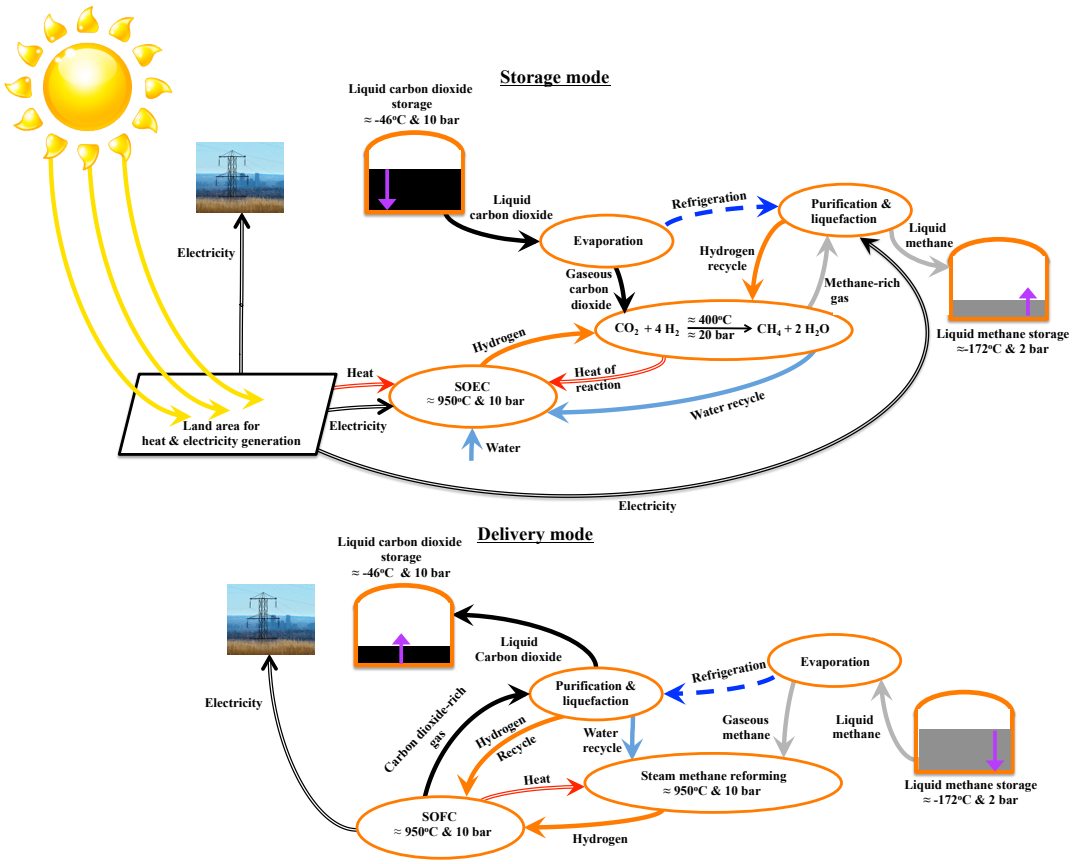

Figure 4.3. Simplified schematic of the proposed LM-C.

uration and its essential characteristics is similar to the developed ERPP presented in chapter 2. All simulations are carried out with Aspen Plus^{TM} using the PSRK thermodynamic model and steam tables (Aspen Technology, 2006; Horstmann et al., 2005). The cycle is simulated for near 140 MW of electrical power output during the delivery mode, with solar energy assumed to be available for one-fifth of a twenty-four hour day. In other words, in a twenty-four hour day, the cycle operates in storage mode for 4.8 hours and delivery mode for 19.2 hours. Detailed simulation basis and material/energy balance are available in chapter 6 and appendix H, respectively.

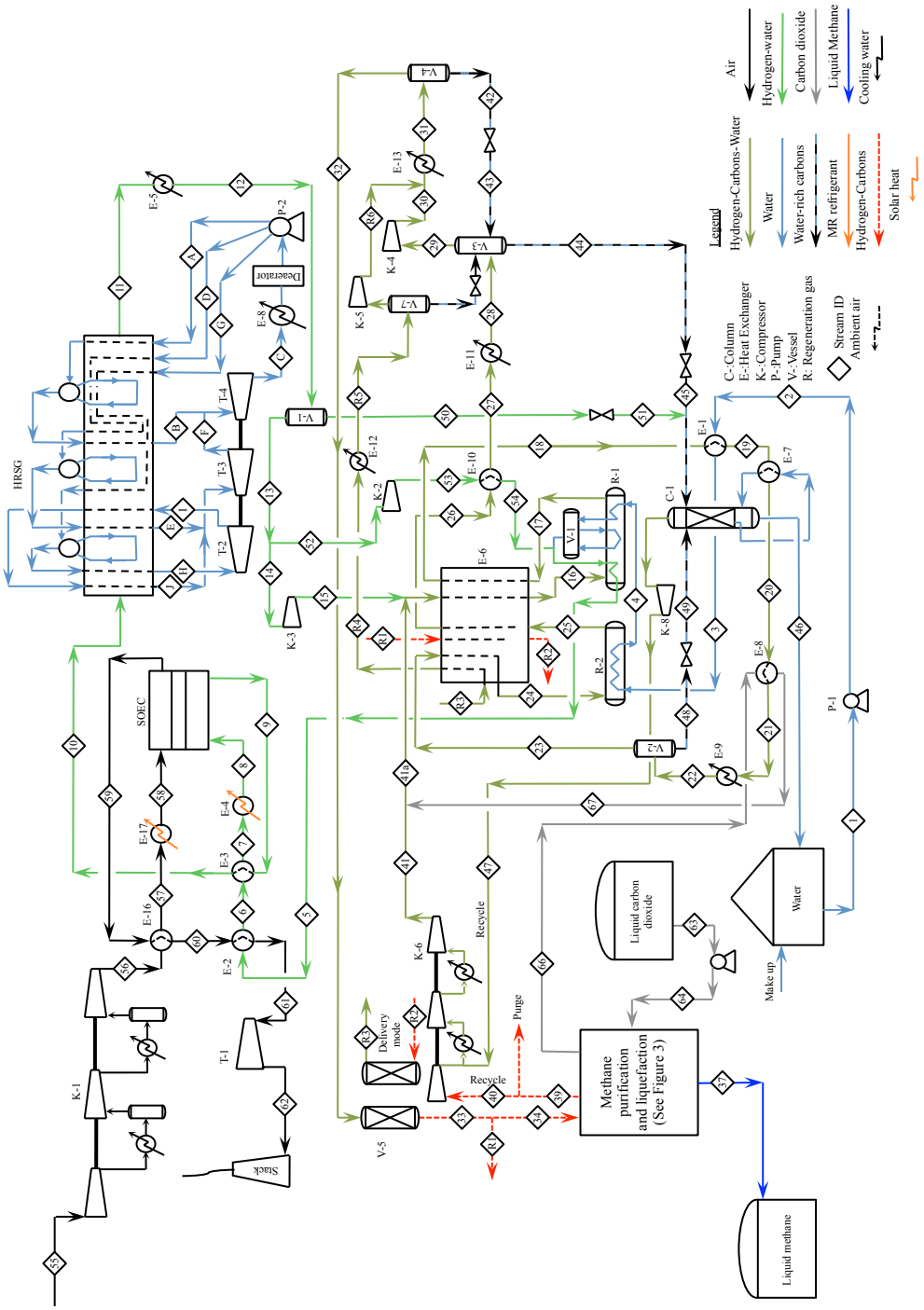

Figure 4.4. Detailed process flowsheet for the storage mode of the proposed LM-C shown Figure 4.3.

4.2.1.1 Hydrogen generation and heat recovery

Due to its high efficiency, steam electrolysis using SOEC was preferred method for hydrogen generation [68]. The SOEC also has the potential to operate as a SOFC during the delivery mode of the cycle, which enables capital cost savings and avoids daily thermal cycling of the device [88]. For the simulation, the model for the SOEC heat and power consumption calculations is based on the work of [31, 32, 89] and implemented in Aspen Plus^{TM} using Aspen Calculator tool [30], see chapter 6. In the model, the electrochemical losses due to experimental based anode/cathode activation polarization, cathode diffusion polarization, electrolyte resistance, and interconnect resistance are considered. Electrochemical losses arising from anode diffusion polarization are neglected [89]. Referring to Figure 4.4, SOEC feed water (sourced from the water storage tank) is pumped via pump P-1 to a pressure of 12 bar. The pressurized water is then converted to superheated steam at 250^{o}C via heat from heat exchanger E-1 and the exothermic reaction heat from the reactors R-2 and R-1. To maintain 10 mole% hydrogen content at the inlet of the SOEC cathode (i.e stream 8), saturated steam (near 11 bar) leaving steam drum V-1, prior to superheating, is mixed with recycle hydrogen from compressor K-2 (stream 54). The presence of hydrogen in the feed to the SOEC cathode is essential to slow down the oxidation and degradation of the nickel cermet electrodes (of the SOEC) when exposed to high steam concentrations [88, 90]. The superheated steam-rich hydrogen mixture, stream 5, is further heated in heat exchangers E-2, E-3, and E-4 to the operating temperature of the SOEC, equal to 950^{o}C. This is close to the maximum operating temperature limit of $1{,}000^{o}$C for existing SOFC systems [50]. As shown in Figure 4.4, heat exchanger E-4 uses concentrated high temperature solar heat, which is assumed in this work to be available at 978^{o}C. At the SOEC cathode, steam is dissociated into gaseous hydrogen and oxygen ions (see equation 4.3). Depending on the steam conversion (i.e. SOEC operating current), the energy balance of the SOEC can be met using either electrical power input or electrical power and heat input (see section 6.2.2 and [88]). To achieve high process efficiency and simplify the heat management of the cycle, the SOEC is

operated at the thermo-neutral condition (steam conversion of around 98%) where the device only requires electrical power input. Here, the heat dissipation of the cell exactly provides the necessary heat for the enthalpy change around the SOEC.

$$Cathode : H_2O(g) + 2e^- \rightarrow H_2(g) + O^{2-} \tag{4.3}$$

The generated oxygen ions diffuse through the yttria-stabilised zirconia electrolyte to the anode where they combine to form molecular oxygen and electrons according to equation 4.4. The generated oxygen at the anode is mixed with sweep air, fed via multistage intercooled compressor K-1 for oxygen dilution. The air flow is specified to maintain 50 mole% oxygen content in stream 59, which reduces the anode material degradation from exposure to high temperature, high purity oxygen [88, 91]. The air feed, stream 56, is heated to 950^{o}C via heat exchange with stream 59 (in E-16) followed by additional heating in E-17 using solar heat available at 978^{o}C). Before it is discharged into the atmosphere, the enriched air, stream 61, is expanded in turbine T-1 to generate additional electrical power.

$$Anode : O^{2-} \rightarrow 2e^- + 0.5O_2(g) \tag{4.4}$$

The hydrogen-rich mixture (stream 10) leaving heat exchanger E-3 at 9.5 bar and 489^{o}C is utilized as a heat source for power generation via a Rankine cycle. The cycle consists of a heat recovery steam generator (HRSG) that generates high pressure (stream H at 120 bar and 460^{o}C), medium pressure (stream E at 30 bar and 320^{o}C), and low pressure (stream B at 5 bar and 230^{o}C) superheated steam. Power is generated via the steam turbines T-2, T-3, and T-4 operating at discharge pressures of 30, 5, and 0.07 bar, respectively. The discharged steam from turbine T-2 (i.e. stream I) is reheated to a temperature of 460^{o}C in the HRSG prior to its expansion in turbine T-3. Sensitivity analyses showing the impact of the cycle operating conditions on the electrical power output is presented section 4.2.2.3.

4.2.1.2 Methane generation (Sabatier reaction)

Methane generation via the exothermic Sabatier reaction of equation 4.5 is favored at higher than ambient pressure and low temperature (near 350^{o}C) operation. Experimental studies revel that the actual carbon dioxide conversion approaches equilibrium for temperatures greater than 300^{o}C with formation of carbon monoxide as a byproduct [87, 92, 93]. In the process of Figure 4.4 methane generation is carried out at near 22 bar in a high temperature sabatier reactor (R-1) followed a low temperature sabatier reactor (R-2) reactor with intermediate byproduct water separation. This approach allows for achieving near 100 mole% per pass carbon dioxide conversion to methane. R-1 at 400^{o}C, and R-2 at 350^{o}C, were simulated using an equilibrium approach, while accounting for carbon monoxide formation via water-gas shift reaction.

$$CO_2 + 4H_2 \rightarrow CH_4 + 2H_2O \tag{4.5}$$

Referring to Figure 4.4, the hydrogen-rich steam mixture leaving the HRSG via stream 11 is cooled to 43^{o}C using cooling water in heat exchanger E-5. The uncondensed hydrogen and water from vapor-liquid separator (99 mole%), stream 13, is split as streams 14 and 52. While stream 52 is recycled to the SOEC via compressor K-2 (see section 3.1.1), stream 14 is compressed via compressor K-3 to produce stream 15 at 22 bar. This stream is then mixed with stream 41a, which is sourced from mixing 99.9 mole% carbon dioxide (i.e. stream 67) and the recycle streams 40 and 47. The mixed stream is then heated in heat exchanger E-6 to near 340^{o}C to be fed to reactor R-1 with a per pass carbon conversion of 96.2%. Stream 17 leaving R-1 is cooled to a temperature of 43^{o}C in the downstream heat exchangers (i.e. E-6, E-1, E-7, E-8, and E-9) for heat recovery and byproduct water condensation. The condensed water is separated in vapor-liquid separator V-2 for further processing in the compression and dehydration part of the process (see section 3.3). Stream 23 leaving V-2 is heated to 300^{o}C in heat exchanger E-6 and fed to R-2 reactor, which has per pass carbon conversion of 99.4 mole%. Similar to stream 17, stream 25 leaving

R-2 is cooled to 43^{o}C in the down stream heat exchangers (i.e. E-6, E-10, and E-11) for heat recovery and byproduct water condensation. Stream 28, containing 89% methane, 7% water, and 4% hydrogen (on a mole basis), is sent to the compression and dehydration part of the process.

4.2.1.3 Compression and dehydration

Prior to its purification and liquefaction, methane needs to be dehydrated to the extent that the water dew point is lower than methane storage temperature (i.e. -172^{o}C). This is necessary to avoid water freezing conditions during purification and liquefaction in the cryogenic heat exchangers E-14 and E-15 (in Figure 4.5). For the same reason of freezing, the unconverted carbon dioxide accompanying methane in stream 28 needs to be completely removed prior to E-14 and E-15. This removal of water and carbon dioxide are best achieved using 4A molecular sieve adsorbers [26,51]. As identified using the flowsheet optimization elaborated in Table 4.2 the energy efficiency of the process is improved by pressurizing the methane-containing stream (i.e. stream 28) prior to the adsorption step. In general, compression followed by cooling to near ambient temperature causes further water condensation which reduces the regeneration heat duty on the molecular sieve adsorbers (see section 2.4.2).

In Figure 4.4, stream 28 (89 mole% methane) is fed to vapor-liquid separator V-3 to remove the condensed water. Vapor stream 29 leaving V-3 is compressed to near50 bar in K-4 (identified using the optimization approach of Table 4.2). Stream 30 is mixed with stream R6 (described below) and then cooled in heat exchanger E-13 to 43^{o}C for further water condensation. The condensed water is separated in vapor-liquid separator V-4, pressure reduced to near 19 bar (stream 43 pressure), and then fed to separator V-3. In separator V-3, any dissolved gases (i.e. hydrogen, methane, and carbon dioxide) are separated for recycle via compressor K-4. On the other hand, the vapor leaving vapor-liquid separator V-4 (stream 32) is routed to molecular sieve adsorber V-5 to remove the residual water and unconverted carbon dioxide (0.35

mole% water and 0.02 mole% carbon dioxide). When the adsorber becomes saturated with water and carbon dioxide, it goes through a regeneration cycle where the water and carbon dioxide are removed by using heat. In this work, adsorber V-5 is designed to be regenerated during the delivery mode of the cycle. Stream 33, leaving V-5 (96 mole% methane) is split into streams 34 and R1. While stream 34 is sent to the methane purification and liquefaction block (see section below), stream R1 is heated in heat exchanger E-6 to a temperature of 310^{o}C to be used as a heat source for regenerating the molecular sieve adsorbers used for carbon dioxide dehydration in the delivery mode (see Figure H.1 in appendix H). Stream R3, containing the desorbed water, at 290^{o}C is cooled in heat exchangers E-6 and E-12 to a temperature of 43^{o}C which condenses the water removed from the delivery mode adsorbers. The condensed water is separated in vapor-liquid separator V-7 and pressure reduced to 19 bar to release a portion of the dissolved gases. These gases are separated in vapor-liquid separator V-3 and recycled to compressor K-4. Stream 44 leaving separator V-3, accounting for 4% of the water generated in the process, is pressure reduced to 2 bar and mixed with stream 51, the hydrogen water mixture (99.7 mole% water) from vapor-liquid separator V-1. The mixed stream along with stream 49 is fed to stripper column C-1. Here, the residual dissolved gases are stripped out of the water using stripping steam supplied by the column reboiler E-7. The stripped gases leave the top of column C-1 to be recycled to reactor R-1 via recycle compressor K-8 (stream 47) followed by recycle multistage intercooled compressor K-6 (stream 41).

4.2.1.4 Methane purification and liquefaction

The purification and liquefaction of methane is carried out using MR vapor compression cycle [40] along with the evaporating liquid carbon dioxide. The MR cycle shown in Figure 4.5, consists of MR multistage intercooled compressor K-7, cryogenic liquefaction heat exchanger E-14, cryogenic subcooling heat exchanger E-15, and a J-T expansion valve. The MR, comprising of 9% nitrogen, 31% methane, 38%

ethane, and 22% propane (mole basis), is circulated via compressor K-7 to provide a low temperate heat sink for heat exchangers E-14 and E-15 by its non isothermal evaporation.

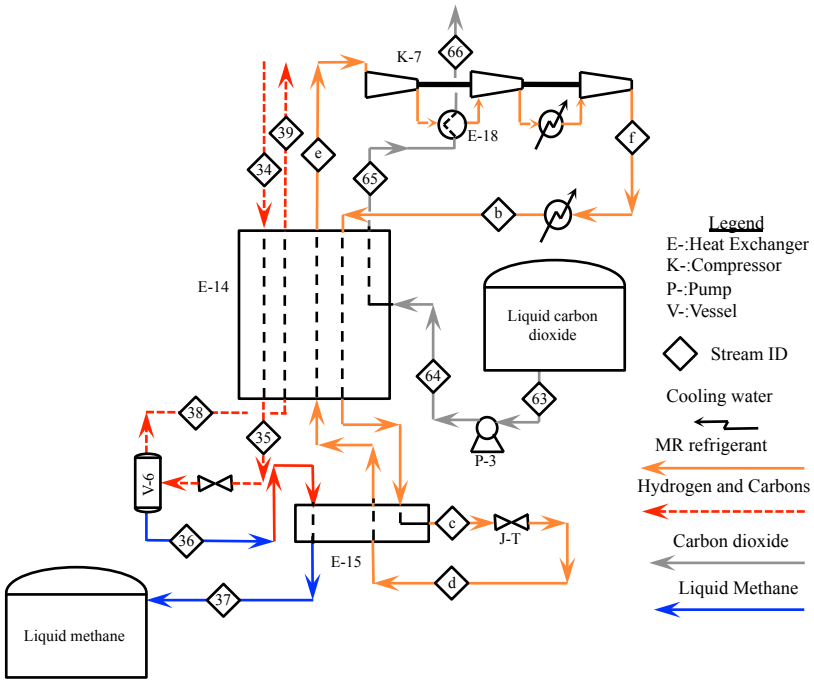

Figure 4.5. Detailed process flowsheet for methane purification and liquefaction part of the LM-C

Referring to Figure 4.5, stream 34 (96 mole% methane) is cooled and condensed in cryogenic heat exchanger E-14 to -170^{o}C. The condensed stream 35 is then pressure reduced to almost 2 bar to release the light gases dissolved in the bulk liquid (i.e. hydrogen and carbon monoxide). Vapor-liquid separator V-6 separates these gases to leave via stream 38 (75 mole% hydrogen, 25 mole% methane, and 46 ppm carbon monoxide) for refrigeration recovery in heat exchanger E-14. The accumulated liquid in separator V-6 is subcooled in heat exchanger E-15 to -172^{o}C and then sent to the liquid methane storage tank. Stored liquid carbon dioxide (99.9 mole%) at -46^{o}C is pumped via pump P-3 to a pressure of 23 bar (reactor R-1 pressure plus pressure

drops) to be then evaporated in heat exchanger E-14. In E-14, liquid carbon dioxide provides refrigeration from latent and sensible heat to cool streams 34 and stream b (high pressure MR) from 43 to close to -45^{o}C. Gaseous carbon dioxide in stream 65 leaves heat exchanger E-14 at -11^{o}C, which is further heated to 43^{o}C (stream 66) via the interstage cooler of K-7. This heat exchange also helps to reduce the compression power of K-7. On the other hand, low pressure MR refrigerant at 1.1 bar and -11^{o}C, is compressed via compressor K-7 to 27 bar (stream f) for cooling and condensation in the downstream heat exchangers. The condensed high pressure refrigerant leaves heat exchanger E-15 via stream c at -173^{o}C to be pressure reduced (using the J-T valve) to 1.2 bar. This further cools the refrigerant (from -173 to -176^{o}C) and ensures the refrigeration available from its latent and sensible heats are greater than the total refrigeration needed by the process. Thus, making the low pressure MR refrigerant in stream d sufficient to provide the refrigeration needed by the process (i.e. refrigeration beyond liquid carbon dioxide capabilities) by its non isothermal evaporation and superheating in heat exchangers E-15 and E-14. The operating conditions of the process are identified using the optimization problem formulation described in Table 4.2. Here, the MR compressor power (i.e. K-7 power) is minimized subject to a minimum temperature approach of 1^{o}C in heat exchangers E-14 and E-15. Aspen Plus^{TM} SQP is used to carry out the power minimization. To ensure a good quality local solution, SQP is run with different starting points for the independent (or varied) variables.

4.2.2 Results and discussion

4.2.2.1 Overall performance

Table 4.3 summarizes the performance of the LM-C as derived from the rigorous simulation. The storage mode energy efficiency, defined as the ratio of the LHV of stored methane to the net electrical power input to the process, is 77.3%. Here, net power includes the electrical power supplied as well as the exergy (or work potential)

Table 4.2
Adopted optimization approach for the methane purification and liquefaction process shown in Figure 4.5

Minimize	Compression power (K-7)
Subject to	E-14 and 15 minimum temperature approach ≥ 1 °C
Independent variables	(1) Mixed Refrigerant composition in stream e o Nitrogen (0 to 90 mole %) o Methane (0 to 90 mole %) o Ethane (0 to 90 mole %) o Propane (0 to 90 mole %) (2) MR flow in stream e (1000 to 5000 kmol/h) (3) K-7 discharge pressure (5 to 40 bar) (4) Stream c temperature (-100 to -180 °C) (5) Stream d pressure (2 to 30 bar) (6) K-4 discharge pressure (20 to 70 bar)
Method	Aspen Plus™ SQP

of the external (solar) heat utilized in heat exchangers E-4 and E-17. Similarly, the energy efficiency of the delivery mode of the cycle, defined as the ratio of net power output to LHV of stored methane, is estimated to be 71%. This results in an overall storage efficiency, defined as ratio of net power output in deliver mode to power input in storage mode, of near 54.9%. For the storage mode, the SOEC consumes the highest fraction of the net power input (96%, including the exergy of the heat exchangers) followed by air compressor K-1 (3%), compressor K-3 (1.5%), and MR compressor K-7 (1.3%). On the other hand, the total power generated from the turbines (i.e. T-1, T-2, T-3, and T-4) is around 49 MW which accounts for near 72% of the power required by the compressors.

If the SOEC pressure is increased, beyond the current maximum pressure rating of 10 bar [48], to almost 24 bar (i.e. reactors pressure plus pressure drops), then compressor K-3 can be eliminated. The net result is an increase in storage mode efficiency from 77.3 to 78.3%, which improves the storage efficiency from 54.9% to 55.6%. Although further increasing the SOEC operating pressure (where R-1 and R-2

pressure also increase) reduces the work of compressor K-4, it will come at the expense of evaporating liquid carbon dioxide at higher temperatures and higher pressures (or lower latent heats). For example, a SOEC operating pressure of 57 bar (i.e. stream 16 pressure plus pressure drops) will eliminate the need for compressors K-3 and K-4. However, liquid carbon dioxide evaporation temperature will increase from -16^{o}C (at 27 bar) to 17^{o}C (at 56 bar). Simultaneously, the rate of latent heat of evaporation available will decrease from near 12 to 7 MW. These two effects increase the work of compressor K-7 by 5.5% compared to the base case and 24 bar case. The overall effect is only a small increase in the storage mode efficiency from 77.3 (base case) to near 78.7%. For the same electrical energy output, the LM-C total storage volume (sum of liquid methane and carbon dioxide volumes) is estimated to be more than 7 and 252 times less than the storage volumes of sodium sulfur battery and compressed air storage systems, respectively (see section 6.6 for calculations). While the volume of liquid hydrogen is comparable to the total storage volume of the LM-C, the LM-C is associated with higher storage efficiency relative to liquid hydrogen storage efficiency of near 33% (see section 6.6.

4.2.2.2 Thermodynamic analysis

As revealed by the process composite curves of the storage mode of the LM-C in Figure 4.6(a), around 124 MW of heat (at maximum temperature of 172^{o}C) is wasted into the cooling water. This is equivalent to around 41 MW of exergy that could have been partially recovered using an organic Rankine cycle [52]. Assuming that a Rankine cycle is capable of recovering 50% of the exergy available from the wasted heat at 172^{o}C, the storage mode efficiency is estimated to increase from 77.3 to 78.8%. The overall effect is an increase in the storage efficiency from 54.9 to 56%. The minimum work of methane purification and liquefaction, calculated using the exergy balance of equation 4.6, is estimated to be 8.8 MW. Here, $W_{Min.}^{Methane}$, $W_{Max.}^{Carbondioxide}$, and EX_j are the exergy (or minimum work) for purifying and liquefying methane,

Table 4.3
Key simulation results of the LM-C.

LM-C			
Storage mode			
Methane to tanks LHV=797.92 MW			
Compressors power, MW		Heat exchangers	
K-1	32.26	Heat duty, MW	
K-2	0.63	E-4	25.30
K-3	16.01	E-17	3.28
K-4	3.82	Exergy, MW	
K-5	0.02	E-4	19.27
K-6	0.55	E-17	2.50
K-7	14.02	Net power, MW	
K-8	0.01	1,032.80	
Turbines power, MW			
T-1	-33.03	Efficiency, %	
T-2	-2.59	77.26	
T-3	-4.59	**Delivery mode**	
		Methane to SOFC LHV=199.6 MW	
T-4	-8.40	Liquid carbon dioxide volume, m^3	718
Pumps power, kW		Net power output, MW	-141.67
P-1	99.60	Efficiency, %	71.00
P-2	283.93	**Overall cycle**	
P-3	72.45	Total storage volume, m^3	1,350
SOEC power, MW	991.87	Storage efficiency, %	54.86

Negative values indicate electrical power generation, positive values indicate electrical power consumption.
Storage mode efficiency=Liquid methane LHV/net power input
Delivery mode efficiency=Net power output/Gaseous methane LHV
Storage mode net power= Compressors power+SOEC power+Turbines power+pump power+ exergy of heat.
Exergy of heat exchanger= Heat duty $\times \frac{\text{Solar heat temperature-Ambiant temperature}}{\text{Solar heat temperature}}$; Solar heat temperature=1,251 K, Ambient temperature= 298 K
Storage efficiency= $\frac{\text{Delivery mode net power output} \times 19.2}{\text{Storage mode net power} \times 4.8}$

exergy (or maximum work) from the vaporizing carbon dioxide, and exergy associated with stream j, respectively. Streams exergy values are listed in appendix H.

$$W_{Min.}^{Methane} = EX_{39} + EX_{37} - EX_{34} \tag{4.6}$$

$$W_{Max.}^{Carbondioxide} = EX_{63} - EX_{66} \tag{4.7}$$

On the other hand, equation 4.7 estimates the maximum work available from vaporizing liquid carbon dioxide to be 3.1 MW. Thus, if liquid carbon dioxide is to be utilized to power a reversible refrigeration cycle for methane purification and liquefaction, then the refrigeration cycle will require an additional 5.7 MW of reversible power. In the actual process, the actual power is almost 2.5 times the reversible power (i.e. 14 MW), a consequence of the different parasitic losses associated with the process, most importantly the temperature differences associated with the heat exchange process. Minimizing the power consumption of methane purification and liquefaction process requires minimizing the temperature differences across heat exchangers E-14 and E-15 [40]. As seen from the composite curves for E-14 and E-15 in Figure 4.6(b), the designed purification and liquefaction process is capable of maintaining a temperature difference of around 1^oC across most of the heat exchangers length. The largest temperature differences are encountered in the warmest section, where the hot streams (i.e. stream 34 and stream b) are cooled from 43 to -25^oC. This is a consequence of the latent heat of vaporization of liquid carbon dioxide, available at a constant temperature of -16^oC. The process simulation also showed that the MR compressor K-7 power would increase from 14 to 21 MW if the refrigeration of liquid carbon dioxide is not utilized and the entire process (i.e. methane purification and liquefaction) refrigeration needs is provided by the MR cycle alone.

4.2.2.3 HRSG sensitivity analysis

The HRSG system considered in Figure 4.4 uses three pressure levels along with reheat for converting heat to electricity. Figure 4.7 reports the impacting of varying different stream pressures on the efficiency of the HRSG system. Here, HRSG effi-

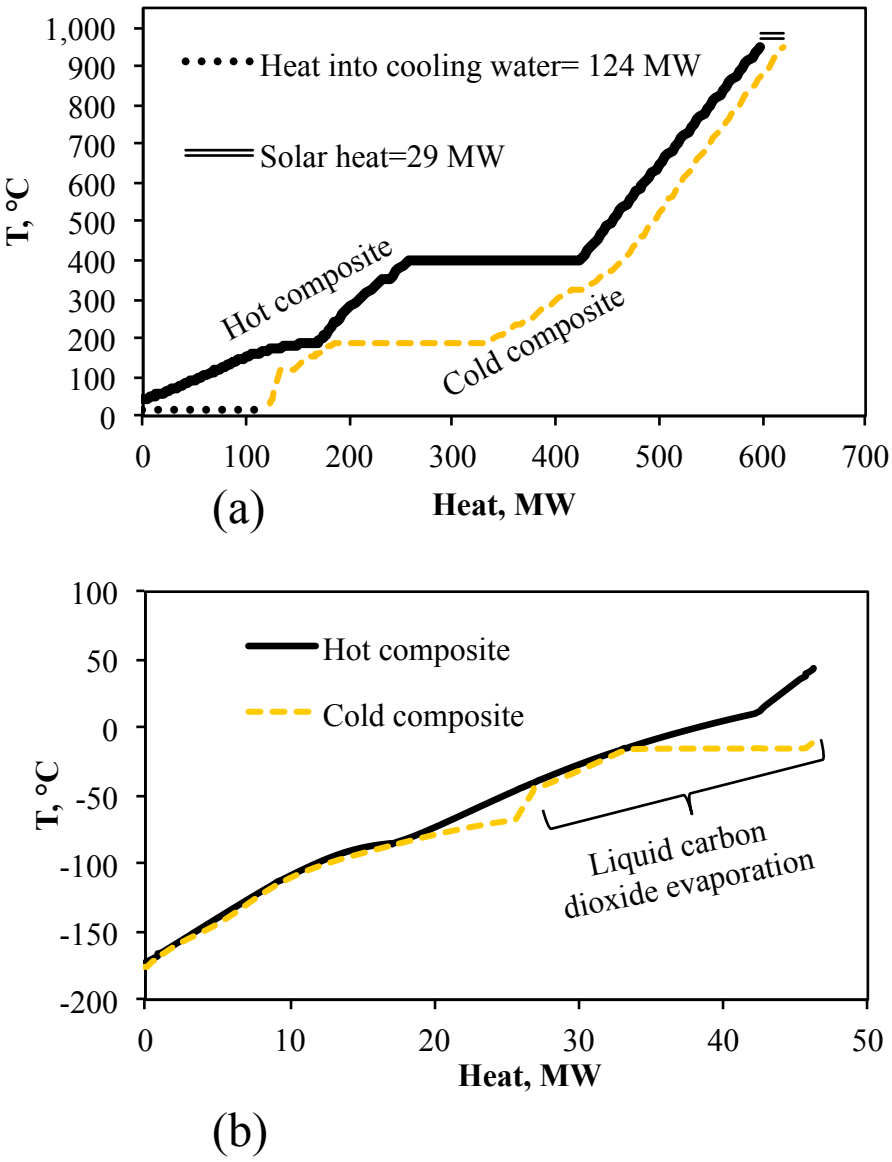

Figure 4.6. a) Process composite curves for the storage mode of the LM-C shown in Figure 4.4. The composite curves do not consider heat exchange below ambient temperature of 25^{o}C (i.e. E-14 and E-15). b) Composite curves for the cryogenic heat exchangers E-14 and E-15 in the process shown in Figure 4.5.

ciency is defined as the ratio of the net power produced (steam turbines power minus feed water pump) to the heat available from cooling stream 10 in Figure 4.4 from 489^{o}C to 43^{o}C).

Referring to Figure 4.7, stream D and G pressures are varied for a fixed stream A pressure of 5 and 10 bar. In each case, the steam flow of each stage (i.e. stream A, D, and G flow) is varied to maintain a minimum temperature approach of 28^oC during heat exchange within the HRSG. The temperatures of stream H and J are fixed at the maximum temperature of 461^oC to maintain a 28^oC temperature approach at the entrance of the HRSG. The temperature of streams E and B are set equal to the saturation temperature of the steam in stream H and E, respectively. At stream D pressures close to 30 bar, reducing the pressure of stream A and increasing the pressure of stream G increase the process efficiency. For the range of pressures considered in Figure 4.7, the maximum HRSG efficiency of 27% occurs at stream A and G pressures of 120 and 5 bar, respectively. Turbine inlet pressure greater than 120 bar and less than 5 bar are avoided due to practical limitations of steam turbines [36, 94]. The HRSG process composite curve of the most efficient case is given in Figure 4.8.

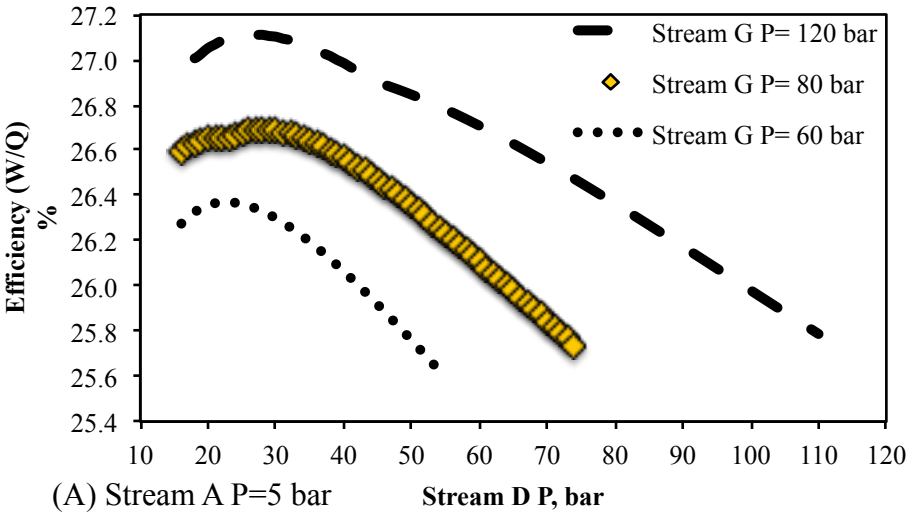

(A) Stream A P=5 bar

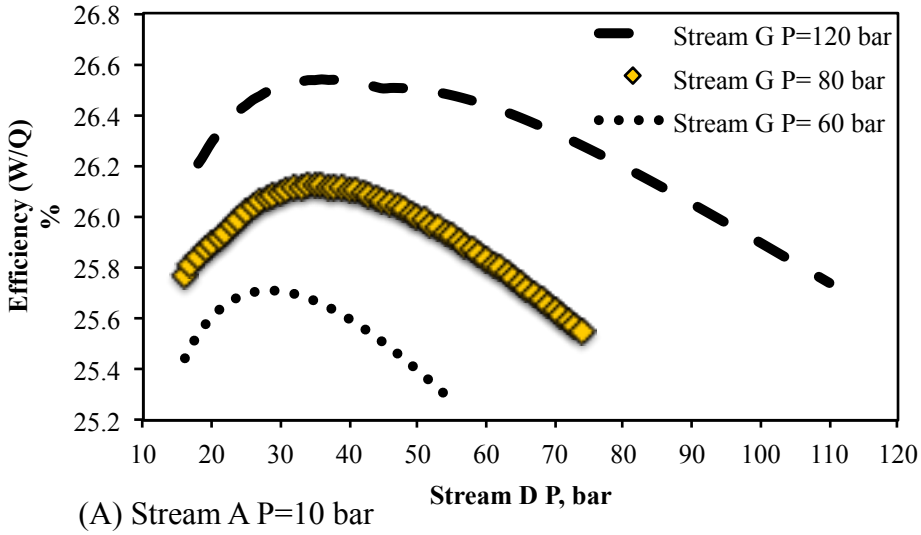

(A) Stream A P=10 bar

Figure 4.7. Impact of the stream D, G, and A (see Figure 4.4) pressure on the HRSG process efficiency.

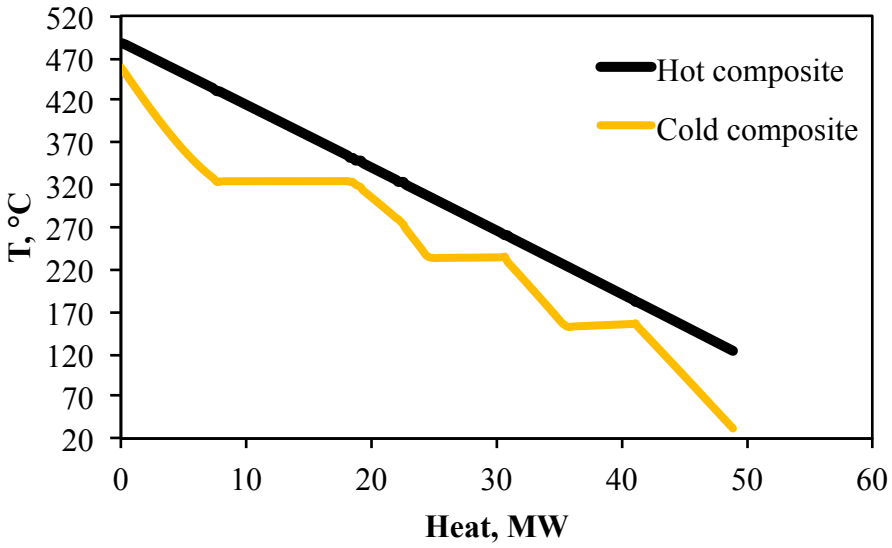

Figure 4.8. Process composite curves of the HRSG at the maximum efficiency as identified from the sensitivity analysis shown in Figure 4.7.

4.3 Gaseous Methane-Cycle (GM-C)

Compressed methane is also investigated as an alternative method of methane storage for the methane based cycle. A simplified schematic is shown in Figure 4.9 with the detailed flowsheet and material/energy balance shown in appendix J. The process is similar to the LM-C with the following exceptions. 1) Methane purification and liquefaction (storage mode) is replaced with the compression and storage unit shown in Figure 4.10. Here, rather than purifying the methane-rich stream (stream 34) leaving the molecular sieve adsorber, it is compressed to 205 bar in multistage compressor K-7. Since compression work is reduced at lower temperatures, stream 34 is cooled to subambient temperature of -45^{o}C prior to compression. This is achieved in heat exchanger E-14 using the refrigeration released from the evaporating liquid carbon dioxide. 2) Since the methane-rich stream is not purified from unconverted hydrogen and byproduct carbon monoxide, the process eliminates a recycle stream (stream 40 in the process of Figure 4.4). 3) Unlike liquid methane, stored gaseous methane has little or no refrigeration. Therefore, carbon dioxide purification and liquefaction during the delivery mode is achieved entirely using the MR vapor compression refrigeration cycle shown in Figure 2.15.

In addition to Aspen Plus^{TM} steady state simulation of the cycle, the process of charging the storage tanks with compressed methane is dynamically simulated, in a stand alone mode, using Aspen Hysys^{TM}. This is carried out to take into consideration the variation of compression power and compressor discharge conditions (i.e. temperature, pressure, volumetric flow) with time; thus, obtain reasonably accurate compression characteristics. It is also to be noted that subambient cooling of the methane in stream 34 (see Figure 4.10) may result in exposing the tanks to very low temperatures that could result in brittle fracture [95]. Therefore, the time variation of the storage tanks inner wall temperate is also calculated to identify conditions that can result in tank failure; hence, avoid them.

The simulation output are shown in Figure 4.11. The gas (i.e. methane) pressure and tank inner walls temperature are found to behave almost linearly. Both the gas

and tank inner walls are at temperatures above the ambient temperature of 25^{o}C; hence, brittle fracture temperature is not encountered. For the gas, the temperature increases rapidly during the first hours of charging with almost flat temperature variation afterword (i.e. time greater than 1h). The rapid increase of the gas temperature seems to be a consequence of the heat of compression (i.e. some of the compression power is transformed into pressure and the remaining is dissipated as heat) which seems to dominate the cooling caused by the outside air surrounding the storage tanks. Beyond the first hour, the ambient cooling appears to dominant the heat of compression; thus, resulting in the flat temperature behavior shown in the figure. The relation of power with time is fitted to a quadratic equation to carry out the integration for compression energy calculation. The result is 10 MWh of compression energy requirements.

The overall features of the GM-C, identified by the process simulations, show that the methane gas storage volume (at 205 bar and 31^{o}C) is higher than methane liquid volume (in the flowsheet of Figure 4.4) by a factor of almost 3.6 with a slightly lower storage efficiency of 54.4%. The reduction in storage efficiency is caused by the need to produce more methane during the storage mode. This additional methane is consumed to supply the electrical power needed for carbon dioxide purification and liquefaction (using MR cycle) during the delivery mode.

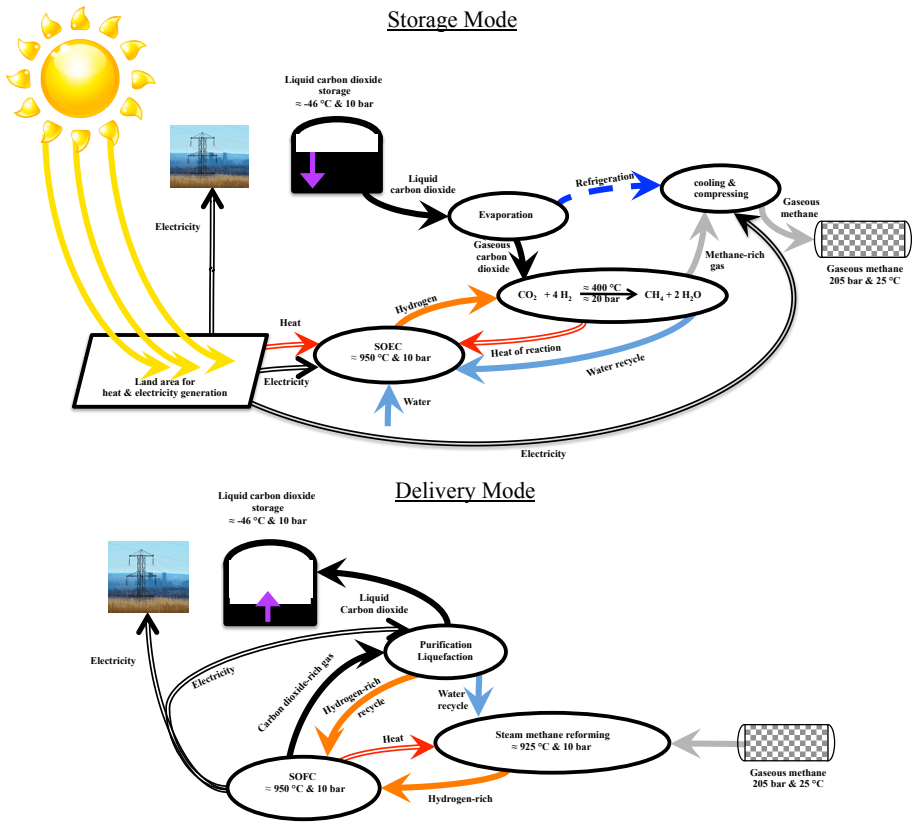

Figure 4.9. Simplified schematic of the proposed GM-C

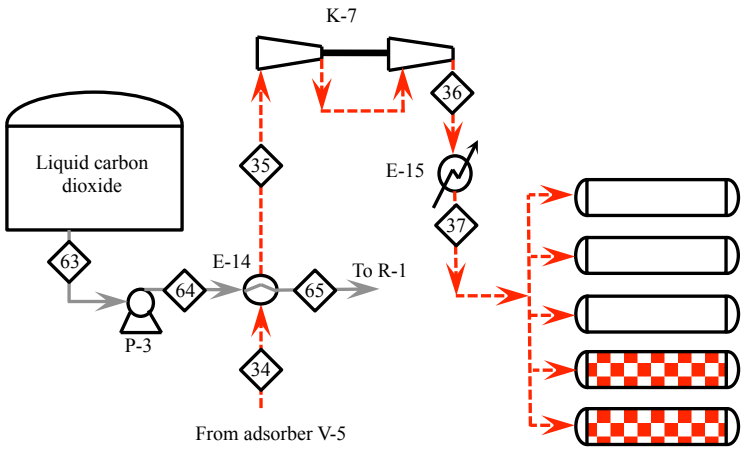

Figure 4.10. Process for storing gaseous methane at 205 bar and 31^{o}C during the storage mode of the GM-C.

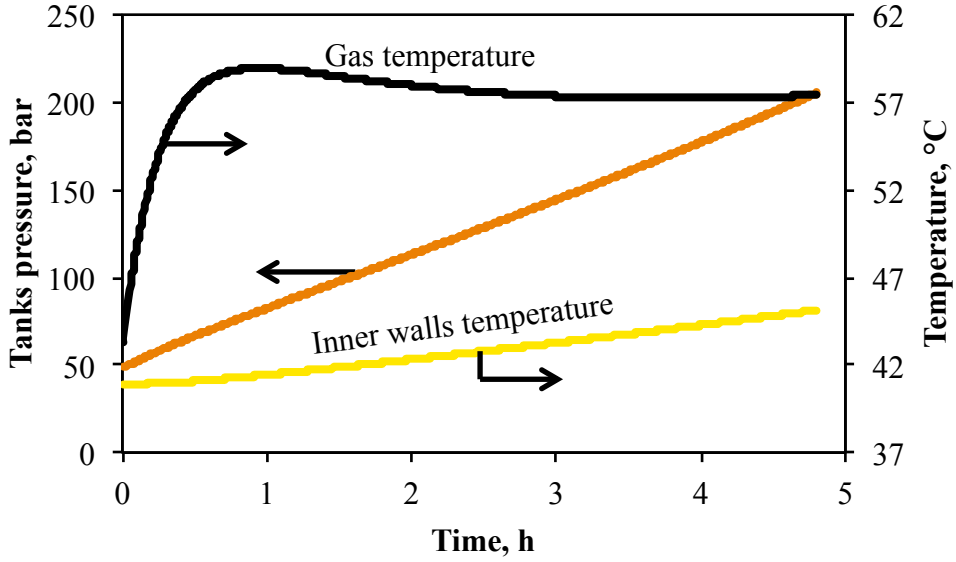

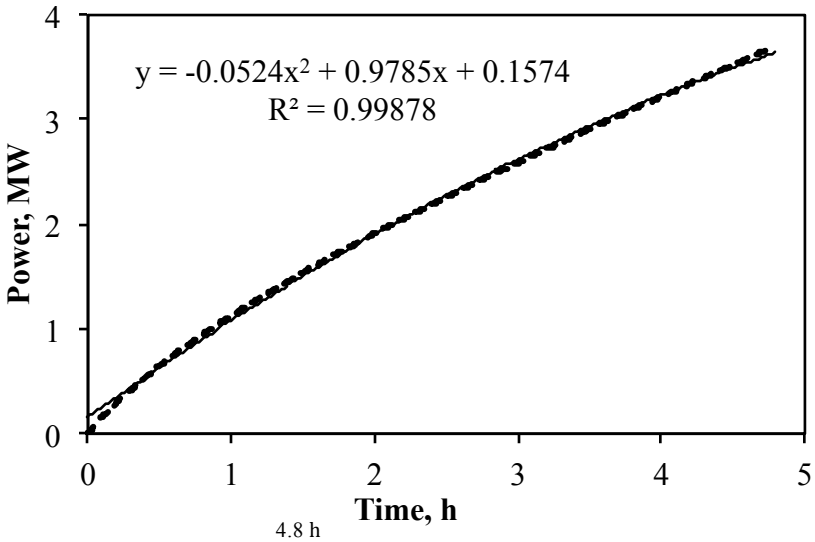

$$\text{Compression energy} = \int_0^{4.8\ \text{h}} -0.0524x^2+0.9785x+0.1574\ dx = 10\ \text{MWh}$$

Figure 4.11. Dynamic simulation results for gaseous methane storage tanks filling (Figure 4.10). The dashed power curve is fitted to a quadratic equation for compression energy calculations.

4.4 Methanol-Cycle (Mo-C)

The Mo-C, shown in Figure 4.12 , shares all the above characteristics and features of the LM-C, with the exception of the following. 1) A refrigeration cycle is required during the delivery mode for CO_2CL (the MR based CO_2CL shown in Figure 2.15 is utilized here;but, without the NG feed). 2) Methanol is generated via single step carbon dioxide hydrogenation at 278^{o}C with recycling of the unconverted reactants to ensure high conversion [86]. Similar to the LM-C, the heat of reaction is recovered to heat the water needed for the SOEC and any additional heating is provided by solar energy. While methanol does not require expensive refrigeration energy for its liquefaction, it leaves the synthesis reactor as almost 50 mole% methanol/water mixture according to the following equation. 3) Thus, a distillation column is employed to produce 99.9 mole% methanol.

$$CO_2 + 3H_2 \rightarrow CH_3OH + H_2O \tag{4.8}$$

4.4.1 Design and simulation of the Mo-C

The detailed storage mode flowsheet, designed and simulated using Aspen Plus^{TM} with the design/simulation basis shown in chapter 6, is shown in Figure 4.13. On the other hand, The delivery mode flowsheet is similar to the process of Figures 2.2 and 2.15 (without the NG feed) and reproduced in appendix K. Appendix K also includes the material and energy balances calculated by the simulation. The storage mode flowsheet consists of the following sections: 1) Hydrogen generation and heat recovery, 2) Methanol generation, 3) Methanol/water purification and distillation.

4.4.1.1 Hydrogen generation and heat recovery

Referring to Figure 4.13, stored water is pumped via pump P-1 to a pressure of 11.5 bar (SOEC pressure plus pressure drops). The pressurized water is then heated and partially evaporated in heat exchanger E-1 and reactor R-1 cooling section,

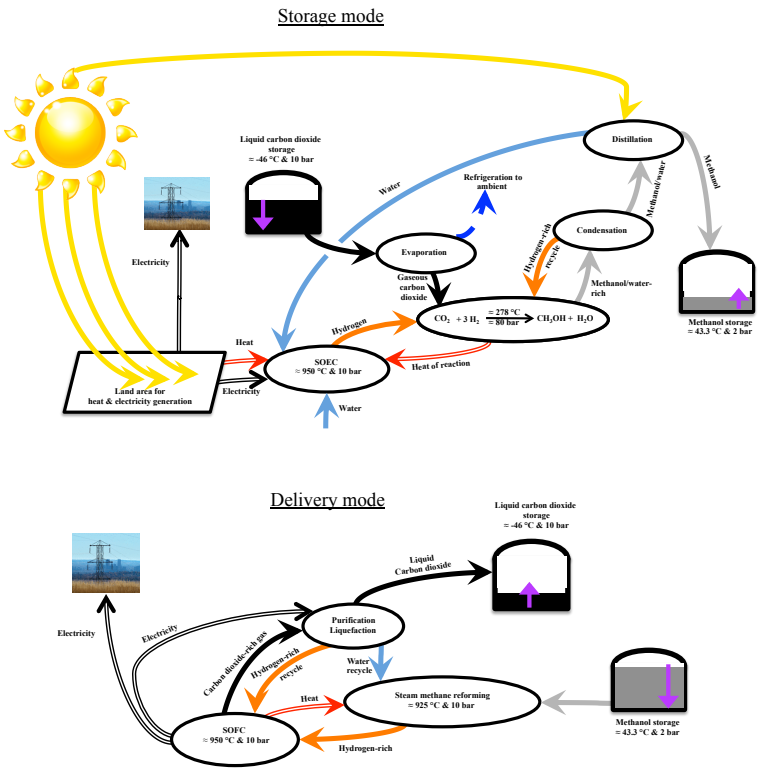

Figure 4.12. Simplified schematic of the proposed Mo-C

respectively. In the reactor cooling section, recycle hydrogen in stream 33 is also added to the water (see section 4.2.1.1 for justification) and the resulting mixture is heated (in which water is evaporating) by removing the reactor exothermic heat. The steam/water/hydrogen mixture (44 mole% vapor percent) leaving the reactor cooling side, via stream 4, is further evaporated and superheated to a temperature of 950°C in heat exchangers E-2, E-3, and E-4. While heat exchangers E-2 and E-3 involve process-to-process heat exchange (i.e. no hot utility is used), heat exchanger E-4 uses external solar heat to offset the additional heat needed for reaching the target temperature of the SOEC (i.e. 950°C). The superheated steam hydrogen mixture (10 mole% hydrogen) leaves heat exchanger E-4 (via stream 7) for electrolysis in the SOEC (see section 4.2.1.1 for SOEC description). On the other hand, air stream 50 is compressed via multistage intercooled compressor K-1 to a pressure of 10.4

bar (SOEC pressure plus pressure drop), heated to 950^{o}C in heat exchanger E-16 (process-to -process heat exchanger) followed by E-17 (using solar heat), and then fed to the anode side of the SOEC.

Enriched oxygen air stream 54 leaves the SOEC for heat and power recovery in the downstream heat exchangers and turbines (i.e. E-16, E-2, E-18, and T-1, respectively). On the other hand, hydrogen-rich stream (98.5 mole% hydrogen) leaves the SOEC cathode side via stream 8 to be cooled down to 43^{o}C in heat recovery heat exchangers E-3,5,6 followed by cooling water based heat exchanger E-7. The cooling of the stream condenses the unreacted steam, which is separated from the vapor hydrogen in vapor-liquid separator V-1. The separated water leaves the separator via stream 34 to be pumped using pump P-3 for mixing with the SOEC fresh water (i.e. water supplied by pump P-1).

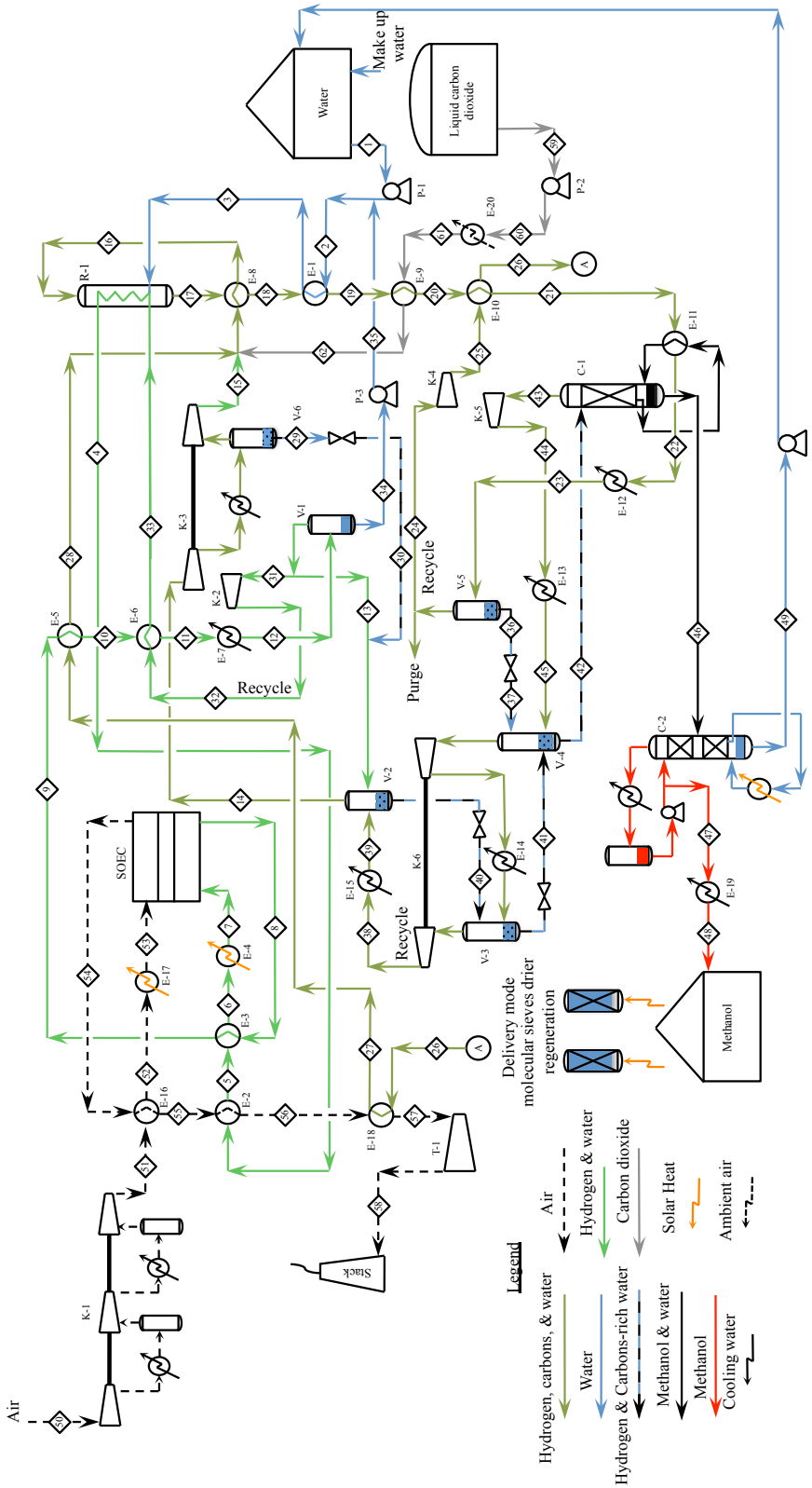

Figure 4.13. Detailed process flowsheet for the storage mode of the proposed Mo-C shown in Figure 4.12

4.4.1.2 Methanol generation

The vapor hydrogen leaving vapor-liquid separator V-1 is split into two streams, stream 13 and stream 31. Hydrogen in stream 31 is compressed via recycle compressor K-2 to be then heated to a temperature of 142^{o}C in heat exchanger E-6. The heated hydrogen leaving heat exchanger E-6, is then mixed with the water in the cooling side of reactor R-1. On the other hand, hydrogen in stream 13 along with the liquid flowing in stream 30 (sourced from vapor-liquid separator V-6) are fed to vapor-liquid separator V-2. The unconverted reactants recovered from methanol/water purification and distillation section (discussed below) are also fed to separator V-2 via stream 39. At the top of the separator, stream 14 (consisting mainly of hydrogen and recycled reactants) leave the separator for compression to 80 bar via multistage intercooled compressor K-3. The compressed vapor mixture leaves compressor K-3 via stream 15 to be mixed with fresh carbon dioxide stream 62 (sourced from liquid carbon dioxide storage tank) and reactor R-1 recycle stream 28. Liquid carbon dioxide from the tank is pumped via pump P-2 to a pressure of almost 80 bar to be then evaporated and heated to a temperature of 136^{o}C in heat exchanger E-20 (using ambient heat) followed by E-9. The resulting mixture is heated to a temperature of 250^{o}C in heat exchanger E-8, using the heat associated with reactor R-1 discharge stream 17, then fed to the methanol synthesis reactor R-1. In R-1, methanol is generated in a single step carbon dioxide hydrogenation with carbon monoxide as a byproduct [86]. At the above mentioned conditions, a per pass carbon conversion of 22.2 mole% is achieved. The synthesis reactor (i.e. R-1) discharge stream 17 is cooled down to a temperature of 114^{o}C using heat recovery heat exchangers E-8, E-1, E-9, E-10, and E-11. The methanol/water mixture in stream 22, leaving heat exchanger E-11, is condensed (by cooling to 43^{o}C) in heat exchanger E-12 using cooling water. The condensed methanol/water mixture is recovered in vapor-liquid separator V-5. On the other hand, the uncondensed gases (which are unconverted hydrogen, carbon dioxide, and carbon monoxide) leave vapor-liquid separator V-5 for recycle to reactor R-1 via recycle compressor K- 4 (which compresses the gaseous stream to near 80

bar). Prior to recycle, the compressed gases in stream 25 are heated to a temperature of almost 162^{o}C in heat exchangers E-10, E-18, and E-5.

4.4.1.3 Methanol/water purification and distillation

Condensed methanol/water mixture leaving vapor-liquid separator V-5 (via stream 36) is pressure reduced to 2 bar then fed to vapor-liquid separator V-4. In V-4, any dissolved gases, released because of the pressure reduction of stream 36, are separated and compressed via multistage intercooled compressor K-6 to a pressure of almost 9 bar for recycle to the methanol synthesis reactor R-1. Prior to recycle, the compressed stream 38 is cooled to 43^{o}C in heat exchanger E-15; thus, condensing the remaining methanol/water mixture which is separated in vapor-liquid separator V-2. Similar to V-4, the water/methanol mixture leaving V-2 is pressure reduced and fed to vapor-liquid separator V-3 for dissolved gas separation (generated from the pressure reduction act). Also to be noted that intercooler E-14 condenses some methanol/water that contains dissolved gases. Hence, the condensed liquid mixture is separated in vapor-liquid separator V-3, pressure reduced, then sent to the upstream vapor-liquid separator V-4 for dissolved gas separation. Last but not least, the methanol/water leaving vapor-liquid separator V-4 is fed to stripping column C-1. Column C-1 purifies the methanol/water mixture from any dissolved gases by mean of stripping steam provided from heat exchanger E-11 (i.e. the column reboiler). The stripped gases leave column C-1 via stream 43 for compression in compressor K-6 to a pressure of almost 2 bar. The compressed gas is cooled in heat exchanger E-13 to a temperature of 43^{o}C (using cooling water) and then fed to vapor-liquid separator V-4. The methanol/water mixture leaving the bottom of column C-1 (via stream 46) is feed to distillation column C-2 to seperate the methanol from water. Methanol leaves the top of the column for cooling and storage. On the other hand, the bottom water product is recycled the SOEC.

4.4.1.4 Results and discussion

Key simulation results of the Mo-C are summarized in Table 4.4 for delivery mode methanol flow of 895 kmol/h (equals to the methane flow during the delivery mode of the LM-C). During the storage mode, the SOEC consumes around 84.2% of the net power. The second highest power consumer is air compressor K-1 followed by the exergies associated with heat exchanger E-4 and distillation column reboiler. Overall, the storage mode efficiency of the cycle is found to be 72.5%. This is around 4.8% lower than the storage mode efficiency of the LM-C. On the other hand, the delivery mode efficiency is identified to be near 67%, around 4% lower than the delivery mode efficiency of the LM-C. The overall storage efficiency, calculated by dividing the energy output during the delivery mode b the energy input during the storage mode, is near 53%.

Table 4.4
Key simulation results of the Mo-C

Mo-C			
Storage mode			
Methanol to tanks LHV=617.1 MW			
Compressors power, MW		Heat exchangers/adsorbers regeneration	
K-1	24.2	Heat duty, MW	
K-2	0.3	E-4	60.1
K-3	27	E-17	3.3
K-4	2.2	Distillation reboiler at 113°C	87.2
K-5	0.1	Q1+Q2 (at 310 °C)	0.7
K-6	0.5	Exergy, MW	
Turbines power, MW		E-4	45.8
T-1	-16.9	E-17	1.9
Pumps power, kW		Distillation reboiler	21.8
P-1	77.4	Q1+Q2	0.4
P-2	399	Net power, MW	
P-3	0.3	850.9	
SOEC power, MW	743.3	Efficiency, %	
		72.52	
Methanol volume, m^3		919	
Delivery mode			
Methanol to SOFC LHV= 168.20 MW			
Liquid carbon dioxide volume, m^3			
717			
Net power output, MW			
-112.7			
Efficiency, %			
66.98			
Overall cycle			
Total storage volume, m^3			
1,636			
Storage efficiency, %			
52.96			

Negative values indicate electrical power generation, positive values indicate electrical power consumption.
Storage mode efficiency=Liquid methanol LHV/net power input
Delivery mode efficiency=Net power output/Gaseous methanol LHV
Storage mode net power= Compressors power+SOEC power+Turbines power+pump power+ exergy of heat.
Exergy of heat exchangers E-4 and E-17 = Heat duty $\times \frac{\text{Solar heat temperature-Ambiant temperature}}{\text{Solar heat temperature}}$;
solar heat temperature=1,251 K, Ambient temperature= 298 K
Exergy of the distillation reboiler and Q1+Q2= Heat duty $\times \frac{\text{Heat source temperature-Ambient temperature}}{\text{Heat source temperature}}$;
Heat source temperature= 338 and 124°C for Q1+Q2 and distillation reboiler, respectively.
Storage efficiency= $\frac{\text{Delivery mode net power output} \times 19.2}{\text{Storage mode net power} \times 4.8}$

4.5 Methanol Water-Cycle (MoW-C)

The energy penalty from an energy intensive methanol/water separation process (i.e. distillation column) seems to have a substantial impact on the storage efficiency of the Mo-C. Additionally, during the delivery mode, steam is needed for methanol reforming for the SOFC. Therefore, instead of Mo-C, cycle with 99.9 mole% pure methanol storage, a unique cycle for methanol is proposed, referred to as MoW-C, where the methanol/water mixture is stored in a single tank. This eliminates the energy penalty associated with methanol purification. A schematic of the cycle is shown in Figure 4.14. The simulation of the cycle shows that the elimination of the distillation column improves the storage efficiency from near 53 to 54.2%. Such improvements of storage efficiency is noticible when investigating the composite curves shown in Figure 4.15. These curves are drown to represents the maximum achievable heat recovery. When compared with the Mo-C, around 122% more heat is required to satisfy the MoW-C heat needs. The Detailed MoW-C flowsheets along with their material and energy balances are presented in appendix L. It worth mentioning that if the cycle were to use combined Brayton/Rankine cycle (or any power generation method that directly oxidizes the fuel) during the delivery mode, then methanol would need to be dehydrated for combustion purposes and its energy benefit will be unrealized.

4.6 Comparison of the proposed cycles

The simulation results of all the proposed cycles are summarized in Table 4.5, with all the cycles sized for an uninterrupted power output of near 140 MW. The simulation results predict base case storage efficiency values between near 53 to 55% for the proposed cycles, with the LM-C having the highest efficiency of almost 54.9%. For the same power output, the LM-C total electrical energy input during the storage mode is near 2.3% higher than that required for the MoW-C. This can be explained by the greater fraction of feed hydrogen exergy lost as heat of reaction (or lower value

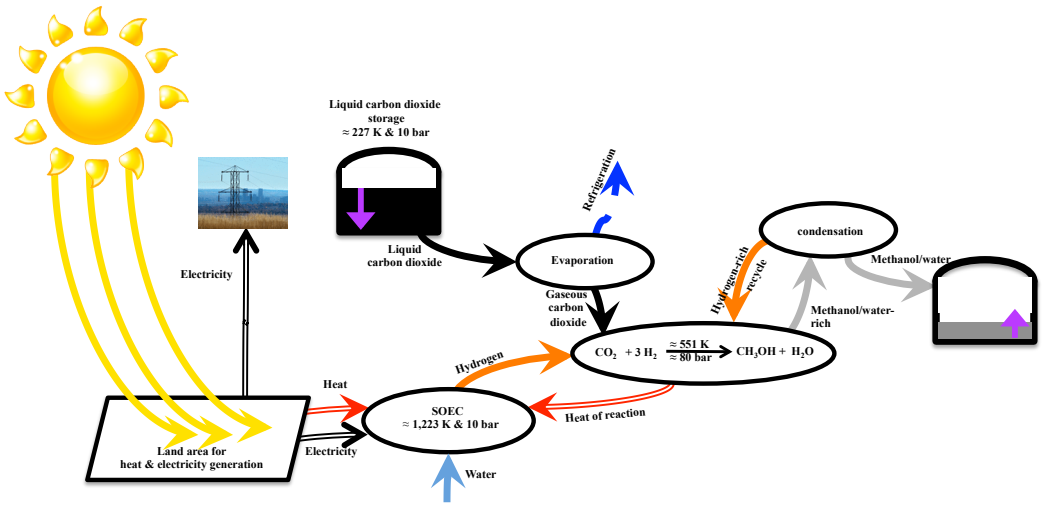

Figure 4.14. Simplified schematic of the proposed MoW-C

of $EX_{H\rightarrow C}$) during the generation of methane along with the additional compression energy required for methane liquefaction compared to MoW-C. For both LM-C and MoW-C, the heat of reaction from carbon fuel synthesis is used to offset a portion of the solar heat requirement (at 950^{o}C) for generating steam feed to the SOEC. However, the higher heat of reaction for methane results in the LM-C having near 64% less external solar heat requirements than the MoW-C. Overall, using the LM-C rather than the MoW-C results in near 60 MWh of exergy savings, which corresponds to 2.2% of the electrical energy output during the delivery mode.

A main reason for the additional exergy input for MoW-C is the 96 MWh of electricity consumption (due to lack of refrigeration source) for CO_2CL during the delivery mode. Consequently, for the same electrical power output, the MoW-C needs to store a greater amount of exergy as carbon fuel (methanol/water mixture) compared to the LM-C. This fact is further compounded due to the lower value of EX_C for methanol compared to methane, which results in methanol oxidation generating greater moles of carbon dioxide than methane for delivering the same amount of power. For the LM-C, if methane liquefaction and CO_2CL steps are carried in a way such that refrig-

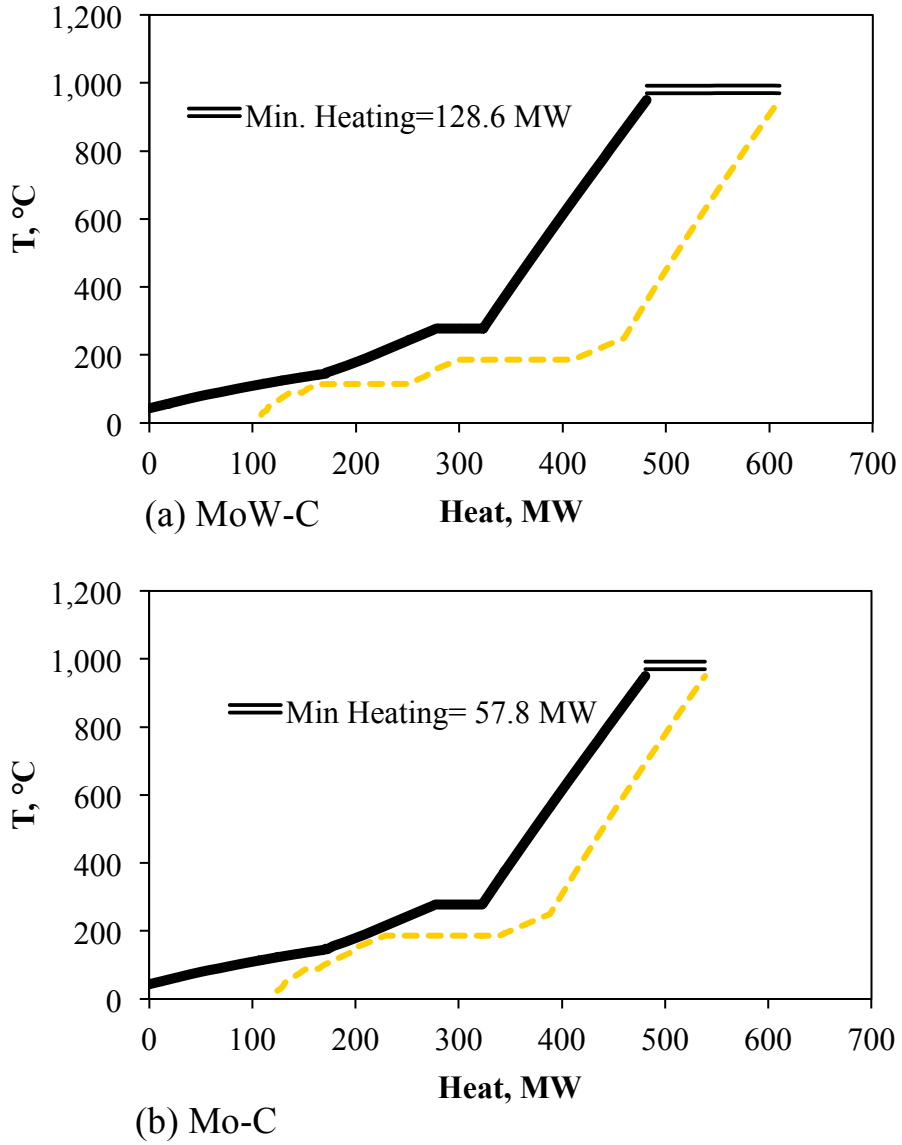

Figure 4.15. a) Process composite curves for the storage mode of the MoW-C shown in Figure 4.14. Detailed flowsheet is shown in Figure L.1. b) Process composite curves for the storage mode of the Mo-C shown in 4.13.

eration is not recovered during evaporation of either of the liquids, then 6% (or 305 MWh) of the total electrical energy input to the cycle will be consumed for methane liquefaction and CO_2CL (see appendix I for flowsheets and matiral/energy balances).

The proposed refrigeration integration between the condensation and evaporation of the two components reduces this number to near 4%. The resulting energy savings compensates for the lower value of $EX_{H\rightarrow C}$ methane over methanol making LM-C, system wise, more efficient than MoW-C. In addition, the LM-C using the synergistic liquefaction schemes has a storage efficiency that is comparable to that of the GM-C, where methane is cooled to -47^{o}C (using vaporizing liquid carbon dioxide) and then compressed to 205 bar for storage (Table 4.5). The GM-C consumes an additional 40 MWh of electricity during the storage mode compared to LM-C, due to the additional methane circulation requirements to compensate for the energy penalty of CO_2CL. In other words, part of the generated methane during the storage mode is oxidized in the delivery mode to provide electricity needed for CO_2CL process. Besides being slightly more efficient, a major benefit for the LM-C is that for the same power output, the liquid methane volume is about one-fifth of the compressed methane volume in the GM-C.

The proposed synergistic liquefaction and evaporation schemes are generally extendable to any gaseous carbon fuel used in the cycle of Figure 4.1. Among carbon fuels candidates evaluated in Table 4.1, ethane, propane and dimethyl ether have their normal boiling point temperatures much closer to carbon dioxide liquefaction temperature of -55^{o}C at 5 bar than that of methane. This is in addition to the other favourable aspects of these fuels discussed earlier. The increased extent of overlapping between the boiling point temperatures of carbon fuels with carbon dioxide suggests the potential for reducing external refrigeration for the carbon fuel liquefaction and/or CO_2CL. However, a direct comparison of boiling points of different carbon fuels to predict external refrigeration needs may only be valid if the corresponding carbon fuel synthesis step has similar conversion and selectivity. To our knowledge, this is currently not the case for ethane, propane, dimethyl ether and methane. For example, synthesizing dimethyl ether in a single step hydrogenation of carbon monoxide gives carbon conversion per pass up to 60% with 95% selectivity [96]. The energy penalty of separating the unconverted reactants and by-products (i.e. hydrogen,

carbon dioxide, carbon monoxide, and methanol) would consume part or all of the available refrigeration of the vaporizing carbon dioxide. Consequently, the remaining refrigeration may not be sufficient to provide the refrigeration needed for liquefying dimethyl ether. Detailed simulations of these select carbon fuels are needed to quantitatively compare them against the LM-C and MoW-C.

Although, there is only slight difference in the storage efficiency between LM-C and MoW-C, there are significant differences in the storage volume. Liquid methane requires near 62% less volume than methanol/water mixture for the same power output from either cycle. The LM-C also stores 21% less volume of liquid carbon dioxide compared to the MoW-C. The lower total storage volume (carbon dioxide and carbon fuel) of the LM-C is primarily a consequence of the higher EX_C and EX_V (Table 4.1) of methane versus 50 mole% methanol/water mixture (EX_V near 8.5 GJ/m3). This unique property of methane allows for delivering the required electricity using fewer moles of carbon fuel (or carbon dioxide). Additionally, the proposed storage of methanol/water mixture in a single storage tank adds larger volume but reduces the energy consumption for the separation of water and increases the storage efficiency, as seen in Table 4.5. If methanol is to be purified, as in the case of the Mo-C, an additional near 121 MWh of exergy input is required for purification, which corresponds to 4.4% of the electrical energy output of the plant during the delivery mode. As seen in Figure 4.16 the amount of water left in the stored methanol may be optimized to provide the required trade-off between storage volume and the energy used in the separation.

In case water produced during the delivery mode is also stored (near 100% pure), then the corresponding volumes for all the four cycles are shown in Table 4.5. The water volume stored for GM-C is near 2% higher than LM-C which is consistent with the trend in volume of carbon dioxide stored. In case of methanol, the volume of water stored for MoW-C is 51% higher than Mo-C, due to the presence of water in carbon fuel stored during the storage mode.

Referring to Figure 4.17, developments in steam methane reforming and SOFC anode catalysis to allow operation at lower steam to carbon ratio (STC) could lead to enhancing the proposed LM-C storage efficiency. A minimum of one mole of steam per mole of methane is required as per the reforming reaction stoichiometry. At this stoichiometry ratio, the storage efficiency is identified to be almost 58.5%. However, currently excess steam (which implies excess water latent heat) is needed to avoid coke formation in the reforming and anode sections of the SOFC (arising from the presence of methane and carbon monoxide) [97, 98]. On the other hand, the steam requirement for methanol steam reforming is not as high as methane reforming (see section 2.7) [24]. Thus, the improvement in storage efficiency that one may obtain by reducing the STC for the MoW-C/Mo-C will not be as significant as that for the LM-C case.

A brief comparison between the proposed LM-C and the hydrogen storage options suggested in the literature (see Figure 4.18 and section 6.6), demonstrate the superiority of the proposed cycle (in terms of storage efficiency). As seen from Figure 4.18 the developed LM-C also compare favourably in terms of storage volume with batteries, represented by sodium-sulfur and lithium-ion batteries, compressed air storage, and pumped hydroelectric storage (see section 6.6) [16, 60, 63, 99].

Table 4.5
Key comparison parameters for the proposed cycles.

Cycle		LM-C	GM-C	Mo-C	MoW-C
Storage mode	Heat in (GWh)	0.14 at 978°C	0.14 at 978°C	0.38/0.53[(2)] at 978 /124°C	0.38 at 978°C
	Exergy of heat (GWh)[(1)]	0.1	0.1	0.42	0.29
	Electricity in (GWh)	4.85	4.89	4.71	4.74
Delivery mode	Electricity out (GWh)	2.72	2.72	2.72	2.72
Overall cycle parameters	Storage efficiency[(3)]	54.86	54.40	52.96	54.24
	Carbon fuel volume (m^3)	632	3,086	1,156	1,679
	Liquid carbon dioxide volume (m^3)	717	728	907	907
	Water volume (m^3)	1,340	1,367	824	1,232

(1) Exergy of the heat = Heat duty × $\frac{\text{Heat source temperature-Ambient temperature}}{\text{Solar heat temperature}}$; Solar heat temperature=1,251 K, Ambient temperature= 298 K

(2) 0.53 GWh is used to purify the methanol from the coproduced water using a distillation column with a reboiler temperature of 113°C.

(3) Storage efficiency is defined as: Electricity out during delivery mode / (Electricity in during storage mode + exergy of heat in during storage mode).

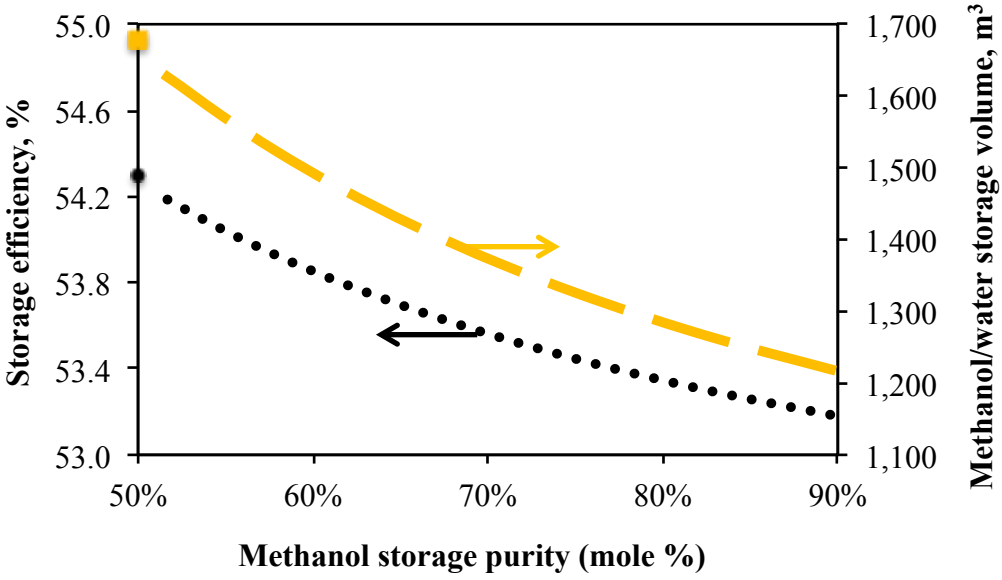

Figure 4.16. Effect of methanol storage purity on the MoW-C storage efficiency and storage volume.

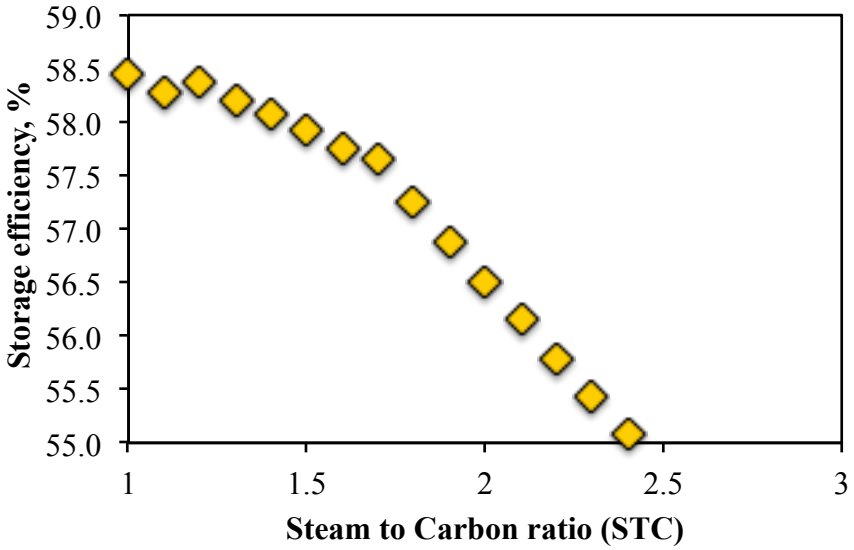

Figure 4.17. Effect of STC on the storage efficiency of the LM-C.

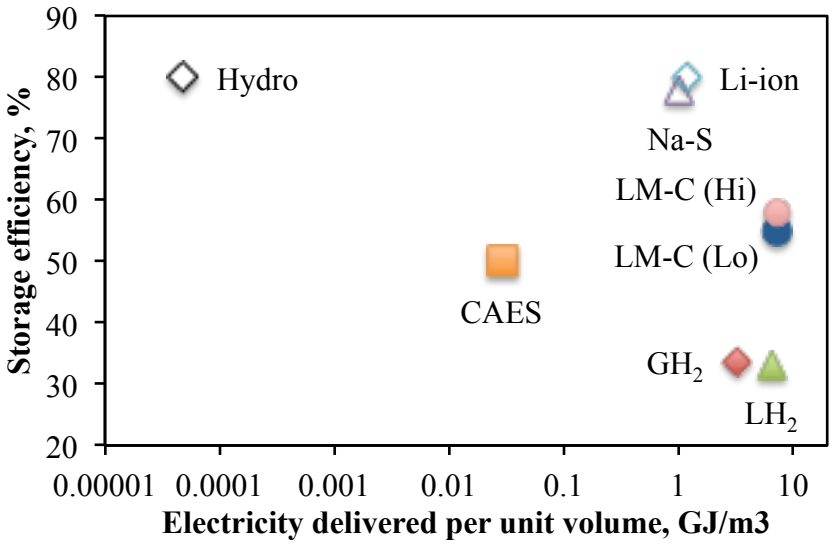

Figure 4.18. Storage efficiency and volumetric energy density of the LM-C, high-hi (STC=1) and low -lo (STC=2.5), vs. hydrogen (gas-GH2, liquid-LH2), batteries (Na-S, Li-ion), compressed air energy storage (CAES), and pumped hydroelectric storage (hydro). Volumetric energy density of LM-C does not consider volume of water stored.

4.7 Performance of the proposed cycles with wind-based electricity

The storage efficiencies of the proposed cycles can also be estimated for the case of using wind-based electricity. In this case, heat needed by the cycles is supplied via resistive heating with electricity-to-heat conversion efficiency of 98% [67]. When compared to the direct heat supply as in the solar energy case, the indirect supply of heat is expected to reduce the storage efficiency of the cycle. For the LM-C and GM-C, the storage efficiency when using wind is estimated to be 54.5% and 54%, respectively. These values are marginally lower than the values when using solar energy, shown in Table 4.5. For the MoW-C, the shift from solar to wind energy results in a more pronounced storage efficiency decline from 54.2% to 52.8%. This is attributed to the higher heat demand of the MoW-C compared to the LM-C and GM-C. For the Mo-C, the increase heat demand arising from the use of a distillation column (for methanol-water separation) results in lower storage efficiency of 48%.

4.8 Performance of the proposed cycles with oxy-fuel CC

While the above cycles designs utilize the efficient SOFC technology for the delivery mode, it worth investigating the cycles performance using the more mature gas turbine based technologies. Thus, the developed oxy-fuel NGCC and MoCC of section 2.8 are used to replace the ERPP deployed for the delivery mode of the LM-C and Mo-C. For the LM-C, see Table 4.6, the storage efficiency of the cycle is estimated to be near 31.8%, which is almost 23% less than the LM-C that uses the ERPP (results shown in Table 4.3). Such substantial efficiency reduction is a consequence of the less efficient oxy-fuel NGCC which is associated with near 40.2% efficiency (on LHV basis). Also to be noted the lower LHV value of methane feed to the storage tank (during the storage mode) when compared to the LM-C results shown in Table 4.3 (i.e. LM-C that uses the ERPP). This is an outcome of the less quantity of stored carbon dioxide (means less storage volume, see Table 4.6 and4.3 for comparison) resulting from the less liquid carbon dioxide recovery in the oxy-fuel NGCC. Unlike the

ERPP, where the unrecovered carbon dioxide is part of unconverted fuel all recycled to the SOFC, the unrecovered carbon dioxide of the oxy-fuel NGCC is associated with inert argon and nitrogen sourced from the ASU. Thus, can not be recycled to the power generating turbines, instead need to be vented to the atmosphere. This also results in higher methane makeup need during the delivery mode of the cycle, see appendix M for detailed material/energy balance and flowsheets.

For the Mo-C, no full scale simulation were conducted. However, the result of the storage mode, reported in Table 4.4, along with MoCC results, reported in table G.5 , are used to estimate the expected storage efficiency. Here, the energy output of the MoCC is divided by the energy input of the Mo-C and found to be almost 30.3%. As mentioned in section 2.8.1, the delivery mode efficiency (i.e. efficiency of the oxy-fuel NGCC and MoCC) can be improved by almost 9% using the specification given by reference [27] and implementing a more efficient ASU designs such as those reported to produce oxygen with a specific power of 631 kj/kg oxygen [57]. As a result, the storage efficiency of the LM-C and Mo-C can be increased to 38.9 and 37.4%, respectively.

4.9 Conclusions

The proposed fuel selection metrics and closed loop carbon transformation between liquid carbon dioxide and liquid carbon fuel provide an array of solutions for GWh level electrical energy storage in a renewable energy economy. Depending on the choice of carbon fuel, we propose the following unique energy integration schemes. If the carbon fuel is a gas, then the carbon fuel and carbon dioxide vaporization and liquefaction steps are integrated to reduce the energy penalty arising from using external refrigeration. If the carbon fuel is a liquid and its purification from water is energy intensive, then storing a carbon fuel/water mixture in conjunction with fuel reforming followed by oxidation is the preferred mode of operation. The fuel/water mixture composition can be adjusted to balance the storage volume and efficiency. The achievable balance between storage volume and storage efficiency for the cycle

Table 4.6
Key simulation results for the LM-C with the oxy-fuel NGCC shown in Figure 2.21.

LM-C with oxy-fuel NGCC			
Storage mode			
Methane to tanks LHV=781.44MW			
Compressors power, MW		Heat exchangers	
K-1	31.60	Heat duty, MW	
K-2	0.61	E-4	24.79
K-3	15.69	E-17	3.22
K-4	3.75	Exergy, MW	
K-5	0.03	E-4	18.88
K-6	0.54	E-17	2.45
K-7	16.70	Net power, MW	
K-8	0.004	1,010.34	
Turbines power, MW			
T-1	-35.56	Efficiency, %	
T-2	-2.54	77.34	
T-3	-4.50	**Delivery mode**	
		Methane to SOFC LHV=199.6MW	
T-4	-8.23	Liquid carbon dioxide volume, m^3	711.25
Pumps power, kW		Net power output, MW	-80.25
P-1	95.54	Efficiency, %	40.20
P-2	279.06	**Overall cycle**	
P-3	71.87	Total storage volume, m^3	1,336
SOEC power, MW	970.47	Storage efficiency, %	31.78

Negative values indicate electrical power generation, positive values indicate electrical power consumption.
Storage mode efficiency=Liquid methane LHV/net power input
Delivery mode efficiency=Net power output/Gaseous methane LHV
Storage mode net power= Compressors power+SOEC power+Turbines power+pump power+ exergy of heat.
Exergy of heat exchanger= Heat duty $\times \frac{\text{Solar heat temperature-Ambiant temperature}}{\text{Solar heat temperature}}$; Solar heat temperature=1,251 K, Ambient temperature= 298 K
Storage efficiency= $\frac{\text{Delivery mode net power output} \times 19.2}{\text{Storage mode net power} \times 4.8}$

also depends on the choice of carbon fuel, as discussed via the proposed fuel selection metrics (EX_C, $EX_{H\rightarrow C}$, EX_V). While there is no single fuel that is simultaneously

most favourable among all the three metrics, we have identified some favourable candidates, such as, methanol, methane, ethane, propane and dimethyl ether. As demonstrated through detailed simulations, the use of methane and methanol in the proposed cycle offer some interesting features. For methane, these include the highest exergy content per mole carbon, dense energy storage as a liquid, and its refrigeration synergy with liquid carbon dioxide. In case of methanol, it does not require refrigeration for liquefaction, minimizes the fraction of hydrogen exergy lost as heat of reaction during its synthesis, and provides an opportunity for eliminating the purification energy requirement by storing 50-50 mole% methanol/water mixture. All these features provide us with cycles with low storage volume while maintaining reasonably high storage efficiency of 55-59%.

CHAPTER 5. USE OF THE STORAGE CYCLE CONCEPT BEYOND ELECTRICITY APPLICATION

The objective of this chapter is to show the possible applicability of the proposed storage cycle concept for baseload chemical energy supply. Although no simulations were conducted for this chapter, the author objective is to motivate the future investigation of what will be subsequently discussed. Here, both baseload renewable synthetic methane and liquid fuels, for the transportation sector, around the clock supply are discussed.

5.1 Synthetic methane

Figure 5.1 shows one possible configuration for uninterrupted supplying of synthetic methane using solar energy and biomass. Here a gasification route is chosen for the generation of syngas necessary for the methane synthesis step. In addition to biomass, oxygen, and steam, hydrogen (produced from SOEC or other mean of water dissociation systems) can be fed to the gasification process to provide the energy needed by the endothermic gasification reaction [3]. Leaving the gasification process is a syngas mixture with carbons to hydrogen ratio less than that required for the methane generation step (typically in the range of 1 to 2, depending on the gasification technology and biomass composition [25]). Therefore, extra hydrogen could be produced from the SOEC for obtaining the desired ratio of 3.5 (i.e. 3.5 mole hydrogen per mole carbons). Also fed to the methane synthesis step is stored carbon dioxide (generated and stored during the storage mode) along with its stoichiometric hydrogen requirements being supplied from the SOEC. While portion of the methane leaving the synthesis step is fed to the pipeline grid, some of the gaseous methane

is purified and liquefied for storage. Methane liquefaction here may be carried out using refrigeration cycles similar to those discussed in chapter 4 and the refrigeration released from liquid carbon dioxide evaporation (see Figure 5.1).

During the delivery mode, the gasification process may be turned down (or used for other purposes) such that the stored liquid methane compensates (or partially compensate) for the lower methane production. Since solar energy is not available to generate hydrogen, the gasifier will need to be operated in a conventional manner in which it burns portion of the biomass for satisfying the gasification energy need. Also the lack of hydrogen source will necessitate the use of WGS reaction to shift the carbon monoxide (with steam) leaving the gasifier into hydrogen; hence, adjusting the hydrogen to carbon monoxide ratio to be 3. Generated carbon dioxide from the shift and gasification steps is recovered to be purified and liquefied for storage. Here, portion of the needed refrigeration may be supplied from the refrigeration released form the liquid methane evaporation step.

Since all of the carbons, sourced from the biomass, are recovered and converted to methane using solar hydrogen, the system is anticipated to be associated with near 100% carbon efficiency. Also the synergistic methane and carbon dioxide purification and liquefaction schemes are expected to result in a relatively high-energy efficiency. Detailed designs and simulations are needed to confirm these claims.

An alternative configuration of Figure 5.1 is to eliminate the methane storage step and operate the delivery mode as a normal biomass to synthetic methane process [100]. Carbon dioxide here, sourced from the WGS step, may be recovered and liquefied to be converted to methane during the storage mode; thus, achieving near 100% carbon efficiency. One may also chose not to store carbon dioxide, instead venting it to the atmosphere. In this case, only the storage mode may be found to be 100% carbon efficient.

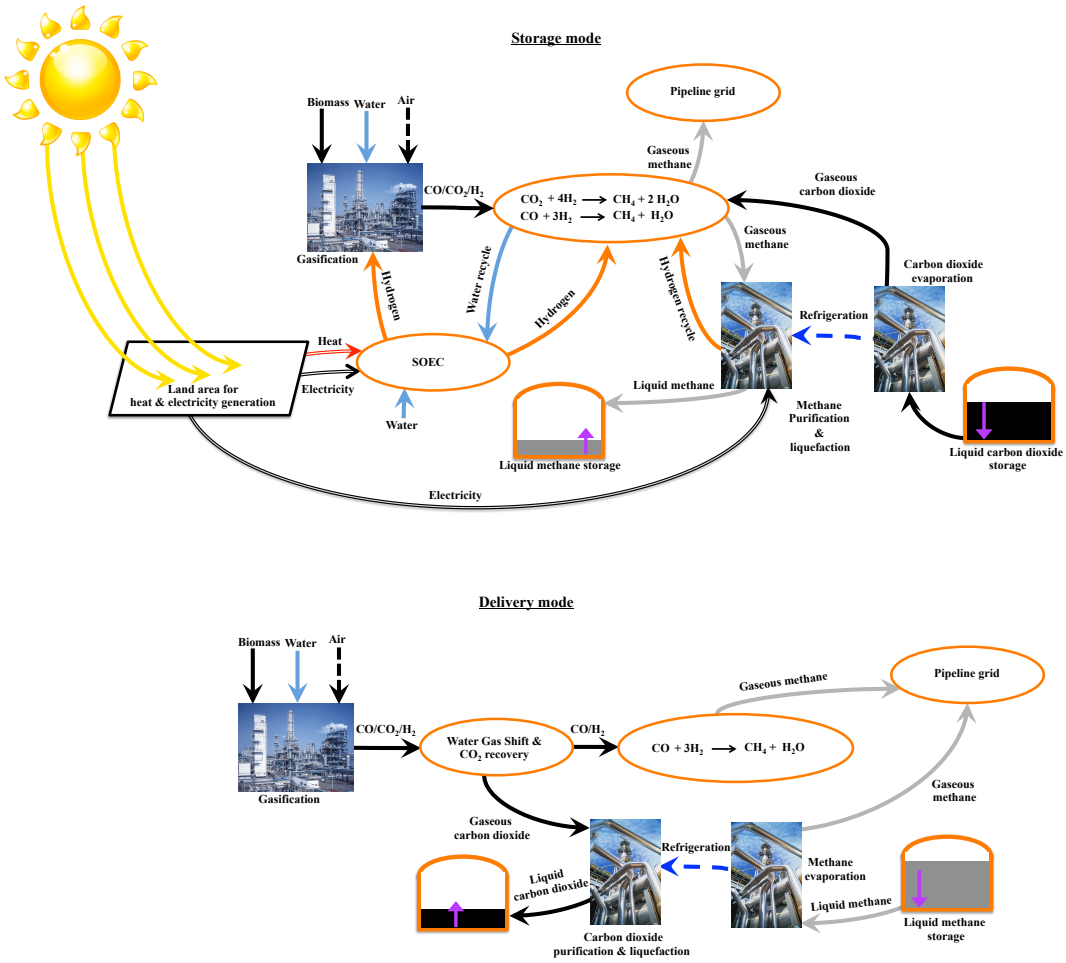

Figure 5.1. A conceptual sketch of continuous synthetic methane supply using the proposed storage cycles concept from solar energy and biomass.

5.2 Liquid Fuels

Using the same concept of synthetic methane, and as demonstrated in Figure 5.2, renewable liquid fuels can also be supplied around the clock from biomass and solar energy. Here the syngas leaving the gasification process is fed to a Fischer Tropsch (FT) process along with hydrogen, from the SOEC, to ensure that the FT hydrogen to carbon ratio is met. On the other hand, stored liquid carbon dioxide, after evaporation, is reacted with hydrogen in a RWGS process to generate additional

syngas for the FT process. This step (i.e. RWGS) recovers the carbon atoms wasted during the WGS step of the delivery mode of the process (see Figure 5.2).

While the process of Figure 5.2 does not store energy, methane can also be synthesized parallel to the FT synthesis for energy storage. Now during the delivery mode, methane is evaporated to replace the WGS step by providing hydrogen to the FT process. This can be achieved by using one of the methane reforming techniques inside or outside the gasifier [101]. Carbon dioxide sourced from methane reforming is recovered, liquefied, and stored to resynthesize some of the methane during the storage mode. Similar to the synthetic methane case, the purification and liquefaction energy need for carbon dioxide and methane can be minimized by integrating thier liquefaction and evaporation steps.

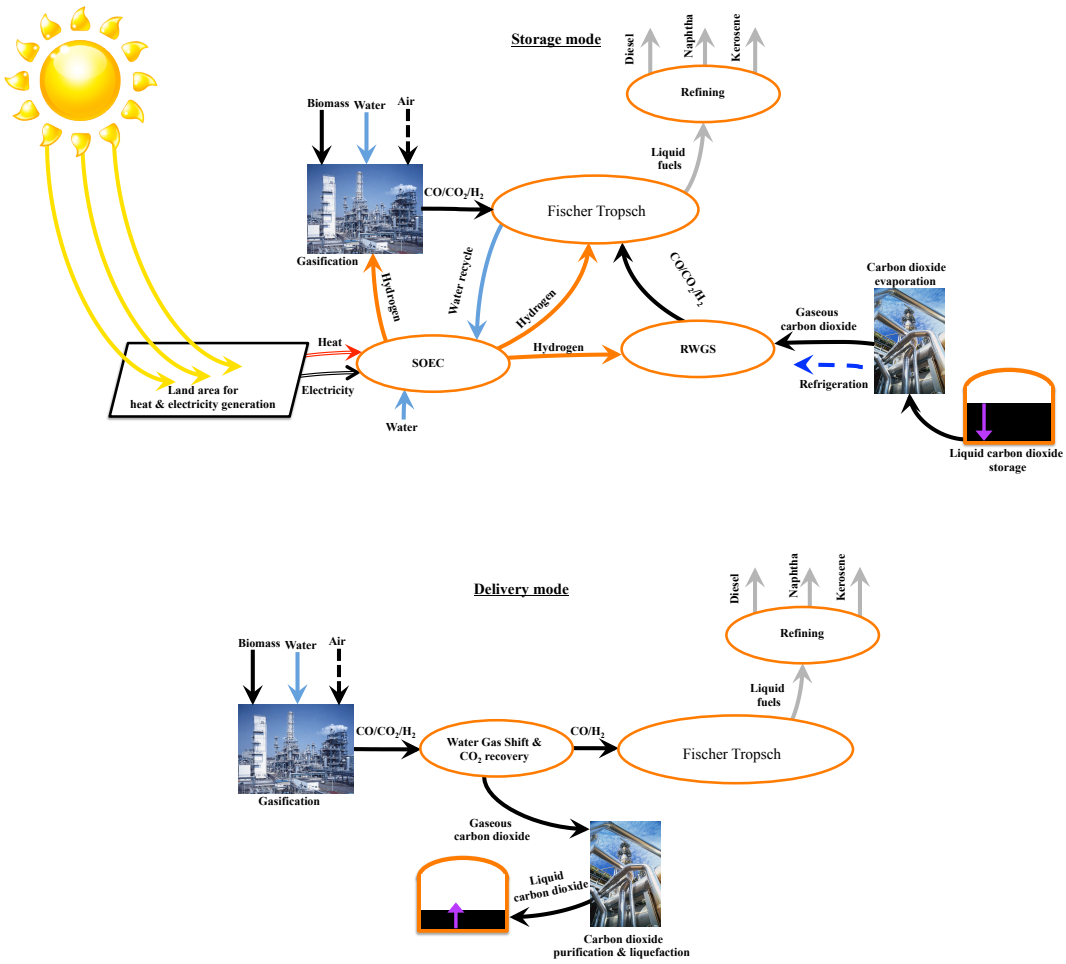

Figure 5.2. A conceptual sketch of continuous liquid fuel supply from solar energy and biomass.

CHAPTER 6. BASIS OF DESIGN AND MODELING/SIMULATION APPROACHES

6.1 Thermodynamic modeling

For the simulations, thermodynamics properties such as enthalpy and chemical equilibrium constants are needed for material and energy balance calculations. While a large number of thermodynamic models are available for such properties calculations, one needs to be careful on which model to use, as some might give unreasonable results. Different guidelines to identify the most proper model for a given system/process are discussed in the literature [102–104]. After considering these guidelines, it has been concluded that steam tables and group contribution equation of state are suitable for the system in hands.

The NBS/NRC steam tables are used to simulate for the flowsheet sections involving only water and/or steam. All other flowsheets are simulated using the Predictive Redlich-Kwong-Soave (PSRK) equation of state. This property method was further validated against experimental Vapor Liquid Equilibrium (VLE) data that approximate the VLE behavior in the different sections of the considered process. A snapshot of the comparison between PSRK predictions and experimental data is provided in Figure 6.1. Overall, the PSRK equation of state is found to be reasonably accurate for the range of temperatures and pressures encountered in the simulations.

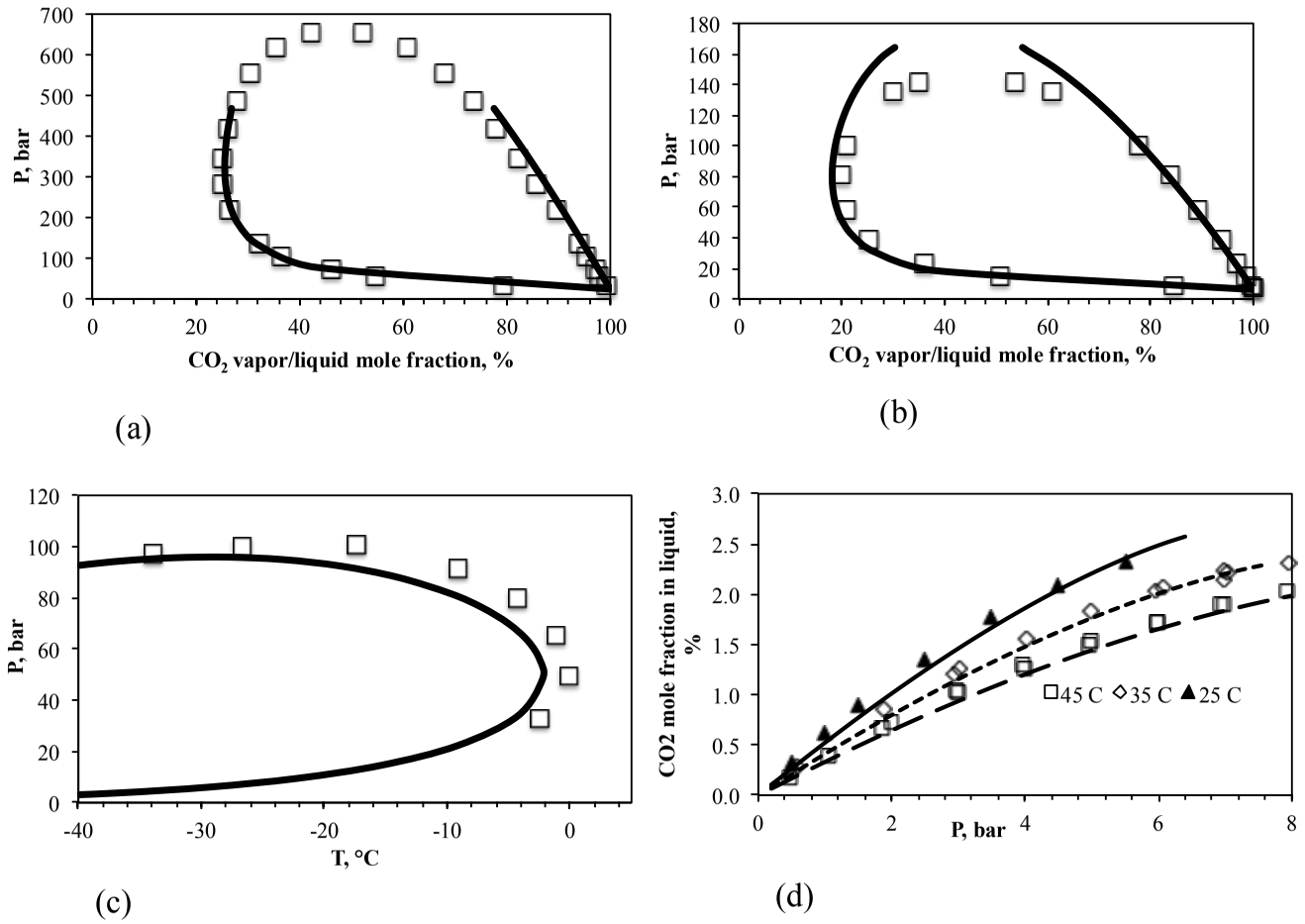

Figure 6.1. PSRK VLE (black line) vs experimental data (dots) for (a) Carbon dioxide-Hydrogen mixture at -13^{o}C [105], (b) Carbon dioxide-Carbon monoxide mixture at -50^{o}C [106], (c) NG [107], and (d) Carbon dioxide-Water mixture [108].

6.2 Non Aspen Plus^{TM} models

All unit operations in the designed flowsheets were modeled and simulated using Aspen Plus^{TM} process simulator version 7.2. Aspen Plus^{TM}; however, does not have built in models for adsorbers, SOFC, and SOEC. Therefore, these models were built using Microsoft Excel^{TM} that is linked to the process simulator through a calculator block [30]. This link is established to export required physical and chemical properties and other model inputs from Aspen Plus^{TM} to Microsoft Excel^{TM}. Results obtained in Microsoft Excel^{TM} are then exported back to Aspen Plus^{TM}. The following sections of this dissertation describe the implemented models along with selected key results.

6.2.1 SOFC model

SOFC modeling approach presented in [31, 32] is adopted and implemented according to equation 6.1 to 6.7 and the algorithm of Figure 6.2. A fuel cell stack with multiple fuel cells is assumed and referred in this work as the SOFC. Internal indirect steam fuel reforming is implemented to generate syngas rich in hydrogen and carbon monoxide to be fed to anode sides of the SOFC. By having the reforming process integrated within the fuel cell stack allows for utilization of the excess heat generated in the fuel cells to supply the endothermic reforming heat of reaction. This internal reforming configuration allows for efficient heat integration, which eliminates the need for any external heat source to drive the reforming reactions, and improves the process efficiency [24]. Surplus heat is evacuated from the stack using excess air fed to the cathode sides of the SOFC. Reforming reactions and fuel electrochemical oxidations were all assumed to be isothermal and modeled using chemical equilibrium approach [31, 32]. Electrical losses, presented in [31, 32] and listed in Table 6.1, are all based on empirical relations fitted to experimental data for pressure close to atmospheric pressure obtained for a planar fuel cell module. The modeled losses are: activation polarization (for the anode and cathode), diffusion polarization (for the anode and cathode), and ohmic losses (for the electrolyte and metal interconnectors).

These losses consume part of the energy associated with the fuel producing heat at the SOFC temperature. Increasing the pressure of SOFC, leads to reducing losses which improve the power generation efficiency [109]. Based on current demonstrations of SOFC technology, operating pressures up to 10 bar seems to be admissible [48]. As a result, in this work, the SOFC is operated at a pressure of around 10bar and the electrical losses calculations were modified, as shown below, to include a pressure adjustment factor (AF) obtained from experimental data in [48]. The main equation's characterizing the SOFC are listed below.

$$W_{Actual}^{LP} = \Delta G - W_{Losses}^{LP} \tag{6.1}$$

$$V_{LP} = \frac{W_{Actual}^{LP}}{I_{Stack}} \tag{6.2}$$

$$I_{Stack} = \frac{nF\lambda_f}{N_{Cell}} = \frac{nFU_f m_{so_2}}{N_{Cell}} \tag{6.3}$$

$$U_f = \frac{m_{o_2}}{m_{so_2}} \tag{6.4}$$

$$V_{HP} = V_{LP} + N_{Cell} \times AF \tag{6.5}$$

$$W_{Actual}^{HP} = V_{HP} \times I_{Stack} \tag{6.6}$$

$$Q_{Net} = W_{Actual}^{HP} + Q_{Reforming} + Q_{Cathode} - Q_{Oxidation} \tag{6.7}$$

where;

W_{Actual}=SOFC Direct Current (DC) electrical power, Watt (W); ΔG=Difference in Gibbs free energy around the SOFC excluding the reformer (W); W_{Losses}=SOFC electrical power losses as a result of activation polarization, diffusion polarization, and ohmic losses (W); LP=Low pressure=1.013bar; V=SOFC voltage (volt); I_{Stack}=SOFC

current (Ampere); n=Number of electors transferred as a result of the electrochemical reaction, 4 mole electrons/mole of fuel. The fuel mainly consists of hydrogen carbon monoxide; therefore, two mole of electrons is produced from each; F=Faradays constant, 96,485 Columb/mol electrons (Columb = Ampere times second); λ_f=Molar rate of fuel conversion (mole/s); N_{Cell}=Number of fuel cells in the SOFC; U_f=Fuel utilization (i.e. conversion); m_{so_2}=Stoichiometric oxygen molar flow rate (mole/s); m_{o_2}=Molar flow rate of oxygen across the electrolyte (mol/s); HP=High pressure= 10bar; AF=Pressure adjustment factor 0.09 Volt/cell at 10 bar [48]; Q_{Net}=SOFC net heat duty (positive: heat is required, negative: heat is produced) (W); $Q_{Cathode}$=SOFC heat absorbed by the air following in the fuel cell cathode (W); $Q_{Reforming}$=SOFC heat required to carry out the reforming reactions (W).

Referring to Figure 6.2, the simulation of the SOFC starts with defining the reformer feed conditions (i.e. temperature, pressure, and component's flow). The calculations relevant to the reforming reactions are carried out using the Aspen Plus^{TM} equilibrium reactor model Requil. In Requil, the reforming heat need and product conditions (i.e. components flow, temperature, and pressure) are calculated using a chemical equilibrium approach [110]. Following the reforming simulation, the anode oxygen flow that corresponds to the user specified current, I_{Stack}, is calculated using equation's 6.3 and 6.4. Here, the molar rate of fuel conversion, λ_f, is first calculated using equation 6.3. Giving λ_f, the fuel utilization, U_f, is calculated given that the stoichiometric oxygen for oxidation (oxidizing the fuel to give a value equals to λ_f) can be calculated from material balance. Anode oxygen flow is then calculated using equation 6.4 for export to Aspen Plus^{TM} component splitter model that represent the cathode-electrolyte section of the device. . The air feed to the cathode can then be determined by dividing the anode oxygen flow by the oxygen mole fraction of air (i.e. near 21 mole%). The temperature of the air leaving the cathode is specified in Aspen Plus^{TM} heater model which represent, with the component splitter, the cathode of the SOFC. The heater model is responsible for calculating the heat absorbed by cathode air stream. Given the anode oxygen mole flow, reformed fuel

conditions, and anode temperature and pressure (user specified), the electrochemical oxidation simulation (i.e. anode simulation) is ready to be conducted in Requil. Similar to the reformer, Requil here determines the product conditions of the anode side of the SOFC, which will enable us to calculate the actual produced work and the heat duty of the SOFC. The sequence these calculations (i.e. actual work and heat duty) are carried out is as follow. 1) The actual DC work, W^{LP}_{Actual} is calculated at LP condition (i.e. close to atmospheric pressure) using equation 6.1 with the Gibbs free energy, ΔG, calculated by Aspen Plus^{TM}. The power losses at LP, W^{LP}_{Losses}, are estimated using the formulas listed in Table 6.1. It is to be noted that the anode and cathode activation polarizations (η_{Anode} $\eta_{Cathode}$, respectively) are solved using an iterative approach using Aspen Plus^{TM} Design Spec tool [30]. Here, the relations (i.e. activation polarizations relations) are defined in Microsoft Excel^{TM} with the activation polarization value being imported from a dummy variable stream, such as temperature. The equation output (i.e. current density j) is exported from Microsoft Excel^{TM} to another dummy variable stream (e.g. temperature). Now the Design Spec can be used to vary the dummy variable defined for the activation polarization such that the dummy variable of the current density satisfy a certain value (determined by dividing the user specified SOFC current by the specified active area). 2) Given W^{LP}_{Actual}, the LP voltage, V_{LP}, is calculated using equation 6.2. Following this, the HP voltage, V_{HP}, is estimated according to equation 6.5 with AF value that corresponds to the actual operating pressure of the SOFC. Finally, the actual DC power, W^{HP}_{Actual}, corresponding to the actual operating pressure and the SOFC heat duty, Q_{Net}, are estimated using equation's 6.6 and 6.7, respectively. If Q_{Net} is greater than zero, then there is no enough heat to run the reforming reactions making it necessary to increase the SOFC current (assuming that no external heat is to be supplied for the reformer). On the other hand, if Q_{Net} is less than zero, then the SOFC is producing excess heat which must be evacuated by increasing the air flow through the device.

Figure 6.3 shows the well-known electrical power and net heat responses as function of fuel utilization derived from the SOFC model using methane as the fuel [50].

Alternatively, the same curves could be plotted as a function of the current I_{Stack} by converting the U_f into current using 6.3. It is essential to note that up to U_f values of almost 82%, the generated heat in the SOFC stack is not sufficient to drive the reforming reactions. In other words, the positive values on the right vertical axis indicate the amount of the external (outside the boundary of the SOFC) heat required by the reforming process. Beyond U_f value of 82%, the stack will be producing excess heat (more than the reforming requirements) that needs to be evacuated by excess airflow.

Table 6.1
SOFC electrochemical losses adopted from [31, 32]

Description	Equation
Anode activation polarization, η_{Anode}	$j = j_{0,Anode}\left[\exp\left(\frac{2F}{RT}\eta_{Anode}\right) - \exp\left(-\frac{F}{RT}\eta_{Anode}\right)\right]$
	$j_{0,Anode} = \frac{RT\sigma_{Anode}}{3F}$
	$\sigma_{Anode} = \sigma_{0,Anode}\exp\left(-\frac{E_{A,Anode}}{RT}\right)$
Cathode activation polarization, η_{Cathode}	$j = j_{0,Cathode}\left[\exp\left(\frac{F}{2RT}\eta_{Cathode}\right) - \exp\left(-\frac{F}{2RT}\eta_{Cathode}\right)\right]$
	$j_{0,Cathode} = \frac{2RT\sigma_{Cathode}}{F}$
	$\sigma_{Cathode} = \sigma_{0,Cathode}\exp\left(-\frac{E_{A,Cathode}}{RT}\right)$
Diffusion anode polarization, θ_{Anode}	$\theta_{Anode} = \left(\frac{RT}{2F}\right)\ln\left(1 - U_f\right)$
Diffusion cathode polarization, θ_{Cathode}	$\theta_{Cathode} = \left(\frac{RT}{2F}\right)\ln\left(1 - \frac{U_f}{\lambda}\right)$
Electrolyte resistive, $R_{\text{Electrolyte}}$	$R_{Electrolyte} = \frac{1}{\sigma_{Electrolyte}}\frac{L_{Electrolyte}}{A_{Cell}}N_{Cell}f_{cc}$
	$\sigma_{Electrolyte} = \sigma_{0,Electrolyte}\exp\left(-\frac{E_{A,Electrolyte}}{RT}\right)$
Interconnect resistive, $R_{\text{Interconnect}}$	$R_{Interconnect} = \frac{R_{Interconnect,Anode} + R_{Interconnect,Cathode}}{A_{Cell}}N_{Cell}$
Electrical power losses, W_{Losses}	$W_{Losses} = \left(R_{Interconnect} + R_{Electrolyte}\right)I_{Stack}^2 +$
	$\left(\eta_{Anode} + \eta_{Cathode} + \theta_{Anode} + \theta_{Cathode}\right)N_{Cell}I_{Stack}$
Current density	$j = \frac{I_{Stack}}{A_{Cell}} \equiv \frac{A}{cm^2}$
	Where
j: Current density (Ampere/cm^2), A_{Cell}: Active area of a single cell (cm^2)	F : Faradays constant , R: Universal Gas constant,
$E_{lectrolyte}$: Thickness of the electrolyte (cm^2)	T: SOFC Stack operating temperature
	U_f :Fuel conversion (utlization), λ:excess air factor
	$E_{A,Anode} = 115{,}781$ j/mol, $E_{A,Cathode} = 157{,}659$ j/mol ,
	$E_{A,electrolyte} = 79{,}535$j/mol, $f_{cc} = 4$, $R_{Interconnect,Cathode} = 0.1\ \Omega\,\text{cm}^2$,
	$R_{Interconnect,Anode} = 0.03\ \Omega\,\text{cm}^2$, $\sigma_{0,Anode} = 433{,}033\ \Omega^{-1}\text{cm}^{-1}$,
	$\sigma_{0,Cathode} = 61{,}527{,}821\ \Omega^{-1}\text{cm}^{-1}$, $\sigma_{0,Electrolyte} = 372.33\ \Omega^{-1}\text{cm}^{-1}$

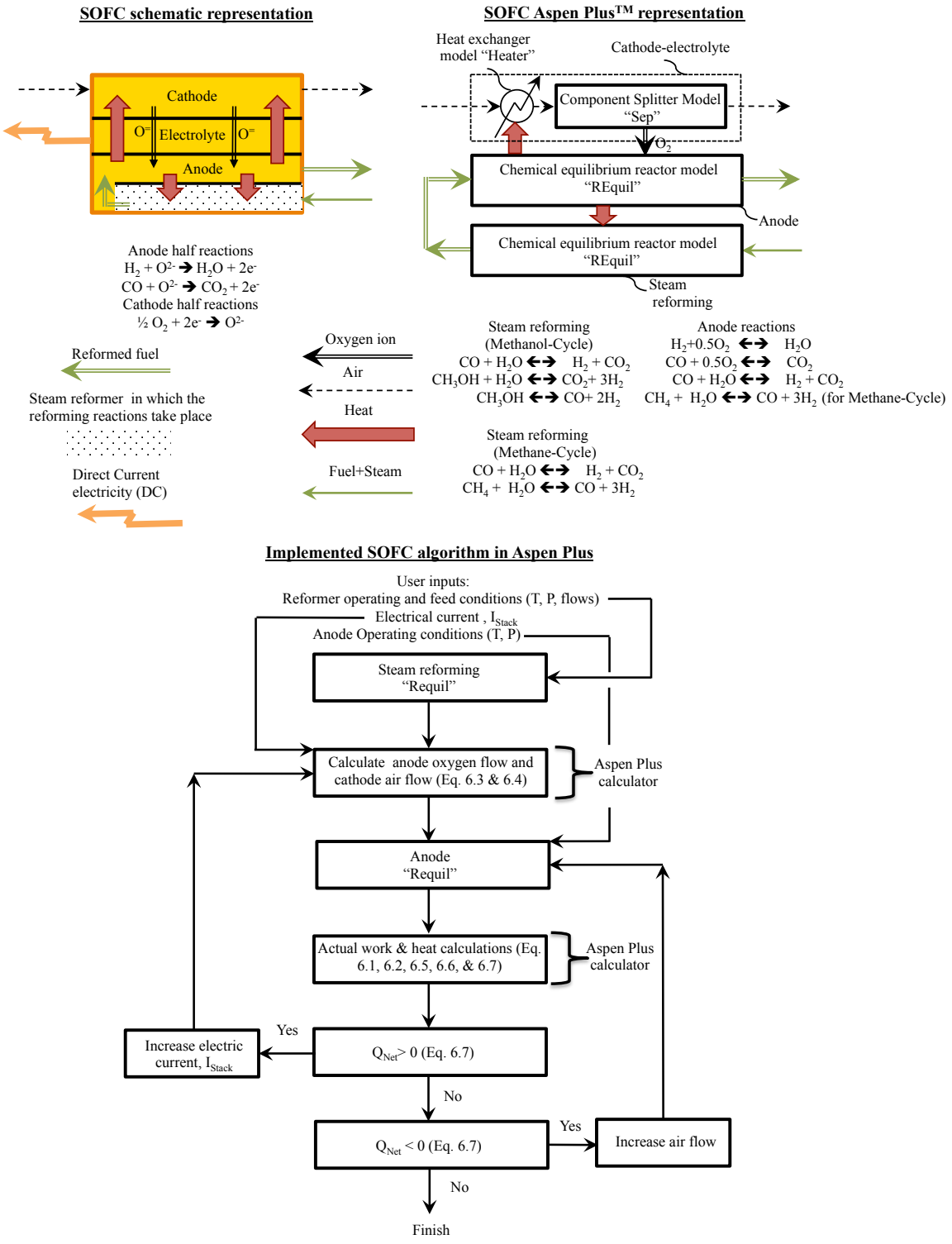

Figure 6.2. Modeling approach for SOFC. Details of REquil, Sep, and Heaters models are available in [30].

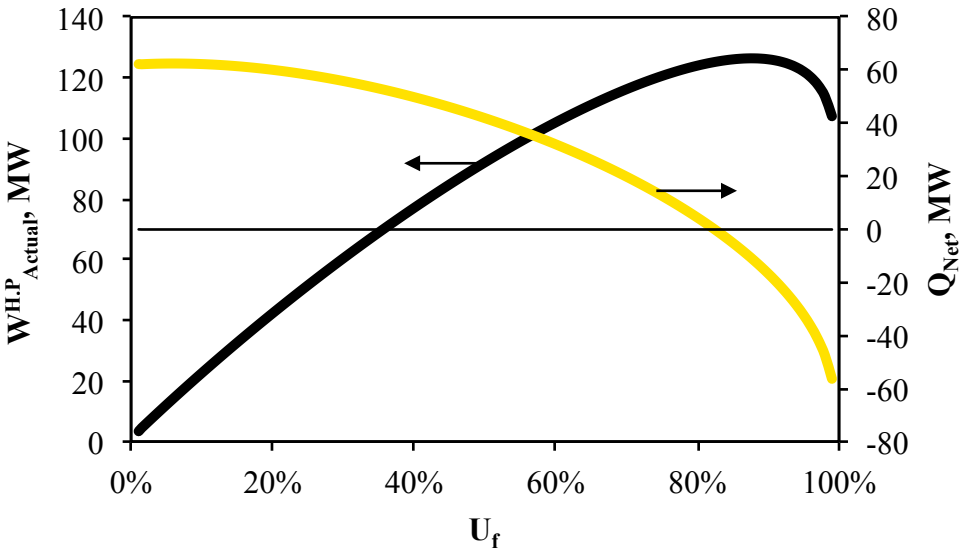

Figure 6.3. SOFC characteristics curves for methane inlet flow, STC ratio, operating temperature, and operating pressure of 895kmol/h, 2.5, 850^{o}C, 10bar, respectively. Air flow is fixed at 1.1 times the stoichiometric requirements.

6.2.2 SOEC model

The below equations and Figure 6.4 elaborate on the SOEC model used for this study. An electrolysis cell stack with multiple electrolysis cells is assumed and referred in this work as SOEC. Electrical current along with the cathodes, anodes, and steam (to be dissociated) conditions are provided as inputs to the model. Steam conversion, actual work, and stack net heat requirements are calculated using equations 6.8 to 6.11.

The flow rate of the sweep air flowing into the anode side is calculated from material balance such that the discharge stream contains 50 mole% oxygen [91]. The relations for electrical losses are assumed to be the same as those adopted for the SOFC model described earlier, with the exception of anode diffusion polarization which has been neglected [89]. These losses consume part of the electrical power input producing heat at the SOEC operating temperature. The dissociating steam forms a feasible heat sink for such high temperature heat. Thus, it is assumed that all the generated heat is transferred to the cathode side in which the steam is dissociating. To ensure no heat leaks to the anode side, the sweep air is fed at the operating temperature of the SOEC; thus, eliminating the heat transfer-driving force from the cathode sides to anode sides. Although, in this work the SOEC is operated at around 10 bar, the SOEC model has not been modified to take into consideration the high pressure effect due to lack of data on this subject.

$$I_{Stack} = \frac{n_s F \lambda_s}{N_{Cell}} = \frac{nFU_s m_s^{Feed}}{N_{Cell}} \tag{6.8}$$

$$U_f = \frac{2m_{o_2}}{m_s^{Feed}} \tag{6.9}$$

$$W_{Actual} = \Delta G + W_{Losses} = I_{Stack} \times V \tag{6.10}$$

$$Q_{Net} = Q_{Dissociation} - W_{Actual} \tag{6.11}$$

$$V_{TN} = \frac{\Delta H_{Dissociation}}{n_s F} \tag{6.12}$$

where;

W_{Actual}= SOEC electrical power (W); ΔG= Difference in Gibbs free energy around the SOEC (W); W_{Losses}= SOEC electrical power losses as a result of activation polarization and ohmic losses (W); V= SOEC voltage (volt); I_{Stack}= SOEC current (Ampere); n_s= Number of electors transferred as a result of the electrochemical reaction, 2 mole electrons/mole of steam; λ_s= Molar rate of steam conversion (mole/s); U_s= Steam utilization (i.e. conversion); m_s^{Feed}= Steam feed molar flow rate (mole/s); m_{o_2}= Molar flow rate of oxygen across the electrolyte (mol/s); Q_{Net}= SOEC net heat duty across (positive: heat is required, negative: heat is produced) (W); $Q_{Dissociation}$= Heat required by the steam dissociation reaction in the cathode sides at the defined operating conditions (W); V_{TN}=Thermal-neutral voltage (volt); $\Delta H_{Dissociation}$= Heat of dissociation reaction at operating temperature (J/mole).

Referring to Figure 6.4, the simulation of the SOEC starts with defining the steam conditions (i.e. steam flow, temperature, and pressure) and the SOEC current I_{Stack}. Steam utilization is then calculated using equation 6.8 for use in Aspen Plus^{TM} Rstoic model. Rstoic is a reactor model that carries out material and energy balances for a given feed (steam in this case), reaction (water dissociation in this case), and reaction fractional conversion (steam utilization in this case). The Rstoic product is then fed to the component splitter model Sep. Here, all of the generated oxygen, generated from water electrolysis, is separated; hence, acting as the SOEC cathode-electrolyte. Sweep air flow is calculated for air/oxygen mixing in the Mixer model to represents the anode side of the SOEC. Given the above information, the Gibbs free energy, ΔG, is calculated around the SOEC for actual electric power, W_{Actual}, and heat duty, Q_{Net}, calculations using equations 6.10 and 6.11, respectively. If Q_{Net} is greater than zero (heat is needed), then the I_{Stack} is increased and vice versa.

Figure 6.5 shows the well-known electrical power and net heat responses as function of steam utilization U_s derived from the above SOEC model [88, 90]. Alterna-

tively, the same curves could be plotted as function of the current by converting the U_s into current using 6.8. With increasing steam utilization, the SOEC heat input initially increases, reaches a maximum, and then starts to decrease to zero and below. When the heat requirement drops to zero, only external electric power is needed to drive the dissociation reaction and the stack voltage at this point is referred as the thermal-neutral voltage [88]. The thermal-neutral voltage can also be calculated using equation 6.12. Beyond the thermal-neutral voltage, excess heat is generated.

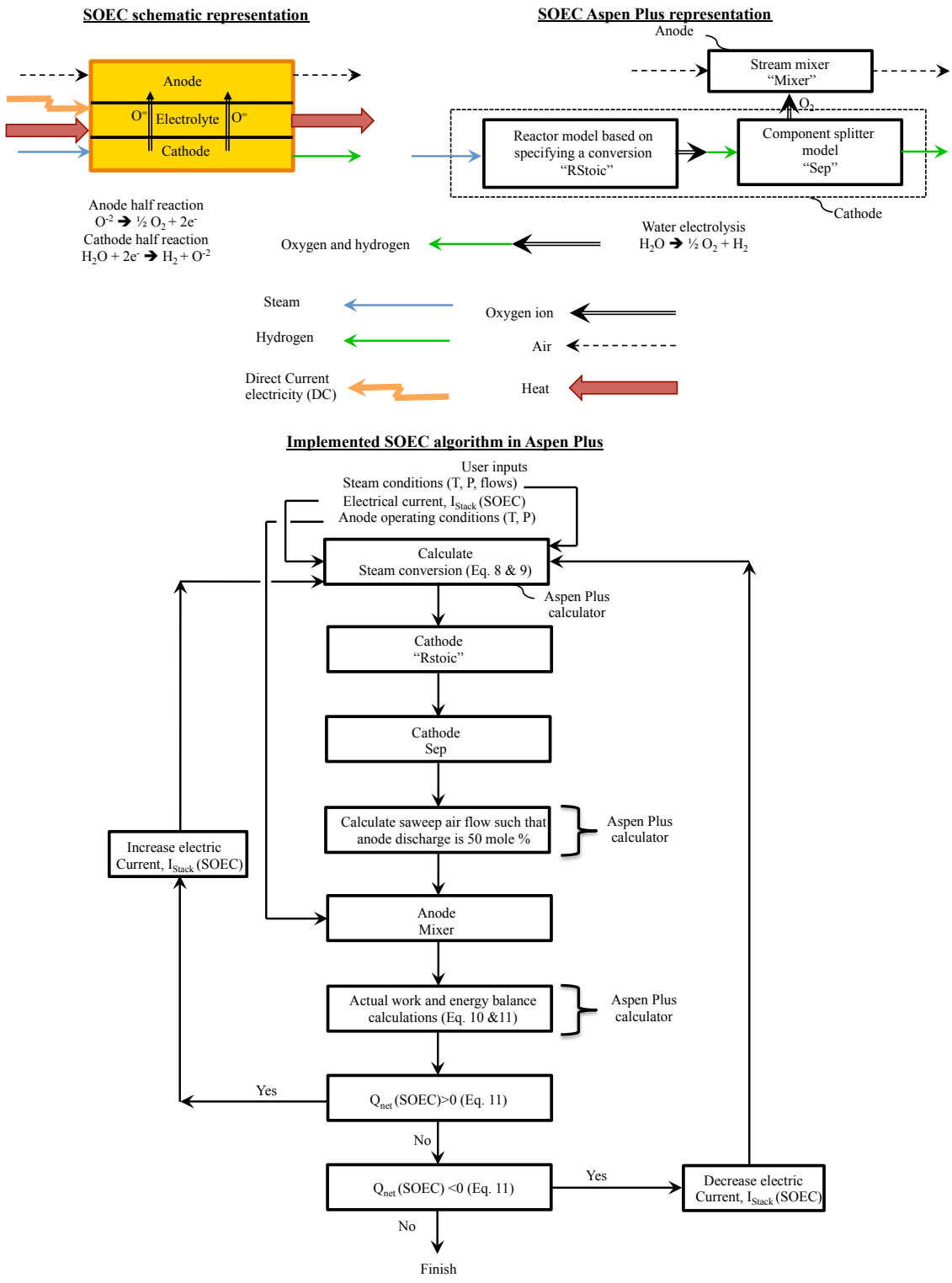

Figure 6.4. Modeling approach for SOEC. Details of RStoic, Sep, Mixer, and calculator models are available in [30].

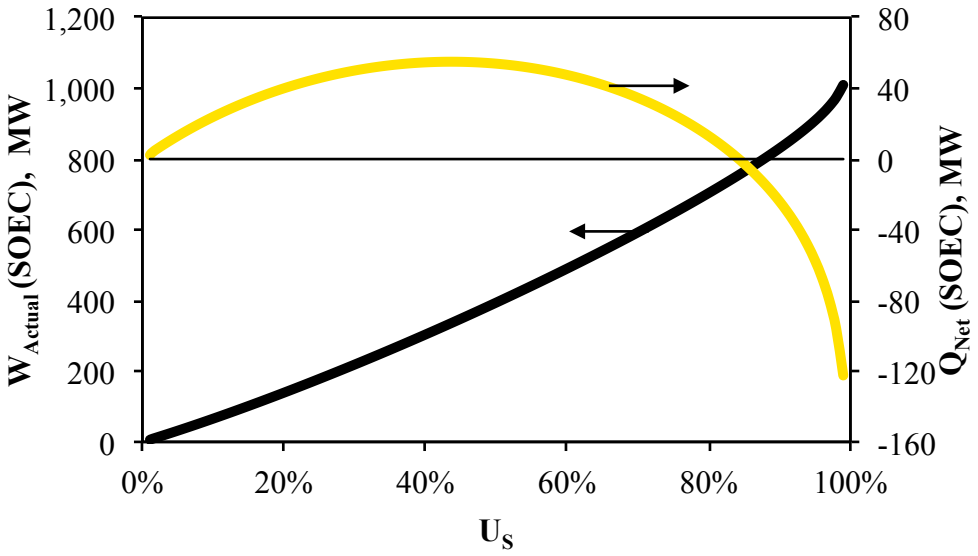

Figure 6.5. SOEC characteristics curves for steam flow, steam composition, operating temperature, operating pressure of 12,975 kmol/h, 90 mole% (the balance is hydrogen), 850^{o}C, and 10bar, respectively.

6.2.3 Adsorber model

The liquefaction of methane and carbon dioxide requires almost complete removal of water (dehydration) to avoid solid formation in the downstream liquefaction heat exchangers. This is best achieved using adsorption dehydration using molecular sieve [51]. In this work, the adsorption unit is modeled using two models: 1) Aspen Plus^{TM} component splitter Sep, for adsorption simulation and 2) Aspen Plus^{TM} Mixer and Heater models for regeneration (desorption) simulation [30]. The approach presented in [51] is adopted and implemented in Aspen Plus^{TM} according to the following equations and Figure 6.6.

For the regeneration calculations, the adsorber need to be sized to identify the adsorbent and vessel masses in which each contributes to near 50% of the needed regeneration heat [51]. During the adsorption step, see Figure 6.6, all of the water is removed in the component splitter Sep model. The gas superficial velocity (v_g), adsorber diameter (D), and molecular sieve bed height (h_B) are then calculated using equations 6.13, 6.14, and 6.15, respectively. After that the bed height to diameter ratio (h_B/D) is checked to ensure that the bed is not too short or high. This is an important test, as a too long bed can result in excessive pressure drop and a too short bed may result in reduced adsorbent capacity. Increasing the number of adsorbers and/or cycle (i.e. adsorption) time should overcome a low height to diameter ratio and vice versa. With the above information in hand, the adsorbent and vessel masses ($m_{Adsorbent}$ and m_{Vessel}, respectively) can be calculated using equations 6.16 and 6.17, respectively. The regeneration heat , $Q_{Adsorber}$, is then estimated by applying the energy balance relation given by equation 6.18. This relation adds up the total heat needed by the different components as follow: heat needed to heat up the vessel, adsorbent, and piping from the initial temperature to the regeneration temperature + sensible heat needed to heat the water to its saturation temperature (T_{Sat}) + water heat of desorption, $\Delta H_{Desorption}$, for the utilized adsorbent type + heat losses. The calculated regeneration heat is then used to estimate the regeneration gas flow, m_{RGas}, that will carry the regeneration heat into the adsorber using equation 6.19.

Finally, the pressure drop across the adsorber is calculated using Ergun relation given by equation 6.20).

$$v_g = \frac{67}{\sqrt{\rho_g}} \tag{6.13}$$

$$D = \sqrt{\frac{4q_g}{\pi v_g}} \tag{6.14}$$

$$h_B = \frac{400 m_{Water}}{\pi x \rho_B d^2} \tag{6.15}$$

$$m_{Adsorbent} = \frac{\pi \frac{D^2}{4} h_B}{\rho_B} \tag{6.16}$$

$$m_{Vessel} = 0.0347 hDt \tag{6.17}$$

$$\begin{aligned} Q_{Adsorber} = {} & m_{Vessel} C_p^{Vessel} (T_{Out} - T_{Initial}) \\ & + m_{Adsorbent} C_p^{Adsorbent} (T_{Out} - T_{Initial}) \\ & + m_{Water} C_p^{Water} (T_{Sat} - T_{Initial}) + m_{Water} \Delta H_{Desorption} \\ & + Losses + Piping \end{aligned} \tag{6.18}$$

$$m_{RGas} = \frac{Q_{Adsorber}}{t_R C_p^{RGas} (T_{Regeneration} - T_{Initial})} \tag{6.19}$$

$$\frac{\Delta P}{h} = 4.16 \mu v_g + 0.00135 \rho_g v_g^2 \tag{6.20}$$

where;

v_g=Superficial gas (i.e. gas to be dehydrated) velocity (m/min); ρ_g=Gas (i.e. gas to be dehydrated) density (kg/m^3); D=Vessel diameter (m); q_g=Actual gas (i.e. gas to be dehydrated) volumetric flow rate (m^3/min); h_B=Adsorbent bed height (m); m_{water}=Mass of adsorbed water (kg); x=Adsorbent capacity (Fraction);

ρ_B=Adsorbent bulk density (kg/m^3); $m_{Adsorbent}$=Adsorbent mass (kg); m_{Vessel}=Vessel mass (kg); h=Vessel height (m)=h_B + 1.5; t=Vessel thickness, see Figure 19.11 in [51](mm); $Q_{Adsorber}$=Regeneration heat (kj); C_p^{Vessel}=Vessel constant pressure heat capacity=0.5 kj/kg ^{o}C (for steel); C_p^{Water}=Water constant pressure heat capacity (kj/kg ^{o}C); T_{Out}=Temperature of the regeneration gas leaving the adsorber under regeneration (^{o}C); $T_{Initial}$=Initial temperature of the adsorber prior the regeneration; T_{Sat}=Water saturation temperature at the regeneration pressure (^{o}C); $\Delta H_{Desorption}$= Water heat of desorption (kj/kg); $Losses + Piping$=Heat losses plus heat needed to heat up the piping =25% of the $Q_{Adsorber} - losses - piping$; m_{RGas}=Mass flow of the regeneration gas (kg/min); t_R=Length of the regeneration cycle (min); C_p^{RGas}=Regeneration gas constant pressure heat capacity (kj/kg ^{o}C); ΔP= Pressure drop (kPa) across the adsorber; μ= gas (i.e. gas to be dehydrated) viscosity (cp).

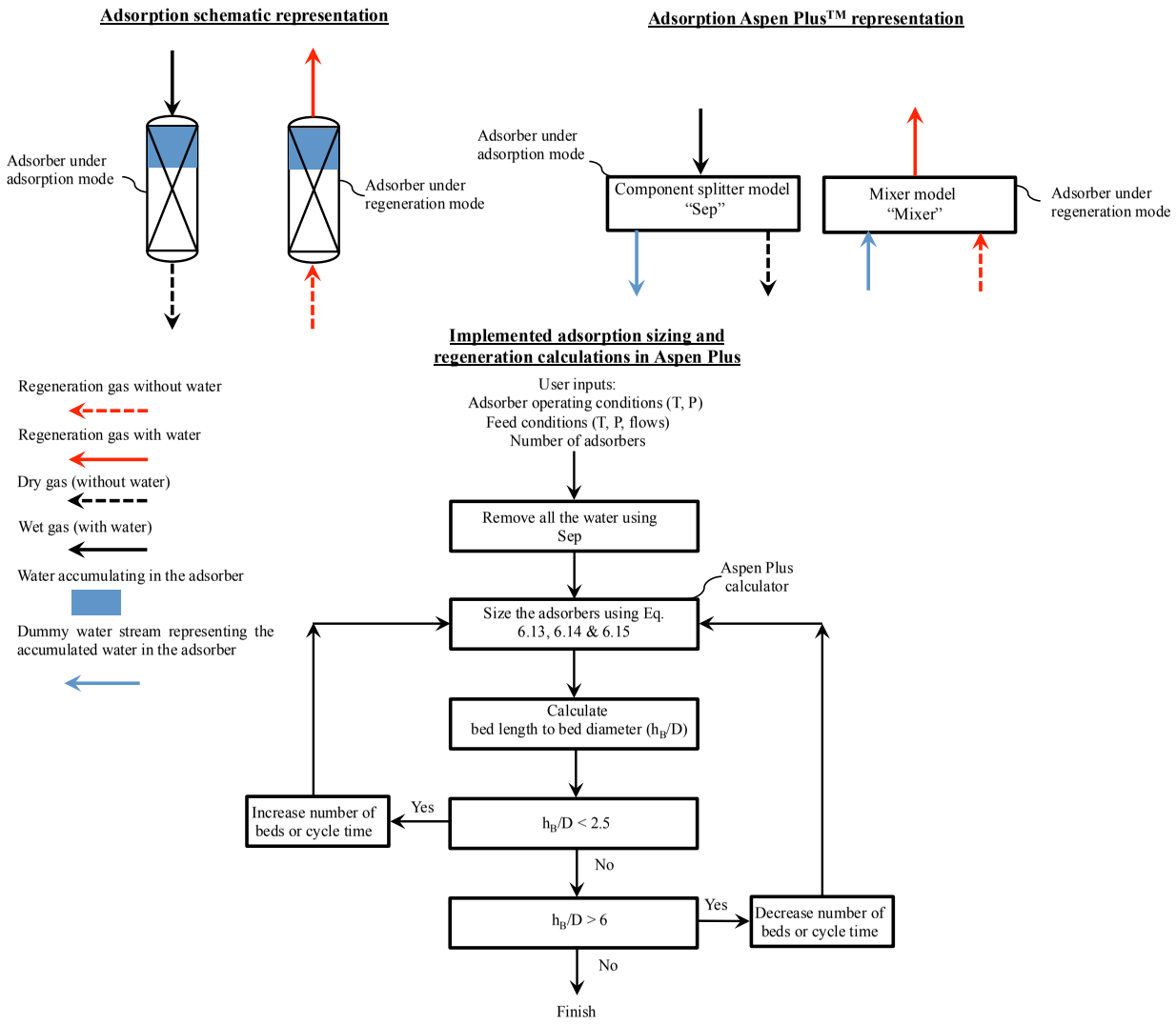

Figure 6.6. Modeling approach for Adsorbers. Details of Mixer, calculator, and Sep models are available in [30].

6.3 General model and simulation specification

Table 6.2 to 6.4 summarize all the specification and assumptions utilized in this work. Ambient conditions are assumed to be standard at sea level with 50% relative humidity. Cooling water is assumed to be coming from a cooling tower at a temperature of 32^{o}C [102]. Turbines with outlet streams discharged into the atmosphere are constrained to operate at no lower than 1.1bar to allow for some pressure drop before reaching the atmosphere (which is at 1.01bar). As demonstrated by Heatric, heat exchangers manufacturer, heat exchangers pressure and temperatures shall not exceed 100bar and 800^{o}C. For heating above 1000^{o}C, solar concentrators such as dish engine systems are assumed to be available [16]. Heat exchangers pressure drops are specified based on the phase of the fluid and whether phase change occurs or not [102]. For example, for heat exchangers involving boiling or condensation, a pressure drop of 0.1bar is used. On the other hand, heat exchangers involving gaseous stream are simulated with a pressure drop of 0.21bar. Minimum temperature difference in heat exchangers is chosen based on the temperature level encountered in the exchanger. For temperatures lower than the ambient, 1^{o}C is used to minimize compression power of the refrigeration system [40]. Higher temperature level uses higher temperature difference to avoid high heat transfer area made of expensive alloys. For example, for temperature levels higher than 148^{o}C, the near optimum minimum temperature difference is near 28^{o}C [102]. Heat leakage into all equipment is assumed to be negligible.

In addition to the discussed SOFC/SOEC assumptions and basis (see section 6.2.1 and 6.2.2), the SOFC minimum temperature approach is set to be 270^{o}C [48]. Higher temperature approach across the device increases the heat transfer driving force which ultimately reduces the amount of excess air fed to the cathode side for cooling. Although, reducing the air flow will reduce the compression power, high temperature approaches could severely damage the SOFC components because of the large temperature gradient [111]. The SOFC produces DC power; however, the electricity fed to the electric grid need to be AC type. This conversion step, which is

considered in all of the simulations, will typically reduce the electrical power by near 4% [109].

Depending on the pressure ratio (P_{out}/P_{in}), gas compression is carried out on multistage fashion with intercoolers between each stage. Such compression scheme reduces the compression power at the expense of additional capital cost (i.e. piping heat, exchangers, etc.). At high-pressure ratio; however, the additional capital cost could be justifiable. For example, it is proposed to use single compression stage for a pressure ratio less than four and three stages for a ratio falling between 16 to 64 [102]. For multistage schemes, optimization studies reveal that equal pressure ratio across each stage gives near optimum compression power [40, 112]. Thus, this (i.e. equal pressure ratio) is implemented in the simulation with each stage operating at an isentropic efficiency of 80% [51]. On the other hand, expanders are simulated with isentropic efficiency of 85% [113] without constraining the pressure ratio (i.e. without multistage) across the device.

To avoid the accumulation of inerts and unconverted marital in recycle streams, purge streams are deployed with a mole flow equivalent to 1% of the total recycle mole flow. For the adsorbers, molecular sieve 4A and 3A are used for the dehydration of methane and carbon dioxide, respectively, [51] with an adsorber maximum pressure of 120bar [114]. Last but not least, HRSG is used to generate three pressure superheated steam with single reheat at a maximum temperature of 518^o [36]. For the steam turbines, used to generate electric power from the HRSG steam, maximum turbine inlet pressure and minimum turbine outlet pressure of 128 and 0.07 bar are utilized, respectively, in the simulation [36, 115]. Maximum moisture content of turbines discharge is assumed to be 15% [94]. Also in the simulation, pure water is assumed for the steam system.

Table 6.2
Assumptions and basis of model and simulation

Description		Value/description
Ambient conditions		1.013 bar (1 atm) 25°C 50% relative humidity
Cooling water supply temperature		32°C
Expansion minimum pressure	Assumption	1.1 bar
Heat exchangers maximum pressure		100 bar
Heat exchangers maximum temperature		800°C
Heating above maximum heat exchanger temperature is carried out using solar concentrators with maximum temperature		1000°C
Pressure drops in heat exchangers		
For boiling/condensation		0.10 bar
For gases		0.21 bar
For low viscosity liquid		0.34 bar
Heat exchangers minimum temperature approach		
T < 25°C		1°C
T = 32 to 148°C		11.1°C
T > 148°C		27.8°C
Heat exchangers heat leakage	Assumption	0
Storage tanks heat leakage	Assumption	0
SOFC/SOEC[(1)]		
Modeling and simulation approach		
Maximum temperature approach		270 °C
Maximum temperature		1000°C
DC to AC efficiency		96%
Maximum pressure		10bar
Electrical current-SOFC		Sufficient to provide heat for the steam reformer
Electrical current-SOEC		At thermal neutral voltage
Fuel reforming		Steam reforming integrated inside the fuel cell

Table 6.3
Assumptions and basis of model and simulation (continue)

Description		Value/description
Oxygen concentration at SOEC anode discharge		50 % mole
Hydrogen concentration at SOEC cathode inlet		10 % mole
Phase separators pressure drop	Assumption	0.21 bar
Number of compression stages		
Pout/ Pin		Stages
< 4		1
4 to 16		2
16 to 64		3
Compressor discharge maximum temperature	Assumption	200°C
Gas turbines maximum inlet temperature		1300°C
Compressor isentropic efficiency		80 %
Expanders isentropic efficiency		85 %
Expander motor efficiency	Assumption	97 %
Adsorber maximum pressure		120 bar
Methane dehydration molecular sieve		4A
Carbon dioxide dehydration molecular sieve		3A
Sabatier reaction modeling approach		Equilibrium
Methanol reaction modeling approach		Equilibrium
Cryogenic refrigeration for LM-C storage mode		Mixed Refrigerant (MR)
Cryogenic refrigeration for Mo-C and MoW-C delivery mode		Mixed Refrigerant (MR)
Storage mode sun availability	Assumption	4.8 h
Purge percentage	Assumption	
Storage mode		1%
Delivery mode		1%

Table 6.4
Assumptions and basis of model and simulation (continue)

Description		Value/description
Heat Recovery Steam Generator (HRSG)		
Water contamination	Assumption	Pure water
Maximum steam pressure		128 bar
Maximum steam turbine temperature		518°C
Minimum steam turbine outlet pressure		0.07 bar
Minimum steam turbine inlet pressure		5 bar
Steam turbine discharge moisture content		10 to 15 %
Number of steam pressure stages	Assumption	3
Number of reheats	Assumption	1
Minimum temperature for carbon dioxide-rich streams	Avoiding freezing	-55°C
Minimum pressure for carbon dioxide-rich streams	Avoiding freezing	9 bar
Carbon dioxide liquid purity	Basis	>99 mole%

6.4 Aspen Plus^{TM} models

6.4.1 Columns simulation

In the designed flowsheets, three types of columns were encountered; these are distillation, stripper (or reboiled column), and rectifying (or column with reflux liquid) columns. Although, this work uses Aspen Plus^{TM} RadFrac model for column simulations, near optimum model inputs and simulation convergence are still not a trivial task. Therefore, this section of the dissertation is dedicated for discussing the effective simulation approach adopted in this work.

6.4.1.1 Methanol water distillation

Figure 6.7 shows the approach adopted to conduct the methanol/water distillation simulation in Aspen Plus^{TM}. The simulation is started with a short-cut model available in Aspen Plus^{TM} known as DSTWU [30]. This model uses the Winn-Underwood-Gilliland method to identify the minimum reflux ratio, material/energy balance, minimum number of stages, optimum feed stage, and actual number of stages for 1) a given feed stream, 2) condenser type, 3) column pressure, 4) and a multiplication factor of the minimum reflux ratio. Here, the DSTWU is run with a reflux ratio of 1.5 times the minimum reflux. This reflux is used as a starting point for the more rigorous RadFrac model. The calculated distillate rate, feed stage, and actual number of stages (at the 1.5 times the minimum reflux) were inserted in the rigorous model. In case the required purities are not met, the reflux is increased until such specifications are met. The choice of column pressure was based on the minimum temperature heat sink available in the process. Although, lowering the pressure usually makes the separation easier (because it usually increase the relative volatility between the components), too low pressure may necessitate the need for expensive refrigeration energy and/or vacuum operation. Since, both methanol and water condenses at ambient temperature, atmospheric pressure is a feasible option. In this work, a

pressure of 1.6bar (at the last bottom stage) is used with the pressure drop being calculated using the built in tray sizing/tray rating tool [30]. For the condenser type, a total condenser is chosen because methanol (which leaves at the top of the column) is finally stored in a liquid state. No tray efficiency has been used in the simulation; thus, it is expected that the actual column will be longer than the one reported in this dissertation. It also worth mentioning that the trade off between reflux ratio and number of stages (the higher the reflux is, the more energy consumption is, and the lower the number of stages is which means less capital cost, and vice versa [115]) is not considered in this work because the focus here is on energy consumption minimization. Thus, a rationally sound number of stages (in this case number of stages equivalent to 1.5 times minimum reflux) is used.

6.4.1.2 Water purification column

The water purification column, encountered, in almost all of the developed flowsheet uses a reboiled column (or stripper) to remove any dissolved gases from the generated water streams. In principle, this is similar to deaerator units found in most steam plants [94]. RadFrac model with a reboiler only is used for the simulation in which the reboiler duty is varied (using RadFrac Design Specs tool) to provide water (which leaves the bottom of the column) mole fraction of near 100 mole%.

6.4.1.3 Cryogenic Air Separation Unit (ASU)

While different schemes exist for oxygen production using cryogenic ASU (each with different capital cost, energy efficiency, and operational characteristics) [116,117], this work uses the basic configuration shown in Figure 6.8. Here, gaseous oxygen is produced from the low pressure column C-5 which utilizes a single reboiler to provide the column boilup. Increasing the number of reboilers should reduce the energy consumption in the air compressor K-1 [117, 118] but perhaps at the expense of the capital cost of the process. Also, instead of gaseous oxygen, liquid oxygen may be

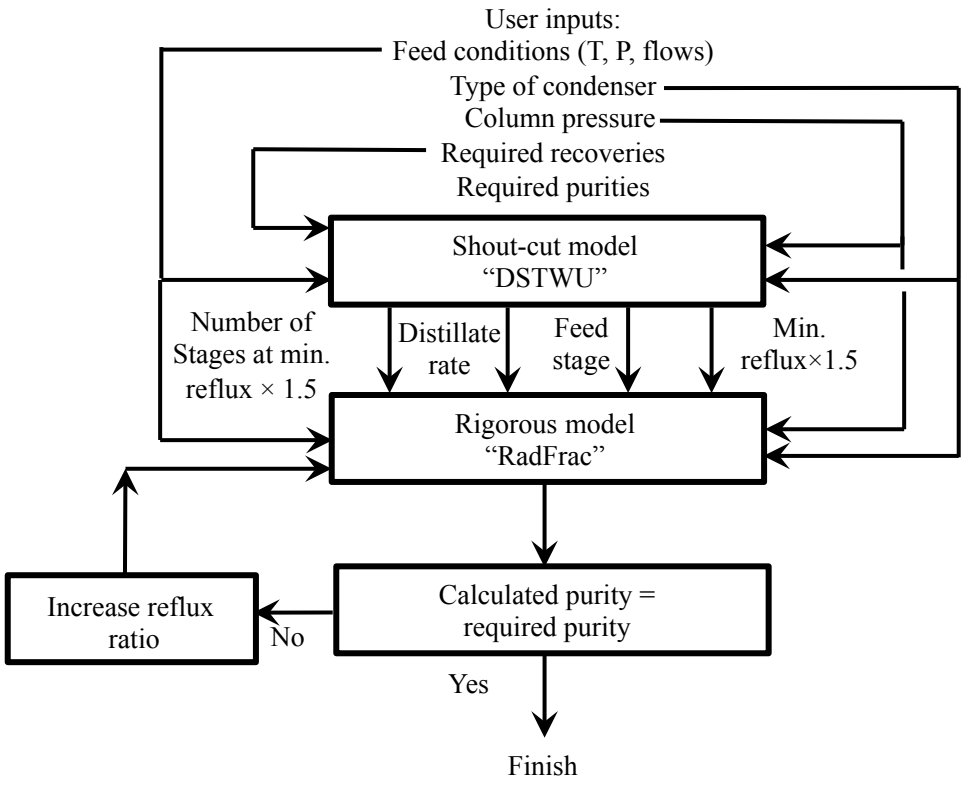

Figure 6.7. Simulation approach for a distillation column.

generated from column C-5; thus, enabling oxygen pumping (prior to the heating in the main heat exchanger E-13) instead of compression (as in the case of Figure 6.8). However, it should be noted that in the basic configuration of Figure 6.8, liquid oxygen boils in the bottom of column C-5 to provide the refrigeration need for producing column C-4 reflux (see section 2.8 for details). Hence, pulling liquid oxygen from the column bottom will reduce the refrigeration available for providing column C-4 reflux. To overcome the lack of refrigeration, a booster air compressor at the air side is used to enable the generation of more refrigeration in the low pressure column, see [116] for details. The efficiency difference between the two processes (i.e. gaseous oxygen vs. liquid oxygen) depends on the final oxygen pressure requirements and the power consumption of the oxygen compressor vs. oxygen pump.

For the simulation, Aspen Plus^{TM} RadFrac, MHeatX, and MCompr library models are utilized to simulate columns C-5 and C-4, heat exchangers E-13 and E-14, and multistage intercooled air compressor K-1, respectively. Two RadFrac models are used, one with a reboiler only (i.e. stripper) to represent the low pressure column C-5 and the other with a condenser (i.e. rectifying) only for the representation of the high pressure column C-4. Twenty one and eleven equilibrium stages (including the condenser and reboiler) were defined for C-5 and C-4, respectively. Streams 64 and 56 are fed to stage 12 of column C-5. The bottom rate of column C-5 (i.e. stream 65 containing separated oxygen) is varied using RadFrac Design Specs tool [30] to provide the required gaseous oxygen recovery of 98 mole%. On the other hand, the reflux ratio of column C-4 is varied using Aspen Plus^{TM} flowsheet level Design Spec to achieve the target oxygen purity of 95 mole% in stream 65. For columns pressure, column C-5 and C-4 were varied using the flowsheet level Design Spec to obtain the needed temperature difference (which is 1^{o}C) in the reboiler/condenser (i.e. stream 60 temperature minus stream 65 temperature). This also fixes stream 62 and 56 pressures. The discharge pressure of compressor K-1, on the other hand, is set to ensure a minimum temperature difference of 1^{o}C is achieved in heat exchanger E-13, again using the flowsheet level Design Spec. Cold streams 58 and 65 are warmed in heat exchangers E-13 all the way to close to the ambient temperature by not defining any temperature for these streams in the MHeatX model. The only specification defined for heat exchanger E-13 (MHeatX model) is stream 54 and 63 temperatures. For stream 54, the temperature is varied accordingly (using the flowsheet level Design Spec) such that C-5 reboiler duty matches C-4 condenser duty, which together simulates the thermally linked reboiler/condenser heat exchanger placed at the bottom of column C-5. Stream 63 is fixed at -150^{o}C with minimum flow. The flow and temperature of stream 63 (which is used, after its expansion in T-9, to provide refrigeration for column C-5) is usually determined based on how much heat leak takes place in the process (the higher the leak is, the more the flow is needed) [116]. Last but not least, heat exchanger E-14 (which is used to minimize the flash gas generation as

stream 61 is reduced in pressure) is simulated by defining a temperature change of stream 60 such that a minimum temperature difference of 1^{o}C is not violated (using the flowsheet level Design Spec).

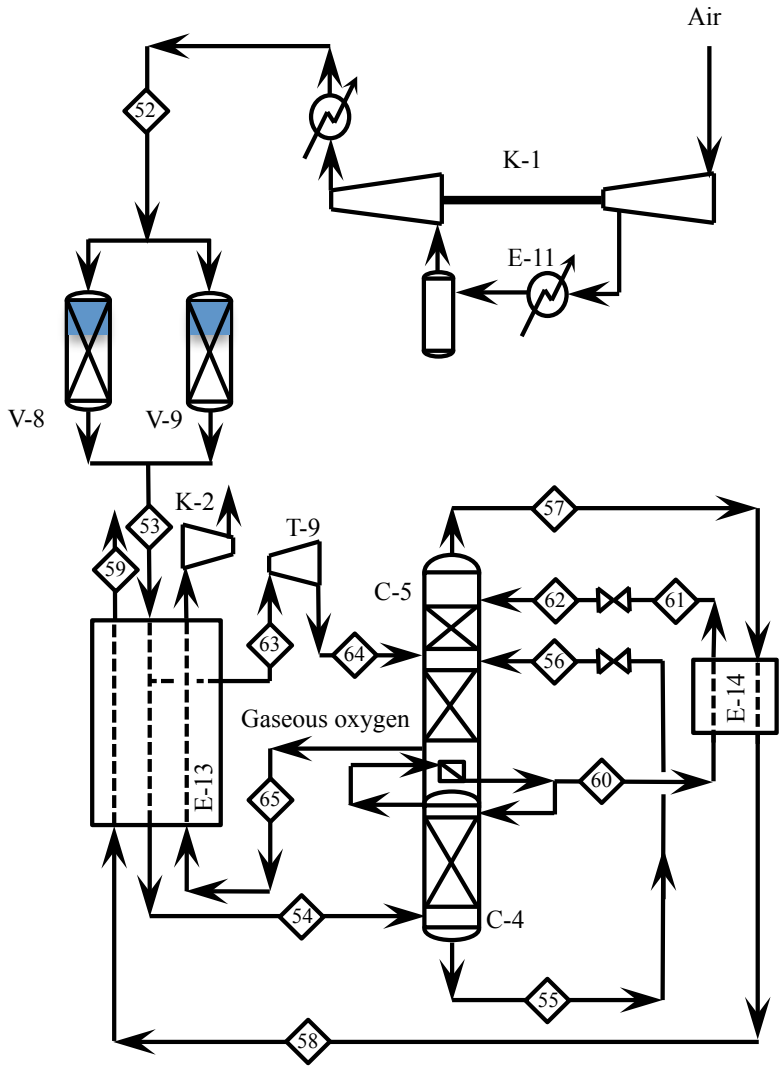

Figure 6.8. Double column single reboiler gaseous oxygen cryogenic ASU.

6.4.2 Refrigeration cycles simulation

A basic refrigeration cycle consist of four fundamental components, 1) compressor(s), 2) condenser, 3) throttling valve, 4) and evaporator (see Figure 6.9). Referring to Figure 6.9, compressors B3 and B1 compresses the refrigerant such that it can be condensed, in the condenser (i.e. in B2), using ambient heat. The high-pressure refrigerant is then reduced in pressure using B5 throttling valve; hence, generating low-pressure refrigerated liquid. This cold refrigerant is then evaporated in the evaporator (the kettle type heat exchanger) to provide the refrigeration needed by the process stream HOTIN. For the simulation of the process, giving the type of refrigerant, one needs to specify 1) compressor outlet pressure, 2) throttling valve outlet pressure, 3) and refrigerant flow. For the compressor, a pressure that results in above ambient condensation temperature (boiling temperature if the refrigerant is pure components) need to be chosen for ambient heat condensation in the condenser. While different pressures can achieve this objective, lowering the pressure is desirable for compression power savings. Such pressure can either be identified by flash calculations or consulting published thermodynamic (for a given refrigerant) charts such as pressure enthalpy diagrams. The throttling valve outlet pressure; on the other hand, is specified such that it results in a discharge temperature (i.e. COLDIN temperature) that is lower than the HOTOUT stream temperature. How low this temperature should be depends on the desired minimum temperature approach. The throttling valve outlet pressure can also be estimated with flash calculations or pressure enthalpy diagrams. Increasing the pressure is desirable (which mean smaller minimum temperature difference) to minimize the pressure ratio across the compressor (compressor outlet pressure/compressor inlet pressure); hence, reducing the compression power. For the refrigerant flow, a value that results in the complete evaporation of the refrigerant without violating the minimum temperature approach must be chosen. Usually, some refrigerant superheating (i.e. COLDOUT is at superheated temperature) is desirable to ensure zero liquid content at the compressor inlet. This is essential to avoid damaging the machine [51]. Superheating also means reduced refrigerant circulation

rate that should give reduced compression power. To estimate the flow of the refrigerant, one may divide the evaporator heat duty (or how much refrigeration is required by the process stream) by the sum of the latent heat of vaporization (at the valve discharge pressure) and the amount of required superheating (i.e. sensible heat).

For cryogenic temperature cooling (temperature below -150^{o}C), more sophisticated configurations are used. Consider for example the MR cycle shown in Figure 6.10 for NG liquefaction. Since a very cold temperature is required at the discharge of the valve (-163^{o}C), a refrigerant that exists as liquid at such temperatures is needed (MR will be feasible). This also means excessive cooling of the high-pressure refrigerant (leaving the compressor) to the above stated subambiant temperature for condensation. For this reason, as shown in Figure 6.10, the refrigerant condensation and process stream cooling (in this case NG) are carried out by evaporating the LP liquid refrigerant (unlike the case of Figure 6.9, where the ambient is used for condensing the refrigerant). For such low temperature refrigeration it is essential to minimize the compression power not only for energy savings but also for capital cost reasons. Consider for example a process that require in excess of 200 MW of compression energy. If one will chose to use General Electric Frame 9 gas turbine (with a maximum ISO power rating of near 128MW) machine to drive the compressors, then the process will need two of this gas turbine systems. This means extra piping, control, instrumentation, infrastructure, and etc. Now choosing the most optimum values for the process variables, such that compression power is minimized, is not a trivial task because of the large number of variables (i.e. steady state degree of freedom) which are as follow. 1) Refrigerant composition (usually contains nitrogen, methane, ethane and propane), 2) compressor pressure, 3) throttling valve outlet pressure, 4) refrigerant flow, and 5) high pressure refrigerant temperature. Ultimately, one need to chose values that minimize the temperature difference across the length of the heat exchanger. This means that the temperature profiles of the streams need to be cooled (stream NG and HP Refrigerant in Figure 6.10) and the low pressure refrigerant (LP liquid Refrigerant in Figure 6.10) are closely matched with each other. These pro-

files, example is given in Figure 6.11, are often referred as the cooling curves (or heat exchanger composite hot and cold curves) and provide a useful tool to evaluate how good the chosen operating variables are. The gab between the hot and cold composite curves (which is indication of the temperature difference between the two curves across the length of the heat exchanger) gives indication of exergy losses in the heat exchanger. The bigger the gab is, the more the exergy losses are. High exergy losses eventually translate into higher compression power [40]. Now minimizing this gab requires certain curvature for the condensing and evaporating refrigerant. In other words, the temperature variation of the low- and high-pressure refrigerants across the heat exchanger need to follow a certain trend (or functionality) that is determined by 1) the composition of the refrigerant, 2) the temperature upstream the valve, and 3) the compressor pressure ratio (i.e. valve and compressor pressures). Until today, there is no established procedure that can assist on choosing the optimum conditions of these variables, instead, mathematical optimization tools are utilized.

All of the refrigeration cycles presented in this work were simulated using MHeatX, MCompr, and Valve library models. A minimum temperature approach design methodology is adopted to estimate the operating conditions of each cycle. For cryogenic systems, a temperature approach is specified to be a design basis with compression power, refrigerant flow, refrigerant composition, and throttling pressure (i.e. valve outlet pressure) being estimated using SQP optimization approach. The optimization problem is formulated to minimize compression power subject to a minimum temperature difference (i.e. 1^oC in this work) and other relevant constraints (depending on the objective of the process). It worth mentioning that a major problem with such numerical based optimization is its local solution characteristics [40, 112]. In an attempt to overcome this, multiple initial points are used to assess the solution obtained by the optimizer. At each time the simulation converges, the heat exchanger cooling curves (or heat exchanger composite hot and cold curves) are examined against others to get a feel of how good the optimization results are.

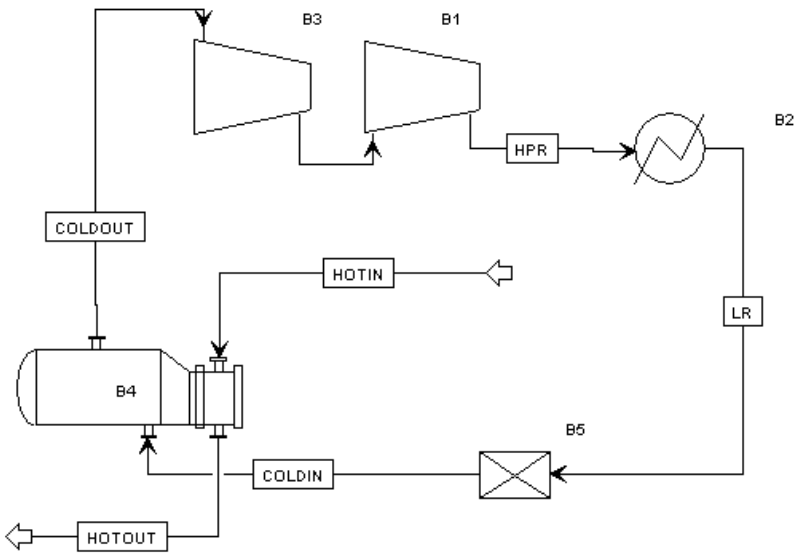

Figure 6.9. Basic vapor compression refrigeration cycle.

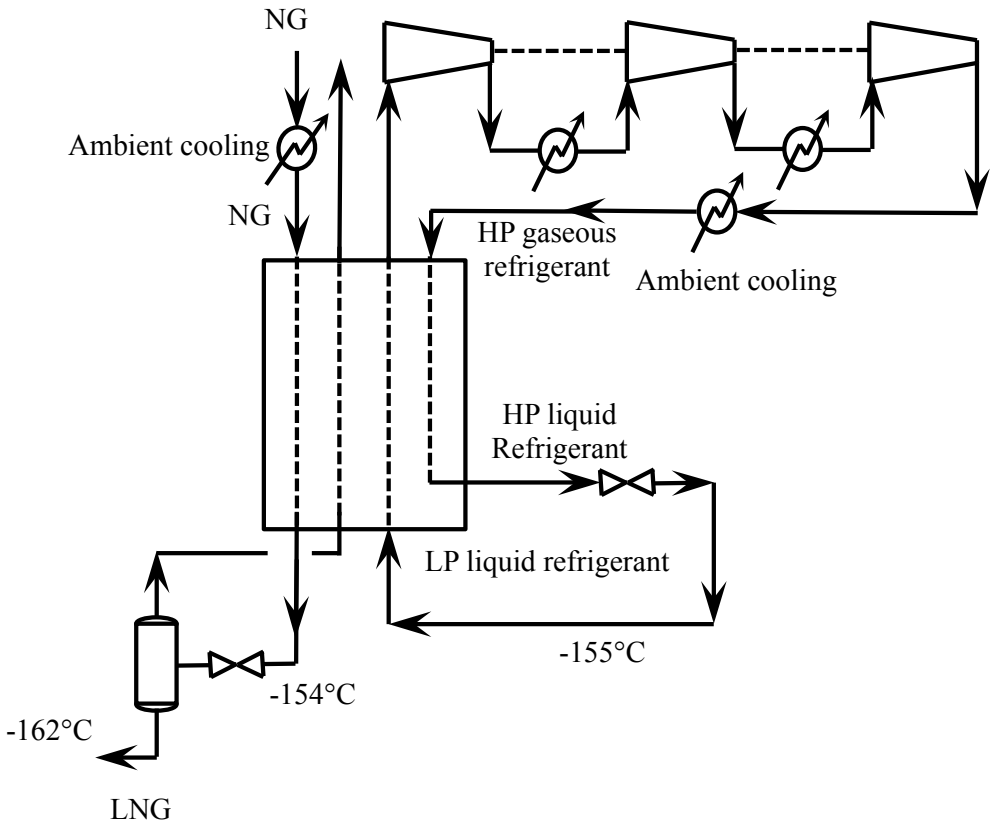

Figure 6.10. Cryogenic refrigeration cycle for NG liquefaction.

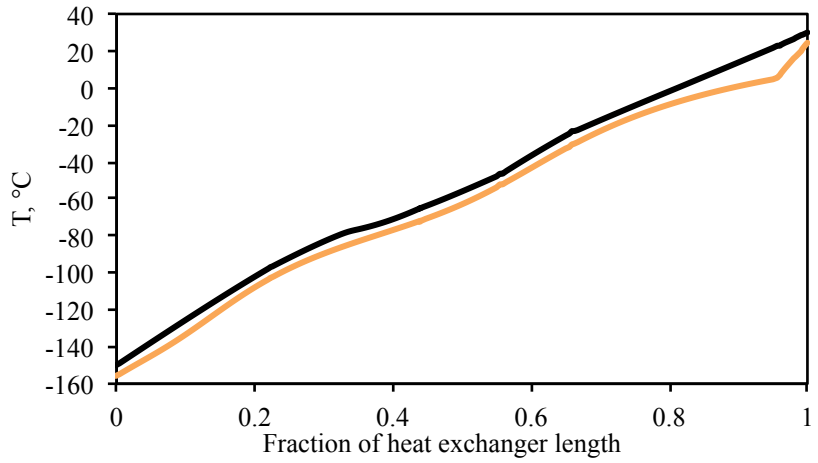

Figure 6.11. Cooling curve for the multi stream heat exchanger shown in Figure 6.10.

6.4.3 Pinch analysis

Pinch analysis is a technique that can be used to identify the minimum heating and cooling requirements for a given flowsheet [119]. Thus making it a valuable tool for assessing the quality of the implanted heat integration scheme. The composite curve plot (see Figure 4.6 for example) is a visualization mean of representing pinch analysis results. In Aspen Plus^{TM} the MHeatX model and transfer tool are used to draw the composite curves [30]. Here, each stream going through cooling or heating is identified to export its conditions (i.e. temperature, pressure, flow, and composition) and target temperature to a corresponding stream connected to the MHeatX model using the transfer tool [30]. MHeatX is a rigorous model that not only can be used to carry on heat exchange between multiple streams; but, it can also estimate the temperature profiles in a composite manner similar to pinch analysis composite curves. Also to be noted that using such model (i.e. MHeatX) means that the user can access the rigorous Aspen Plus^{TM} thermodynamic models (in this case PSRK); hence, calculating the essential physical properties (i.e. constant pressure heat capacity, latent heat of vaporization, etc.) for the composite curve plot while taking into consideration their temperature, pressure, and composition dependency.

Since heat exchangers that use external heating (e.g. heat exchanger E-17 in Figure 4.4) and cooling (such as heat exchanger E-5 in Figure 4.4) are simulated using Heater model, no heat source or sink stream need to be defined. Instead, the target temperature (or heat duty or vapor fraction) of the process stream (e.g. outlet temperature of heat exchanger E-17 in Figure 4.4) is specified for the Heater model relevant calculations. Now the way these heats are accounted in the composite curves plot is to define a stream, connected to the MHeatX, with characteristics that represent the heat transfer in the heater model. For example, heat exchanger E-17 in Figure 4.4 assumes to use solar heat supplied at a constant temperature of 978^{o}C. In a stand-alone mode, the temperature profile of the heat source, in which temperature in the y-axis and heat duty on the x-axis, is a horizontal line with a length equivalent to the heat duty of exchanger E-17. The y-axis intersection point of the profile; on

the other hand, will be 978^{o}C. To represent this heat transfer, one can assume the use of a pure component with boiling point of 978^{o}C defined to a corresponding stream connected to the MHeatX. Vapor fraction of 1 and 0 are defined to the stream and its corresponding outlet condition (outlet condition is defined in the MHeatX model), respectively. The flow rate of the stream can be estimated by dividing the heat duty of heat exchanger E-7 by the component latent heat of evaporation. Now in the MHeatX model, this component will go through condensation from a vapor fraction of 1 to 0; thus, giving up its heat to heat the process stream in a horizontal profile behavior .

6.4.4 HRSG simulation

The HRSG is simulated in Aspen Plus^{TM} using Pump, Comp, and MHeatX models for water pumping, steam turbines, and furnace simulations, respectively. Since three steam pressure levels are utilized and optimality dedicates that each steam must starts it evaporation at a point where the minimum temperature approach is met (i.e. pinch point) [120] , three MHeatX models are used (see Figure 6.12 for Aspen Plus^{TM} representation) in which each model is utilize to vaporize a single water pressure level. While a single MHeatX may be utilized, the use of multiple MHeatX models was found to be more robust because it ensures accessing the three pinch points. The author is not aware of a straightforward approach of doing this (i.e. accessing multiple pinch points) in a single MHeatX model.

Referring to Figure 6.12, the LP water is pumped to the desired pressure for evaporation then superheating in heat exchanger E3. The superheating temperature (stream LPOUT temperature) is set to be equal to stream HOTOUT2 temperature minus the utilized minimum temperature difference plus 1^{o}C (i.e. near 29^{o}C), using Aspen Plus^{TM} calculator tool. The one degree centigrade is added for the simulation robustness reason mentioned below. The superheated steam (i.e. LPOUT) is then expanded in T4 to the desired vacuum pressure. For the IP1 water, the stream

is heated in heat exchanger E3 (leaves the exchanger as stream IPOUT1) to its saturation temperature minus 5^oC, utilizing the calculator tool, which represent what is often called temperature approach of the HRSG [120]. In heat exchanger E3, HP1 water is also heated to the temperature target of the IP1 water (i.e, stream IPOUT1 temperature). Leaving heat exchanger E3, the IPOUT1 is evaporated and superheated in heat exchanger E-2 with superheating temperature equals to stream HOTOUT1 minus 29^oC (minimum temperature approach + 1^oC), also using the calculator tool. Also in heat exchanger E2, HPOUT1, sourced from heating the HP1 in E3, is heated to its saturation temperature minus 5^oC (temperature approach of the HRSG). The evaporation and superheating of HPOUT2 (sourced from heating HPOUT1 in E3) takes place in E1 where the superheating temperature is fixed, using a calculator block, to stream HOTIN temperature minus the 29^oC. Also heated to this temperature using the calculator tool is the reheat stream leaving turbine T1.

To ensure that none of the HPOUT1, IPOUT1, and HPOUT2 are heated to temperatures higher than the heat source temperatures (i.e. stream HOTOUT1 and HOTOUT2), If conditions are utilized in the calculator blocks. For example, in heat exchanger E2, although the HPOUT1 is heated to its saturation temperature minus 5^oC, a target temperature equals to HOTOUT1 minus 10^oC is set in case the saturation temperature minus 5^oC is greater than HOTOUT1. For the steam turbines, the discharge pressure of turbine T2 and T3 are fixed to be the pressure of stream IPOUT and LPOUT, respectively, using Aspen Plus^{TM} transfer tool. Here, the pressures of the streams are automatically transferred to the turbines to avoid mixing streams with different pressures. To ensure that the evaporation steps in E1, E2, and E3 take place at the pinch point (a minimum temperature approach of 28^o), the flow of each water stream (i.e. LP, IP, and HP) are varied using Aspen Plus^{TM} Design Spec tool. For the Design Spec not to confuse between the pinch point within the heat exchanger (or at the point where water evaporates) and the pinch point at the hot side of the heat exchanger, all superheating are carried out such that a hot end temperature approach of 29^o are achieved. This explains why the 1^oC is added to

the minimum temperature approach during setting up the superheating temperature of LP1, IPOUT1 and HPOUT2 streams.

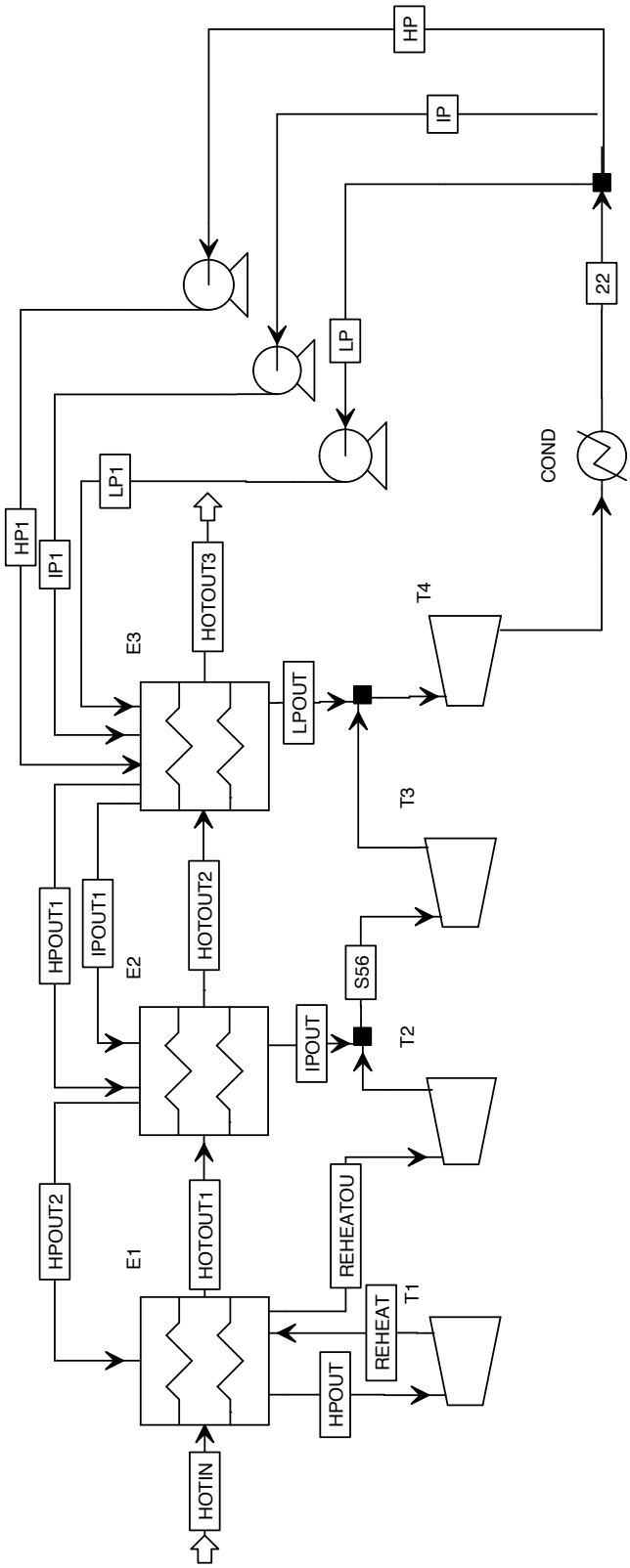

Figure 6.12. Aspen Plus^{TM} representation of the simulated HRSG

6.4.5 Chemical reactors simulation

Except for the water dissociation reaction, taking place in the SOEC, all of the chemical reactors encountered in this work are simulated using equilibrium approach with Aspen Plus^{TM} RGibbs or REquil models. In RGibbs, Gibbs free energy minimization along with vapor liquid equilibrium calculations (at the given temperature and pressure) are carried out to estimate the extent of chemical reactions. The model also does not require defining chemical reactions, instead components exiting the reactor need to be specified [30, 121]. REquil; on the other hand, calculate chemical equilibrium constant for the set of reactions defined to the model [30, 121].

For the irreversible fuel oxidation in the SOFC anode, equilibrium simulation predicts complete conversion of oxygen, which is the case for actual SOFC operation [48]. On the other hand, for endothermic and exothermic reactions, equilibrium conversion increases and decreases, respectively; with increasing temperature with actual conversion approaches equilibriums at high temperatures. Therefore, temperatures at which actual conversion is observed to approach equilibriums are used in the simulation for the different reactions as follow. 1) Temperature greater than 300^{o}C for the Sabatier reaction [87], 2) temperature greater than 250^{o}C for methanol generation [86], and 3) temperature greater than 900^{o}C for the methane and methanol steam reforming reactions [24].

Few tests were carried out to compare kinetic based simulation with equilibriums to further verify the literature claims. For example, Figure 6.13 shows the conversion of carbon dioxide in the Sabatier reaction for the two approaches (i.e. equilibrium and kinetic). Here, both approaches start to give the same carbon dioxide conversion at temperature slightly greater than 200^{o}C for both pressures (i.e. 10 and 20bar). With regards to the heat management, exothermic reactions are cooled by recovering the heat to heat up process streams. In the simulation, this is carried out using heat stream to connect the RGibbs (or REquil) reactor to a Heater model, see Figure 6.14 for Aspen Plus^{TM} representation. Doing so will remove the generated heat of reaction from the reactor to be transferred into the process stream. Caution needs to be taken

here with regards to the feasibility of the heat transfer as sometimes the heat stream might heat the process stream beyond the temperature of the heat (i.e. the reactor temperature).

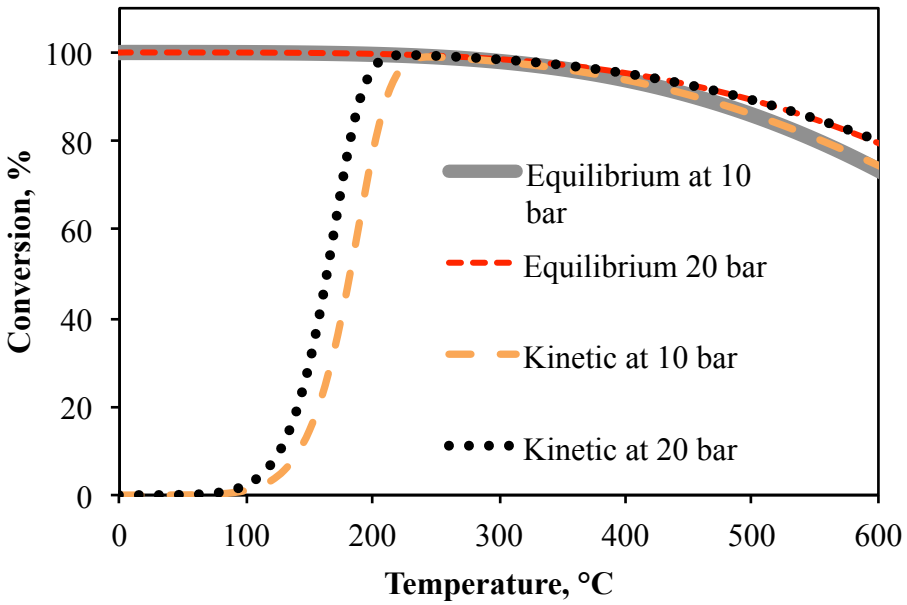

Figure 6.13. Equilibrium and kinetic conversion of carbon dioxide going through Sabatier reaction as function of temperature and pressure. Feeds are at stoichiometric conditions of 4 to 1 carbon dioxide to hydrogen ratio. For the kinetic conversion, a tubular reactor consisting of 1000 tube each with a length and diameter of 1 and 0.02m, respectively. Kinetic data are obtained from [93].

6.5 Recovering refrigeration for cooling vs. recovering refrigeration for power generation

In the developed LM-C (in section 4.2), the refrigeration in the stored liquid methane and liquid carbon dioxide are utilized to provide cooling for each other during their purification and liquefaction steps. On the other hand, for the ERPP and oxy-fuel NGCC (see section 2.2 and 2.8, respectively), vaporizing LNG provides por-

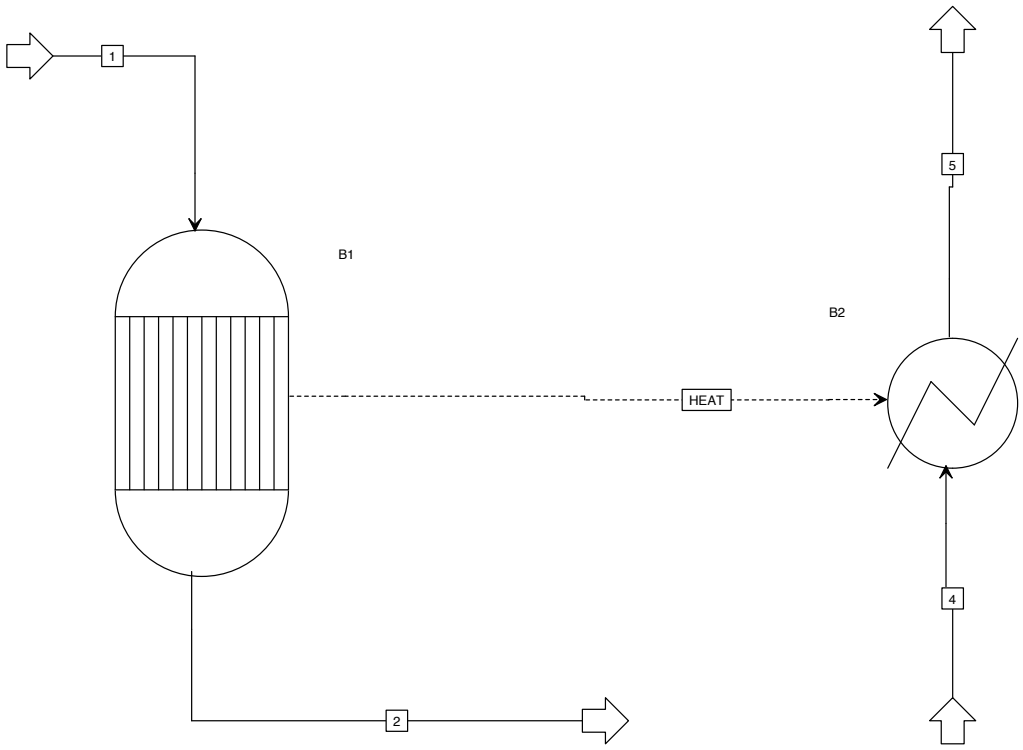

Figure 6.14. Aspen Plus^{TM} representation of how exothermic heat of reaction is utilized to heat process streams.

tion of the cooling needed for carbon dioxide capture and liquefaction. An alternative approach to this cold-to-cold recovery is to utilize such cold refrigeration to generate electrical power using heat engines [44,122–124]. Here, the ambient is the heat source, available at T_o, that provides heat input to the heat engines. The heat engines generate electrical power by dumping portion of the input heat into the refrigerated liquid (i.e. liquid methane or carbon dioxide) . Thus, the refrigerated liquids act as heat sinks with varying temperature. At reversible conditions, see Figure 6.15, multiple number of heat engines are needed to obtain maximum efficiency, given by equation 6.21. The efficiency here is for a single engine and constrained by the temperature difference between the heat source and sink. Highest efficiency is obtained at the coldest temperature where the temperature difference between the heat source and

sink is at maximum. For example, if the heat sink is LNG with coldest temperature of -160^{o}C, a maximum efficiency of 62% is achievable. Meaning that near 38% of the cold energy is wasted. With an actual cycle, this loss will be even higher due to the parasitic losses involved in the actual equipment making up the heat engine. On the other hand, in the ERPP and LM-C, the cold energy (i.e. refrigeration) is 100% recovered as cold energy. The draw back here is the quality of the recovered cold as it will be available at higher temperatures, due to the need of temperature differences for the cold (or heat) transfer to take place. The smaller the temperature differences are, the higher the quality of the recovered cold.

$$\eta^{rev} = \frac{\partial W_i}{\partial Q_i} = 1 - \frac{T_j}{T_o} \tag{6.21}$$

In spite of the lower cold quality, using the developed cold-to-cold recovery processes (i.e. methane purification and liquefaction and CO_2CL) is observed to be more beneficial, from an efficiency viewpoint, than electricity generation. Consider, for example, the ERPP where LNG refrigeration is used to capture and liquefy carbon dioxide. As discussed in section 2.4.1, the maximum electrical power that can be recovered from the vaporizing LNG is near 2.8MW. On the other hand, the CO_2CL process is estimated to require a 5.1MW of actual compression power with the integration of LNG evaporation (which worth of 2.8 MW of reversible power) in the process. If the LNG evaporation will be utilized to generate electrical power, then near 1.68MW will be produced with a 60% (i.e. 60% of the maximum efficiency obtained at reversible conditions) efficient heat engine. While this efficiency is considered to be very high compared to NGCC efficiency (55% LHV efficiency), the net effect on the CO_2CL is 6.22MW of additional compression power input. Hence, it is better to utilize the cold refrigeration directly into the CO_2CL process

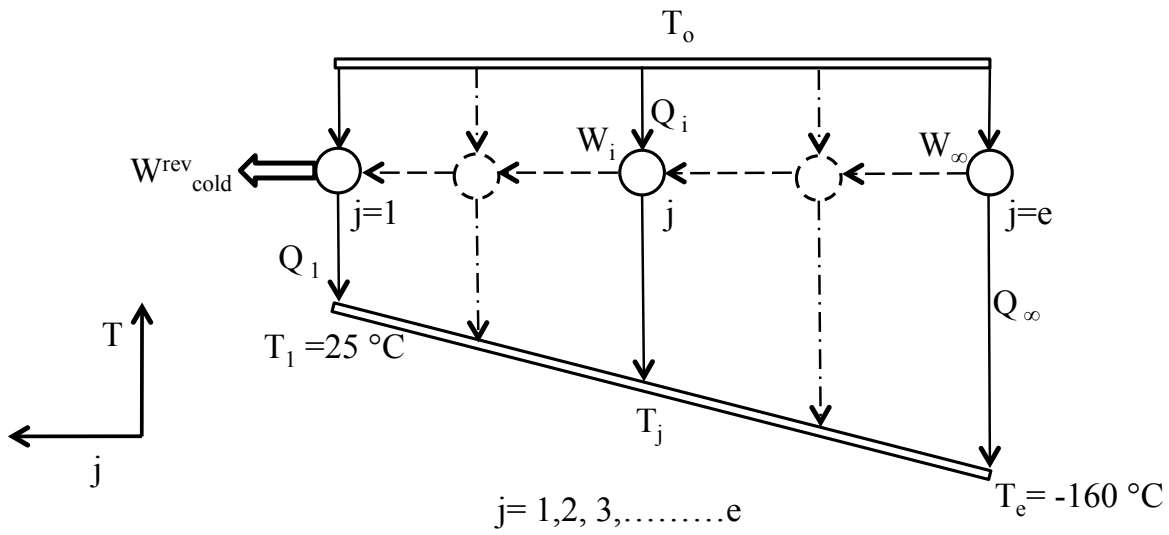

Figure 6.15. Schematic representation of multiple heat engines utilized to generate reversible power (W^{rev}_{Cold}) using evaporating LNG.

6.6 Performance of storage system reported in the literature

6.6.1 Hydrogen storage calculations

The representative performance of the energy storage cycle, discussed in chapter 4, using compressed hydrogen as the storage media is estimated using the simplified cycle shown in Figure 6.16. During the storage mode, hydrogen is produced via water-electrolysis. For this step, an electricity-to-hydrogen efficiency of 60% on an LHV basis was assumed, representative of low-temperature alkaline electrolysis systems [125]. Thereafter, hydrogen is compressed to the desired storage pressure Ps, taken here to be either 200 or 700 bar. During the delivery mode, hydrogen is expanded to 1.01 bar and subsequently fed to a fuel cell to produce electricity. The hydrogen compression work input is derived from literature [126] and the expansion work output is calculated based on the isentropic efficiency reported in Table 6.2. The fuel-to-work efficiency is taken to be 55% on an LHV basis [127], representative of hydrogen proton exchange membrane (PEM) fuel cell systems. It must be reiterated that this simplified

approach is only representative of the possible hydrogen cycle storage efficiency and detailed simulations would be necessary to accurately define its performance.

An alternative way of storing hydrogen involves storing it as liquid, which has a smaller storage volume compared to compressed hydrogen storage. In case of using liquid hydrogen as the storage media, the energy storage efficiency is calculated using the simplified cycle shown in 6.17. During the storage mode, hydrogen produced from the water-electrolysis system is subsequently cooled for storage as liquid at its boiling point, (Tboil = -253^{o}C). Subsequently, in the delivery mode, the liquid hydrogen is vaporized and fed to the fuel cell system for power generation. The work input for hydrogen liquefaction is taken from the literature [126], while the work available from vaporizing liquid hydrogen is calculated at 50% thermodynamic efficiency [128].

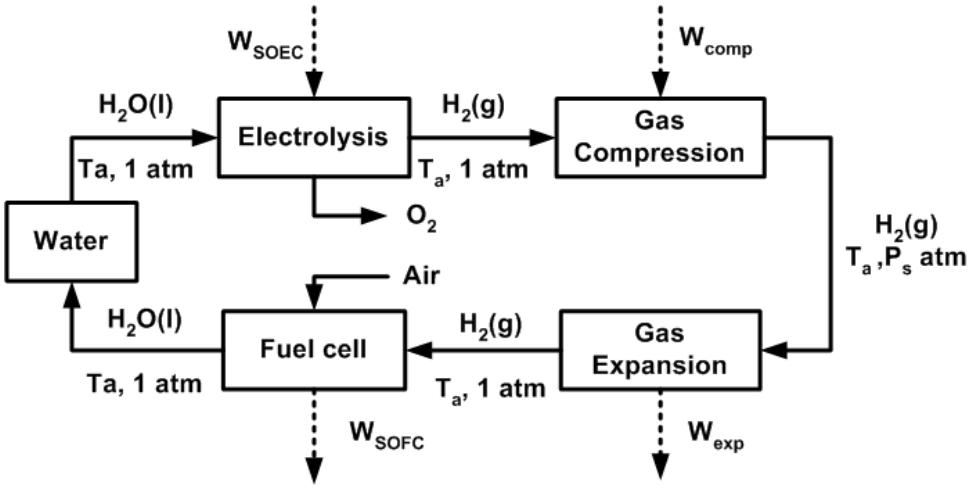

Figure 6.16. Simplified process diagram used to calculate the storage efficiency of compressed Hydrogen-cycle.

6.6.2 Compressed air storage calculations

The storage volume of compressed air to deliver 2.72GWh of electricity is calculated as follows. For a variable pressure reservoir with upper storage pressure of

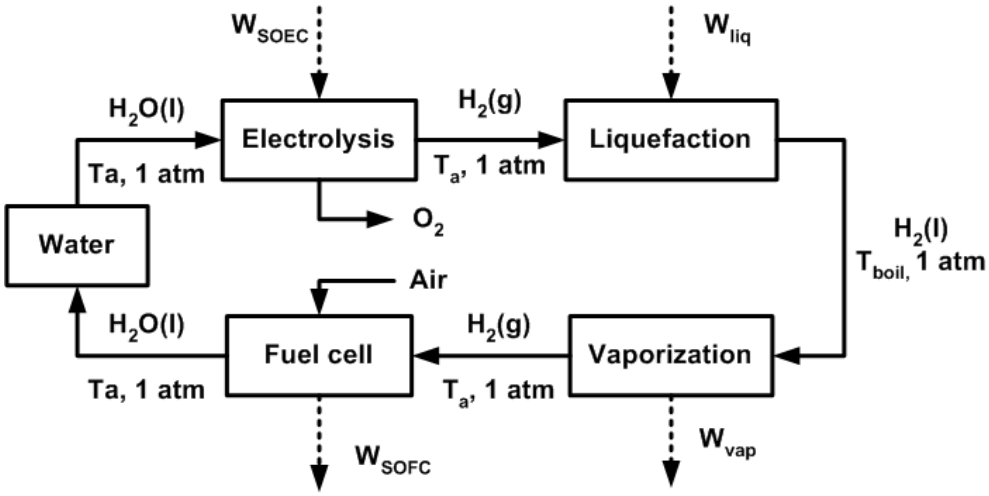

Figure 6.17. Simplified process diagram used to calculate the storage efficiency of liquid Hydrogen-cycle.

80bar, the energy produced per unit volume of compressed air is almost 8 kWh/m^3 (8×10^{-6} GWh/m^3) [129]. Thus, for the delivery of 2.72 GWh, the required storage volume is:

$$\frac{2.72GWh}{8\times10^{-6}\frac{GWh}{m^3}} = 340,000m^3 \tag{6.22}$$

6.6.3 Pumped hydroelectric storage calculations

The storage volume of pumped hydroelectric storage to deliver 2.72GWh of electricity is calculated using the Grand Coulee project as the basis [16]:

1) The Grand Coulee project has an electrical power capacity of 6,480MW with a reservoir volume of 9.4×10^6 acre ft (1.16×10^{10}m^3)

2) For a period of 24 hours, the energy density of the Grand Coulee is

$$\frac{6,480MW\times\frac{3600s}{1hour}\times24hour}{1.16\times10^{10}m^3} = 0.05Mj/m^3(1.34\times10^{-8}GWh/m^3) \tag{6.23}$$

3) Thus, for the delivery of 2.72 GWh, the required storage volume is:

$$\frac{2.72GWh}{1.34 \times 10^{-8} \frac{GWh}{m^3}} = 202,864,429m^3 \tag{6.24}$$

6.6.4 Battery storage calculations

The storage volume of sodium sulfur battery and lithium ion battery are calculated as follow:

Sodium sulfur battery For an energy density of 367kWh/m^3 (3.67×10^{-4}GWh/m^3) [64], the storage volume to deliver 2.72 GWh with an efficiency of 78% [61] is:

$$\frac{2.72GWh \times \frac{1}{0.78}}{3.67 \times 10^{-4} \frac{GWh}{m^3}} = 9,502m^3 \tag{6.25}$$

Lithium ion battery

For an energy density of 420kWh/m^3 (4.2×10^{-4}GWh/m^3) [63], the storage volume to deliver 2.72GWh with an efficiency of 80% [61] is:

$$\frac{2.72GWh \times \frac{1}{0.80}}{4.2 \times 10^{-4} \frac{GWh}{m^3}} = 8,095m^3 \tag{6.26}$$

CHAPTER 7. SUMMARY

The push towards energy generation from renewable energy sources like solar energy is motivated by the need for reducing the use of finite-fossil fuels and minimizing carbon dioxide emissions. However, a grand challenge for the large-scale deployment of baseload renewable energy supply is the intermittent nature of the energy source, which warrants the need for energy efficient storage systems. An alternative approach to reduce carbon dioxide emissions and fossil fuel use is to improve the energy efficiency of energy production systems with or without carbon dioxide capture. This dissertation outline novel, energy-efficient NG based power generation systems that can achieve close to zero carbon dioxide emissions with a power generation efficiency of 70 to 76%, on a LHV basis (see Figure 7.1. These systems make use of SOFC followed by uniquely developed refrigeration based processes for CO_2CL. Unlike conventional SOFC power generation systems, where the unconverted fuel is combusted, the developed power systems recover the unreacted fuel (in the CO_2CL process) for recycle to the SOFC; thus increasing the power output of the devise. If LNG is available for the process, then the refrigeration need in the CO_2CL section can be provided by the refrigeration released from the evaporation of LNG. The developed systems are not only applicable to fossil based fuel; but may also be used for power generation using renewable based fuel such as renewable methanol and methane.

This dissertation also presents solutions for large-scale renewable energy storage involving a closed loop cycle (shown in Figure 7.2) that cyclically transforms carbon atoms between liquid carbon dioxide and carbon fuels like liquid methane and methanol. Carbon fuels offer an attractive storage option owing to their high volumetric energy density and the well-established technology and infrastructure available

for their utilization. Yet, the use of carbon fuels for energy storage is limited by the availability of renewable carbon and hydrogen sources. Hence, it is worth considering a closed system where little additional carbon or water (to provide hydrogen via water dissociation) sources are needed.

The proposed storage cycle operates in energy storage and energy recovery mode, depending on whether the renewable energy is available or not. During energy storage mode of the cycle, renewable energy is stored as liquefied carbon fuel, synthesized from stored water (which is first dissociated to hydrogen) and liquid carbon dioxide using any of the well-known thermochemical carbon dioxide to fuel routes, and later liquefied to be stored onsite. Any energy input necessary for the fuel liquefaction can be partially or fully met by the refrigeration available from vaporizing liquid carbon dioxide (a necessary step prior the fuel synthesis). In the energy recovery mode of the cycle, the stored liquid fuel is vaporized and oxidized to generate electricity via systems like SOFC. The oxidation byproducts, carbon dioxide and water, are separated and liquefied for storage. Here, the energy penalty of carbon dioxide capture and liquefaction can be met partially or fully using the available refrigeration from vaporizing the liquid carbon fuel, if the carbon fuel has subambient boiling temperature.

The dissertation also introduces exergy based metrics to systematically identify candidate carbon fuel for the cycle. Such a search provides trade-off between the exergy stored per carbon atom, exergy lose as exothermic heat of reaction during the carbon fuel synthesis, and the exergy stored per unit volume. The exergy stored per carbon gives indication of how much carbon is circulated in the proposed cycle to store a given amount of energy. The higher the carbon circulation rate is, the higher the parasitic losses are. Therefore, it is best to choose a carbon fuel that has high exergy stored per carbon atom. On the other hand, the lower the exergy lose during the carbon fuel synthesis step, the lower the hydrogen requirement (thus, the lower the energy needed for the water dissociation step) is to store a given amount of energy. Last but not least, the higher the exergy content per unit volume, the lower the storage volume is to store a given amount of energy. While no carbon fuel simultaneously has

the most favorable values for all three metrics, favorable candidates identified include methane, methanol, propane, ethane and dimethyl ether.

Two preferred examples of the proposed cycles designed and simulated for producing nearly 140MW electrical power round the clock, using methane and methanol, respectively as the energy storage media. The methane based cycle relies on a reversible SOFC, carbon dioxide hydrogenation into methane, and synergistic liquefaction schemes involving: 1) liquid carbon dioxide vaporization and vapor methane liquefaction and 2) vapor carbon dioxide capture and liquefaction versus liquid methane vaporization. The salient features of the methanol based cycle include, a reversible SOFC, single step methanol synthesis from carbon dioxide, ease of methanol liquefaction and flexibility to store methanol-water mixtures rather than pure methanol to balance the storage volume and energy requirements for separation of water. In terms of energy storage efficiencies (i.e. the ratio of the net generated electricity during the delivery mode to the net consumed electricity during the storage mode), the methane based cycle is found to be comparable with the methanol based cycle using 50:50 methanol-water storage, at near 55%. Taken together with the storage volume, the proposed cycles compare favorably with alternatives like hydrogen and current batteries. Methane as an energy storage media, in addition to its higher exergy content per carbon atom, requires around 52% lesser volume for storage and 98% (check) less carbon make up than methanol based cycle.

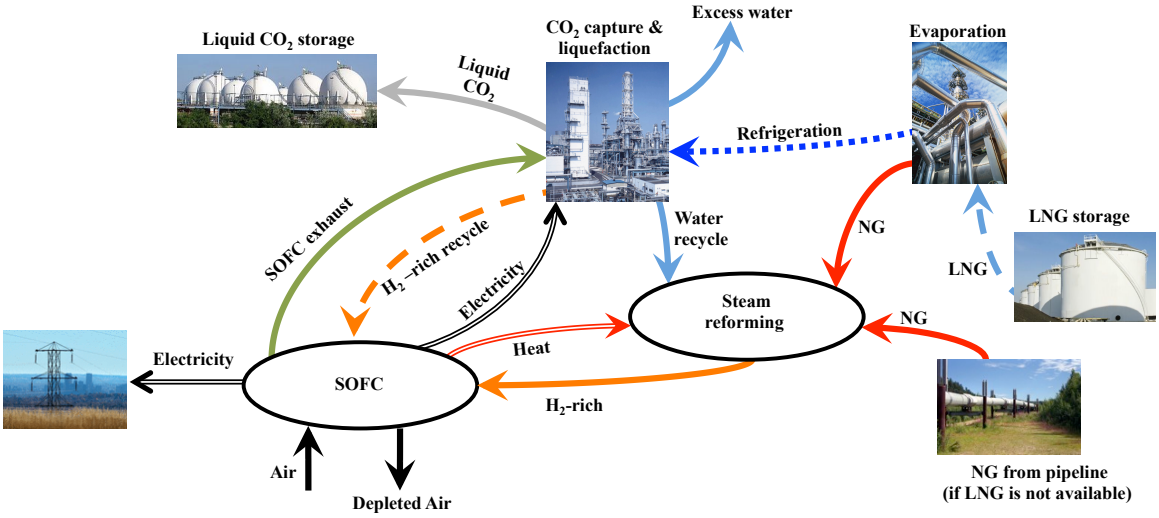

Figure 7.1. A conceptual sketch of the ERPP. SOFC = Solid Oxide Fuel Cell. LNG = Liquefied Natural Gas.

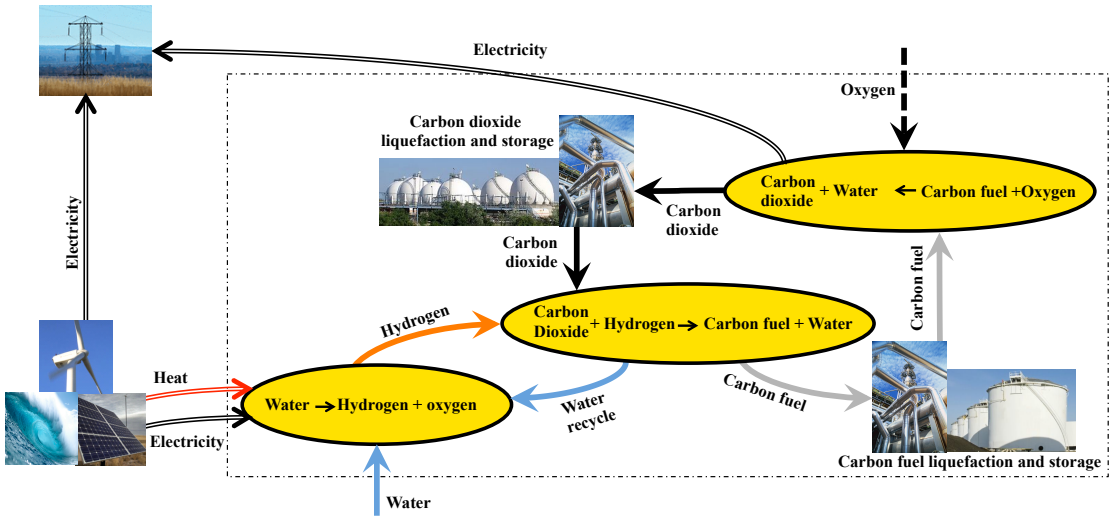

Figure 7.2. Schematic of the proposed energy storage and delivery concept.

LIST OF REFERENCES

LIST OF REFERENCES

[1] IPCC. Special report on carbon dioxide capture and storage. Technical report, Intergovernmental Panel on Climate Change, 2005.

[2] N. R. Singh. *High liquid fuel yielding biofuel processes and a roadmap for the future transportation.* PhD thesis, Purdue Univeristy, 2009.

[3] R. Agrawal, N. R. Singh, F. H. Ribeiro, and W. N. Delgass. Sustainable fuel for the transportation sector. *Proceedings of the National Academy of Sciences of the United States of America*, 104:4828–4833, 2007.

[4] S. Chu and A. Majumdar. Opportunities and challengers for a sustainable energy future. *Nature*, 488:294–303, 2012.

[5] S. Pacala and R. Socolow. Stabilization wedges: Solving the climate problem for the next 50 years with current technologies. *Science*, 205:968–972, 2004.

[6] IEA. Co2 emissions from fuel combustion-highlights. Technical report, International Energy Agency, 2012.

[7] M. L. Szulczewski, C. W. MacMinn, H. J. Herzog, and R. Juanes. Lifetime of carbon capture and storage as a climate-change mitigation technology. *Proceedings of the National Academy of Sciences of the United States of America*, 109:5185–5189, 2012.

[8] BP. Statistical review of world energy 2013. Technical report, British Petroleum, 2013.

[9] REN21. Renewables 2011 global status report. Technical report, Renewable Energy Policy network for the 21st century (REN21), 2011.

[10] B. Dunn, H. Kamath, and J-M. Tarascon. Electrical energy storage for the grid: A battery of choices. *Science*, 334:928–934, 2011.

[11] H. Chen, T. Cong, W. Yang, C. Tan, Y. Li, and Y. Ding. Progress in electrical energy storage system: A critical review. *Progress in Natural Science*, 19(3):291–312, 2009.

[12] EPRI. Electricity energy storage technology options: A white paper primer on applications, costs and benefits. Technical report, Electric Power Research Institute, 2010.

[13] L. K. Rihko-Struckmann, A. Peschel, R. Hanke-Rauschenbach, and K. Sundmacher. Assessment of methanol synthesis utilizing exhaust co2 for chemical storage of electrical energy. *Industrial and Engineering Chemistry Research*, 49(21):11073–11078, 2010.

[14] E. Cartlidge. Saving for a rainy day. *Science*, 334:922–924, 2011.

[15] I. Gur, K. Sawyer, and R. Prasher. Searching for a better thermal battery. *Science*, 335:1454–1455, 2012.

[16] J. W. Tester, E. M. Drake, M. J. Driscoll, M. W. Golay, and W. A. Peters. *Sustainable Energy: Choosing Among Options.* MIT Press, Cambridge, MA, 2005.

[17] E. S. Rubin and H. Zhai. The cost of carbon capture and storage for natural gas combined cycle power plants. *Environmental Science and Technology*, 46(6):3076–3084, 2012.

[18] A. Aspelund and T. Gundersen. A liquefied energy chain for transport and utilization of natural gas for power production with co2 capture and storage - part 2: The offshore and the onshore processes. *Applied Energy*, 86(6):793–804, 2009.

[19] H. Zhai and E. S. Rubin. Comparative performance and cost assessments of coal- and natural-gas-fired power plants under a co2 emission performance standard regulation. *Energy and Fuels*, 27(8):4290–4301, 2013.

[20] A. Aspelund, M. J. Molnvik, and G. De Koeijer. Ship transport of co_2 technical solutions nad analysis of costs, energy utilization, exergy efficiency and co2 emissions. *Chemical Engineering Research and Design*, 84:847–855, 2006.

[21] A. Lee, O. Zinaman, and J. Logan. Opportunities for synergy between natural gas and renewable energy in the electric power and transportation sectors. Technical report, National Renewable Energy Laboratory, 2012.

[22] July 2011.

[23] N. MacDowell, N. Florin, A. Buchard, J. Hallett, A. Galindo, G. Jackson, C. S. Adjiman, C. K. Williams, N. Shah, and P. Fennell. An overview of co_2 capture technologies. *Energy and Environmental Science*, 3:1645–1669, 2010.

[24] J. R. Rostrup-Nielsen and K. Aasberg-Petersen. *Handbook of Fuel Cells*, volume 3, chapter 14, pages 160–176. John Wiley and Sons, New York, 2003.

[25] R.F. Probstein and R.E. Hicks. *Synthetic Fuels.* Dover Publications, Mineola, NY, 2006.

[26] R. N. Maddox and D. J. Morgan. *Gas conditioning and processing:Gas treating and sulfur recovery*, volume 4. Campbell Petroleum Series, Norman, Oklahoma, 1998.

[27] H. M. Kvamsdal, K. Jordal, and O. Bolland. A quantitative comparison of gas turbine cycles with co_2 capture. *Energy*, 32:10–24, 2007.

[28] L-S. Fan. *Chemical Looping Systems for Fossil Energy Conversions.* John Wiley, Hoboken, New Jersey, 2010.

[29] IEA. Capturing co_2. Technical report, International Energy Agency, 2007.

[30] Aspen Technology. *Aspen Plus users guide.* Aspen Technology Inc., 2006.

[31] J. Van herle, F. Marechal, S. Leuenberger, Y. Membrez, O. Bucheli, and D. Favrat. Process flow model of solid oxide fuel cell system supplied with sewage biogas. *Journal of Power Sources*, 131:127–141, 2004.

[32] J. Van herle, F. Maréchal, S. Leuenberger, and D. Favrat. Energy balance model of a sofc cogenerator operated with biogas. *Journal of Power Sources*, 118:375–383, 2003.

[33] S. Campanari. Carbon dioxide separation from high temperature fuel cell power plants. *Journal of Power Sources*, 112:273–289, 2002.

[34] M. Ola, B. Rune, B. Olav, K. H.M., and S. Morgen. Sofc and gas turbine power systems - evaluation of configurations for co_2 capture. In *Greenhouse Gas Control Technologies 7*, pages 273–281. Canada, 2005.

[35] L. Duan, K. Huang, X. Zhang, and Y. Yang. Comparison study on different sofc hybrid systems with zero-co_2 emission. *Energy*, 58:66–77, 2013.

[36] R. Allam, V. White, N. Ivens, and M. Simmonds. *The Oxyfuel Baseline: Revamping Heaters and Boilers to Oxyfiring by Cryogenic Air Separation and Flue Gas Recycle*, volume 1, chapter 26, pages 451–475. Elsevier, New York, 2005.

[37] M. B. Wilkinson, J. C. Boden, R. S. Panesar, M. Babcock, and R. J. Allam. Co_2 capture via oxyfuel firing: Optimisation of a retrofit design concept for a refinery power station boiler. In *First National Conference on Carbon Sequestration*. Washington DC, 2001.

[38] R. S. Gemmen. Oxidation of low calorific value gases—applying optimization techniques to combustor design. In *International Joint Power Generation Conference*, pages 23–26. Baltimore, MD, 1998.

[39] A. Aspelund and T. Gundersen. A liquefied energy chain for transport and utilization of natural gas for power production with co2 capture and storage – part 1. *Applied Energy*, 86:781–792, 2009.

[40] E. I. Al-musleh. *Efficient liquefaction cycles for natural gas*. PhD thesis, Purdue Univeristy, 2010.

[41] N. Zhang and N. Lior. A novel near-zero co_2 emission thermal cycle with lng cryogenic exergy utilization. *Energy*, 31:1666–1679, 2006.

[42] N. Zhang, N. Lior, M. Liu, and W. Han. A novel co2-capturing oxy-fuel power system with lng (liquefied natural gas) coldness energy utilization. *Energy*, 35(2):1200–1210, 2010.

[43] R. Agrawal. *Liquefied natural gas refrigeration transfer to a cryogenics air separation unit using high presure nitrogen stream*. US Patent 5,137,558 ,Air Products and Chemicals, Inc., 1992.

[44] W. Wong. Lng power recovery. *Proceedings of the Institution of Mechanical Engineers, Part A: Journal of Power and Energy*, 208(1):3–12, 1994.

[45] J. Szargut and I. Szczygiel. Utilization of the cryogenic exergy of liquid natural gas (lng) for the production of electricity. *Energy*, 34(7):827–837, 2009.

[46] K. Hassmann. Sofc power plants, the siemens-westinghouse approach. *Fuel Cells*, 1(1):78–84, 2001.

[47] A. B. Stambouli and E. Traversa. Solid oxide fuel cells (sofcs): a review of an environmentally clean and efficient source of energy. *Renewable and Sustainable Energy Reviews*, 6(5):433–455, 2002.

[48] W. L. Lundberg, R. A. Israelson, R. R. Moritz, S. E. Veyo, R. A. Holmes, P. R. Zafred, J. E. King, and R. E. Kothmann. Pressurized solid oxide fuel cell/gas turbine power system. Technical report, Siemens Westinghouse Power Corporation, 2000.

[49] S. A. Barnett. *Handbook of Fuel Cells*, volume 4, chapter 78, pages 1098–1108. John Wiley and Sons, New York, 2010.

[50] EGandG TechnicalServices. Fuel cell handbook. Technical report, US Department of Energy, 2004.

[51] J.M. Campbell and R.A. Hubbard. *Gas Conditioning and Processing: The Equipment Modules*, volume 2. John M Campbell and Company, Norman, Oklahoma, 2001.

[52] A. Bourji and A. Winstead. Optimizing an organic rankine cycle. *Chemical Engineering Progress*, 109(1):35–39, 2013.

[53] J. J. Hartvigsen, S. Elangovan, and A. C. Khandkar. *Handbook of Fuel Cells*, volume 4, chapter 76, pages 1070–1085. John Wiley and Sons, New York, 2003.

[54] NETL. Cost and performance baseline for fossil energy plants volume 1: Bituminous coal and natural gas to electricity revision 2. Technical report, National Energy Technology Laboratory, 2010.

[55] G. A. Olah, A. Goeppert, and G. K. S. Prakash. *Beyond Oil and Gas: The Methanol Economy*. Wiley-VCH Verlag Gmbh and Co. KGaA, 2006.

[56] IEA. Oxy combustion processes for co_2 capture from power plant. Technical report, International Energy Agency, 2005.

[57] G. Beysel and T. Schueler. The proven cryogenic air separation process adapted to the needs of ccs (igcc and oxyfuel) resulting in a considerably lower energy consumption and load following capabilities. In *The 10th European Gasification Conference*. IChemE, 2010.

[58] Y. Hou, R. Vidu, and P. Stroeve. Solar energy storage methods. *Industrial and Engineering Chemistry Research*, 50:8954–8964, 2011.

[59] H. Ibrahim, A. Ilinca, and J. Perron. Energy storage systems-characteristics and comparisons. *Renewable and sustainable energy reviews*, 12(5):1221–1250, 2008.

[60] S. Succar and R. H. Williams. Compressed air energy storage: Theory, resources and applications for wind power. Technical report, Princeton Environmental Institute, 2008.

[61] M. Kintner-Meyer, P. Balducci, W. Colella, M. Elizondo, C. Jin, T. Nguyen, V. Viswanathan, and Y Zhang. National assessment of energy storage for grid balancing and arbitrage: Phase 1, wecc. Technical report, Pacific Northwest National Laboratory, 2012.

[62] P. W. Parfomak. Energy storage for power grids and electric transportation: A technology assessment. Technical report, Congressional Research Service, 2012.

[63] BostonPower. http://www.boston-power.com/products/swing-4400. Accessed on June 2012.

[64] Z. F. Hussien, L. W. Cheung, M. F. M. Siam, and A. B. Ismail. Modeling of sodium sulfur battery for power system applications. *Journal of Electrical Engineering*, 9(2):66–72, 2007.

[65] M. Romero, R. Buck, and J. E. Pacheco. An update on solar central receiver systems, projects, and technologies. *Journal of Solar Energy Engineering*, 123(98-108), 2002.

[66] University of Alabama. http://www1.eere.energy.gov/solar/pdfs/csp-prm2010-alabama.pdf. Accessed on January 2014.

[67] H. Perez-Blanco. *The Dynamics of Energy*. CRC Press, New York, 2009.

[68] C. Graves, S. D. Ebbesen, M. Mogensen, and K. S. Lackner. Sustainable hydrocarbon fuels by recycling co_2 and h_2o with renewable or nuclear energy. *Renewable and Sustainable Energy Reviews*, 15(1):1–23, 2011.

[69] J. D. Fleshman. *Petroleum Refining Processes*, chapter 6.1. McGrawHill, New York, 2003.

[70] N. S. Lewis and D. G. Nocera. Powering the planet: Chemical challenges in solar energy utilization. *Proceedings of the National Academy of Sciences of the United States of America*, 103(43):15729–15735, 2006.

[71] R. J. Pearson, M. D. Eisaman, J. W. G. Turner, P. P. Edwards, J. Zheng, V. L. Kuznetsov, K. A. Littau, L. di Marco, and S. R. G.Taylor. Energy storage via carbon-neutral fuels made from co2, water, and renewable energy. *Proceedings of the IEEE*, 100(2):440–460, 2012.

[72] D. M. Bierschenk, J. R. Wilson, and S. A. Barnett. High efficiency electrical energy storage using a methane-oxygen solid oxide cell. *Energy and Environmental Science*, 4:944–951, 2011.

[73] X. Sun, M. Chen, S. H. Jensen, S. D. Ebbesen, C. Graves, and M. Mogensen. Thermodynamic analysis of synthetic hydrocarbon fuel production in pressurized solid oxide electrolysis cells. *International Journal of Hydrogen Energy*, 37(22):17101–17110, 2012.

[74] D. W. Keith. Why capture co2 from the atmosphere? *Science*, 325(5948):1654–1655, 2012.

[75] G. T. Rochelle. Amine scrubbing for co2 capture. *Science*, 325:1652–1654, 2009.

[76] T. Searchinger, R. Heimlich, R. A. Houghton, F. Dong, A. Elobeid, J. Fabiosa, S. Tokgoz, D. Hayes, and T-H. Yu. Use of u.s. croplands for biofuels increases greenhouse gases through emissions from land-use change. *Science*, 319(5867):1238–1240, 2008.

[77] R. Agrawal and N.R. Singh. Solar energy to biofuels. *Annual Review of Chemical and Biomolecular Engineering*, 1(1):343–364, 2010.

[78] NRC. Liquid transportation fuels from coal and biomass: Technological status, costs, and environmental impacts. Technical report, The national academy, 2009.

[79] Rakesh Agrawal R. Agrawal and D. S. Mallapragada. Chemical engineering in a solar energy-driven sustainable future. *AIChE Journal*, 56(11):2762–2768, 2010.

[80] H. Sano. Co2 global recycling systems: Via co2-methanol or via co2-lng? *Energy Conversion and Management*, 36:895–898, 1995.

[81] K. R. Sridhar and M. Gottmann. *Combined energy storage and fuel generation with reversible fuel cells*. US patent 7,364,810B2, Bloom Energy Corporation, 2008.

[82] T. M. Flynn. *Cryogenic Engineering*. CRC Press, New York, 2 edition, 1997.

[83] EnerSea. http://www.enersea.com/solutions/gas-storage.html. Accessed on June 2013.

[84] EIA. U.s. lng markets and uses: June 2004 update. Technical report, Energy Information Adminstration, U.S. Department of Energy, 2004.

[85] S. Enthaler, J. von Langermann, and T. Schmidt. Carbon dioxide and formic acid-the couple for environmental-friendly hydrogen storage? *Energy and Environmental Science*, 3(9):1207–1217, 2010.

[86] J. Toyier, R. Miloua, N.E. Elkadri, M. Nawdali, H. Toufik, F. Miloua, and M. Saito. Sustainable process for the production of methanol from co_2 and h_2 using cu/zno-based multicomponent catalyst. *Physics Procedia*, 2:1075 – 1079, 2009.

[87] K. P. Brooks, J. Hu, H. Zhu, and R. J. Kee. Methanation of carbon dioxide by hydrogen reduction using the sabatier process in microchannel reactors. *Chemical Engineering Science*, 62(4):1161–1170, 2007.

[88] J. E. O'Brien. Thermodynamic consierations for thermal water splitting processes and high temperature electrolysis. In *Proceedings of the 2008 International Mechanical Engineering Congress and Exposition*, volume 8, pages 639–651, 2008.

[89] J. Udagawa, P. Aguiar, and N.P. Brandon. Hydrogen production through steam electrolysis : Model-based steady state performance of a cathode-supported intermediate temperature solid oxide electrolysis cell. *Journal of Power Sources*, 166:127–136, 2007.

[90] B. Yildiz, K. J. Hohnholt, and M. S. Kazimi. Hydrogen production using high-temperature steam electrolysis supported by advanced gas reactors with supercritical co_2 cycles. *Nuclear Technology*, 155:1–21, 2005.

[91] M. G. McKellar, J.E. O'Brien, E.A. Harvego, and J. S. Herring. Optimized flow sheet for a reference commercial scale nuclear driven high temperature electrolysis hydrogen production plant. Technical report, Idaho National Laboratory, 2007.

[92] P. J. Lunde and F. L. Kester. Rates of methane formation from carbon dioxide and hydrogne over a ruthenium catalyst. *Journal of Catalysis*, 30:423–428, 1973.

[93] P. J. Lunde. Modeling, simulation, and operation of a sabatier reactor. *Industrial and Engineering Chemistry*, 13(3):226–233, 1974.

[94] E. B. Woodruff, H. B. Lammers, and T. F. Lammers. *Steam plant operation*. McGrawHill, New York, 9 edition, 2012.

[95] F. Khazrai, H. B. Haghighi, and H. Kordabadi. Avoid brittle fracture in pressure vessels. *Hydrocarbon Processing*, 2011.

[96] T. Ogawa, N. Inoue, T. Shikada, and Y. Ohno. Direct dimethyl ether synthesis. *Journal of Natural Gas Chemistry*, 12:219–227, 2003.

[97] J. R. Selman. Poison-tolerant fuel cells. *Science*, 326:52–53, 2009.

[98] M. Homel, T. M. Gür, J. H. Koh, and A. V. Virkard. Carbon monoxide-fueled solid oxide fuel cell. *Journal of Power Sources*, 195(19):6367–6372, 2010.

[99] G. L. Soloveichik. Battery technologies for large-scale stationary energy storage. *Annual Review of Chemical and Biomolecular Engineering*, 2(1):503–527, 2011.

[100] NETL. Cost and performance baseline for fossil energy plants, volume :2 coal to synthetic natural gas and ammonia. Technical report, National Energy Technology Laboratory, 2011.

[101] T. Adams and P. Barton. Combining coal gasification and natural gas reforming for efficient polygeneration. *Fuel Processing Technology*, 92:639–655, 2011.

[102] W. Seider, J. Seader, D. Lewin, and S. Widagdo. *Product and Process Design Principles*. Wiley, New Jersey, 3 edition, 2009.

[103] R. Sinnott. *Chemical Engineering Design*, volume 6. Elsevier, New York.

[104] E. Carlson. Don't gamble with physical properties for simulations. *Chemical Engineering Progress*, October, 1996.

[105] C. Tsang and W. Streett. Phase equilibria in the h2/co2 system at temperatures from 220 to 290 k and pressures to 172 mpa. *Chemical Engineering Science*, 36(36):993–1000, 1981.

[106] G. Kaminishi, Y. Arai, S. Saito, and S. Maeda. Vapor-liquid equilibria for binary and ternary systems containing carbon dioxide. *Journal of Chemical Engineering of Japan*, 1(2):109–116, 1968.

[107] M. Atilhan, S. Aparicio, S. Ejaz, D. Cristancho, I. Mantilla, and K.R. Hall. pft behavior of three lean synthetic natural gas mixtures using a magnetic suspension densimeter and isochoric apparatus from (250 to 450) k with pressures up to 150 mpa: Part ii. *Journal of Chemical and Engineering Data*, 56:3766–3774, 2011.

[108] A. Valtz, A. Chapoy, C. Coquelet, P. Paricaud, and D. Richon. Vapor-liquid equilibria in the carbon dioxide-water system, measurement adn modeling from 278.2 to 318.2 k. *Fluid Phase Equilibria*, 226:333–344, 2004.

[109] T. Adams and P. Barton. High-efficiency power production from coal with carbon capture. *AIChE Journal*, 56(12):3120–3136, 2010.

[110] J. M. Smith, H.C. Van Ness, and M. M. Abbott. *Introduction to Chemical Engineering Thermodynamics*. McGrawHill, New York, 6 edition, 2001.

[111] P. Aguiar, D. Chadwick, and L. Kershenbaum. Modelling of an indirect internal reforming solid oxide fuel cell. *Chemical Engineering Science*, 57:1665–1677, 2002.

[112] T. Edgar, D. Himmelblau, and L. Lasdon. *Optimization of chemical processes*. McGrawHill, New York, 2 edition, 2001.

[113] J. Foglietta. Consider dual independent expander refrigeration for lng production. *hydrocarbon processing*, 83:39–44, 2004.

[114] HydrocarbonProcessing. *Gas Processes Handbook 2004*. Gulf publishing, Texas, 2004.

[115] R. Smith. *Chemical Process Design and Integration*. Wiley, England, 1 edition, 2005.

[116] R. McGuinness and W. Kleinberg. *Oxygen-Enhanced combustion*, chapter 3. CRC Press, New York, 2 edition, 2013.

[117] A. Smith, J. Klosek, and D. Woodward. Next generation integration concepts for air separation units and gas turbines. *Journal of Engineering for Gas Turbines and Power*, 119:298–304, 1997.

[118] R. Agrawal and D. Herron. Efficient use of an intermediate reboiler or condenser in a binary distillation. *AIChE Journal*, 44(6):1303–1315, 1998.

[119] I. Kemp. *Pinch Analysis and Process Integration-A User Guide on Process Integration for the Efficient Use of Energy*. Institution of Chemical Engineers, 2 edition, 2007.

[120] V. Ganapathy. Heat-recovery steam generators: Understand the basics. *Chemical Engineering Progress*, August:32–45, 1996.

[121] H. Fogler. *Elements of Chemical Reaction Engineering*. Prentice-Hall International,New Jersey, third edition, 1999.

[122] X. Shi and D. Che. A combined power cycle utilizing low-temperature waste heat and lng cold energy. *Energy Conversion and Management*, 50:567–575, 2009.

[123] V. Rocca. Cold recovery during regasification of lng part one: Cold utilization far from the regasification facility. *Energy*, 35:2049–2058, 2010.

[124] C. Dispenza, G. Dispenza, V. Rocca, and G. Panno. Exergy recovery in regasification facilities – cold utilization: A modular unit. *Applied Thermal Engineering*, 29:3595–3608, 2009.

[125] K. Zeng and D. Zhang. Recent progress in alkaline water electrolysis for hydrogen production and applications. *Progress in Energy and Combustion Science*, 36:307–326, 2010.

[126] U. Bossel. Does a hydrogen economy make sense? *Proceedings of the IEEE*, 94:1826–1837, 2006.

[127] F. de Bruijn. The current status of fuel cell technology for mobile and stationary applications. *Green chemistry*, 7:132–150, 2005.

[128] S. Huang, N. Tsai, and P. Shah. A shortcut thermodynamic model for simulating lng liquefaction facilities. In H. Alfadada, G. Reklaitis, and M. El-Halwagi, editors, *Advances in Gas Processing*, pages 113–122, 2009.

[129] S. Succar and R. Williams. Compressed air energy storage: Theory, resources and applications for wind power. Technical report, Princeton Environmental Institute, 2008.

APPENDICES

APPENDIX A. MATERIAL AND ENERGY BALANCES FOR THE ERPP-LNG PROCESS

Table A.1
Material and energy balance for ERPP-LNG, see Figures 2.2 and 2.3 for flowsheet.

Stream	1	2	3	4	5	6	8	9	10	11	12	13	14
Temperature, °C	-160	-152.8	34.6	-24	-45.9	34.6	683.3	950	941.6	156.7	153.7	43.3	43.2
Pressure, bar	1.3	100.0	99.9	40.0	11.1	10.9	10.0	9.7	9.3	9.1	9.0	8.9	15.3
Total Flow, kmol/hr	895.0	895.0	895.0	895.0	895.0	895.0	3,473.3	6,907.8	6,907.8	6,907.8	6,907.8	6,907.8	2,437.1
Mole Flow, kmol/hr													
H_2	-	-	-	-	-	-	-	696.2	696.2	696.2	696.2	696.2	696.2
N_2	3.6	3.6	3.6	3.6	3.6	3.6	3.6	249.5	249.5	249.5	249.5	249.5	249.5
O_2	-	-	-	-	-	-	-	-	-	-	-	-	-
CO	-	-	-	-	-	-	-	292.1	292.1	292.1	292.1	292.1	292.1
CO_2	-	-	-	-	-	-	-	1,183.0	1,183.0	1,183.0	1,183.0	1,183.0	1,183.0
CH_4	804.6	804.6	804.6	804.6	804.6	804.6	804.6	0.0	0.0	0.0	0.0	0.0	0.0
C_2H_6	53.7	53.7	53.7	53.7	53.7	53.7	53.7	-	-	-	-	-	-
C_3H_8	19.7	19.7	19.7	19.7	19.7	19.7	19.7	-	-	-	-	-	-
nC_4H_{10}	13.4	13.4	13.4	13.4	13.4	13.4	13.4	-	-	-	-	-	-
H_2O	-	-	-	-	-	-	2,578.3	4,487.0	4,487.0	4,487.0	4,487.0	4,487.0	16.3
Exergy, MW	-8.1	-8.1	-9.6	-10.1	-10.8	-10.9	-158.8	-381.7	-382.5	-420.3	-422.5	-435.0	-139.4

Exergy = H-T_oS, where T_o =298 K, H, S: enthalpy and entropy of the stream

Stream	15	16	17	18	19	20	21	22	23	24	25	26	27
Temperature, °C	43.3	43.2	43.2	43.2	43.3	117.9	118.1	25	152.1	680	922.2	831.6	179.8
Pressure, bar	11.5	8.9	8.7	1.9	8.9	1.9	10.6	1.0	10.2	10.0	9.7	6.7	6.4
Total Flow, kmol/hr	4.9	10.8	4,479.9	4,479.9	9.2	1,908.7	2,561.9	10,288.7	10,288.7	10,288.7	8,312.1	8,312.1	8,312.1
Mole Flow, kmol/hr													
H_2	<0.1	-	0.1	0.1	0.1	-	-	-	-	-	-	-	-
N_2	<0.1	-	0.0	0.0	0.0	-	-	7,978.3	7,978.3	7,978.3	7,978.3	7,978.3	7,978.3
O_2	-	-	-	-	-	-	-	2,117.3	2,117.3	2,117.3	140.7	140.7	140.7
CO	<0.1	-	0.1	0.1	0.1	-	-	-	-	-	-	-	-
CO_2	<0.1	<0.001	6.5	6.5	6.5	-	-	30.7	30.7	30.7	30.7	30.7	30.7
CH_4	-	-	-	-	-	-	-	-	-	-	-	-	-
C_2H_6	-	-	-	-	-	-	-	-	-	-	-	-	-
C_3H_8	-	-	-	-	-	-	-	-	-	-	-	-	-
nC_4H_{10}	-	-	-	-	-	-	-	-	-	-	-	-	-
H_2O	4.8	10.8	4,473.2	4,473.2	2.5	1,908.7	2,561.9	162.4	162.4	162.4	162.4	162.4	162.4
Exergy, MW	-0.3	-0.7	-295.6	-295.6	-0.9	-125.4	-168.3	-18.0	0.2	26.1	33.6	26.3	-2.2

Exergy = H-T_oS, where T_o =298 K, H, S: enthalpy and entropy of the stream

Table A.2
Material and energy balance for ERPP-LNG, see Figures 2.2 and 2.3 for flowsheet (continue).

Stream	28	29	30	31	32	33	34	35	36	37	38	39	40
Temperature, °C	28.1	43.1	-0.3	-2.6	-52.2	-52.2	34.6	43.3	0.6	-41.5	-26.7	34.6	43.3
Pressure, bar	1.1	14.8	14.7	10.0	9.8	9.8	9.6	33.8	33.7	10.0	33.5	33.3	99.8
Total Flow, kmol/hr	8,312.1	2,420.7	2,420.7	2,420.7	1,021.7	3,089.5	3,089.5	3,089.5	3,089.5	1,690.5	2,976.3	2,976.3	2,976.3
Mole Flow, kmol/hr													
H_2	-	696.2	696.2	696.2	0.5	701.5	701.5	701.5	701.5	5.8	716.4	716.4	716.4
N_2	7,978.3	249.5	249.5	249.5	1.0	256.1	256.1	256.1	256.1	7.6	282.3	282.3	282.3
O_2	140.7	-	-	-	-	-	-	-	-	-	-	-	-
CO	-	292.1	292.1	292.1	2.1	305.3	305.3	305.3	305.3	15.4	354.4	354.4	354.4
CO_2	30.7	1,183.0	1,183.0	1,183.0	1,018.1	1,826.6	1,826.6	1,826.6	1,826.6	1,661.7	1,623.1	1,623.1	1,623.1
CH_4	-	-	-	-	-	-	-	-	-	-	-	-	-
C_2H_6	-	-	-	-	-	-	-	-	-	-	-	-	-
C_3H_8	-	-	-	-	-	-	-	-	-	-	-	-	-
nC_4H_{10}	-	-	-	-	-	-	-	-	-	-	-	-	-
H_2O	162.4	-	-	-	-	-	-	-	-	-	-	-	-
Exergy, MW	-14.4	-138.4	-138.4	-139.0	-108.6	-209.0	-209.4	-206.9	-206.8	-178.3	-186.6	-186.8	-184.7

Exergy = H-T_oS, where T_o =298 K, H, S: enthalpy and entropy of the stream

Stream	41	42	43	44	45	46	47	48	49	50	R1	R2	R3
Temperature, °C	-52.7	-52.9	-52.7	34.6	-54.9	34.6	-14.6	34.6	34.6	800	310	290	680
Pressure, bar	99.7	33.7	99.5	99.3	22.2	21.9	10.4	10.2	10.2	10.0	10.7	10.2	10.0
Total Flow, kmol/hr	2,976.3	1,577.3	1,399.0	1,399.0	1,399.0	1,399.0	1,399.0	1,399.0	1,384.9	1,384.9	706.4	722.7	722.7
Mole Flow, kmol/hr													
H_2	716.4	20.7	695.7	695.7	695.7	695.7	695.7	695.7	688.8	688.8	-	-	-
N_2	282.3	33.8	248.4	248.4	248.4	248.4	248.4	248.4	245.9	245.9	2.8	2.8	2.8
O_2	-	-	-	-	-	-	-	-	-	-	-	-	-
CO	354.4	64.5	289.9	289.9	289.9	289.9	289.9	289.9	287.0	287.0	-	-	-
CO_2	1,623.1	1,458.3	164.9	164.9	164.9	164.9	164.9	164.9	163.2	163.2	-	-	-
CH_4	-	-	-	-	-	-	-	-	-	-	635.0	635.0	635.0
C_2H_6	-	-	-	-	-	-	-	-	-	-	42.4	42.4	42.4
C_3H_8	-	-	-	-	-	-	-	-	-	-	15.5	15.5	15.5
nC_4H_{10}	-	-	-	-	-	-	-	-	-	-	10.6	10.6	10.6
H_2O	-	-	-	-	-	-	-	-	-	-	-	16.3	16.3
Exergy, MW	-183.2	-157.7	-25.7	-25.9	-27.2	-27.4	-28.0	-28.1	-27.8	-22.9	-7.7	-8.9	-5.8

Exergy = H-T_oS, where T_o =298 K, H, S: enthalpy and entropy of the stream

APPENDIX B. MATERIAL AND ENERGY BALANCES FOR THE ERPP-NG PROCESS WITH GASEOUS CARBON DIOXIDE

Table B.1
Material and energy balance for ERPP-NG with gaseous carbon dioxide, see Figure 2.14 for flowsheet.

Stream	1	2	3	29	30	31	32	33	34	35	36	37	38	39
Temperature, °C	38.0	-20.8	39.4	43.1	-0.3	-2.6	-52.2	-53.7	-52.2	44.4	0.6	-41.5	-26.6	39.4
Pressure, bar	31.0	11.1	10.9	14.9	14.8	10.0	9.8	6.0	9.8	34.0	33.9	10.0	33.7	33.5
Total mole flow, kmol/hr	895.0	895.0	895.0	2,420.5	2,420.5	2,420.5	1,021.7	1,021.7	3,092.1	3,092.1	3,092.1	1,693.3	2,975.0	2,975.0
Mole Flow, kmol/hr														
H_2	-	-	-	696.2	696.2	696.2	0.5	0.5	701.6	701.6	701.6	5.9	716.4	716.4
N_2	3.6	3.6	3.6	249.3	249.3	249.3	1.0	1.0	256.0	256.0	256.0	7.7	282.1	282.1
O_2	-	-	-	-	-	-	-	-	-	-	-	-	-	-
CO	-	-	-	292.1	292.1	292.1	2.1	2.1	305.4	305.4	305.4	15.5	354.4	354.4
CO_2	-	-	-	1,182.9	1,182.9	1,182.9	1,018.1	1,018.1	1,829.1	1,829.1	1,829.1	1,664.2	1,622.1	1,622.1
CH_4	804.6	804.6	804.6	0.0	0.0	0.0	-	-	0.0	0.0	0.0	0.0	0.0	0.0
C_2H_6	53.7	53.7	53.7	-	-	-	-	-	-	-	-	-	-	-
C_3H_8	19.7	19.7	19.7	-	-	-	-	-	-	-	-	-	-	-
nC_4H_{10}	13.4	13.4	13.4	-	-	-	-	-	-	-	-	-	-	-
H_2O	-	-	-	-	-	-	-	-	-	-	-	-	-	-
Exergy, MW	-10.2	-10.8	-10.9	-138.4	-138.4	-139.0	-108.6	-108.6	-209.3	-207.1	-207.1	-178.6	-186.5	-186.6

Exergy = H-T_oS, where T_o =298 K, H, S: enthalpy and entropy of the stream

Stream	40	41	42	43	44	45	46	47	48	A	B		
Temperature, °C	43.3	-52.7	-52.9	-52.7	39.4	-55.0	39.4	-5.8	39.4	39.4	30.0		
Pressure, bar	99.8	99.7	33.9	99.5	99.3	20.5	20.3	10.4	10.2	5.9	99.7	**Compressors power, MW**	
Total mole flow, kmol/hr	2,975.0	2,975.0	1,576.2	1,398.8	1,398.8	1,398.8	1,398.8	1,398.7	1,398.7	1,021.7	1,021.7	K-4	2.68
Mole Flow, kmol/hr												K-5	3.08
H_2	716.4	716.4	20.7	695.7	695.7	695.7	695.7	695.7	695.7	0.5	0.5	K-6	2.89
N_2	282.1	282.1	33.8	248.3	248.3	248.3	248.3	248.2	248.2	1.0	1.0		
O_2	-	-	-	-	-	-	-	-	-	-	-		
CO	354.4	354.4	64.5	289.9	289.9	289.9	289.9	289.9	289.9	2.1	2.1	**Turbines power, MW**	
CO_2	1,622.1	1,622.1	1,457.3	164.8	164.8	164.8	164.8	164.8	164.8	1,018.1	1,018.1	T-1	0.46
CH_4	0.0	0.0	0.0	0.0	0.0	0.0	0.0	0.0	0.0	-	-	T-5	1.12
C_2H_6	-	-	-	-	-	-	-	-	-	-	-	T-6	0.51
C_3H_8	-	-	-	-	-	-	-	-	-	-	-		
nC_4H_{10}	-	-	-	-	-	-	-	-	-	-	-	**Pumps power, MW**	
H_2O	-	-	-	-	-	-	-	-	-	-	-	P-1	0.15
Exergy, MW	-184.6	-183.1	-157.6	-25.7	-25.9	-27.3	-27.4	-28.1	-28.1	-110.5	-109.0		

Exergy = H-T_oS, where T_o =298 K, H, S: enthalpy and entropy of the stream

APPENDIX C. MATERIAL AND ENERGY BALANCES FOR THE ERPP-NG PROCESS WITH LIQUID CARBON DIOXIDE

Table C.1
Material and energy balance for ERPP-NG with liquid carbon dioxide, see Figure 2.15 for flowsheet.

Stream	1	2	3	29	30	31	32	33	34	35	36	37	38	39
Temperature, °C	38.0	-20.8	41.8	43.1	-0.3	-2.6	-52.3	-52.3	41.8	43.3	0.6	-41.5	-26.7	41.8
Pressure, bar	31.0	11.1	10.9	14.8	14.7	10.0	9.8	9.8	9.6	33.8	33.7	10.0	33.5	33.3
Total mole Flow, kmol/hr	895.0	895.0	895.0	2,423.3	2,423.3	2,423.3	1,021.7	3,092.4	3,092.4	3,092.4	3,092.4	1,690.8	2,979.8	2,979.8
Mole Flow, kmol/hr														
H_2	-	-	-	696.1	696.1	696.1	0.5	701.5	701.5	701.5	701.5	5.8	716.4	716.4
N_2	3.6	3.6	3.6	251.7	251.7	251.7	1.0	258.3	258.3	258.3	258.3	7.7	284.7	284.7
O_2	-	-	-	-	-	-	-	-	-	-	-	-	-	-
CO	-	-	-	292.1	292.1	292.1	2.1	305.3	305.3	305.3	305.3	15.3	354.4	354.4
CO_2	-	-	-	1183.4	1183.4	1183.4	1018.1	1827.2	1827.2	1827.2	1827.2	1662.0	1624.3	1624.3
CH_4	804.6	804.6	804.6	-	-	-	-	-	-	-	-	-	-	-
C_2H_6	53.7	53.7	53.7	-	-	-	-	-	-	-	-	-	-	-
C_3H_8	19.7	19.7	19.7	-	-	-	-	-	-	-	-	-	-	-
nC_4H_{10}	13.4	13.4	13.4	-	-	-	-	-	-	-	-	-	-	-
H_2O	0.0	0.0	0.0	-	-	-	-	-	-	-	-	-	-	-
Exergy, MW	-10.2	-10.8	-10.9	-138.4	-138.4	-139.0	-108.6	-209.1	-209.5	-206.9	-206.9	-178.4	-186.7	-186.9

Exergy = H-T_oS, where T_o =298 K, H, S: enthalpy and entropy of the stream

Stream	40	41	42	43	44	45	46	47	48	A	B	C
Temperature, °C	43.3	-52.7	-52.9	-52.7	41.8	-55.1	41.8	-1.3	41.8	41.8	43.3	-53.7
Pressure, bar	99.8	99.7	33.7	99.5	99.3	19.8	19.6	10.4	10.2	13.0	19.4	19.3
Total Flow, kmol/hr	2,979.8	2,979.8	1,578.3	1,401.6	1,401.6	1,401.6	1,401.6	1,401.5	1,401.5	5,380.1	5,380.1	5,380.1
Mole Flow, kmol/hr												
H_2	716.4	716.4	20.7	695.7	695.7	695.7	695.7	695.7	695.7	-	-	-
N_2	284.8	284.8	34.1	250.6	250.6	250.6	250.6	250.6	250.6	-	-	-
O_2	-	-	-	-	-	-	-	-		-	-	-
CO	354.4	354.4	64.4	290.0	290.0	290.0	290.0	290.0	290.0	-	-	-
CO_2	1624.3	1624.3	1459.0	165.3	165.3	165.3	165.3	165.3	165.3	-	-	-
CH_4	-	-	-	-	-	-	-	-	-	756.5	756.5	756.5
C_2H_6	-	-	-	-	-	-	-	-	-	3,116.5	3,116.5	3,116.5
C_3H_8	-	-	-	-	-	-	-	-	-	64.4	64.4	64.4
nC_4H_{10}	-	-	-	-	-	-	-	-	-	1,442.7	1,442.7	1,442.7
H_2O	-	-	-	-	-	-	-	-	-	-	-	-
Exergy, MW	-184.8	-183.3	-157.8	-25.7	-25.9	-27.3	-27.5	-28.1	-28.1	-41.2	-40.2	-37.7

Exergy = H-T_oS, where T_o =298 K, H, S: enthalpy and entropy of the stream

Table C.2
Material and energy balance for ERPP-NG with liquid carbon dioxide, see Figure 2.15 for flowsheet (continue).

Stream	**D**		
Temperature, °C			
Pressure, bar		**Compressors power, MW**	
Total Flow, kmol/hr		**K-4**	3.98
Mole Flow, kmol/hr		**K-5**	3.09
H_2	-	**K-6**	1.76
N_2	-	**Turbines power, MW**	
O_2	-	**T-1**	0.46
CO	-	**T-5**	1.15
CO_2	-	**T-6**	0.49
CH_4	756.5		
C_2H_6	3,116.5		
C_3H_8	64.4		
nC_4H_{10}	1,442.7		
H_2O	-		
Exergy, MW	-37.8		

Exergy = H-T_oS, where T_o =298 K, H, S: enthalpy and entropy of the stream

APPENDIX D. MATERIAL AND ENERGY BALANCES FOR THE CONVENTIONAL SOFC POWER PLANT WITHOUT CARBON DIOXIDE CAPTURE

Table D.1
Material and energy balance for conventional SOFC power plant without carbon dioxide capture, see Figure 2.18 for flowsheet.

Stream	1	2	3	4	5	6	7	8	9	10	11	12	13	14
Temperature, °C	-160.0	-159.3	24.0	683.1	950.0	1188.8	902.4	902.4	179.1	94.5	76.5	43.3	40.9	40.9
Pressure, bar	1.3	10.9	10.8	10.0	9.7	9.5	2.8	2.8	2.5	2.5	1.5	1.3	1.1	1.1
Total mole flow, kmol/hr	895.0	895.0	895.0	3,456.9	5,506.5	13,322.5	7,011.3	6,311.1	6,311.1	7,011.3	13,322.5	13,322.5	9,360.3	3,962.1
Mole Flow, kmol/hr														
H_2	-	-	-	-	382.4	-	-	-	-	-	-	-	-	-
N_2	3.6	3.6	3.6	3.6	3.6	7,602.0	4,000.8	3,601.3	3,601.3	4,000.8	7,602.0	7,602.0	7,602.0	0.0
O_2	-	-	-	-	-	33.6	17.7	15.9	15.9	17.7	33.6	33.6	33.6	-
CO	-	-	-	-	133.1	-	-	-	-	-	-	-	-	-
CO_2	-	-	-	0.1	891.8	1,054.1	554.8	499.4	499.4	554.8	1,054.1	1,054.1	1,053.9	0.2
CH_4	804.6	804.6	804.6	804.6	0.0	-	-	-	-	-	-	-	-	-
C_2H_6	53.7	53.7	53.7	53.7	-	-	-	-	-	-	-	-	-	-
C_3H_8	19.7	19.7	19.7	19.7	-	-	-	-	-	-	-	-	-	-
NC_4H_{10}	13.4	13.4	13.4	13.4	-	-	-	-	-	-	-	-	-	-
H_2O	-	-	-	2,561.8	4,095.6	4,632.7	2,438.1	2,194.6	2,194.6	2,438.1	4,632.7	4,632.7	670.7	3,961.9
Exergy, MW	-8.1	-8.1	-10.9	-157.9	-326.4	-303.7	-182.7	-164.5	-192.5	-215.6	-414.2	-421.7	-161.6	-261.2

Exergy = H-T_oS, where T_o =298 K, H, S: enthalpy and entropy of the stream

Stream	15	16	17	18	19	20		
Temperature, °C	40.0	40.2	25.0	152.1	680.0	922.2	**Compressors power, MW**	
Pressure, bar	1.1	10.7	1.0	10.2	10.0	9.7	K-1	26.12
Total mole flow, kmol/hr	2,561.9	2,561.9	9,798.9	9,798.9	9,798.9	8,073.8		
Mole flow, kmol/hr							**Turbines power, MW**	
H_2	-	-	-	-	-	-	**T-1**	40.4
N_2	0.0	0.0	7,598.4	7,598.4	7,598.4	7,598.4	**T-2**	4.8
O_2	-	-	2,016.5	2,016.5	2,016.5	291.4		
CO	-	-	-	-	-	-	**SOFC AC power, MW**	
CO_2	0.1	0.1	29.2	29.2	29.2	29.2	142.81	
CH_4	-	-	-	-	-	-		
C_2H_6	-	-	-	-	-	-		
C_3H_8	-	-	-	-	-	-		
nC_4H_{10}	-	-	-	-	-	-		
H_2O	2,561.8	2,561.8	154.7	154.7	154.7	154.7		
Exergy, MW	-168.9	-168.9	-17.1	0.2	24.8	32.6		

Exergy = H-T_oS, where T_o =298 K, H, S: enthalpy and entropy of the stream

APPENDIX E. FLOWSHEET, MATERIAL BALANCE, AND ENERGY BALANCE FOR THE METHANOL BASED ERPP

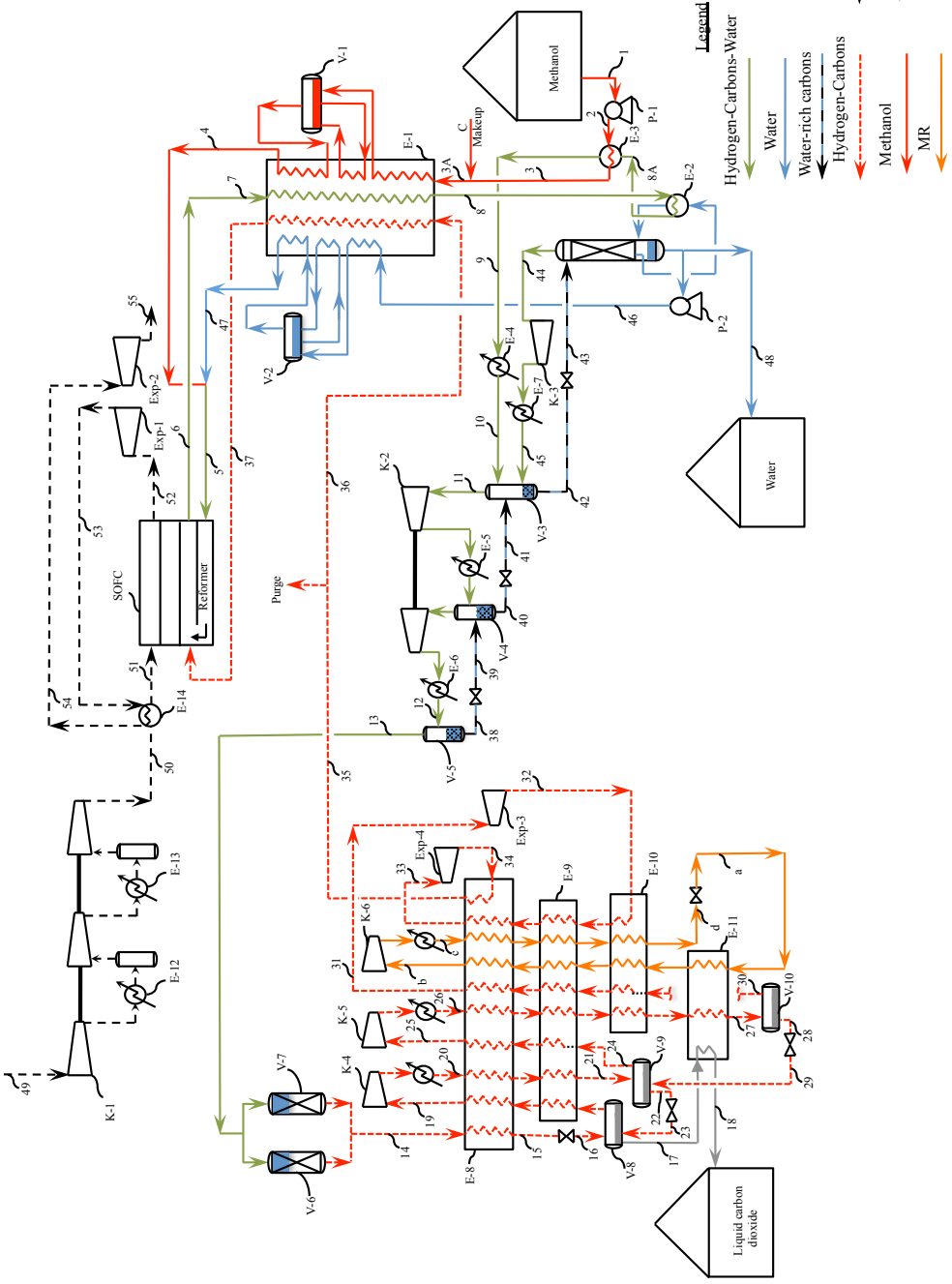

Figure E.1. Detailed flowsheet for the methanol based ERPP.

Table E.1
Material and energy balance for the methanol based ERPP, see Figure E.1 for flowsheet.

Stream	1	2	3	3A	4	5	6 and 7	8	8A
Temperature, ° C	43	44	134	132	680	680	950	165	162
Pressure, bar	1.16	11.00	10.66	10.66	10.00	10.00	9.70	9.48	9.38
Vapor Fraction	0.00	0.00	0.00	0.00	1.00	1.00	1.00	0.96	0.84
Mole Flow, kmol/hr	871	871	871	896	896	2,059	3,940	3,940	3,940
Volume Flow, m^3/hr	47.9	47.9	56.3	57.6	7,118.4	16,325.7	41,333.4	13,891.0	12,364.9
Mole Flow, kmol/h									
H_2	-	-	-	-	-	-	55.81	55.81	55.81
N_2	-	-	-	-	-	-	-	-	-
O_2	-	-	-	-	-	-	-	-	-
CO	-	-	-	-	-	-	27.19	27.19	27.19
CO_2	-	-	-	-	-	-	904.12	904.12	904.12
CH_4	-	-	-	-	-	-	-	-	-
C_2H_6	-	-	-	-	-	-	-	-	-
C_3H_8	-	-	-	-	-	-	-	-	-
CH_3OH	870.23	870.23	870.23	895.00	895.00	895.00	-	-	-
H_2O	0.87	0.87	0.87	0.87	0.87	1,163.50	2,952.78	2,952.78	2,952.78
Exergy, MW	-40.4	-40.4	-40.0	-41.2	-33.5	-102.8	-260.3	-283.3	-284.9

Exergy = H-T_oS, where T_o =298 K, H, S: enthalpy and entropy of the stream

Stream	9	10	11	12	13	14	15	16	17
Temperature, ° C	160	43	43	43	43	43	-1	-42	-42
Pressure, bar	9.28	9.17	8.97	43.69	43.48	43.02	42.92	10.00	9.79
Vapor Fraction	0.79	0.25	1.00	1.00	1.00	1.00	0.57	0.73	0.00
Mole Flow, kmol/hr	3,940	3,940	998	993	990	987	987	987	895
Volume Flow, m^3/hr	11,689.5	2,815.1	2,833.3	497.5	499.9	504.5	241.0	1,260.6	37.9
Mole Flow, kmol/h									
H_2	55.81	55.81	55.81	55.81	55.81	55.81	55.81	55.81	0.16
N_2	-	-	-	-	-	-	-	-	-
O_2	-	-	-	-	-	-	-	-	-
CO	27.19	27.19	27.19	27.19	27.19	27.19	27.19	27.19	0.67
CO_2	904.12	904.12	904.16	904.14	904.12	904.12	904.12	904.12	893.96
CH_4	-	-	-	-	-	-	-	-	-
C_2H_6	-	-	-	-	-	-	-	-	-
C_3H_8	-	-	-	-	-	-	-	-	-
CH_3OH	-	-	-	-	-	-	-	-	-
H_2O	2,952.78	2,952.78	10.67	5.46	3.18	-	-	-	-
Exergy, MW	-285.6	-293.5	-99.6	-98.3	-98.2	-98.0	-97.9	-98.4	-95.5

Exergy = H-T_oS, where T_o =298 K, H, S: enthalpy and entropy of the

Table E.2
Material and energy balance for the methanol based ERPP, see Figure E.1 for flowsheet (continue).

Stream	18	19	20	21	22	23	24	25	26
Temperature, ° C	-46	41	43	-12	-25	-40	-25	41	43
Pressure, bar	9.79	9.59	20.79	20.69	20.48	10.00	20.48	20.28	79.79
Vapor Fraction	0.00	1.00	1.00	1.00	0.00	0.15	1.00	1.00	1.00
Mole Flow, kmol/hr	895	847	847	847	754	754	703	703	703
Volume Flow, m^3/hr	37.4	2,225.3	993.9	762.5	34.7	216.0	600.6	847.0	171.8
Mole Flow, kmol/h									
H_2	0.16	56.25	56.25	56.25	0.60	0.60	61.99	61.99	61.99
N_2	-	-	-	-	-	-	-	-	-
O_2	-	-	-	-	-	-	-	-	-
CO	0.67	29.35	29.35	29.35	2.83	2.83	54.66	54.66	54.66
CO_2	893.96	761.08	761.08	761.08	750.93	750.93	586.81	586.81	586.81
CH_4	-	-	-	-	-	-	-	-	-
C_2H_6	-	-	-	-	-	-	-	-	-
C_3H_8	-	-	-	-	-	-	-	-	-
CH_3OH	-	-	-	-	-	-	-	-	-
H_2O	-	-	-	-	-	-	-	-	-
Exergy, MW	-95.4	-83.5	-83.1	-83.0	-80.4	-80.4	-65.2	-65.3	-64.7

Exergy = H-T_oS, where T_o =298 K, H, S: enthalpy and entropy of the

Stream	27	28	29	30	31	32	33	34	35
Temperature, ° C	-55	-55	-56	-55	41	-55	41	11	41
Pressure, bar	79.69	79.48	20.70	79.48	79.28	16.00	15.79	10.41	10.21
Vapor Fraction	0.13	0.00	0.05	1.00	1.00	1.00	1.00	1.00	1.00
Mole Flow, kmol/hr	703	611	611	92	92	92	92	92	92
Volume Flow, m^3/hr	45.9	24.5	46.7	21.4	32.1	104.8	154.0	211.1	237.4
Mole Flow, kmol/h									
H_2	61.99	6.35	6.35	55.64	55.64	55.64	55.64	55.64	55.64
N_2	-	-	-	-	-	-	-	-	-
O_2	-	-	-	-	-	-	-	-	-
CO	54.66	28.15	28.15	26.52	26.52	26.52	26.52	26.52	26.52
CO_2	586.81	576.66	576.66	10.15	10.15	10.15	10.15	10.15	10.15
CH_4	-	-	-	-	-	-	-	-	-
C_2H_6	-	-	-	-	-	-	-	-	-
C_3H_8	-	-	-	-	-	-	-	-	-
CH_3OH	-	-	-	-	-	-	-	-	-
H_2O	-	-	-	-	-	-	-	-	-
Exergy, MW	-64.3	-62.4	-62.5	-1.9	-1.9	-2.0	-2.0	-2.0	-2.0

Exergy = H-T_oS, where T_o =298 K, H, S: enthalpy and entropy of the

Table E.3
Material and energy balance for the methanol based ERPP, see Figure E.1 for flowsheet (continue).

Stream	36	37	38	39	40	41	42	43	44
Temperature, ° C	41	800	43	43	43	43	43	43	43
Pressure, bar	10.21	10.00	43.48	19.48	19.27	9.17	8.97	1.88	1.88
Vapor Fraction	1.00	1.00	0.00	0.01	0.00	0.00	0.00	0.00	1.00
Mole Flow, kmol/hr	91	91	2	2	8	8	2,958	2,958	9
Volume Flow, m^3/hr	235.1	817.6	0.1	0.1	0.2	0.2	71.9	166.3	122.2
Mole Flow, kmol/h									
H_2	55.09	55.09	-	-	-	-	0.02	0.02	0.02
N_2	-	-	-	-	-	-	-	-	-
O_2	-	-	-	-	-	-	-	-	-
CO	26.25	26.25	-	-	-	-	0.01	0.01	0.01
CO_2	10.05	10.05	0.03	0.03	0.05	0.05	8.38	8.38	8.38
CH_4	-	-	-	-	-	-	-	-	-
C_2H_6	-	-	-	-	-	-	-	-	-
C_3H_8	-	-	-	-	-	-	-	-	-
CH_3OH	-	-	-	-	-	-	-	-	-
H_2O	-	-	2.28	2.28	7.49	7.49	2,950.02	2,950.02	0.41
Exergy, MW	-2.0	-1.7	-0.2	-0.2	-0.5	-0.5	-195.4	-195.4	-0.9

Exergy = H-T_oS, where T_o =298 K, H, S: enthalpy and entropy of the

Stream	45	46	47	48	49	50	51	52	53
Temperature, ° C	43	118	680	118	25	152	680	922	768
Pressure, bar	9.17	10.66	10.00	1.90	1.01	10.21	10.00	9.70	5.05
Vapor Fraction	0.96	0.00	1.00	0.00	1.00	1.00	1.00	1.00	1.00
Mole Flow, kmol/hr	9	1,163	1,163	1,787	12,339	12,339	12,339	10,997	10,997
Volume Flow, m^3/hr	23.2	22.2	9,184.1	34.1	301,822.7	42,921.7	98,059.9	112,796.8	188,868.5
Mole Flow, kmol/h									
H_2	0.02	-	-	-	-	-	-	-	-
N_2	-	-	-	-	9,568.12	9,568.12	9,568.12	9,568.12	9,568.12
O_2	-	-	-	-	2,539.23	2,539.23	2,539.23	1,197.56	1,197.56
CO	0.01	-	-	-	-	-	-	-	-
CO_2	8.38	-	-	-	36.80	36.80	36.80	36.80	36.80
CH_4	-	-	-	-	-	-	-	-	-
C_2H_6	-	-	-	-	-	-	-	-	-
C_3H_8	-	-	-	-	-	-	-	-	-
CH_3OH	-	-	-	-	-	-	-	-	-
H_2O	0.41	1,162.63	1,162.63	1,786.98	194.78	194.78	194.78	194.78	194.78
Exergy, MW	-0.9	-76.4	-68.3	-117.4	-21.6	0.2	31.3	44.6	28.2

Exergy = H-T_oS, where T_o =298 K, H, S: enthalpy and entropy of the

Table E.4
Material and energy balance for the methanol based ERPP, see Figure E.1 for flowsheet (continue).

Stream	54	55	Purge	C Makeup	a	b	c	d
Temperature, ° C	180	48	41	43	-59	41	43	-53
Pressure, bar	4.84	1.10	10.21	10.66	12.15	11.84	34.34	34.24
Vapor Fraction	1.00	1.00	1.00	0.00	0.10	1.00	0.51	0.00
Mole Flow, kmol/hr	10,997	10,997	1	25	2,300	2,300	2,300	2,300
Volume Flow, m^3/hr	85,782.2	267,139.4	2.4	1.4	469.4	4,505.7	782.7	162.0
Mole Flow, kmol/h								
H_2	-	-	0.56	-	-	-	-	-
N_2	9,568.12	9,568.12	-	-	-	-	-	-
O_2	1,197.56	1,197.56	-	-	-	-	-	-
CO	-	-	0.27	-	-	-	-	-
CO_2	36.80	36.80	0.10	-	-	-	-	-
CH_4	-	-	-	-	526.37	526.37	526.37	526.37
C_2H_6	-	-	-	-	293.50	293.50	293.50	293.50
C_3H_8	-	-	-	-	1,480.13	1,480.13	1,480.13	1,480.13
CH_3OH	-	-	-	24.77	-	-	-	-
H_2O	194.78	194.78	-	-	-	-	-	-
Exergy, MW	-5.3	-19.1	0.0	-1.1	-15.9	-17.5	-16.4	-15.7

Exergy = H-T_oS, where T_o =298 K, H, S: enthalpy and entropy of the

Compressors power, MW		**Turbines power**	
K-1	32.9	**Exp-1**	15.1
K-2	1.5	**Exp-2**	11.5
K-3	0.0	**Exp-3**	0.1
K-4	0.6	**Exp-4**	0.0
K-5	0.9		
K-6	2.0		
Pumps power, kW		**SOFC power, MW**	
P-1	20.9	124.0	
P-2	10.1		

APPENDIX F. MATERIAL AND ENERGY BALANCES FOR THE DEVELOPED OXY-FUEL NGCC PROCESS

Table F.1
Material and energy balance for the oxy-fuel NGCC process shown in Figure 2.21 and Figure 2.23.

Stream	1	2	3	4	6	7	8	9	13
Temperature, °C	-160	-153	40	-35	40	818	1327	847	432
Pressure, bar	1.30	100.00	99.90	27.00	26.79	26.59	25.25	1.84	1.64
Vapor Fraction	0.00	0.00	1.00	0.99	1.00	1.00	1.00	1.00	1.00
Mole Flow, kmol/hr	895	895	895	895	895	556	28,968	28,968	28,968
Volume Flow, m^3/hr	35.8	35.8	202.1	562.7	830.4	1,913.3	153,257.4	1,463,610.0	1,037,600.0
Mole Flow, kmol/h									
N_2	3.58	3.58	3.58	3.58	3.58	2.22	795.56	795.56	795.56
Ar	-	-	-	-	-	-	1,585.40	1,585.40	1,585.40
O_2	-	-	-	-	-	-	44.83	44.83	44.83
CO	-	-	-	-	-	-	-	-	-
CO_2	-	-	-	-	-	-	22,668.23	22,668.23	22,668.23
CH_4	804.61	804.61	804.61	804.61	804.61	499.69	-	-	-
C_2H_6	53.70	53.70	53.70	53.70	53.70	33.35	-	-	-
C_3H_8	19.69	19.69	19.69	19.69	19.69	12.23	-	-	-
nC_4H_{18}	13.43	13.43	13.43	13.43	13.43	8.34	-	-	-
H_2O	-	-	-	-	-	-	3,873.76	3,873.76	3,873.76
Exergy, MW	-8.1	-8.1	-9.6	-10.2	-10.3	-2.2	-2,356.7	-2,572.7	-2,684.5

Exergy = H-T_oS, where T_o =298 K, H, S: enthalpy and entropy of the stream

Stream	14	15	16	17	18	19	20	21	22
Temperature, °C	134	126	43	40	411	418	818	43	43
Pressure, bar	1.43	1.33	1.22	1.02	26.79	26.79	26.59	15.00	14.79
Vapor Fraction	1.00	1.00	0.93	1.00	1.00	1.00	1.00	0.98	1.00
Mole Flow, kmol/hr	28,968	28,968	28,968	25,909	25,909	27,998	27,998	1,163	1,142
Volume Flow, m^3/hr	684,413.7	722,335.1	579,263.1	661,709.3	55,211.4	60,317.7	96,041.4	1,896.4	1,922.6
Mole Flow, kmol/h									
N_2	795.56	795.56	795.56	759.61	759.61	791.98	791.98	35.95	35.95
Ar	1,585.40	1,585.40	1,585.40	1,513.76	1,513.76	1,585.40	1,585.40	71.64	71.64
O_2	44.83	44.83	44.83	42.81	42.81	2,027.70	2,027.70	2.03	2.03
CO	-	-	-	-	-	-	-	-	-
CO_2	22,668.23	22,668.23	22,668.23	21,643.45	21,643.45	21,643.45	21,643.45	1,024.87	3.00
CH_4	-	-	-	-	-	-	-	-	-
C_2H_6	-	-	-	-	-	-	-	-	-
C_3H_8	-	-	-	-	-	-	-	-	-
nC_4H_{18}	-	-	-	-	-	-	-	-	-
H_2O	3,873.76	3,873.76	3,873.76	1,949.73	1,949.73	1,949.73	1,949.73	28.43	7.83
Exergy, MW	-2,734.0	-2,736.2	-2,743.7	-2,507.6	-2,407.1	-2,403.5	-2,303.8	-112.5	-111.1

Exergy = H-T_oS, where T_o =298 K, H, S: enthalpy and entropy of the stream

Table F.2
Material and energy balance for the oxy-fuel NGCC process shown in Figure 2.21 and Figure 2.23 (continue).

Stream	23	24	25	26	27	28	29	30	31
Temperature, °C	43	43	40	101	99	275	43	-32	-42
Pressure, bar	3.81	1.22	1.02	1.04	1.02	3.92	14.79	14.69	10
Vapor Fraction	0.00	0.00	0.00	0.00	1.00	1.00	1.00	0.93	0.94
Mole Flow, kmol/hr	21	103	1,935	1,916	19	19	1,134	1,134	1,134
Volume Flow, m^3/hr	0.97	4.23	46.87	48.80	573.39	218.67	1,910.69	1,240.93	1,838.64
Mole Flow, kmol/h									
N_2	-	-	-	-	-	-	35.95	35.95	35.95
Ar	-	-	0.00	-	0.00	0.00	71.64	71.64	71.64
O_2	-	-	-	-	-	-	2.03	2.03	2.03
CO	-	-	-	-	-	-	-	-	-
CO_2	0.09	0.12	0.62	-	0.62	0.62	1,024.78	1,024.78	1,024.78
CH_4	-	-	-	-	-	-	-	-	-
C_2H_6	-	-	-	-	-	-	-	-	-
C_3H_8	-	-	-	-	-	-	-	-	-
nC_4H_{18}	-	-	-	-	-	-	-	-	-
H_2O	20.61	102.81	1,934.56	1,916.20	18.36	18.36	-	-	-
Exergy, MW	-1.4	-6.8	-127.6	-126.0	-1.2	-1.2	-110.6	-110.4	-110.7

Exergy = H-T_oS, where T_o =298 K, H, S: enthalpy and entropy of the stream

Stream	32	33	34	35	36	37	38	39	40
Temperature, °C	-42	-42	40	43	1	-43	-25	40	43
Pressure, bar	9.79	9.79	9.59	33.79	33.69	10	33.48	33.28	99.79
Vapor Fraction	0.00	1.00	1.00	1.00	1.00	0.20	1.00	1.00	1.00
Mole Flow, kmol/hr	1,005	1,299	1,299	1,299	1,299	1,170	1,466	1,466	1,466
Volume Flow, m^3/hr	42.6	2,287.1	3,404.6	888.8	683.5	448.3	737.6	1,066.0	314.3
Mole Flow, kmol/h									
N_2	0.42	42.57	42.57	42.57	42.57	7.04	152.30	152.30	152.30
Ar	1.29	97.90	97.90	97.90	97.90	27.55	445.90	445.90	445.90
O_2	0.04	2.66	2.66	2.66	2.66	0.68	10.27	10.27	10.27
CO	-	-	-	-	-	-	-	-	-
CO_2	1,003.15	1,156.10	1,156.10	1,156.10	1,156.10	1,134.48	857.48	857.48	857.48
CH_4	-	-	-	-	-	-	-	-	-
C_2H_6	-	-	-	-	-	-	-	-	-
C_3H_8	-	-	-	-	-	-	-	-	-
nC_4H_{18}	-	-	-	-	-	-	-	-	-
H_2O	-	-	-	-	-	-	-	-	-
Exergy, MW	-107.1	-125.0	-125.1	-124.1	-124.1	-121.4	-91.4	-91.5	-90.6

Exergy = H-T_oS, where T_o =298 K, H, S: enthalpy and entropy of the stream

Table F.3
Material and energy balance for the oxy-fuel NGCC process shown in Figure 2.21 and Figure 2.23 (continue).

Stream	41	42	43	44	45	46	47	48	49
Temperature, °C	-53	-62.3	-53	39.8	-55.8	39.8	-55	39.8	-55
Pressure, bar	99.69	33.69	99.48	99.28	27.39	27.18	7.24	7.03	1.82
Vapor Fraction	0.09	0.36	1.00	1.00	1.00	1.00	1.00	1.00	1.00
Mole Flow, kmol/hr	1,466	1,336	129	129	129	129	129	129	129
Volume Flow, m^3/hr	75.3	251.0	16.6	32.7	77.5	122.1	316.8	477.3	1,282.6
Mole Flow, kmol/h									
N_2	152.30	116.78	35.53	35.53	35.52	35.52	35.52	35.52	35.53
Ar	445.90	375.55	70.35	70.35	70.35	70.35	70.35	70.35	70.35
O_2	10.27	8.29	1.98	1.98	1.98	1.98	1.98	1.98	1.98
CO	-	-	-	-	-	-	-	-	-
CO_2	857.48	835.86	21.63	21.63	21.63	21.63	21.63	21.63	21.63
CH_4	-	-	-	-	-	-	-	-	-
C_2H_6	-	-	-	-	-	-	-	-	-
C_3H_8	-	-	-	-	-	-	-	-	-
nC_4H_{18}	-	-	-	-	-	-	-	-	-
H_2O	-	-	-	-	-	-	-	-	-
Exergy, MW	-89.8	-88.0	-2.0	-2.1	-2.2	-2.2	-2.3	-2.3	-2.4

Exergy = H-T_oS, where T_o =298 K, H, S: enthalpy and entropy of the stream

Stream	50	51	52	53	54	55	56	57	58
Temperature, °C	40	25	43	43	-175	-175	-190	-192	-192
Pressure, bar	1.61	1.01	5.78	5.28	5.17	5.17	1.46	1.46	1.26
Vapor Fraction	1.00	1.00	1.00	1.00	0.96	0.00	0.15	1.00	1.00
Mole Flow, kmol/hr	129	9,853	9,853	9,668	9,668	6,315	6,315	7,579	7,579
Volume Flow, m^3/hr	2,086	241,010	44,869	48,232	12,931	229	4,424	33,020	38,839
Mole Flow, kmol/h									
N_2	35.53	7,552.49	7,552.49	7,552.49	7,552.42	4,212.84	4,212.84	7,520.12	7,520.12
Ar	70.35	89.91	89.91	89.91	89.91	87.25	87.25	18.27	18.27
O_2	1.98	2,025.41	2,025.41	2,025.41	2,025.39	2,014.74	2,014.74	40.51	40.51
CO	-	-	-	-	-	-	-	-	-
CO_2	21.63	28.81	28.81	-	-	-	-	-	-
CH_4	-	-	-	-	-	-	-	-	-
C_2H_6	-	-	-	-	-	-	-	-	-
C_3H_8	-	-	-	-	-	-	-	-	-
nC_4H_{18}	-	-	-	-	-	-	-	-	-
H_2O	-	156.27	156.27	-	-	-	-	-	-
Exergy, MW	-2.4	-17.5	-5.7	7.3	19.2	29.9	29.4	12.4	11.6

Exergy = H-T_oS, where T_o =298 K, H, S: enthalpy and entropy of the stream

Table F.4
Material and energy balance for the oxy-fuel NGCC process shown in Figure 2.21 and Figure 2.23 (continue).

Stream	59	60	61	62	63	64	65	66	A
Temperature, °C	42	-179	-179	-192	-150	-183	-180	42	43
Pressure, bar	1.05	5.17	4.97	1.46	5.07	1.46	1.46	1.26	5.8
Vapor Fraction	1.00	0.00	0.00	0.15	1.00	1.00	1.00	1.00	0.00
Mole Flow, kmol/hr	7,579	3,353	3,353	3,353	0	0	2,089	2,089	1,270
Volume Flow, m^3/hr	189,236.8	132.6	131.8	2,221.3	0.2	0.5	10,672.1	43,546.8	23.1
Mole Flow, kmol/h									
N_2	7,520.12	3,339.58	3,339.58	3,339.58	0.08	0.08	32.37	32.37	-
Ar	18.27	2.66	2.66	2.66	0.00	0.00	71.64	71.64	-
O_2	40.51	10.64	10.64	10.64	0.02	0.02	1,984.90	1,984.90	-
CO	-	-	-	-	-	-	-	-	-
CO_2	-	-	-	-	-	-	-	-	-
CH_4	-	-	-	-	-	-	-	-	-
C_2H_6	-	-	-	-	-	-	-	-	-
C_3H_8	-	-	-	-	-	-	-	-	-
nC_4H_{18}	-	-	-	-	-	-	-	-	-
H_2O	-	-	-	-	-	-	-	-	1,269.81
Exergy, MW	0.0	17.5	17.6	17.3	0.0	0.0	2.6	0.0	-83.7

Exergy = H-T_oS, where T_o =298 K, H, S: enthalpy and entropy of the stream

Stream	B	C	D	E	F	G	H	I	J
Temperature, °C	221	39	44	304	164	45	402	264	402
Pressure, bar	4.94	0.07	25.00	24.14	4.94	120.00	119.14	39.46	39.25
Vapor Fraction	1.00	0.87	0.00	1.00	1.00	0.00	1.00	1.00	1.00
Mole Flow, kmol/hr	1,269.8	6,819.5	2,125.6	2,125.6	5,549.7	3,424.1	3,424.1	3,424.1	3,424.1
Volume Flow, m^3/hr	10,318.9	2,187,530.0	51.6	3,970.3	39,227.5	62.0	1,330.8	3,296.9	4,636.7
Mole Flow, kmol/h									
N_2	-	-	-	-	-	-	-	-	-
Ar	-	-	-	-	-	-	-	-	-
O_2	-	-	-	-	-	-	-	-	-
CO	-	-	-	-	-	-	-	-	-
CO_2	-	-	-	-	-	-	-	-	-
CH_4	-	-	-	-	-	-	-	-	-
C_2H_6	-	-	-	-	-	-	-	-	-
C_3H_8	-	-	-	-	-	-	-	-	-
nC_4H_{18}	-	-	-	-	-	-	-	-	-
H_2O	1,269.81	6,819.47	2,125.61	2,125.61	5,549.66	3,424.05	3,424.05	3,424.05	3,424.05
Exergy, MW	-78.8	-446.4	-140.1	-129.2	-345.7	-225.5	-204.3	-208.3	-205.2

Exergy = H-T_oS, where T_o =298 K, H, S: enthalpy and entropy of the stream

Table F.5
Material and energy balance for the oxy-fuel NGCC process shown in Figure 2.21 and Figure 2.23 (continue).

Stream	R1	R2	R3
Temperature, °C	310	290	293
Pressure, bar	26.59	26.13	26.79
Vapor Fraction	1.00	1.00	1.00
Mole Flow, kmol/hr	339	347	347
Volume Flow, m^3/hr	623.8	626.3	613.9
Mole Flow, kmol/h			
N_2	1.36	1.36	1.36
Ar	-	-	-
O_2	-	-	-
CO	-	-	-
CO_2	-	-	-
CH_4	304.91	304.91	304.91
C_2H_6	20.35	20.35	20.35
C_3H_8	7.46	7.46	7.46
nC_4H_{18}	5.09	5.09	5.09
H_2O	-	7.83	7.83
Exergy, MW	-3.5	-4.1	-4.1

Exergy = H-T_oS, where T_o =298 K, H, S: enthalpy and entropy of the stream

APPENDIX G. FLOWSHEET, MATERIAL BALANCE, AND ENERGY BALANCE FOR THE DEVELOPED OXY-FUEL MOCC

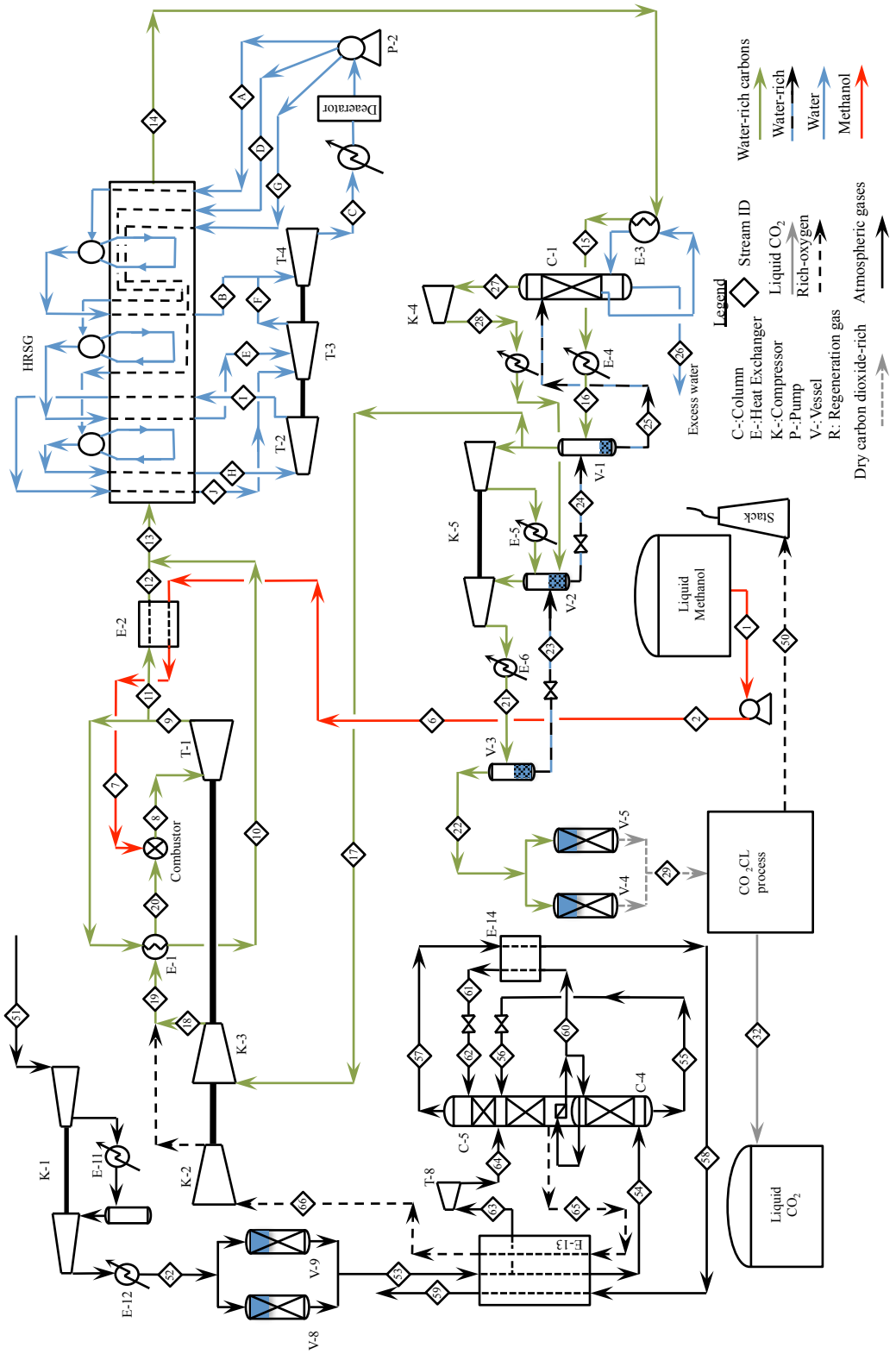

Figure G.1. Detailed flowsheet for the oxy-fuel MoCC.

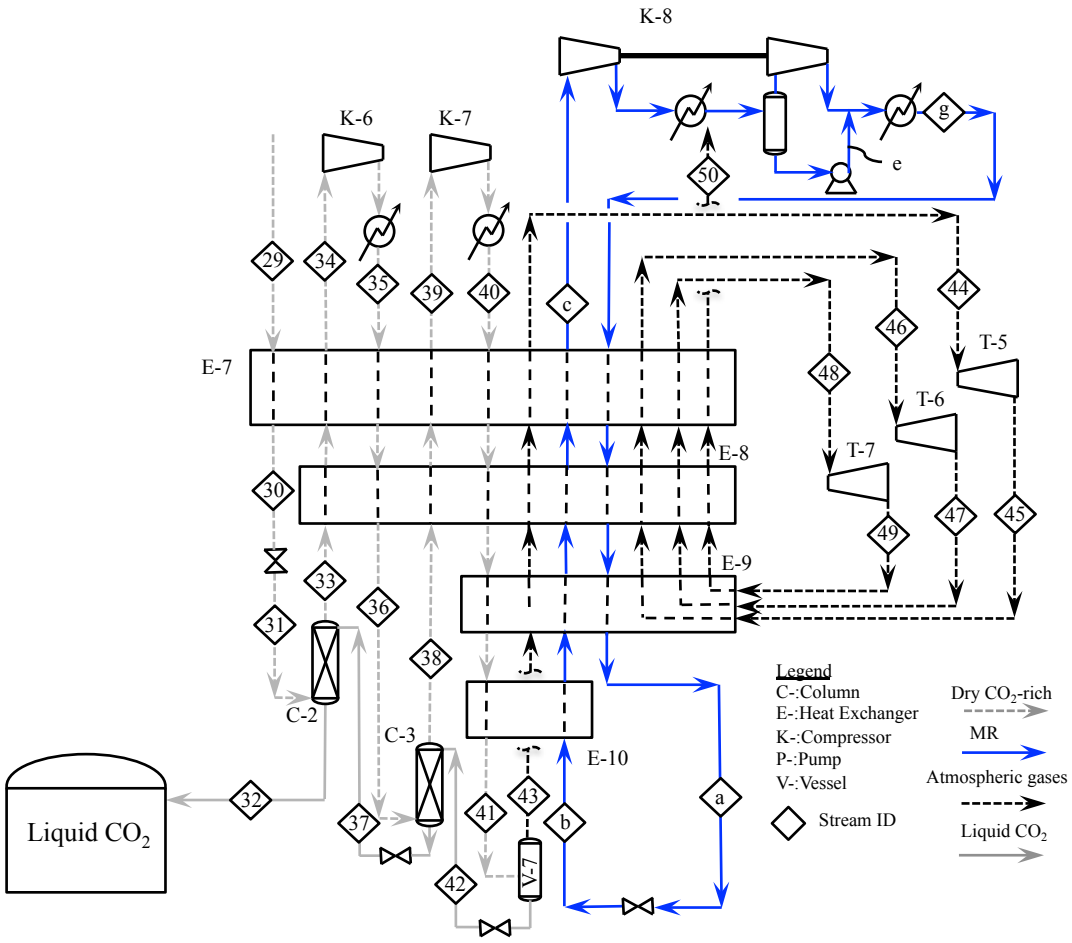

Figure G.2. Detailed flowsheet for the CO_2CL section of the oxy-fuel MoCC shown in Figure G.1.

Table G.1
Material and energy balance for the oxy-fuel MoCC, see Figures G.1 and G.2 for flowsheets.

Stream	1	6	7	8	9	13	14	15	16
Temperature, °C	43	45	822	1328	851	393	140	130	43
Pressure, bar	1.01	26.79	26.59	25.25	1.84	1.64	1.43	1.33	1.22
Vapor Fraction	0.00	0.00	1.00	1.00	1.00	1.00	1.00	1.00	0.92
Mole Flow, kmol/hr	895	895	785	21,811	21,811	21,811	21,811	21,811	21,811
Volume Flow, m^3/hr	49	49	2,716	115,512	1,106,290	737,473	523,043	549,604	428,965
Mole Flow, kmol/hr									
N_2	-	-	-	393.49	393.49	393.49	393.49	393.49	393.49
Ar	-	-	-	942.44	942.44	942.44	942.44	942.44	942.44
O_2	-	-	-	26.40	26.40	26.40	26.40	26.40	26.40
CO	-	-	-	-	-	-	-	-	-
CO_2	-	-	-	17,223.15	17,223.15	17,223.15	17,223.15	17,223.15	17,223.15
CH_4	-	-	-	-	-	-	-	-	-
C_2H_6	-	-	-	-	-	-	-	-	-
C_3H_8	-	-	-	-	-	-	-	-	-
NC4	-	-	-	-	-	-	-	-	-
CH_3OH	895.00	895.00	785.12	-	-	-	-	-	-
H_2O	-	-	-	3,225.40	3,225.40	3,225.40	3,225.40	3,225.40	3,225.40
Exergy, MW	-41.51	-41.47	-26.85	-1808.14	-1971.17	-2063.23	-2094.11	-2095.91	-2102.21

Exergy = H-T_oS, where T_o =298 K, H, S: enthalpy and entropy of the stream

Stream	17	18	19	20	21	22	23	24	25
Temperature, °C	41	407	417	822	43	43	43	43	41
Pressure, bar	1.02	26.79	26.79	26.59	15.00	14.79	3.82	1.22	1.02
Vapor Fraction	1.00	1.00	1.00	1.00	0.98	1.00	0.00	0.00	0.00
Mole Flow, kmol/hr	19,055	19,055	20,468	20,468	990	972	18	89	1,801
Volume Flow, m^3/hr	486,629	40,365	44,049	70,507	1,611	1,633	1	4	44
Mole Flow, kmol/hr									
N_2	373.06	373.06	393.49	393.49	20.44	20.44	-	-	-
Ar	893.49	893.49	942.44	942.44	48.95	48.95	-	-	0.00
O_2	25.03	25.03	1,368.90	1,368.90	1.37	1.37	-	-	-
CO	-	-	-	-	-	-	-	-	-
CO_2	16,328.15	16,328.15	16,328.15	16,328.15	895.08	895.00	0.08	0.10	0.59
CH_4	-	-	-	-	-	-	-	-	-
C_2H_6	-	-	-	-	-	-	-	-	-
C_3H_8	-	-	-	-	-	-	-	-	-
NC4	-	-	-	-	-	-	-	-	-
CH_3OH	-	-	-	-	-	-	-	-	-
H_2O	1,435.40	1,435.40	1,435.40	1,435.40	24.20	6.66	17.54	89.13	1,800.49
Exergy, MW	-1888.43	-1814.79	-1811.86	-1737.08	-98.17	-97.02	-1.17	-5.89	-118.76

Exergy = H-T_oS, where T_o =298 K, H, S: enthalpy and entropy of the stream

Table G.2
Material and energy balance for the oxy-fuel MoCC, see Figures G.1 and G.2 for flowsheets (continue).

Stream	26	27	28	29	30	31	32	33	34
Temperature, °C	101	99	275	43	-32	-42	-43	-43	40
Pressure, bar	1.04	1.02	3.92	14.79	14.69	10.00	9.79	9.79	9.59
Vapor Fraction	0.00	1.00	1.00	1.00	0.62	0.66	0.00	1.00	1.00
Mole Flow, kmol/hr	1,783	18	18	966	966	966	883	777	777
Volume Flow, m^3/hr	45	536	204	1,623	723	1,114	37	1,367	2,035
Mole Flow, kmol/hr									
N_2	-	-	-	20.44	20.44	20.44	0.35	23.88	23.88
Ar	-	0.00	0.00	48.95	48.95	48.95	1.27	65.41	65.41
O_2	-	-	-	1.37	1.37	1.37	0.04	1.76	1.76
CO	-	-	-	-	-	-	-	-	-
CO_2	-	0.59	0.59	895.00	895.00	895.00	881.22	685.81	685.81
CH_4	-	-	-	-	-	-	-	-	-
C_2H_6	-	-	-	-	-	-	-	-	-
C_3H_8	-	-	-	-	-	-	-	-	-
NC4	-	-	-	-	-	-	-	-	-
CH_3OH	-	-	-	-	-	-	-	-	-
H_2O	1,783.34	17.15	17.15	-	-	-	-	-	-
Exergy, MW	-117.27	-1.16	-1.13	-96.58	-96.17	-96.31	-94.07	-74.15	-74.23

Exergy = H-T_oS, where T_o =298 K, H, S: enthalpy and entropy of the stream

Stream	35	36	37	38	39	40	41	42	43
Temperature, °C	43	1	-43	-25	40	43	-53	-63	-53
Pressure, bar	33.79	33.69	10.00	33.48	33.28	99.79	99.69	33.69	99.48
Vapor Fraction	1.00	1.00	0.20	1.00	1.00	1.00	0.09	0.37	1.00
Mole Flow, kmol/hr	777	777	694	895	895	895	895	812	83
Volume Flow, m^3/hr	532	410	262	450	651	193	46	155	11
Mole Flow, kmol/hr									
N_2	23.88	23.88	3.80	84.24	84.24	84.24	84.24	64.15	20.09
Ar	65.41	65.41	17.73	291.61	291.61	291.61	291.61	243.94	47.68
O_2	1.76	1.76	0.43	6.71	6.71	6.71	6.71	5.38	1.33
CO	-	-	-	-	-	-	-	-	-
CO_2	685.81	685.81	672.03	512.39	512.39	512.38	512.38	498.60	13.78
CH_4	-	-	-	-	-	-	-	-	-
C_2H_6	-	-	-	-	-	-	-	-	-
C_3H_8	-	-	-	-	-	-	-	-	-
NC4	-	-	-	-	-	-	-	-	-
CH_3OH	-	-	-	-	-	-	-	-	-
H_2O	-	-	-	-	-	-	-	-	-
Exergy, MW	-73.61	-73.61	-71.90	-54.60	-54.65	-54.07	-53.59	-52.48	-1.30

Exergy = H-T_oS, where T_o =298 K, H, S: enthalpy and entropy of the stream

Table G.3
Material and energy balance for the oxy-fuel MoCC, see Figures G.1 and G.2 for flowsheets (continue).

Stream	44	45	46	47	48	49	51	52	53
Temperature, °C	40	-55	40	-55	40	-55	25	43	43
Pressure, bar	99.28	28.16	27.95	7.58	7.37	1.94	1.01	4.80	4.30
Vapor Fraction	1.00	1.00	1.00	1.00	1.00	1.00	1.00	1.00	1.00
Mole Flow, kmol/hr	83	83	83	83	83	83	6,671	6,671	6,546
Volume Flow, m^3/hr	21	48	76	193	291	769	163,173	36,584	40,095
Mole Flow, kmol/hr									
N_2	20.09	20.09	20.09	20.09	20.09	20.09	5,113.40	5,113.40	5,113.40
Ar	47.68	47.68	47.68	47.68	47.68	47.67	60.87	60.87	60.87
O_2	1.33	1.33	1.33	1.33	1.33	1.33	1,371.30	1,371.30	1,371.30
CO	-	-	-	-	-	-	-	-	-
CO_2	13.78	13.78	13.78	13.78	13.78	13.78	19.51	19.51	-
CH_4	-	-	-	-	-	-	-	-	-
C_2H_6	-	-	-	-	-	-	-	-	-
C_3H_8	-	-	-	-	-	-	-	-	-
NC4	-	-	-	-	-	-	-	-	-
CH_3OH	-	-	-	-	-	-	-	-	-
H_2O	-	-	-	-	-	-	105.70	105.70	-
Exergy, MW	-1.31	-1.37	-1.38	-1.45	-1.46	-1.52	-11.86	-4.69	4.00

Exergy = H-T_oS, where T_o =298 K, H, S: enthalpy and entropy of the stream

Stream	54	55	56	57	58	59	60	61	62
Temperature, °C	-177	-178	-192	-195	-195	42	-181	-182	-195
Pressure, bar	4.19	4.19	1.12	1.12	0.92	0.71	4.19	3.99	1.12
Vapor Fraction	0.95	0.00	0.14	1.00	1.00	1.00	0.00	0.00	0.14
Mole Flow, kmol/hr	6,546	4,487	4,487	5,132	5,132	5,132	2,059	2,059	2,059
Volume Flow, m^3/hr	10,694	160	3,820	28,557	35,368	189,596	80	79	1,639
Mole Flow, kmol/hr									
N_2	5,113.35	3,058.25	3,058.25	5,092.96	5,092.96	5,092.96	2,055.10	2,055.10	2,055.10
Ar	60.87	60.09	60.09	11.92	11.92	11.92	0.79	0.79	0.79
O_2	1,371.28	1,368.67	1,368.67	27.43	27.43	27.43	2.61	2.61	2.61
CO	-	-	-	-	-	-	-	-	-
CO_2	-	-	-	-	-	-	-	-	-
CH_4	-	-	-	-	-	-	-	-	-
C_2H_6	-	-	-	-	-	-	-	-	-
C_3H_8	-	-	-	-	-	-	-	-	-
NC4	-	-	-	-	-	-	-	-	-
CH_3OH	-	-	-	-	-	-	-	-	-
H_2O	-	-	-	-	-	-	-	-	-
Exergy, MW	12.38	21.72	21.38	7.72	6.96	-1.42	10.97	11.02	10.88

Exergy = H-T_oS, where T_o =298 K, H, S: enthalpy and entropy of the stream

Table G.4
Material and energy balance for the oxy-fuel MoCC, see Figures G.1 and G.2 for flowsheets (continue).

Stream	63	64	65	66	A	B	C	D	E
Temperature, °C	-150	-184	-182	42	43	221	39	44	313
Pressure, bar	4.09	1.12	1.12	0.92	5.80	4.94	0.07	25.00	24.14
Vapor Fraction	1.00	1.00	1.00	1.00	0.00	1.00	0.86	0.00	1.00
Mole Flow, kmol/hr	0	0	1,413	1,413	1,060	1,060	4,542	2,000	2,000
Volume Flow, m^3/hr	0	0	9,208	40,405	19	8,619	1,436,150	49	3,808
Mole Flow, kmol/hr									
N_2	0.05	0.05	20.44	20.44	-	-	-	-	-
Ar	0.00	0.00	48.95	48.95	-	-	-	-	-
O_2	0.01	0.01	1,343.87	1,343.87	-	-	-	-	-
CO	-	-	-	-	-	-	-	-	-
CO_2	-	-	-	-	-	-	-	-	-
CH_4	-	-	-	-	-	-	-	-	-
C_2H_6	-	-	-	-	-	-	-	-	-
C_3H_8	-	-	-	-	-	-	-	-	-
NC4	-	-	-	-	-	-	-	-	-
CH_3OH	-	-	-	-	-	-	-	-	-
H_2O	-	-	-	-	1,059.61	1,059.61	4,541.52	2,000.00	2,000.00
Exergy, MW	0.00	0.00	1.57	-0.31	-69.85	-65.78	-297.31	-131.81	-121.42

Exergy = H-T_oS, where T_o =298 K, H, S: enthalpy and entropy of the stream

Stream	F	G	H	I	J	a	b	c	d
Temperature, °C	151	46	363	270	363	-53	-58	40	43
Pressure, bar	4.94	120.00	119.14	52.92	52.71	29.48	14.19	14.09	20.28
Vapor Fraction	0.99	0.00	1.00	1.00	1.00	0.00	0.07	1.00	0.00
Mole Flow, kmol/hr	3,482	1,482	1,482	1,482	1,482	4,391	4,391	4,391	173
Volume Flow, m^3/hr	23,438	27	504	1,003	1,346	300	614	7,132	19
Mole Flow, kmol/hr									
N_2	-	-	-	-	-	-	-	-	-
Ar	-	-	-	-	-	-	-	-	-
O_2	-	-	-	-	-	-	-	-	-
CO	-	-	-	-	-	-	-	-	-
CO_2	-	-	-	-	-	-	-	-	-
CH_4	-	-	-	-	-	857.05	857.05	857.05	4.12
C_2H_6	-	-	-	-	-	2,475.48	2,475.48	2,475.48	46.32
C_3H_8	-	-	-	-	-	38.35	38.35	38.35	1.88
NC4	-	-	-	-	-	1,019.72	1,019.72	1,019.72	120.82
CH_3OH	-	-	-	-	-	-	-	-	-
H_2O	3,481.91	1,481.91	1,481.91	1,481.91	1,481.91	-	-	-	-
Exergy, MW	-217.23	-97.60	-88.90	-90.09	-89.03	-32.20	-32.40	-35.39	-0.95

Exergy = H-T_oS, where T_o =298 K, H, S: enthalpy and entropy of the stream

Table G.5
Material and energy balance for the oxy-fuel MoCC, see Figures G.1 and G.2 for flowsheets (continue).

Stream	e	f	g				
				Feed LHV, MW	168.2	158.67	
Temperature, °C	45	43	44	**Compressors power, MW**		**Turbines power, MW**	
Pressure, bar	29.59	29.59	29.59	**K-1**	12.21	**T-1**	-153.86
Vapor Fraction	0.00	0.84	0.80	**K-2**	7.17	**T-2**	-1.05
Mole Flow, kmol/hr	173	4,217	4,391	**K-3**	81.12	**T-3**	-5.87
Volume Flow, m^3/hr	19	2,551	2,558	**K-4**	0.03	**T-4**	-11.83
Mole Flow, kmol/hr				**K-5**	2.98	**T-5**	-0.05
N_2	-	-	-	**K-6**	0.97	**T-6**	-0.05
Ar	-	-	-	**K-7**	0.99	**T-7**	-0.05
O_2	-	-	-	**K-8**	2.55	**Pumps, kW**	
CO	-	-	-			**P-1**	216.35
CO_2	-	-	-	**Net Power, MW**		**P-2**	9.44
CH_4	4.12	852.93	857.05	-64.51			
C_2H_6	46.32	2,429.16	2,475.48	**Power generation efficiency, %**			
C_3H_8	1.88	36.47	38.35	38.35			
NC4	120.82	898.90	1,019.72				
CH_3OH	-	-	-				
H_2O	-	-	-				
Exergy, MW	-0.95	-32.90	-33.86				

Exergy = $H-T_oS$, where T_o =298 K, H, S: enthalpy and entropy of the stream

APPENDIX H. MATERIAL AND ENERGY BALANCES FOR THE LM-C

H.1 Storage mode

Table H.1
Material and energy balance for the storage mode of the LM-C, see Figure 4.4 for flowsheet.

Stream	1	2	3	4	5	6	7	8	9
Temperature, ° C	118	118	160	172	250	461	818	950	950
Pressure, bar	1.9	12.0	11.6	11.3	10.6	10.4	10.2	10.0	9.7
Vapor Fraction	0.00	0.00	0.00	0.00	1.00	1.00	1.00	1.00	1.00
Mole Flow, kmol/hr	14,646	14,646	14,646	14,646	16,316	16,316	16,316	16,316	16,316
Volume Flow, m^3/hr	279.2	279.1	290.8	294.6	64,931.2	94,932.8	145,050.8	166,114.6	171,412.5
Mole Flow, kmol/h									
H_2	0.00	0.00	0.00	0.00	1,650.06	1,650.06	1,650.06	1,650.06	15,964.56
N_2	0.00	0.00	0.00	0.00	0.00	0.00	0.00	0.00	0.00
O_2	0.00	0.00	0.00	0.00	0.00	0.00	0.00	0.00	0.00
CO	0.00	0.00	0.00	0.00	0.00	0.00	0.00	0.00	0.00
CO_2	0.00	0.00	0.00	0.00	0.00	0.00	0.00	0.00	0.00
CH_4	0.00	0.00	0.00	0.00	0.00	0.00	0.00	0.00	0.00
C_2H_6	0.00	0.00	0.00	0.00	0.00	0.00	0.00	0.00	0.00
C_3H_8	0.00	0.00	0.00	0.00	0.00	0.00	0.00	0.00	0.00
H_2O	14,646.15	14,646.15	14,646.15	14,646.15	14,665.75	14,665.75	14,665.75	14,665.75	351.25
Exergy, MW	-962.0	-961.9	-958.2	-957.0	-901.5	-883.3	-840.7	-822.2	71.0

Exergy = H-T_oS, where T_o =298 K, H, S: enthalpy and entropy of the stream

Stream	10	11	12	13	14	15	16	17	18
Temperature, ° C	489	124	43	43	43	180	339	400	188
Pressure, bar	9.5	8.1	8.0	7.8	7.8	22.1	21.9	20.9	20.8
Vapor Fraction	1.00	1.00	0.99	1.00	1.00	1.00	1.00	1.00	0.96
Mole Flow, kmol/hr	16,316	16,316	16,316	16,154	14,485	14,485	18,284	11,391	11,391
Volume Flow, m^3/hr	109,200.8	66,658.8	53,291.8	54,663.3	49,013.4	24,916.2	42,456.8	30,191.8	19,094.2
Mole Flow, kmol/h									
H_2	15,964.56	15,964.56	15,964.56	15,964.55	14,314.49	14,314.49	14,476.72	692.34	692.34
N_2	0.00	0.00	0.00	0.00	0.00	0.00	0.00	0.00	0.00
O_2	0.00	0.00	0.00	0.00	0.00	0.00	0.00	0.00	0.00
CO	0.00	0.00	0.00	0.00	0.00	0.00	3.23	1.16	1.16
CO_2	0.00	0.00	0.00	0.00	0.00	0.00	3,577.41	132.87	132.87
CH_4	0.00	0.00	0.00	0.00	0.00	0.00	55.76	3,502.38	3,502.38
C_2H_6	0.00	0.00	0.00	0.00	0.00	0.00	0.00	0.00	0.00
C_3H_8	0.00	0.00	0.00	0.00	0.00	0.00	0.00	0.00	0.00
H_2O	351.25	351.25	351.25	189.66	170.06	170.06	170.91	7,062.07	7,062.07
Exergy, MW	26.3	1.7	-0.3	10.1	9.0	23.0	-356.1	-480.2	-495.2

Exergy = H-T_oS, where T_o =298 K, H, S: enthalpy and entropy of the stream

Table H.2
Material and energy balance for the storage mode of the LM-C, see Figure 4.4 for flowsheet (continue).

Stream	19	20	21	22	23	24	25	26	27
Temperature, ° C	184	178	176	43	43	300	350	188	169
Pressure, bar	20.7	20.6	20.5	20.4	20.2	20.0	19.0	18.8	18.6
Vapor Fraction	0.85	0.75	0.71	0.38	1.00	1.00	1.00	1.00	1.00
Mole Flow, kmol/hr	11,391	11,391	11,391	11,391	4,349	4,349	4,086	4,086	4,086
Volume Flow, m^3/hr	16,907.0	14,999.0	14,289.1	5,698.4	5,584.7	10,441.9	11,218.3	8,340.0	8,070.1
Mole Flow, kmol/h									
H_2	692.34	692.34	692.34	692.34	692.04	692.04	166.29	166.29	166.29
N_2	0.00	0.00	0.00	0.00	0.00	0.00	0.00	0.00	0.00
O_2	0.00	0.00	0.00	0.00	0.00	0.00	0.00	0.00	0.00
CO	1.16	1.16	1.16	1.16	1.16	1.16	0.03	0.03	0.03
CO_2	132.87	132.87	132.87	132.87	131.43	131.43	0.85	0.85	0.85
CH_4	3,502.38	3,502.38	3,502.38	3,502.38	3,500.35	3,500.35	3,632.07	3,632.07	3,632.07
C_2H_6	0.00	0.00	0.00	0.00	0.00	0.00	0.00	0.00	0.00
C_3H_8	0.00	0.00	0.00	0.00	0.00	0.00	0.00	0.00	0.00
H_2O	7,062.07	7,062.07	7,062.07	7,062.07	24.47	24.47	286.78	286.78	286.78
Exergy, MW	-499.9	-504.0	-505.7	-522.3	-58.4	-54.2	-57.2	-61.2	-61.5

Exergy = H-T_oS, where T_o =298 K, H, S: enthalpy and entropy of the stream

Stream	28	29	30	31	32	33	34	35	36
Temperature, ° C	43	43	139	43	43	43	43	-170	-170
Pressure, bar	18.5	18.3	49.6	49.4	49.2	48.8	48.8	48.6	2.1
Vapor Fraction	0.94	1.00	1.00	1.00	1.00	1.00	1.00	0.01	0.00
Mole Flow, kmol/hr	4,086	3,823	3,823	4,410	4,400	4,384	3,798	3,798	3,582
Volume Flow, m^3/hr	5,346.1	5,399.7	2,643.6	2,242.9	2,251.9	2,266.8	1,964.0	145.0	132.7
Mole Flow, kmol/h									
H_2	166.29	166.28	166.28	191.92	191.92	191.92	166.28	166.28	3.79
N_2	0.00	0.00	0.00	0.00	0.00	0.00	0.00	0.00	0.00
O_2	0.00	0.00	0.00	0.00	0.00	0.00	0.00	0.00	0.00
CO	0.03	0.03	0.03	0.03	0.03	0.03	0.03	0.03	0.02
CO_2	0.85	0.85	0.85	0.85	0.85	0.00	0.00	0.00	0.00
CH_4	3,632.07	3,632.00	3,632.00	4,191.89	4,191.89	4,191.89	3,631.98	3,631.98	3,577.79
C_2H_6	0.00	0.00	0.00	0.00	0.00	0.00	0.00	0.00	0.00
C_3H_8	0.00	0.00	0.00	0.00	0.00	0.00	0.00	0.00	0.00
H_2O	286.78	23.41	23.41	25.47	15.24	0.00	0.00	0.00	0.00
Exergy, MW	-63.2	-45.9	-42.6	-50.0	-49.3	-48.2	-41.8	-32.3	-32.5

Exergy = H-T_oS, where T_o =298 K, H, S: enthalpy and entropy of the stream

H.2 Delivery mode

Table H.3
Material and energy balance for the storage mode of the LM-C, see Figure 4.4 for flowsheet (continue).

Stream	37	38	39	40	41	42	43	44	45
Temperature, ° C	-172	-170	-11	-11	153	43	44	43	44
Pressure, bar	2.1	2.1	1.9	1.9	22.1	49.2	18.5	18.3	1.9
Vapor Fraction	0.00	1.00	1.00	1.00	1.00	0.00	0.00	0.00	0.00
Mole Flow, kmol/hr	3,582	217	217	215	219	10	10	285	285
Volume Flow, m^3/hr	131.6	883.8	2,519.0	2,493.8	354.6	0.2	0.3	6.9	8.1
Mole Flow, kmol/h									
H_2	3.79	162.50	162.50	160.87	161.19	0.00	0.00	0.00	0.00
N_2	0.00	0.00	0.00	0.00	0.00	0.00	0.00	0.00	0.00
O_2	0.00	0.00	0.00	0.00	0.00	0.00	0.00	0.00	0.00
CO	0.02	0.01	0.01	0.01	0.01	0.00	0.00	0.00	0.00
CO_2	0.00	0.00	0.00	0.00	1.43	0.00	0.00	0.00	0.00
CH_4	3,577.79	54.19	54.19	53.65	55.76	0.01	0.01	0.09	0.09
C_2H_6	0.00	0.00	0.00	0.00	0.00	0.00	0.00	0.00	0.00
C_3H_8	0.00	0.00	0.00	0.00	0.00	0.00	0.00	0.00	0.00
H_2O	0.00	0.00	0.00	0.00	0.85	10.22	10.22	284.82	284.82
Exergy, MW	-32.3	-0.5	-0.8	-0.7	-0.6	-0.7	-0.7	-18.8	-18.8

Exergy = H-T_oS, where T_o =298 K, H, S: enthalpy and entropy of the stream

Stream	46	47	48	49	50	51	52	53	54
Temperature, ° C	119	154	43	44	43	43	43	90	160
Pressure, bar	1.9	4.3	20.2	1.9	7.8	1.9	7.8	11.5	11.3
Vapor Fraction	0	1.00	0.00	0.00	0.00	0.00	1.00	1.00	1.00
Mole Flow, kmol/hr	7483	5	7,041	7,041	162	162	1,670	1,670	1,670
Volume Flow, m^3/hr	194.0	39.1	170.9	210.4	3.9	4.1	5,649.9	4,416.9	5,367.3
Mole Flow, kmol/h									
H_2	0	0.32	0.30	0.30	0.02	0.02	1,650.06	1,650.06	1,650.06
N_2	0	0.00	0.00	0.00	0.00	0.00	0.00	0.00	0.00
O_2	0	0.00	0.00	0.00	0.00	0.00	0.00	0.00	0.00
CO	0	0.00	0.00	0.00	0.00	0.00	0.00	0.00	0.00
CO_2	0	1.43	1.43	1.43	0.00	0.00	0.00	0.00	0.00
CH_4	0	2.12	2.03	2.03	0.00	0.00	0.00	0.00	0.00
C_2H_6	0	0.00	0.00	0.00	0.00	0.00	0.00	0.00	0.00
C_3H_8	0	0.00	0.00	0.00	0.00	0.00	0.00	0.00	0.00
H_2O	7,483.15	0.85	7,037.60	7,037.60	161.58	161.58	19.60	19.60	19.60
Exergy, MW	-491.4	-0.2	-464.0	-464.1	-10.7	-10.7	1.0	1.6	1.8

Exergy = H-T_oS, where T_o =298 K, H, S: enthalpy and entropy of the stream

Table H.4
Material and energy balance for the storage mode of the LM-C, see Figure 4.4 for flowsheet (continue).

Stream	55	56	57	58	59	60	61	62	63
Temperature, ° C	25	152	922	950	949	489	282	72	-46
Pressure, bar	1.0	10.4	10.2	10.0	9.7	9.5	9.3	1.1	9.8
Vapor Fraction	1.00	1.00	1.00	1.00	1.00	1.00	1.00	1.00	0.00
Mole Flow, kmol/hr	12,164	12,164	12,164	12,164	19,321	19,321	19,321	19,321	3,580
Volume Flow, m^3/hr	297,531.6	41,418.9	118,511.3	123,839.6	202,740.2	129,351.1	96,409.8	504,134.5	149.5
Mole Flow, kmol/h									
H_2	0.00	0.00	0.00	0.00	0.00	0.00	0.00	0.00	1.04
N_2	9,432.09	9,432.09	9,432.09	9,432.09	9,432.09	9,432.09	9,432.09	9,432.09	0.00
O_2	2,503.13	2,503.13	2,503.13	2,503.13	9,660.39	9,660.39	9,660.39	9,660.39	0.00
CO	0.00	0.00	0.00	0.00	0.00	0.00	0.00	0.00	3.22
CO_2	36.28	36.28	36.28	36.28	36.28	36.28	36.28	36.28	3,575.98
CH_4	0.00	0.00	0.00	0.00	0.00	0.00	0.00	0.00	0.00
C_2H_6	0.00	0.00	0.00	0.00	0.00	0.00	0.00	0.00	0.00
C_3H_8	0.00	0.00	0.00	0.00	0.00	0.00	0.00	0.00	0.00
H_2O	192.01	192.01	192.01	192.01	192.01	192.01	192.01	192.01	0.00
Exergy, MW	-21.3	0.4	50.7	53.0	92.7	34.4	15.0	-24.6	-381.7

Exergy = H-T_oS, where T_o =298 K, H, S: enthalpy and entropy of the stream

Stream	64	65	66	67	A	B	C	D	E
Temperature, ° C	-45	-11	43	151	32	230	39	32	320
Pressure, bar	22.7	22.6	22.3	22.1	5.7	5.0	0.07	30.4	29.8
Vapor Fraction	0.00	1.00	1.00	1.00	0.00	1.00	0.90	0.00	1.00
Mole Flow, kmol/hr	3,580	3,580	3,580	3,580	548	548	3,005	672	672
Volume Flow, m^3/hr	149.1	2,788.8	3,801.8	5,552.4	9.9	4,485.8	995,582.8	12.2	1,035.9
Mole Flow, kmol/h									
H_2	1.04	1.04	1.04	1.04	0.00	0.00	0.00	0.00	0.00
N_2	0.00	0.00	0.00	0.00	0.00	0.00	0.00	0.00	0.00
O_2	0.00	0.00	0.00	0.00	0.00	0.00	0.00	0.00	0.00
CO	3.22	3.22	3.22	3.22	0.00	0.00	0.00	0.00	0.00
CO_2	3,575.98	3,575.98	3,575.98	3,575.98	0.00	0.00	0.00	0.00	0.00
CH_4	0.00	0.00	0.00	0.00	0.00	0.00	0.00	0.00	0.00
C_2H_6	0.00	0.00	0.00	0.00	0.00	0.00	0.00	0.00	0.00
C_3H_8	0.00	0.00	0.00	0.00	0.00	0.00	0.00	0.00	0.00
H_2O	0.00	0.00	0.00	0.00	547.91	547.91	3,004.56	672.07	672.07
Exergy, MW	-381.7	-384.7	-384.8	-383.9	-36.1	-34.0	-196.6	-44.3	-40.7

Exergy = H-T_oS, where T_o =298 K, H, S: enthalpy and entropy of the stream

Table H.5
Material and energy balance for the storage mode of the LM-C, see Figure 4.4 for flowsheet (continue).

Stream	F	G	H	I	J	b	c	d	e
Temperature, ° C	218	32	460	278	460	43	-173	-176	-11
Pressure, bar	5.0	120.0	119.3	30.0	29.8	26.3	26.2	1.2	1.1
Vapor Fraction	1.00	0.00	1.00	1.00	1.00	1.00	0.00	0.07	1.00
Mole Flow, kmol/hr	2,457	1,785	1,785	1,785	1,785	4,846	4,846	4,846	4,846
Volume Flow, m^3/hr	19,582.4	32.1	797.9	2,466.8	3,545.3	4,243.6	229.6	2,361.1	95,637.4
Mole Flow, kmol/h									
H_2	0.00	0.00	0.00	0.00	0.00	0.00	0.00	0.00	0.00
N_2	0.00	0.00	0.00	0.00	0.00	441.66	441.66	441.66	441.66
O_2	0.00	0.00	0.00	0.00	0.00	0.00	0.00	0.00	0.00
CO	0.00	0.00	0.00	0.00	0.00	0.00	0.00	0.00	0.00
CO_2	0.00	0.00	0.00	0.00	0.00	0.00	0.00	0.00	0.00
CH_4	0.00	0.00	0.00	0.00	0.00	1,486.45	1,486.45	1,486.45	1,486.45
C_2H_6	0.00	0.00	0.00	0.00	0.00	1,864.84	1,864.84	1,864.84	1,864.84
C_3H_8	0.00	0.00	0.00	0.00	0.00	1,052.73	1,052.73	1,052.73	1,052.73
H_2O	2,456.65	1,784.58	1,784.58	1,784.58	1,784.58	0.00	0.00	0.00	0.00
Exergy, MW	-152.5	-117.6	-105.6	-108.5	-106.5	-38.8	-24.6	-25.2	-48.8

Exergy = H-T_oS, where T_o =298 K, H, S: enthalpy and entropy of the stream

Stream	f	R1	R2	R3	R4	R5	R6	Make up	Purge
Temperature, ° C	116	43	310	290	188	43	47	32	-11
Pressure, bar	26.5	48.8	48.5	48.0	47.8	47.6	49.6	1.9	1.9
Vapor Fraction	1.00	1.00	1.00	1.00	1.00	0.98	1.00	0.00	1.00
Mole Flow, kmol/hr	4,845.7	586	586	599	599	599	588	1.5	2.2
Volume Flow, m^3/hr	5,592.8	302.8	596.0	593.8	484.1	311.1	303.1	0.0	25.2
Mole Flow, kmol/h									
H_2	0.00	25.63	25.63	25.63	25.63	25.63	25.63	0.00	1.63
N_2	441.66	0.00	0.00	0.00	0.00	0.00	0.00	0.00	0.00
O_2	0.00	0.00	0.00	0.00	0.00	0.00	0.00	0.00	0.00
CO	0.00	0.00	0.00	0.00	0.00	0.00	0.00	0.00	0.00
CO_2	0.00	0.00	0.00	0.00	0.00	0.00	0.00	0.00	0.00
CH_4	1,486.45	559.91	559.91	559.91	559.91	559.91	559.90	0.00	0.54
C_2H_6	1,864.84	0.00	0.00	0.00	0.00	0.00	0.00	0.00	0.00
C_3H_8	1,052.73	0.00	0.00	0.00	0.00	0.00	0.00	0.00	0.00
H_2O	0.00	0.00	0.00	13.28	13.28	13.28	2.06	1.54	0.00
Exergy, MW	-37.9	-6.4	-5.8	-6.7	-7.1	-7.3	-6.6	-0.1	0.0

Exergy = H-T_oS, where T_o =298 K, H, S: enthalpy and entropy of the stream

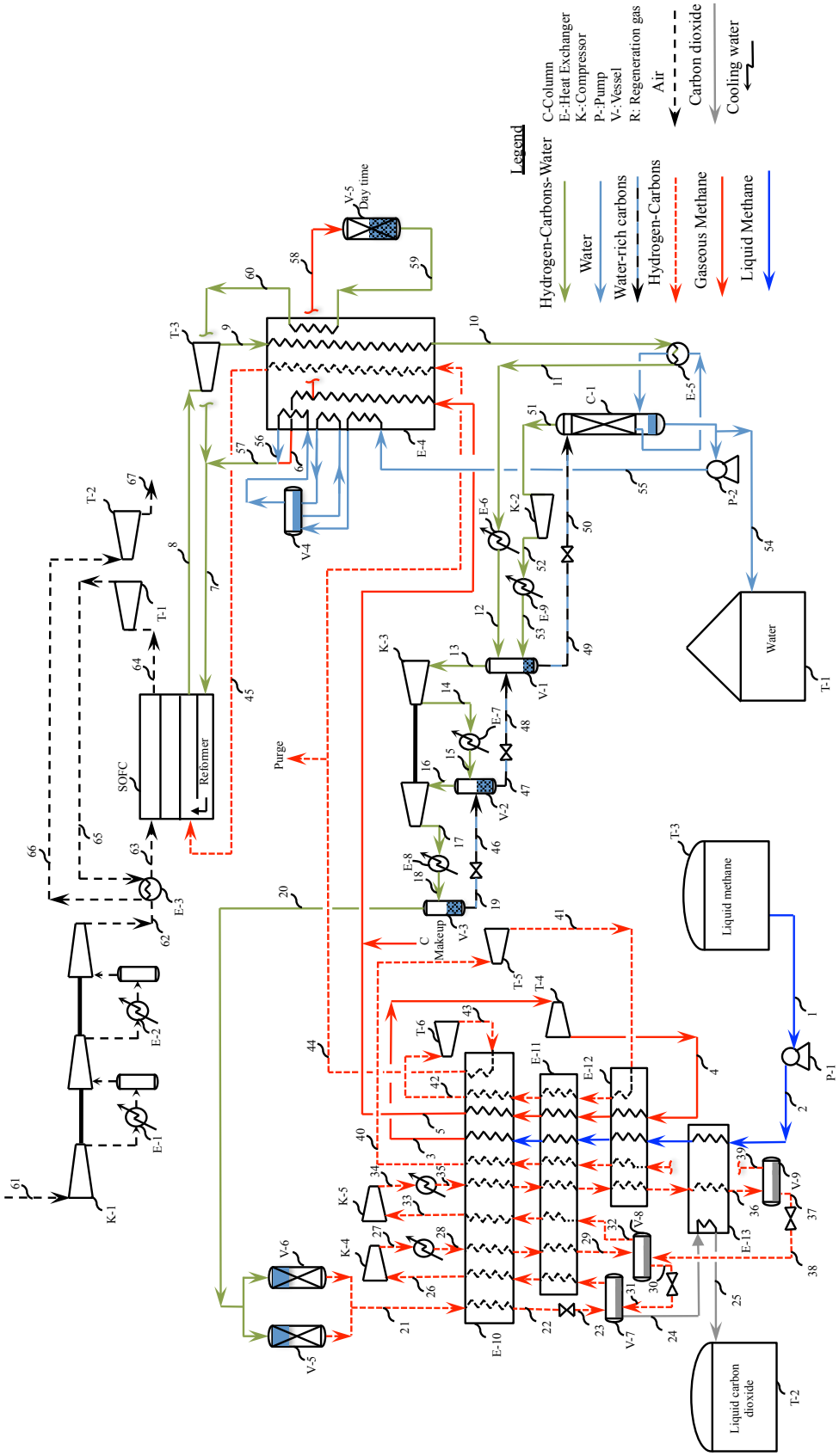

Figure H.1. Detailed flowsheet for the LM-C delivery mode.

Table H.6
Material and energy balance for the delivery mode of the LM-C, see Figure H.1 for flowsheet.

Stream	1	2	3	4	5	6	7	8	9
Temperature, ° C	-172	-165	22	-100	41	680	683	950	946
Pressure, bar	2.1	100.0	99.8	10.9	10.7	10.0	10.0	9.7	9.5
Vapor Fraction	0.00	0.00	1.00	1.00	1.00	1.00	1.00	1.00	1.00
Mole Flow, kmol/hr	895	895	895	895	895	743	3,137	5,049	5,049
Volume Flow, m^3/hr	32.9	32.9	194.4	1,039.2	2,152.8	5,912.2	24,873.1	52,964.8	53,969.9
Mole Flow, kmol/h									
H_2	0.95	0.95	0.95	0.95	0.95	0.79	0.95	81.37	81.37
N_2	-	-	-	-	-	-	-	-	-
O_2	-	-	-	-	-	-	-	-	-
CO	0.01	0.01	0.01	0.01	0.01	0.00	0.01	29.31	29.31
CO_2	-	-	-	-	-	-	0.21	907.17	907.17
CH_4	894.45	894.45	894.45	894.45	894.45	742.59	895.00	-	-
C_2H_6	-	-	-	-	-	-	-	-	-
C_3H_8	-	-	-	-	-	-	-	-	-
H_2O	-	-	-	-	-	-	2,241.32	4,031.20	4,031.20
Exergy, MW	-8.1	-8.1	-9.9	-10.9	-11.2	-5.7	-139.8	-321.7	-322.0

Exergy = H-T_oS, where T_o =298 K, H, S: enthalpy and entropy of the stream

Stream	10	11	12	13	14	15	16	17	18
Temperature, ° C	167	164	43	43	114	43	43	112	43
Pressure, bar	9.3	9.2	9.1	8.9	19.4	19.3	19.1	42.2	42.1
Vapor Fraction	0.96	0.84	0.20	1.00	1.00	1.00	1.00	1.00	1.00
Mole Flow, kmol/hr	5,049	5,049	5,049	1,029	1,029	1,029	1,024	1,024	1,024
Volume Flow, m^3/hr	18,362.9	16,215.7	2,957.3	2,960.8	1,647.5	1,306.1	1,320.4	714.6	541.9
Mole Flow, kmol/h									
H_2	81.37	81.37	81.37	81.37	81.37	81.37	81.37	81.37	81.37
N_2	-	-	-	-	-	-	-	-	-
O_2	-	-	-	-	-	-	-	-	-
CO	29.31	29.31	29.31	29.31	29.31	29.31	29.31	29.31	29.31
CO_2	907.17	907.17	907.17	907.22	907.22	907.22	907.20	907.20	907.20
CH_4	-	-	-	-	-	-	-	-	-
C_2H_6	-	-	-	-	-	-	-	-	-
C_3H_8	-	-	-	-	-	-	-	-	-
H_2O	4,031.20	4,031.20	4,031.20	11.12	11.12	11.12	5.68	5.68	5.68
Exergy, MW	-350.8	-352.9	-365.1	-100.1	-99.4	-99.6	-99.2	-98.6	-98.7

Exergy = H-T_oS, where T_o =298 K, H, S: enthalpy and entropy of the stream

Table H.7
Material and energy balance for the delivery mode of the LM-C, see Figure H.1 for flowsheet (continue).

Stream	19	20	21	22	23	24	25	26	28
Temperature, ° C	43	43	43	-7	-44	-44	-46	41	43
Pressure, bar	41.9	41.9	41.5	41.4	10.0	9.8	9.8	9.6	20.8
Vapor Fraction	0.00	1.00	1.00	0.45	0.64	0.00	0.00	1.00	1.00
Mole Flow, kmol/hr	2	1,021	1,018	1,018	1,018	895	895	742	742
Volume Flow, m^3/hr	0.1	544.7	549.8	223.7	1,155.6	37.7	37.4	1,960.2	878.1
Mole Flow, kmol/h									
H_2	-	81.37	81.37	81.37	81.37	0.26	0.26	82.01	82.01
N_2	-	-	-	-	-	-	-	-	-
O_2	-	-	-	-	-	-	-	-	-
CO	-	29.31	29.31	29.31	29.31	0.81	0.81	31.09	31.09
CO_2	0.03	907.17	907.17	907.17	907.17	893.99	893.99	628.69	628.69
CH_4	-	-	-	-	-	-	-	-	-
C_2H_6	-	-	-	-	-	-	-	-	-
C_3H_8	-	-	-	-	-	-	-	-	-
H_2O	2.36	3.32	-	-	-	-	-	-	-
Exergy, MW	-0.2	-98.6	-98.4	-98.2	-98.7	-95.5	-95.4	-69.2	-68.9

Exergy = H-T_oS, where T_o =298 K, H, S: enthalpy and entropy of the stream

Stream	29	30	31	32	33	35	36	37	38
Temperature, ° C	-27	-30	-40	-30	41	43	-55	-55	-55
Pressure, bar	20.7	20.5	10.0	20.5	20.3	79.8	79.7	79.5	20.7
Vapor Fraction	0.71	0.00	0.11	1.00	1.00	1.00	0.27	0.00	0.04
Mole Flow, kmol/hr	742	619	619	455	455	455	455	333	333
Volume Flow, m^3/hr	460.3	27.8	137.4	395.5	558.7	122.9	41.9	13.3	23.3
Mole Flow, kmol/h									
H_2	82.01	0.90	0.90	84.82	84.82	84.82	84.82	3.71	3.71
N_2	-	-	-	-	-	-	-	-	-
O_2	-	-	-	-	-	-	-	-	-
CO	31.09	2.59	2.59	40.79	40.79	40.79	40.79	12.29	12.29
CO_2	628.69	615.51	615.51	329.88	329.88	329.88	329.88	316.70	316.70
CH_4	-	-	-	-	-	-	-	-	-
C_2H_6	-	-	-	-	-	-	-	-	-
C_3H_8	-	-	-	-	-	-	-	-	-
H_2O	-	-	-	-	-	-	-	-	-
Exergy, MW	-68.7	-65.9	-65.9	-37.0	-37.0	-36.7	-36.4	-34.2	-34.2

Exergy = H-T_oS, where T_o =298 K, H, S: enthalpy and entropy of the stream

Table H.8
Material and energy balance for the delivery mode of the LM-C, see Figure H.1 for flowsheet (continue).

Stream	39	40	41	42	43	44	45	46	47
Temperature, ° C	-55	41	-55	41	13	41	800	43	43
Pressure, bar	79.5	79.3	15.8	15.6	10.4	10.2	10.0	19.3	19.1
Vapor Fraction	1.00	1.00	1.00	1.00	1.00	1.00	1.00	0.01	0.00
Mole Flow, kmol/hr	123	123	123	123	123	123	122	2	8
Volume Flow, m^3/hr	28.7	42.6	141.4	207.9	282.1	316.3	1,087.5	0.1	0.2
Mole Flow, kmol/h									
H_2	81.11	81.11	81.11	81.11	81.11	81.11	80.30	-	-
N_2	-	-	-	-	-	-	-	-	-
O_2	-	-	-	-	-	-	-	-	-
CO	28.51	28.51	28.51	28.51	28.51	28.51	28.22	-	-
CO_2	13.18	13.18	13.18	13.18	13.18	13.18	13.05	0.03	0.05
CH_4	-	-	-	-	-	-	-	-	-
C_2H_6	-	-	-	-	-	-	-	-	-
C_3H_8	-	-	-	-	-	-	-	-	-
H_2O	-	-	-	-	-	-	-	2.36	7.80
Exergy, MW	-2.2	-2.2	-2.4	-2.4	-2.4	-2.4	-2.0	-0.2	-0.5

Exergy = H-T_oS, where T_o =298 K, H, S: enthalpy and entropy of the stream

Stream	48	49	50	51	52	53	54	55	56
Temperature, ° C	43	43	43	48	204	43	118	118	688
Pressure, bar	9.1	8.9	1.9	1.9	9.2	9.1	1.9	10.7	10.0
Vapor Fraction	0.00	0.00	0.00	1.00	1.00	0.95	0.00	0.00	1.00
Mole Flow, kmol/hr	8	4,040	4,040	12	12	12	1,790	2,238	2,238
Volume Flow, m^3/hr	0.2	98.2	221.1	166.1	50.5	31.2	34.1	42.7	17,825.5
Mole Flow, kmol/h									
H_2	-	0.04	0.04	0.04	0.04	0.04	-	-	-
N_2	-	-	-	-	-	-	-	-	-
O_2	-	-	-	-	-	-	-	-	-
CO	-	0.01	0.01	0.01	0.01	0.01	-	-	-
CO_2	0.05	11.00	11.00	11.00	11.00	11.00	-	-	-
CH_4	-	-	-	-	-	-	-	-	-
C_2H_6	-	-	-	-	-	-	-	-	-
C_3H_8	-	-	-	-	-	-	-	-	-
H_2O	7.80	4,028.60	4,028.60	0.72	0.72	0.72	1,790.37	2,237.51	2,237.51
Exergy, MW	-0.5	-266.7	-266.8	-1.2	-1.2	-1.2	-117.6	-146.9	-131.4

Exergy = H-T_oS, where T_o =298 K, H, S: enthalpy and entropy of the stream

Table H.9
Material and energy balance for the delivery mode of the LM-C, see Figure H.1 for flowsheet (continue).

Stream	58	59	60	61	62	63	64	65	66
Temperature, ° C	310	290	680	25	146	680	922	797	173
Pressure, bar	10.5	10.2	10.0	1.0	10.2	10.0	9.7	5.7	5.5
Vapor Fraction	1.00	1.00	1.00	1.00	1.00	1.00	1.00	1.00	1.00
Mole Flow, kmol/hr	153	157	157	12,310	12,310	12,310	10,521	10,521	10,521
Volume Flow, m^3/hr	705.8	720.8	1,244.6	301,125.6	42,161.7	97,833.4	107,909.4	164,347.5	71,275.4
Mole Flow, kmol/h									
H_2	0.16	0.16	0.16	-	-	-	-	-	-
N_2	-	-	-	9,546.03	9,546.03	9,546.03	9,546.03	9,546.03	9,546.03
O_2	-	-	-	2,533.37	2,533.37	2,533.37	743.97	743.97	743.97
CO	0.00	0.00	0.00	-	-	-	-	-	-
CO_2	-	0.21	0.21	36.72	36.72	36.72	36.72	36.72	36.72
CH_4	152.41	152.41	152.41	-	-	-	-	-	-
C_2H_6	-	-	-	-	-	-	-	-	-
C_3H_8	-	-	-	-	-	-	-	-	-
H_2O	-	3.81	3.81	194.33	194.33	194.33	194.33	194.33	194.33
Exergy, MW	-1.7	-2.0	-1.4	-21.5	0.0	31.2	42.5	29.6	-4.4

Exergy = H-T_oS, where T_o =298 K, H, S: enthalpy and entropy of the stream

Stream	67	make up	Purge
Temperature, ° C	35	43	41
Pressure, bar	1.1	10.7	10.2
Vapor Fraction	1.00	1.00	1.00
Mole Flow, kmol/hr	10,521	1	1
Volume Flow, m^3/hr	244,712.8	1.3	3.2
Mole Flow, kmol/h			
H_2	-	-	0.81
N_2	9,546.03	-	-
O_2	743.97	-	-
CO	-	-	0.29
CO_2	36.72	-	0.13
CH_4	-	0.55	-
C_2H_6	-	-	-
C_3H_8	-	-	-
H_2O	194.33	-	-
Exergy, MW	-18.4	0.0	0.0

Exergy = H-T_oS, where T_o =298 K, H, S: enthalpy and entropy of the stream

APPENDIX I. FLOWSHEET, MATERIAL BALANCE, AND ENERGY BALANCE FOR THE LM-C WITHOUT USING THE LIQUID METHANE AND LIQUID CARBON DIOXIDE REFRIGERATION SYNERGY

I.1 Storage mode

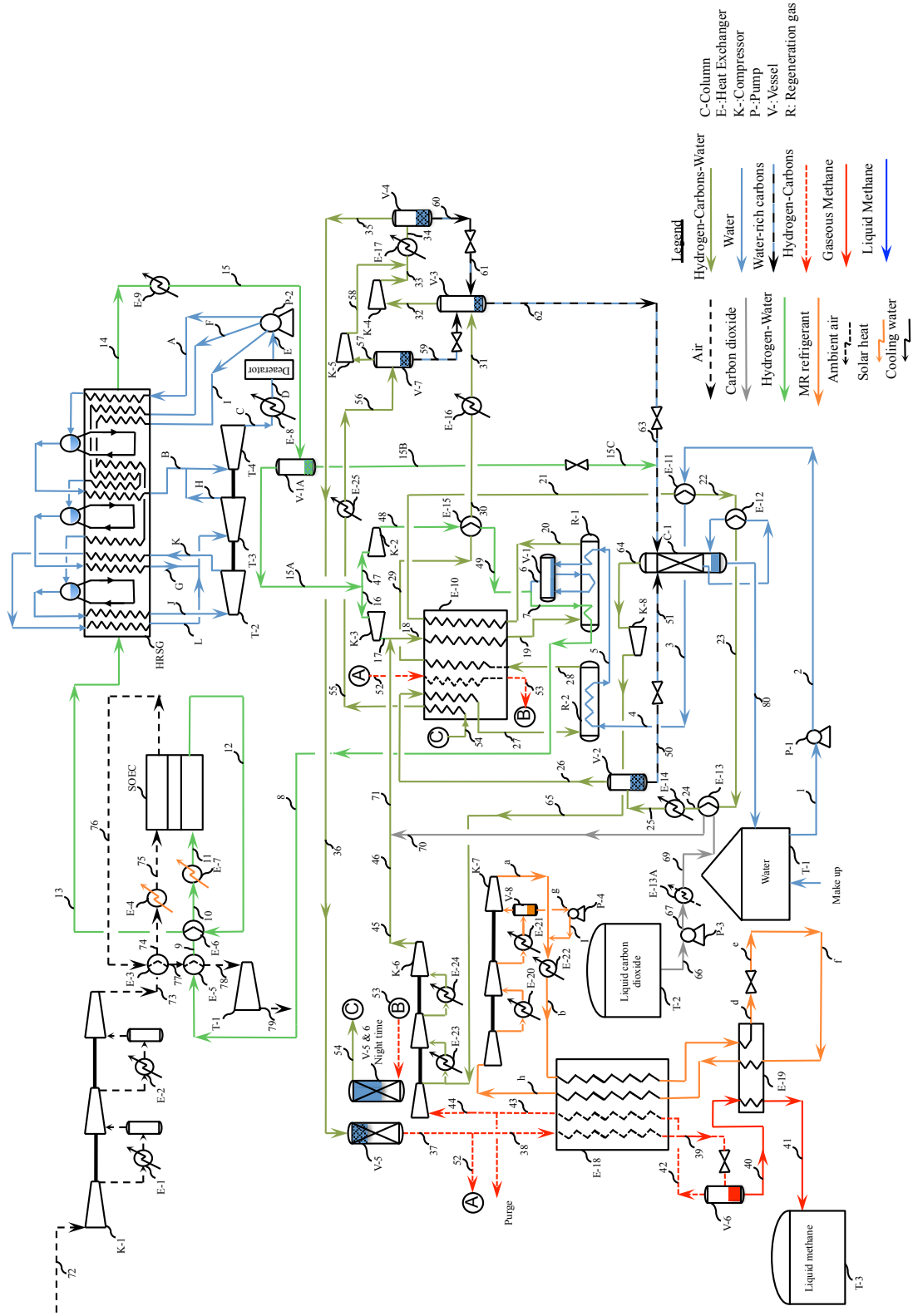

Figure I.1. Detailed flowsheet for the storage mode of LM-C without using the liquid methane and liquid carbon dioxide refrigeration synergy.

Table I.1
Material and energy balance for the storage mode of the LM-C without using the liquid methane and liquid carbon dioxide refrigeration synergy, see Figure I.1 for flowsheet.

Stream	1	2	3 and 4	5	8	9	10	11	12
Temperature, ° C	118	118	160	172	250	461	818	950	950
Pressure, bar	1.9	12.0	11.6	11.3	10.6	10.4	10.2	10.0	9.7
Vapor Fraction	0.00	0.00	0.00	0.00	1.00	1.00	1.00	1.00	1.00
Mole Flow, kmol/hr	14,647	14,647	14,647	14,647	16,317	16,317	16,317	16,317	16,317
Volume Flow, m^3/hr	279.3	279.2	290.8	294.6	64,919.3	94,939.6	145,061.2	166,126.5	171,424.9
Mole Flow, kmol/h									
H_2	-	-	-	-	1,650.18	1,650.18	1,650.18	1,650.18	15,965.71
N_2	-	-	-	-	-	-	-	-	-
O_2	-	-	-	-	-	-	-	-	-
CO	-	-	-	-	-	-	-	-	-
CO_2	-	-	-	-	-	-	-	-	-
CH_4	-	-	-	-	-	-	-	-	-
C_2H_6	-	-	-	-	-	-	-	-	-
C_3H_8	-	-	-	-	-	-	-	-	-
nC_4H_{10}	-	-	-	-	-	-	-	-	-
nC_5H_{12}	-	-	-	-	-	-	-	-	-
H_2O	14,647.20	14,647.20	14,647.20	14,647.20	14,666.81	14,666.81	14,666.81	14,666.81	351.27
Exergy, MW	-962.0	-961.9	-958.3	-957.1	-901.5	-883.4	-840.8	-822.2	71.0

Exergy = H-T_oS, where T_o =298 K, H, S: enthalpy and entropy of the stream

Stream	13	14	15	15A	15B	15C	16	17	18
Temperature, ° C	489	124	43	43	43	43	43	180	171
Pressure, bar	9.5	8.1	8.0	7.8	7.8	1.9	7.8	22.1	22.1
Vapor Fraction	1.00	1.00	0.99	1.00	0.00	0.00	1.00	1.00	1.00
Mole Flow, kmol/hr	16,317	16,317	16,317	16,155	162	162	14,486	14,486	18,285
Volume Flow, m^3/hr	109,208.7	66,722.8	53,295.6	54,667.2	3.9	4.1	49,016.9	24,917.9	30,495.4
Mole Flow, kmol/h									
H_2	15,965.71	15,965.71	15,965.71	15,965.70	0.02	0.02	14,315.52	14,315.52	14,477.51
N_2	-	-	-	-	-	-	-	-	-
O_2	-	-	-	-	-	-	-	-	-
CO	-	-	-	-	-	-	-	-	2.41
CO_2	-	-	-	-	-	-	-	-	3,578.22
CH_4	-	-	-	-	-	-	-	-	55.77
C_2H_6	-	-	-	-	-	-	-	-	-
C_3H_8	-	-	-	-	-	-	-	-	-
nC_4H_{10}	-	-	-	-	-	-	-	-	-
nC_5H_{12}	-	-	-	-	-	-	-	-	-
H_2O	351.27	351.27	351.27	189.68	161.59	161.59	170.07	170.07	170.93
Exergy, MW	26.3	1.7	-0.3	10.1	-10.7	-10.7	9.0	23.0	-368.1

Exergy = H-T_oS, where T_o =298 K, H, S: enthalpy and entropy of the stream

I.2 Delivery mode

Table I.2
Material and energy balance for the storage mode of the LM-C without using the liquid methane and liquid carbon dioxide refrigeration synergy, see Figure I.1 for flowsheet (continue).

Stream	19	20	21	22	23	24	25	26	27
Temperature, ° C	339	400	188	184	178	175	43	43	300
Pressure, bar	21.9	20.9	20.8	20.7	20.6	20.5	20.4	20.2	20.0
Vapor Fraction	1.00	1.00	0.96	0.85	0.75	0.71	0.38	1.00	1.00
Mole Flow, kmol/hr	18,285	11,392	11,392	11,392	11,392	11,392	11,392	4,349	4,349
Volume Flow, m^3/hr	42,459.2	30,194.0	19,095.4	16,908.2	15,000.2	14,158.8	5,698.5	5,584.7	10,442.0
Mole Flow, kmol/h									
H_2	14,477.51	692.39	692.39	692.39	692.39	692.39	692.39	692.09	692.09
N_2	-	-	-	-	-	-	-	-	-
O_2	-	-	-	-	-	-	-	-	-
CO	2.41	1.16	1.16	1.16	1.16	1.16	1.16	1.16	1.16
CO_2	3,578.22	132.87	132.87	132.87	132.87	132.87	132.87	131.44	131.44
CH_4	55.77	3,502.36	3,502.36	3,502.36	3,502.36	3,502.36	3,502.36	3,500.33	3,500.33
C_2H_6	-	-	-	-	-	-	-	-	-
C_3H_8	-	-	-	-	-	-	-	-	-
nC_4H_{10}	-	-	-	-	-	-	-	-	-
nC_5H_{12}	-	-	-	-	-	-	-	-	-
H_2O	170.93	7,062.86	7,062.86	7,062.86	7,062.86	7,062.86	7,062.86	24.47	24.47
Exergy, MW	-356.2	-480.2	-495.3	-500.0	-504.1	-506.0	-522.4	-58.4	-54.2

Exergy = H-T_oS, where T_o =298 K, H, S: enthalpy and entropy of the stream

Stream	28	29	30	31	32	33	34	35 and 36	37
Temperature, ° C	350	188	169	43	43	139	43	43	43
Pressure, bar	19.0	18.8	18.6	18.5	18.3	49.6	49.4	49.2	48.8
Vapor Fraction	1.00	1.00	1.00	0.94	1.00	1.00	1.00	1.00	1.00
Mole Flow, kmol/hr	4,086	4,086	4,086	4,086	3,823	3,823	4,410	4,400	4,384
Volume Flow, m^3/hr	11,218.4	8,340.1	8,070.1	5,346.1	5,399.8	2,643.6	2,242.9	2,251.9	2,266.8
Mole Flow, kmol/h									
H_2	166.30	166.30	166.30	166.30	166.30	166.30	191.94	191.94	191.94
N_2	-	-	-	-	-	-	-	-	-
O_2	-	-	-	-	-	-	-	-	-
CO	0.03	0.03	0.03	0.03	0.03	0.03	0.03	0.03	0.03
CO_2	0.85	0.85	0.85	0.85	0.85	0.85	0.85	0.85	-
CH_4	3,632.06	3,632.06	3,632.06	3,632.06	3,631.99	3,631.99	4,191.89	4,191.88	4,191.88
C_2H_6	-	-	-	-	-	-	-	-	-
C_3H_8	-	-	-	-	-	-	-	-	-
nC_4H_{10}	-	-	-	-	-	-	-	-	-
nC_5H_{12}	-	-	-	-	-	-	-	-	-
H_2O	286.80	286.80	286.80	286.80	23.41	23.41	25.47	15.24	-
Exergy, MW	-57.2	-61.2	-61.5	-63.2	-45.9	-42.6	-50.0	-49.3	-48.2

Exergy = H-T_oS, where T_o =298 K, H, S: enthalpy and entropy of the stream

Table I.3
Material and energy balance for the storage mode of the LM-C without using the liquid methane and liquid carbon dioxide refrigeration synergy, see Figure I.1 for flowsheet (continue).

Stream	38	39	40	41	42	43	44	45 and 46	47
Temperature, ° C	43	-170	-170	-172	-170	39	39	153	43
Pressure, bar	48.8	48.6	2.1	2.1	2.1	1.9	1.9	22.1	7.8
Vapor Fraction	1.00	0.01	0.00	0.00	1.00	1.00	1.00	1.00	1.00
Mole Flow, kmol/hr	3,798	3,798	3,582	3,582	217	217	215	219	1,670
Volume Flow, m^3/hr	1,964.0	145.0	132.7	131.6	883.9	2,991.5	2,961.6	354.6	5,650.3
Mole Flow, kmol/h									
H_2	166.30	166.30	3.79	3.79	162.51	162.51	160.89	161.21	1,650.18
N_2	-	-	-	-	-	-	-	-	-
O_2	-	-	-	-	-	-	-	-	-
CO	0.03	0.03	0.02	0.02	0.01	0.01	0.01	0.01	-
CO_2	-	-	-	-	-	-	-	1.43	-
CH_4	3,631.98	3,631.98	3,577.78	3,577.78	54.20	54.20	53.65	55.77	-
C_2H_6	-	-	-	-	-	-	-	-	-
C_3H_8	-	-	-	-	-	-	-	-	-
nC_4H_{10}	-	-	-	-	-	-	-	-	-
nC_5H_{12}	-	-	-	-	-	-	-	-	-
H_2O	-	-	-	-	-	-	-	0.85	19.61
Exergy, MW	-41.8	-32.3	-32.5	-32.3	-0.5	-0.8	-0.8	-0.6	1.0

Exergy = H-T_oS, where T_o =298 K, H, S: enthalpy and entropy of the stream

Stream	48	49	50	51	52	53	54	55	56
Temperature, ° C	90	161	43	44	43	310	290	188	43
Pressure, bar	11.5	11.3	20.2	1.9	48.8	48.5	48.0	47.8	47.6
Vapor Fraction	1.00	1.00	0.00	0.00	1.00	1.00	1.00	1.00	0.98
Mole Flow, kmol/hr	1,670	1,670	7,042	7,042	586	586	599	599	599
Volume Flow, m^3/hr	4,417.2	5,367.7	170.9	210.4	302.8	596.0	593.6	483.9	311.1
Mole Flow, kmol/h									
H_2	1,650.18	1,650.18	0.30	0.30	25.64	25.64	25.64	25.64	25.64
N_2	-	-	-	-	-	-	-	-	-
O_2	-	-	-	-	-	-	-	-	-
CO	-	-	-	-	0.00	0.00	0.00	0.00	0.00
CO_2	-	-	1.43	1.43	-	-	-	-	-
CH_4	-	-	2.03	2.03	559.90	559.90	559.90	559.90	559.90
C_2H_6	-	-	-	-	-	-	-	-	-
C_3H_8	-	-	-	-	-	-	-	-	-
nC_4H_{10}	-	-	-	-	-	-	-	-	-
nC_5H_{12}	-	-	-	-	-	-	-	-	-
H_2O	19.61	19.61	7,038.39	7,038.39	-	-	13.05	13.05	13.05
Exergy, MW	1.6	1.8	-464.1	-464.1	-6.4	-5.8	-6.7	-7.1	-7.3

Exergy = H-T_oS, where T_o =298 K, H, S: enthalpy and entropy of the stream

Table I.4
Material and energy balance for the storage mode of the LM-C without using the liquid methane and liquid carbon dioxide refrigeration synergy, see Figure I.1 for flowsheet (continue).

Stream	57	58	59	60	61	62	63	64	65
Temperature, ° C	43	47	43	43	44	43	44	72	154
Pressure, bar	47.4	49.6	47.4	49.2	18.5	18.3	1.9	1.9	4.3
Vapor Fraction	1.00	1.00	0.00	0.00	0.00	0.00	0.00	1.00	1.00
Mole Flow, kmol/hr	588	588	11	10	10	285	285	5	5
Volume Flow, m^3/hr	312.2	303.1	0.3	0.2	0.3	6.9	8.1	71.6	39.1
Mole Flow, kmol/h									
H_2	25.64	25.64	-	-	-	0.00	0.00	0.32	0.32
N_2	-	-	-	-	-	-	-	-	-
O_2	-	-	-	-	-	-	-	-	-
CO	0.00	0.00	-	-	-	-	-	-	-
CO_2	-	-	-	-	-	-	-	1.43	1.43
CH_4	559.90	559.90	0.01	0.01	0.01	0.09	0.09	2.12	2.12
C_2H_6	-	-	-	-	-	-	-	-	-
C_3H_8	-	-	-	-	-	-	-	-	-
nC_4H_{10}	-	-	-	-	-	-	-	-	-
nC_5H_{12}	-	-	-	-	-	-	-	-	-
H_2O	2.06	2.06	10.99	10.22	10.22	284.60	284.60	0.85	0.85
Exergy, MW	-6.6	-6.6	-0.7	-0.7	-0.7	-18.8	-18.8	-0.2	-0.2

Exergy = H-T_oS, where T_o =298 K, H, S: enthalpy and entropy of the stream

Stream	66	67	69	70	72	73	74	75	76
Temperature, ° C	-46	-45	24	151	25	152	922	950	949
Pressure, bar	9.8	22.7	22.3	22.1	1.0	10.4	10.2	10.0	9.7
Vapor Fraction	0.00	0.00	1.00	1.00	1.00	1.00	1.00	1.00	1.00
Mole Flow, kmol/hr	3,580	3,580	3,580	3,580	12,164	12,164	12,164	12,164	19,322
Volume Flow, m^3/hr	149.5	149.1	3,478.1	5,551.9	297,553.1	41,421.9	118,519.9	123,848.5	202,754.8
Mole Flow, kmol/h									
H_2	0.79	0.79	0.79	0.79	-	-	-	-	-
N_2	-	-	-	-	9,432.77	9,432.77	9,432.77	9,432.77	9,432.77
O_2	-	-	-	-	2,503.31	2,503.31	2,503.31	2,503.31	9,661.08
CO	2.40	2.40	2.40	2.40	-	-	-	-	-
CO_2	3,576.79	3,576.79	3,576.79	3,576.79	36.28	36.28	36.28	36.28	36.28
CH_4	-	-	-	-	-	-	-	-	-
C_2H_6	-	-	-	-	-	-	-	-	-
C_3H_8	-	-	-	-	-	-	-	-	-
nC_4H_{10}	-	-	-	-	-	-	-	-	-
nC_5H_{12}	-	-	-	-	-	-	-	-	-
H_2O	-	-	-	-	192.03	192.03	192.03	192.03	192.03
Exergy, MW	-381.8	-381.7	-384.9	-384.0	-21.3	0.4	50.7	53.0	92.7

Exergy = H-T_oS, where T_o =298 K, H, S: enthalpy and entropy of the stream

Table I.5
Material and energy balance for the storage mode of the LM-C without using the liquid methane and liquid carbon dioxide refrigeration synergy, see Figure I.1 for flowsheet (continue).

Stream	77	78	79	80	A	B	C	D	F
Temperature, ° C	489	282	72	119	32	230	39	39	32
Pressure, bar	9.5	9.3	1.1	1.9	5.7	5.0	0.1	0.1	30.4
Vapor Fraction	1.00	1.00	1.00	0.00	0.00	1.00	0.90	0.00	0.00
Mole Flow, kmol/hr	19,322	19,322	19,322	7,484	546	546	3,001	3,001	670
Volume Flow, m^3/hr	129,360.4	96,396.4	504,057.0	194.0	9.9	4,470.5	994,557.0	54.5	12.1
Mole Flow, kmol/h									
H_2	-	-	-	-	-	-	-	-	-
N_2	9,432.77	9,432.77	9,432.77	-	-	-	-	-	-
O_2	9,661.08	9,661.08	9,661.08	-	-	-	-	-	-
CO	-	-	-	-	-	-	-	-	-
CO_2	36.28	36.28	36.28	-	-	-	-	-	-
CH_4	-	-	-	-	-	-	-	-	-
C_2H_6	-	-	-	-	-	-	-	-	-
C_3H_8	-	-	-	-	-	-	-	-	-
nC_4H_{10}	-	-	-	-	-	-	-	-	-
nC_5H_{12}	-	-	-	-	-	-	-	-	-
H_2O	192.03	192.03	192.03	7,483.74	546.04	546.04	3,001.33	3,001.33	669.79
Exergy, MW	34.4	14.9	-24.6	-491.5	-36.0	-33.9	-196.4	-197.9	-44.2

Exergy = H-T_oS, where T_o =298 K, H, S: enthalpy and entropy of the stream

Stream	G	H	I	J	K	L	a	b	d
Temperature, ° C	320	218	32	460	278	460	101	43	-175
Pressure, bar	29.8	5.0	120.0	119.3	30.0	29.8	22.5	22.3	22.0
Vapor Fraction	1.00	1.00	0.00	1.00	1.00	1.00	1.00	0.70	0.00
Mole Flow, kmol/hr	670	2,455	1,786	1,786	1,786	1,786	7,151	8,211	8,211
Volume Flow, m^3/hr	1,032.4	19,575.3	32.2	798.3	2,468.1	3,547.2	9,080.2	6,380.5	486.9
Mole Flow, kmol/h									
H_2	-	-	-	-	-	-	-	-	-
N_2	-	-	-	-	-	-	729.26	730.74	730.74
O_2	-	-	-	-	-	-	-	-	-
CO	-	-	-	-	-	-	-	-	-
CO_2	-	-	-	-	-	-	-	-	-
CH_4	-	-	-	-	-	-	1,782.27	1,792.74	1,792.74
C_2H_6	-	-	-	-	-	-	3,290.26	3,385.73	3,385.73
C_3H_8	-	-	-	-	-	-	2.54	2.77	2.77
nC_4H_{10}	-	-	-	-	-	-	241.87	308.77	308.77
nC_5H_{12}	-	-	-	-	-	-	1,105.08	1,990.22	1,990.22
H_2O	669.79	2,455.30	1,785.51	1,785.51	1,785.51	1,785.51	-	-	-
Exergy, MW	-40.6	-152.4	-117.6	-105.7	-108.6	-106.6	-50.1	-55.6	-29.0

Exergy = H-T_oS, where T_o =298 K, H, S: enthalpy and entropy of the stream

Table I.6
Material and energy balance for the storage mode of the LM-C without using the liquid methane and liquid carbon dioxide refrigeration synergy, see Figure I.1 for flowsheet (continue).

Stream	e and f	h	i	g	Make up	Purge			
							Compressors power, MW		**E-4 Heat, MW**
Temperature, ° C	-177	39	44	43	32	39	**K-1**	32.3	3.3
Pressure, bar	1.4	1.3	22.5	8.3	1.9	1.9	**K-2**	0.6	**E-7 Heat, MW**
Vapor Fraction	0.07	1.00	0.00	0.00	0.00	1.00	**K-3**	16.0	25.3
Mole Flow, kmol/hr	8,211	8,211	1,060	1,060	2	2	**K-4**	3.8	
Volume Flow, m^3/hr	3,457.0	159,582.0	131.8	132.5	0.0	29.9	**K-5**	0.0	
Mole Flow, kmol/h							**K-6**	0.6	
H_2	-	-	-	-	-	1.63	**K-7**	21.3	
N_2	730.74	730.74	1.48	1.48	-	-	**K-8**	0.004	
O_2	-	-	-	-	-	-	**Turbines power, MW**		
CO	-	-	-	-	-	-	**T-1**	33.0	
CO_2	-	-	-	-	-	-	**T-2**	15.6	
CH_4	1,792.74	1,792.74	10.47	10.47	-	0.54	**SOEC**		
C_2H_6	3,385.73	3,385.73	95.47	95.47	-	-	**Power, MW**	**Heat, MW**	
C_3H_8	2.77	2.77	0.23	0.23	-	-	991.9	-0.3	
nC_4H_{10}	308.77	308.77	66.90	66.90	-	-	**Pumps power, kW**		
nC_5H_{12}	1,990.22	1,990.22	885.14	885.14	-	-	**P-1**	99.6	
H_2O	-	-	-	-	1.52	-	**P-2**	283.7	
Exergy, MW	-30.1	-68.8	-3.7	-3.7	-0.1	0.0	**P-3**	72.6	
							P-4	71.6	

Exergy = H-T_oS, where T_o =298 K, H, S: enthalpy and entropy of the stream

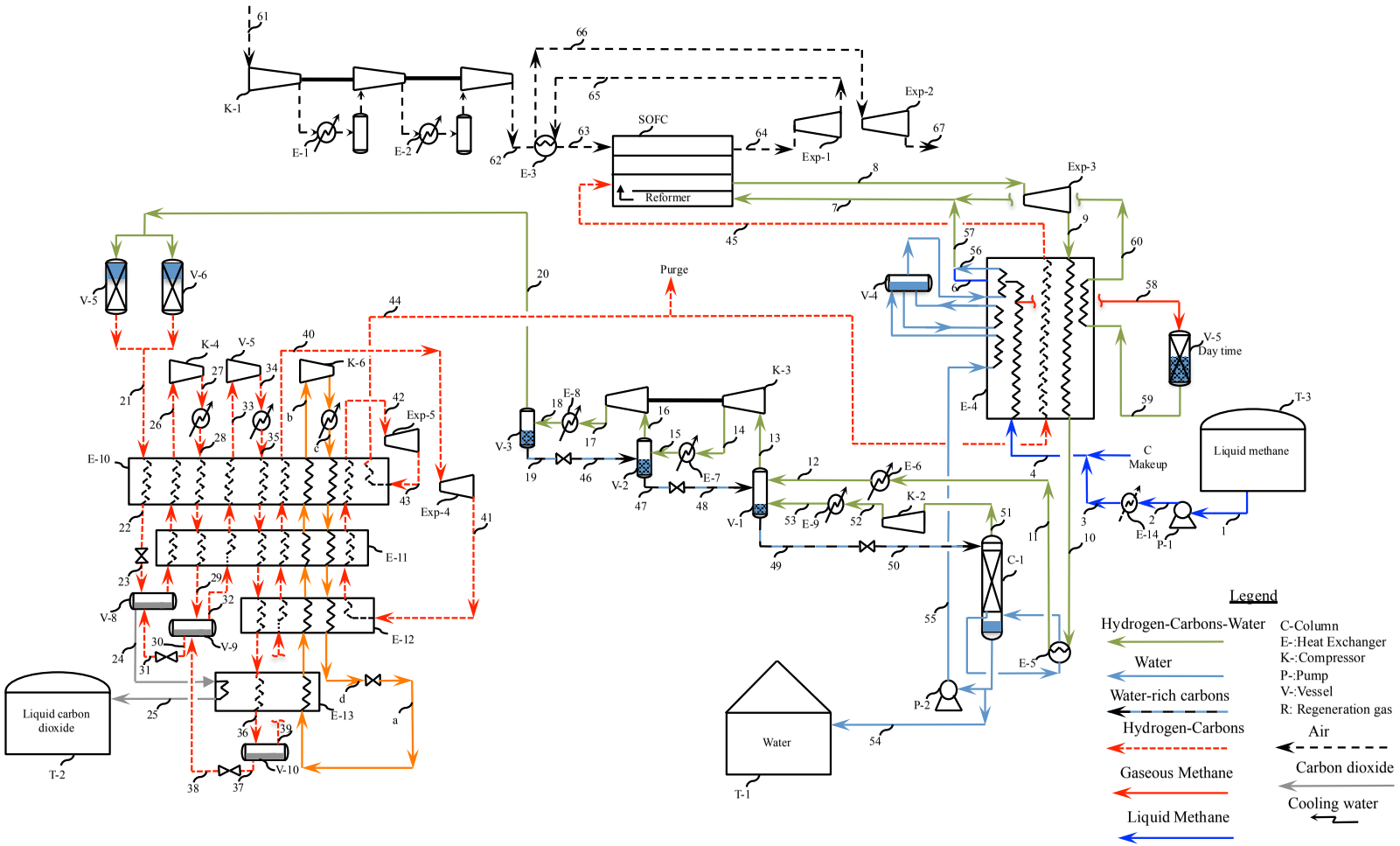

Figure I.2. Detailed flowsheet for the delivery mode of LM-C without using the liquid methane and liquid carbon dioxide refrigeration synergy.

Table I.7

Material and energy balance for the delivery mode of the LM-C without using the liquid methane and liquid carbon dioxide refrigeration synergy, see Figure I.2 for flowsheet.

Stream	1	2	3	4	6	7	8	9	10
Temperature, ° C	-172	-171	24	24	680	683	950	946	167
Pressure, bar	2.1	11.1	10.7	10.7	10.0	10.0	9.7	9.5	9.3
Vapor Fraction	0.00	0.00	1.00	1.00	1.00	1.00	1.00	1.00	0.96
Mole Flow, kmol/hr	895	895	895	896	743	3,137	5,049	5,049	5,049
Volume Flow, m^3/hr	32.9	32.9	2,028.6	2,029.9	5,912.2	24,873.1	52,968.1	53,973.2	18,307.8
Mole Flow, kmol/h									
H_2	0.95	0.95	0.95	0.95	0.79	0.95	81.37	81.37	81.37
N_2	-	-	-	-	-	-	-	-	-
O_2	-	-	-	-	-	-	-	-	-
CO	0.01	0.01	0.01	0.01	0.00	0.01	29.32	29.32	29.32
CO_2	-	-	-	-	-	0.21	907.42	907.42	907.42
CH_4	894.45	894.45	894.45	895.00	742.59	895.00	-	-	-
C_2H_6	-	-	-	-	-	-	-	-	-
C_3H_8	-	-	-	-	-	-	-	-	-
nC_4H_{10}	-	-	-	-	-	-	-	-	-
nC_5H_{12}	-	-	-	-	-	-	-	-	-
H_2O	-	-	-	-	-	2,241.32	4,031.26	4,031.26	4,031.26
Exergy, MW	-8.1	-8.1	-11.2	-11.2	-5.7	-139.8	-321.7	-322.0	-350.9

Exergy = H-T_oS, where T_o =298 K, H, S: enthalpy and entropy of the stream

Stream	11	12	13	14	15	16	17	18	19
Temperature, ° C	164	43	43	116	43	43	114	43	43
Pressure, bar	9.2	9.1	8.9	19.7	19.6	19.4	43.8	43.7	43.5
Vapor Fraction	0.84	0.20	1.00	1.00	1.00	1.00	1.00	1.00	0.00
Mole Flow, kmol/hr	5,049	5,049	1,029	1,029	1,029	1,024	1,024	1,024	2
Volume Flow, m^3/hr	16,160.3	2,958.0	2,961.6	1,625.4	1,281.7	1,295.5	690.4	519.1	0.1
Mole Flow, kmol/h									
H_2	81.37	81.37	81.37	81.37	81.37	81.37	81.37	81.37	-
N_2	-	-	-	-	-	-	-	-	-
O_2	-	-	-	-	-	-	-	-	-
CO	29.32	29.32	29.32	29.32	29.32	29.32	29.32	29.32	-
CO_2	907.42	907.42	907.46	907.46	907.46	907.45	907.45	907.45	0.03
CH_4	-	-	-	-	-	-	-	-	-
C_2H_6	-	-	-	-	-	-	-	-	-
C_3H_8	-	-	-	-	-	-	-	-	-
nC_4H_{10}	-	-	-	-	-	-	-	-	-
nC_5H_{12}	-	-	-	-	-	-	-	-	-
H_2O	4,031.26	4,031.26	11.12	11.12	11.12	5.60	5.60	5.60	2.33
Exergy, MW	-353.0	-365.1	-100.1	-99.4	-99.6	-99.2	-98.6	-98.7	-0.2

Exergy = H-T_oS, where T_o =298 K, H, S: enthalpy and entropy of the stream

Table I.8
Material and energy balance for the delivery mode of the LM-C without using the liquid methane and liquid carbon dioxide refrigeration synergy, see Figure I.2 for flowsheet (continue).

Stream	20	21	22	23	24	25	26	28	29
Temperature, ° C	43	43	-1	-42	-43	-46	41	43	-12
Pressure, bar	43.5	43.0	42.9	10.0	9.8	9.8	9.6	20.8	20.7
Vapor Fraction	1.00	1.00	0.75	0.85	0.00	0.00	1.00	1.00	1.00
Mole Flow, kmol/hr	1,021	1,018	1,018	1,018	895	895	1,015	1,015	1,015
Volume Flow, m^3/hr	521.6	526.4	313.9	1,509.3	37.9	37.4	2,671.9	1,193.6	918.6
Mole Flow, kmol/h									
H_2	81.37	81.37	81.37	81.37	0.20	0.20	82.02	82.02	82.02
N_2	-	-	-	-	-	-	-	-	-
O_2	-	-	-	-	-	-	-	-	-
CO	29.32	29.32	29.32	29.32	0.60	0.60	31.55	31.55	31.55
CO_2	907.42	907.42	907.42	907.42	894.20	894.20	901.21	901.21	901.21
CH_4	-	-	-	-	-	-	-	-	-
C_2H_6	-	-	-	-	-	-	-	-	-
C_3H_8	-	-	-	-	-	-	-	-	-
nC_4H_{10}	-	-	-	-	-	-	-	-	-
nC_5H_{12}	-	-	-	-	-	-	-	-	-
H_2O	3.26	-	-	-	-	-	-	-	-
Exergy, MW	-98.6	-98.4	-98.3	-99.0	-95.5	-95.4	-98.7	-98.2	-98.2

Exergy = H-T_oS, where T_o =298 K, H, S: enthalpy and entropy of the stream

Stream	30	31	32	33	35	36	37	38	39
Temperature, ° C	-26	-39	-26	41	43	-55	-55	-55	-55
Pressure, bar	20.5	10.0	20.5	20.3	79.8	79.7	79.5	20.7	79.5
Vapor Fraction	0.00	0.14	1.00	1.00	1.00	0.15	0.00	0.04	1.00
Mole Flow, kmol/hr	892	892	843	843	843	843	720	720	123
Volume Flow, m^3/hr	41.0	250.7	722.0	1,017.2	207.6	57.5	28.8	50.5	28.8
Mole Flow, kmol/h									
H_2	0.85	0.85	89.18	89.18	89.18	89.18	8.01	8.01	81.18
N_2	-	-	-	-	-	-	-	-	-
O_2	-	-	-	-	-	-	-	-	-
CO	2.82	2.82	55.43	55.43	55.43	55.43	26.71	26.71	28.72
CO_2	887.99	887.99	698.25	698.25	698.25	698.25	685.03	685.03	13.22
CH_4	-	-	-	-	-	-	-	-	-
C_2H_6	-	-	-	-	-	-	-	-	-
C_3H_8	-	-	-	-	-	-	-	-	-
nC_4H_{10}	-	-	-	-	-	-	-	-	-
nC_5H_{12}	-	-	-	-	-	-	-	-	-
H_2O	-	-	-	-	-	-	-	-	-
Exergy, MW	-95.1	-95.1	-77.2	-77.3	-76.6	-76.1	-73.9	-74.0	-2.2

Exergy = H-T_oS, where T_o =298 K, H, S: enthalpy and entropy of the stream

Table I.9
Material and energy balance for the delivery mode of the LM-C without using the liquid methane and liquid carbon dioxide refrigeration synergy, see Figure I.2 for flowsheet (continue).

Stream	40	41	42	43	44	45	46	47	48
Temperature, ° C	41	-55	41	12	41	800	43	43	43
Pressure, bar	79.3	15.8	15.6	10.4	10.2	10.0	19.6	19.4	9.1
Vapor Fraction	1.00	1.00	1.00	1.00	1.00	1.00	0.01	0.00	0.00
Mole Flow, kmol/hr	123	123	123	123	123	122	2	8	8
Volume Flow, m^3/hr	42.7	141.6	208.3	282.6	316.9	1,090.3	0.1	0.2	0.3
Mole Flow, kmol/h									
H_2	81.18	81.18	81.18	81.18	81.18	80.36	-	-	-
N_2	-	-	-	-	-	-	-	-	-
O_2	-	-	-	-	-	-	-	-	-
CO	28.72	28.72	28.72	28.72	28.72	28.43	-	-	-
CO_2	13.22	13.22	13.22	13.22	13.22	13.09	0.03	0.05	0.05
CH_4	-	-	-	-	-	-	-	-	-
C_2H_6	-	-	-	-	-	-	-	-	-
C_3H_8	-	-	-	-	-	-	-	-	-
nC_4H_{10}	-	-	-	-	-	-	-	-	-
nC_5H_{12}	-	-	-	-	-	-	-	-	-
H_2O	-	-	-	-	-	-	2.33	7.86	7.86
Exergy, MW	-2.2	-2.4	-2.4	-2.4	-2.4	-2.0	-0.2	-0.5	-0.5

Exergy = H-T_oS, where T_o =298 K, H, S: enthalpy and entropy of the stream

Stream	49	50	51	52	53	54	55	56	58
Temperature, ° C	43	43	48	204	43	118	118	688	310
Pressure, bar	8.9	1.9	1.9	9.2	9.1	1.9	10.7	10.0	10.5
Vapor Fraction	0.00	0.00	1.00	1.00	0.95	0.00	0.00	1.00	1.00
Mole Flow, kmol/hr	4,040	4,040	12	12	12	1,790	2,238	2,238	153
Volume Flow, m^3/hr	98.2	221.1	166.0	50.5	31.2	34.1	42.7	17,825.5	705.8
Mole Flow, kmol/h									
H_2	0.04	0.04	0.04	0.04	0.04	-	-	-	0.16
N_2	-	-	-	-	-	-	-	-	-
O_2	-	-	-	-	-	-	-	-	-
CO	0.01	0.01	0.01	0.01	0.01	-	-	-	0.00
CO_2	11.00	11.00	11.00	11.00	11.00	-	-	-	-
CH_4	-	-	-	-	-	-	-	-	152.41
C_2H_6	-	-	-	-	-	-	-	-	-
C_3H_8	-	-	-	-	-	-	-	-	-
nC_4H_{10}	-	-	-	-	-	-	-	-	-
nC_5H_{12}	-	-	-	-	-	-	-	-	-
H_2O	4,028.72	4,028.72	0.72	0.72	0.72	1,790.49	2,237.51	2,237.51	-
Exergy, MW	-266.8	-266.8	-1.2	-1.2	-1.2	-117.6	-146.9	-131.4	-1.7

Exergy = H-T_oS, where T_o =298 K, H, S: enthalpy and entropy of the stream

Table I.10
Material and energy balance for the delivery mode of the LM-C without using the liquid methane and liquid carbon dioxide refrigeration synergy, see Figure I.2 for flowsheet (continue).

Stream	59	60	61	62	63	64	65	66	67
Temperature, ° C	290	680	25	152	680	922	796	180	40
Pressure, bar	10.2	10.0	1.0	10.2	10.0	9.7	5.7	5.5	1.1
Vapor Fraction	1.00	1.00	1.00	1.00	1.00	1.00	1.00	1.00	1.00
Mole Flow, kmol/hr	157	157	12,314	12,314	12,314	10,524	10,524	10,524	10,524
Volume Flow, m^3/hr	720.8	1,244.6	301,204.4	42,833.8	97,859.0	107,941.0	165,014.8	72,695.8	248,691.6
Mole Flow, kmol/h									
H_2	0.16	0.16	-	-	-	-	-	-	-
N_2	-	-	9,548.52	9,548.52	9,548.52	9,548.52	9,548.52	9,548.52	9,548.52
O_2	-	-	2,534.03	2,534.03	2,534.03	744.50	744.50	744.50	744.50
CO	0.00	0.00	-	-	-	-	-	-	-
CO_2	0.21	0.21	36.73	36.73	36.73	36.73	36.73	36.73	36.73
CH_4	152.41	152.41	-	-	-	-	-	-	-
C_2H_6	-	-	-	-	-	-	-	-	-
C_3H_8	-	-	-	-	-	-	-	-	-
nC_4H_{10}	-	-	-	-	-	-	-	-	-
nC_5H_{12}	-	-	-	-	-	-	-	-	-
H_2O	3.81	3.81	194.39	194.39	194.39	194.39	194.39	194.39	194.39
Exergy, MW	-2.0	-1.4	-21.5	0.2	31.2	42.5	29.5	-4.2	-18.4

Exergy = H-T_oS, where T_o =298 K, H, S: enthalpy and entropy of the stream

Stream	a	b	c	d	Make up	Purge	Compressors power, MW	
							K-1	32.8
Temperature, ° C	-58	41	43	-54	43	41	**K-2**	0.0
Pressure, bar	20.0	19.9	46.6	46.5	10.7	10.2	**K-3**	1.6
Vapor Fraction	0.07	1.00	0.60	0.00	1.00	1.00	**K-4**	0.7
Mole Flow, kmol/hr	2,947	2,947	2,947	2,947	1	1.2	**K-5**	1.1
Volume Flow, m^3/hr	339.9	3,252.9	804.7	198.3	1.3	3.2	**K-6**	2.0
Mole Flow, kmol/h							**Turbines power, MW**	
H_2	-	-	-	-	-	0.81	**T-1**	12.0
N_2	-	-	-	-	-	-	**T-2**	11.7
O_2	-	-	-	-	-	-	**T-3**	0.3
CO	-	-	-	-	-	0.29	**T-4**	0.1
CO_2	-	-	-	-	-	0.13	**T-5**	0.0
CH_4	860.46	860.46	860.46	860.46	0.56	-	**SOFC**	
C_2H_6	639.02	639.02	639.02	639.02	-	-	**AC Power, MW**	**Heat, MW**
C_3H_8	1,447.96	1,447.96	1,447.96	1,447.96	-	-	152.5	0
nC_4H_{10}	-	-	-	-	-	-	**Pumps power, kW**	
nC_5H_{12}	-	-	-	-	-	-	**P-1**	14.1
H_2O	-	-	-	-	-	-	**P-2**	16.9
Exergy, MW	-22.2	-23.9	-22.9	-22.0	0.0	0.0		

Exergy = H-T_oS, where T_o =298 K, H, S: enthalpy and entropy of the stream

APPENDIX J. FLOWSHEET, MATERIAL BALANCE, AND ENERGY BALANCE FOR THE GM-C

J.1 Storage mode

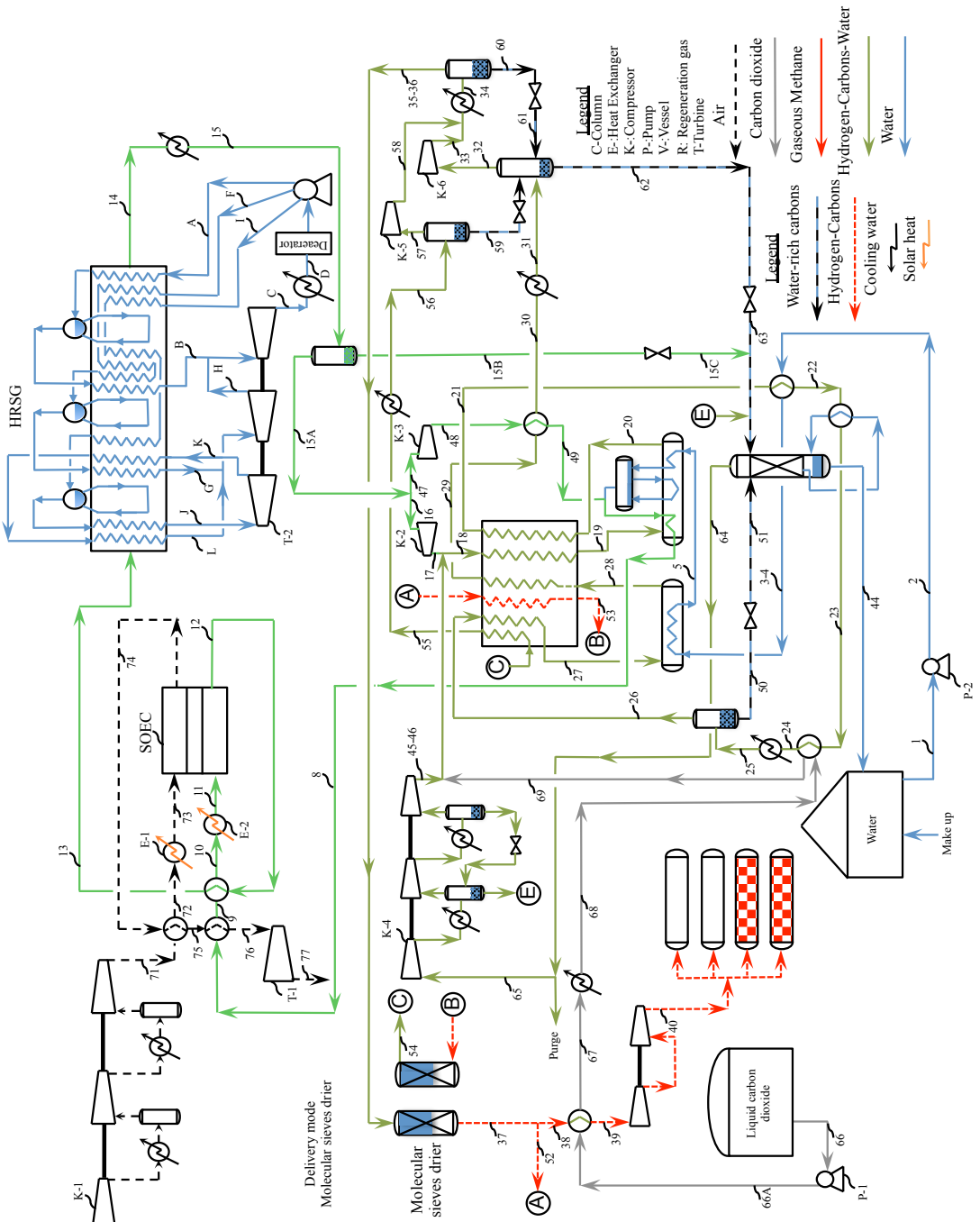

Figure J.1. Detailed flowsheet for the GM-C storage mode.

Table J.1
Material and energy balance for the storage mode of the GM-C, see Figure J.1 for flowsheet.

Stream	**1**	**2**	**3, 4**	**5**	**8**	**9**	**10**	**11**	**12**
Temperature, °C	118	118	161	174	246	461	818	950	950
Pressure, bar	1.9	12.0	11.6	11.3	10.6	10.4	10.2	10.0	9.7
Vapor Fraction	0	0	0	0	1	1	1	1	1
Mole Flow, kmol/hr	14,722	14,722	14,722	14,722	16,400	16,400	16,400	16,400	16,400
Volume Flow, m^3/hr	280.7	280.6	292.4	296.9	64,674.8	95,424.8	145,802.6	166,975.5	172,301.0
Mole Flow, kmol/hr									
H_2	-	-	-	-	1,658.61	1,658.61	1,658.61	1,658.61	16,047.31
N_2	-	-	-	-	-	-	-	-	-
O_2	-	-	-	-	-	-	-	-	-
CO	-	-	-	-	-	-	-	-	-
CO_2	-	-	-	-	-	-	-	-	-
CH_4	-	-	-	-	-	-	-	-	-
C_2H_6	-	-	-	-	-	-	-	-	-
C_3H_8	-	-	-	-	-	-	-	-	-
H_2O	14,722.19	14,722.19	14,722.06	14,722.06	14,741.76	14,741.76	14,741.76	14,741.76	353.07
Exergy, MW	-966.9	-966.9	-963.1	-961.7	-906.4	-887.9	-845.1	-826.4	71.3

Exergy = H-T_oS, where T_o =298 K, H, S: enthalpy and entropy of the stream

Stream	**13**	**14**	**15**	**15A**	**15B**	**15C**	**16**	**17**	**18**
Temperature, °C	488.7	124.4	43.3	43.1	43.1	43.2	43.1	180.2	171.7
Pressure, bar	9.5	8.1	8.0	7.8	7.8	1.9	7.8	22.1	22.1
Vapor Fraction	1	1	0.99	1	0	0	1	1	1
Mole Flow, kmol/hr	16,400	16,400	16,400	16,238	162	162	14,560	14,560	18,162
Volume Flow, m^3/hr	109,766.8	67,065.7	53,568.0	54,946.6	3.9	4.1	49,267.4	25,045.3	30,305.3
Mole Flow, kmol/hr									
H_2	16,047.31	16,047.31	16,047.31	16,047.29	0.02	0.02	14,388.68	14,388.68	14,389.70
N_2	-	-	-	-	-	-	-	-	-
O_2	-	-	-	-	-	-	-	-	-
CO	-	-	-	-	-	-	-	-	2.20
CO_2	-	-	-	-	-	-	-	-	3,596.98
CH_4	-	-	-	-	-	-	-	-	2.10
C_2H_6	-	-	-	-	-	-	-	-	-
C_3H_8	-	-	-	-	-	-	-	-	-
H_2O	353.07	353.07	353.07	190.65	162.42	162.42	170.94	170.94	170.99
Exergy, MW	26.5	1.7	-0.3	10.1	-10.7	-10.7	9.1	23.1	-369.4

Exergy = H-T_oS, where T_o =298 K, H, S: enthalpy and entropy of the stream

J.2 Delivery mode

Table J.2
Material and energy balance for the storage mode of the GM-C, see Figure J.1 for flowsheet (continue).

Stream	19	20	21	22	23	24	25	26	27
Temperature, °C	338.3	400	188.5	183.9	178.6	175.8	43.3	43.3	300
Pressure, bar	21.9	20.9	20.8	20.7	20.6	20.5	20.4	20.2	20.0
Vapor Fraction	1	1	0.957	0.843	0.746	0.709	0.378	1	1
Mole Flow, kmol/hr	18,162	11,292	11,292	11,292	11,292	11,292	11,292	4,272	4,272
Volume Flow, m^3/hr	42,150.2	29,923.6	18,936.6	16,721.5	14,811.0	14,094.2	5,596.4	5,482.1	10,255.1
Mole Flow, kmol/hr									
H_2	14,389.70	651.02	651.02	651.02	651.02	651.02	651.02	650.74	650.74
N_2	-	-	-	-	-	-	-	-	-
O_2	-	-	-	-	-	-	-	-	-
CO	2.20	1.34	1.34	1.34	1.34	1.34	1.34	1.34	1.34
CO_2	3,596.98	162.96	162.96	162.96	162.96	162.96	162.96	161.17	161.17
CH_4	2.10	3,436.98	3,436.98	3,436.98	3,436.98	3,436.98	3,436.98	3,434.96	3,434.96
C_2H_6	-	-	-	-	-	-	-	-	-
C_3H_8	-	-	-	-	-	-	-	-	-
H_2O	170.99	7,039.90	7,039.90	7,039.90	7,039.90	7,039.90	7,039.90	24.05	24.05
Exergy, MW	-357.6	-481.4	-496.4	-501.1	-505.2	-506.9	-523.4	-60.8	-56.8

Exergy = H-T_oS, where T_o =298 K, H, S: enthalpy and entropy of the stream

Stream	28	29	30	31	32	33	34	35-36	37
Temperature, °C	350	188.5	169	43.3	43.2	138.3	43.3	43.2	43.1
Pressure, bar	19.0	18.8	18.6	18.5	18.3	49.6	49.4	49.2	48.8
Vapor Fraction	1	1	1	0.928	1	1	0.998	1	1
Mole Flow, kmol/hr	3,985	3,985	3,985	3,985	3,698	3,698	4,269	4,259	4,244
Volume Flow, m^3/hr	10,939.9	8,133.2	7,859.2	5,165.2	5,216.2	2,550.1	2,162.1	2,170.7	2,185.5
Mole Flow, kmol/hr									
H_2	78.19	78.19	78.19	78.19	78.19	78.19	90.28	90.28	90.28
N_2	-	-	-	-	-	-	-	-	-
O_2	-	-	-	-	-	-	-	-	-
CO	0.24	0.24	0.24	0.24	0.24	0.24	0.28	0.28	0.28
CO_2	18.86	18.86	18.86	18.86	18.85	18.85	21.77	21.77	21.77
CH_4	3,578.37	3,578.37	3,578.37	3,578.37	3,578.29	3,578.29	4,131.83	4,131.82	4,131.82
C_2H_6	-	-	-	-	-	-	-	-	-
C_3H_8	-	-	-	-	-	-	-	-	-
H_2O	309.77	309.77	309.77	309.77	22.69	22.69	24.70	14.85	-
Exergy, MW	-60.1	-64.0	-64.3	-66.1	-47.2	-44.0	-51.6	-51.0	-50.0

Exergy = H-T_oS, where T_o =298 K, H, S: enthalpy and entropy of the stream

Table J.3
Material and energy balance for the storage mode of the GM-C, see Figure J.1 for flowsheet (continue).

Stream	38	39	40	44	45-46	47	48	49	50
Temperature, °C	43.1	-44	74.2	118.7	131.4	43.1	90	160.7	43.3
Pressure, bar	48.8	48.5	205.0	1.9	22.1	7.8	11.5	11.3	20.2
Vapor Fraction	1	1	1	0	1	1	1	1	0
Mole Flow, kmol/hr	3,676	3,676	3,676	7,486	4	1,678	1,678	1,678	7,020
Volume Flow, m^3/hr	1,892.7	1,146.8	512.4	194.1	6.3	5,679.1	4,439.8	5,398.8	170.3
Mole Flow, kmol/hr									
H_2	78.19	78.19	78.19	-	0.30	1,658.61	1,658.61	1,658.61	0.29
N_2	-	-	-	-	-	-	-	-	-
O_2	-	-	-	-	-	-	-	-	-
CO	0.24	0.24	0.24	-	0.00	-	-	-	0.00
CO_2	18.85	18.85	18.85	-	1.77	-	-	-	1.78
CH_4	3,578.27	3,578.27	3,578.27	-	2.10	-	-	-	2.02
C_2H_6	-	-	-	-	-	-	-	-	-
C_3H_8	-	-	-	-	-	-	-	-	-
H_2O	-	-	-	7,486.49	0.04	19.71	19.71	19.71	7,015.85
Exergy, MW	-43.3	-42.9	-39.9	-491.7	-0.2	1.0	1.6	1.8	-462.6

Exergy = H-T_oS, where T_o =298 K, H, S: enthalpy and entropy of the stream

Stream	51	52	53	54	55	56	57	58	59
Temperature, °C	43.7	43.1	310	290	188.5	43.3	43.2	47.4	43.2
Pressure, bar	1.9	48.8	48.5	48.0	47.8	47.6	47.4	49.6	47.4
Vapor Fraction	0	1	1	1	1	0.981	1	1	0
Mole Flow, kmol/hr	7,020	569	569	582	582	582	571	571	11
Volume Flow, m^3/hr	212.0	292.8	578.6	576.8	470.3	300.9	301.9	293.1	0.3
Mole Flow, kmol/hr									
H_2	0.29	12.10	12.10	12.10	12.10	12.10	12.10	12.10	-
N_2	-	-	-	-	-	-	-	-	-
O_2	-	-	-	-	-	-	-	-	-
CO	0.00	0.04	0.04	0.04	0.04	0.04	0.04	0.04	-
CO_2	1.78	2.92	2.92	2.92	2.92	2.92	2.92	2.92	0.00
CH_4	2.02	553.55	553.55	553.55	553.55	553.55	553.54	553.54	0.01
C_2H_6	-	-	-	-	-	-	-	-	-
C_3H_8	-	-	-	-	-	-	-	-	-
H_2O	7,015.85	-	-	13.35	13.35	13.35	2.01	2.01	11.34
Exergy, MW	-462.7	-6.7	-6.1	-7.0	-7.3	-7.6	-6.8	-6.8	-0.7

Exergy = H-T_oS, where T_o =298 K, H, S: enthalpy and entropy of the stream

Table J.4
Material and energy balance for the storage mode of the GM-C, see Figure J.1 for flowsheet (continue).

Stream	60	61	62	63	64	65	66	66A	67
Temperature, °C	43.2	43.9	43.2	43.6	43.7	43.7	-45.7	-45.3	-21.1
Pressure, bar	49.2	18.5	18.3	1.9	1.9	1.9	9.8	22.7	22.7
Vapor Fraction	0	0.001	0	0	1	1	0	0	0
Mole Flow, kmol/hr	10	10	308	308	4	4	3,598	3,598	3,598
Volume Flow, m^3/hr	0.239	0.246	7.482	8.829	61.838	61.219	150.219	149.832	169.102
Mole Flow, kmol/hr									
H_2	-	-	0.00	0.00	0.31	0.30	0.72	0.72	0.72
N_2	-	-	-	-	-	-	-	-	-
O_2	-	-	-	-	-	-	-	-	-
CO	-	-	-	-	0.00	0.00	2.20	2.20	2.20
CO_2	0.00	0.00	0.01	0.01	1.79	1.77	3,595.21	3,595.21	3,595.21
CH_4	0.01	0.01	0.10	0.10	2.12	2.10	-	-	-
C_2H_6	-	-	-	-	-	-	-	-	-
C_3H_8	-	-	-	-	-	-	-	-	-
H_2O	9.85	9.85	308.27	308.27	0.22	0.21	-	-	-
Exergy, MW	-0.6	-0.6	-20.3	-20.3	-0.2	-0.2	-383.7	-383.7	-384.6

Exergy = H-T_oS, where T_o =298 K, H, S: enthalpy and entropy of the stream

Stream	68	69	70	71	72	73	74	75	76
Temperature, °C	42.5	150.8	25	151.5	921.5	950	949.3	488.7	277.7
Pressure, bar	22.344	22.138	1.013	10.414	10.207	10	9.7	9.493	9.286
Vapor Fraction	1	1	1	1	1	1	1	1	1
Mole Flow, kmol/hr	3,598	3,598	12,227	12,227	12,227	12,227	19,421	19,421	19,421
Volume Flow, m^3/hr	3,820.5	5,583.7	299,073.7	41,633.6	119,125.6	124,481.4	203,791.0	130,021.5	96,181.0
Mole Flow, kmol/hr									
H_2	0.72	0.72	-	-	-	-	-	-	-
N_2	-	-	9,480.98	9,480.98	9,480.98	9,480.98	9,480.98	9,480.98	9,480.98
O_2	-	-	2,516.11	2,516.11	2,516.11	2,516.11	9,710.45	9,710.45	9,710.45
CO	2.20	2.20	-	-	-	-	-	-	-
CO_2	3,595.21	3,595.21	36.47	36.47	36.47	36.47	36.47	36.47	36.47
CH_4	-	-	-	-	-	-	-	-	-
C_2H_6	-	-	-	-	-	-	-	-	-
C_3H_8	-	-	-	-	-	-	-	-	-
H_2O	-	-	193.01	193.01	193.01	193.01	193.01	193.01	193.01
Exergy, MW	-386.8	-385.9	-21.4	0.4	51.0	53.3	93.2	34.6	14.7

Exergy = H-T_oS, where T_o =298 K, H, S: enthalpy and entropy of the stream

Table J.5
Material and energy balance for the storage mode of the GM-C, see Figure J.1 for flowsheet (continue).

Stream	77	A	B	C	D	F	G	H	I
Temperature, °C	69.2	32	229.7	39	39	32	319.7	217.8	32
Pressure, bar	1.1	5.7	5.0	0.1	0.1	30.4	29.8	5.0	120.0
Vapor Fraction	1	0	1	0.896	0	0	1	1	0
Mole Flow, kmol/hr	19,421	549	549	3,016	3,016	670	670	2,467	1,797
Volume Flow, m^3/hr	502,677.3	9.9	4,494.3	999,513.3	54.7	12.1	1,033.0	19,675.3	32.4
Mole Flow, kmol/hr									
H_2	-	-	-	-	-	-	-	-	-
N_2	9,480.98	-	-	-	-	-	-	-	-
O_2	9,710.45	-	-	-	-	-	-	-	-
CO	-	-	-	-	-	-	-	-	-
CO_2	36.47	-	-	-	-	-	-	-	-
CH_4	-	-	-	-	-	-	-	-	-
C_2H_6	-	-	-	-	-	-	-	-	-
C_3H_8	-	-	-	-	-	-	-	-	-
H_2O	193.01	548.94	548.94	3,016.08	3,016.08	670.18	670.18	2,467.14	1,796.96
Exergy, MW	-24.8	-36.2	-34.1	-197.4	-198.8	-44.2	-40.6	-153.2	-118.4

Exergy = H-T_oS, where T_o =298 K, H, S: enthalpy and entropy of the stream

Stream	J	K	L	PURGE				
					Compressors power, MW		**Pumps power, kW**	
Temperature, °C	459.7	278.2	459.7	43.7	**K-1**	32.42	**P-1**	72.75
Pressure, bar	119.3	30.0	29.8	1.9	**K-2**	16.10	**P-2**	100.07
Vapor Fraction	1	1	1	1	**K-3**	0.63		
Mole Flow, kmol/hr	1,797	1,797	1,797	0	**K-4**	0.01	**SOEC power, MW**	
Volume Flow, m^3/hr	803.4	2,484.0	3,569.9	0.6	**K-5**	0.02	997.32	
Mole Flow, kmol/hr					**K-6**	3.69		
H_2	-	-	-	0.00				
N_2	-	-	-	-	**Turbines power, MW**			
O_2	-	-	-	-	**T-1**	32.94		
CO	-	-	-	-	**T-2**	15.66		
CO_2	-	-	-	0.02				
CH_4	-	-	-	0.02				
C_2H_6	-	-	-	-				
C_3H_8	-	-	-	-				
H_2O	1,796.96	1,796.96	1,796.96	0.00				
Exergy, MW	-106.3	-109.3	-107.2	0.0				

Exergy = H-T_oS, where T_o =298 K, H, S: enthalpy and entropy of the stream

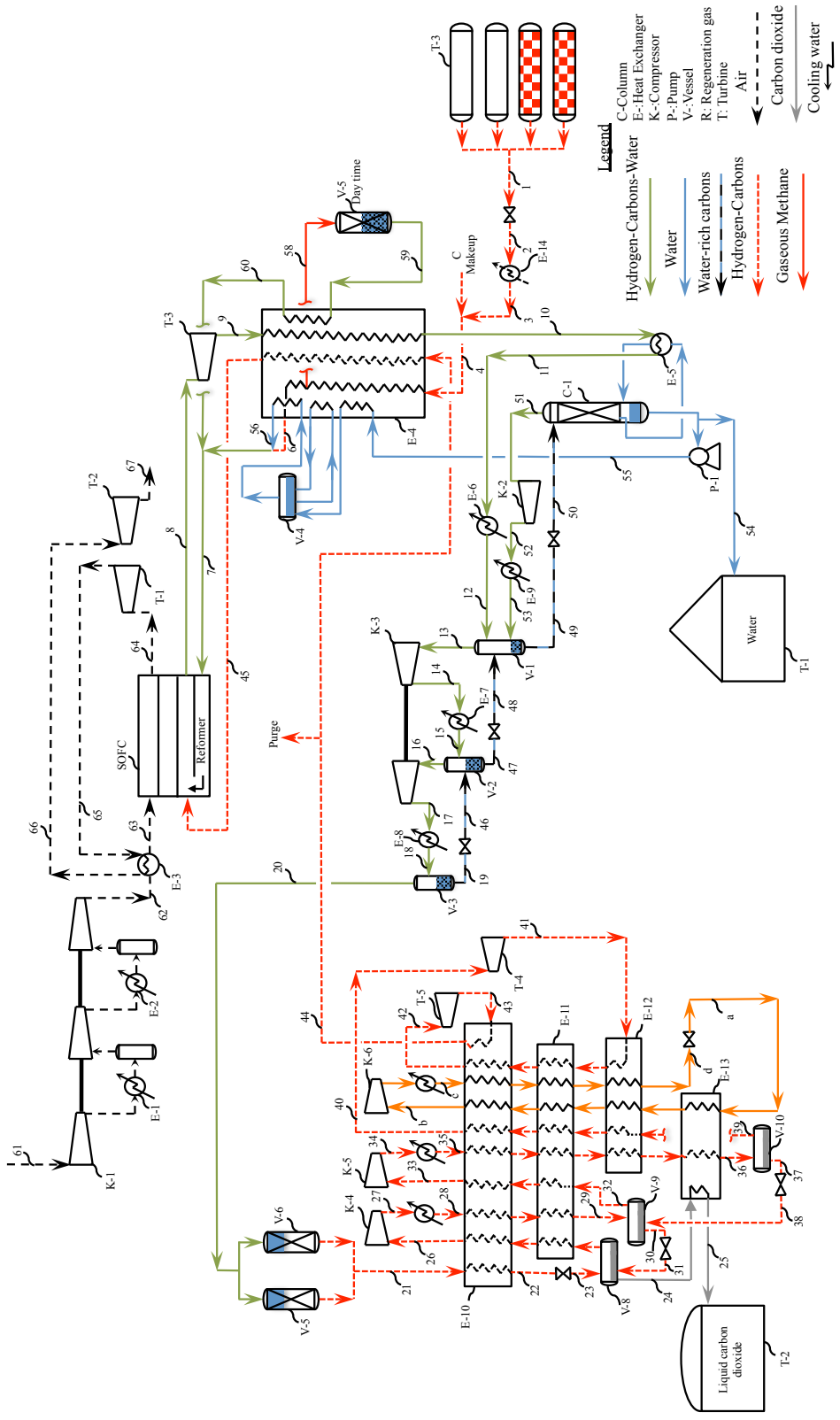

Figure J.2. Detailed flowsheet for the GM-C delivery mode.

Table J.6
Material and energy balance for the delivery mode of the GM-C, see Figure J.2 for flowsheet.

Stream	2	3	6	7	8	9	10	11	12
Temperature, °C	25	43	680	683	950	946	167	165	43
Pressure, bar	10.9	10.7	10.0	10.0	9.7	9.5	9.3	9.2	9.1
Vapor Fraction	1	1	1	1	1	1	0.963	0.843	0.202
Mole Flow, kmol/hr	918.9	918.9	765.4	3,160.7	5,073.3	5,073.3	5,073.3	5,073.3	5,073.3
Volume Flow, m^3/hr	2,051.18	2,227.99	6,087.33	25,058.46	53,218.97	54,228.89	18,489.89	16,332.88	2,973.25
Mole Flow, kmol/hr									
H_2	19.55	19.55	16.27	19.55	81.79	81.79	81.79	81.79	81.79
N_2	-	-	-	-	-	-	-	-	-
O_2	-	-	-	-	-	-	-	-	-
CO	0.06	0.06	0.05	0.06	29.49	29.49	29.49	29.49	29.49
CO_2	4.71	4.71	3.92	4.71	912.10	912.10	912.10	912.10	912.10
CH_4	894.57	894.57	745.16	895.00	-	-	-	-	-
C_2H_6	-	-	-	-	-	-	-	-	-
C_3H_8	-	-	-	-	-	-	-	-	-
H_2O	-	-	-	2,241.36	4,049.91	4,049.91	4,049.91	4,049.91	4,049.91
Exergy, MW	-11.8	-11.8	-6.1	-140.3	-323.3	-323.6	-352.5	-354.6	-366.8

Exergy = H-T_oS, where T_o =298 K, H, S: enthalpy and entropy of the stream

Stream	13	14	15	16	17	18	19	20	21
Temperature, °C	43	114	43	43	112	43	43	43	43
Pressure, bar	8.9	19.4	19.3	19.1	42.2	42.1	41.9	41.9	41.5
Vapor Fraction	1	1	0.995	1	1	0.998	0	1	1
Mole Flow, kmol/hr	1,034.6	1,034.6	1,034.6	1,029.1	1,029.1	1,029.1	2.4	1,026.7	1,023.4
Volume Flow, m^3/hr	2,976.89	1,656.46	1,313.18	1,327.53	718.45	544.88	0.06	547.61	552.80
Mole Flow, kmol/hr									
H_2	81.79	81.79	81.79	81.79	81.79	81.79	-	81.79	81.79
N_2	-	-	-	-	-	-	-	-	-
O_2	-	-	-	-	-	-	-	-	-
CO	29.49	29.49	29.49	29.49	29.49	29.49	-	29.49	29.49
CO_2	912.15	912.15	912.15	912.13	912.13	912.13	0.03	912.10	912.10
CH_4	-	-	-	-	-	-	-	-	-
C_2H_6	-	-	-	-	-	-	-	-	-
C_3H_8	-	-	-	-	-	-	-	-	-
H_2O	11.18	11.18	11.18	5.71	5.71	5.71	2.37	3.34	-
Exergy, MW	-100.6	-100.0	-100.1	-99.8	-99.1	-99.3	-0.2	-99.1	-98.9

Exergy = H-T_oS, where T_o =298 K, H, S: enthalpy and entropy of the stream

Table J.7
Material and energy balance for the delivery mode of the GM-C, see Figure J.2 for flowsheet (continue).

Stream	22	23	24	25	26	28	29	30	31
Temperature, °C	-1	-42	-42	-46	42	43	-12	-25	-39
Pressure, bar	41.4	10.0	9.8	9.8	9.6	20.8	20.7	20.5	10.0
Vapor Fraction	0.899	0.939	0	0	1	1	1	0	0.145
Mole Flow, kmol/hr	1,023.4	1,023.4	899.5	899.5	1,131.8	1,131.8	1,131.8	1,008.0	1,008.0
Volume Flow, m^3/hr	376.53	1,671.74	38.15	37.56	2,987.13	1,328.92	1,020.30	46.44	289.63
Mole Flow, kmol/hr									
H_2	81.79	81.79	0.18	0.18	82.50	82.50	82.50	0.89	0.89
N_2	-	-	-	-	-	-	-	-	-
O_2	-	-	-	-	-	-	-	-	-
CO	29.49	29.49	0.55	0.55	32.02	32.02	32.02	3.08	3.08
CO_2	912.10	912.10	898.80	898.80	1,017.29	1,017.29	1,017.29	1,003.99	1,003.99
CH_4	-	-	-	-	-	-	-	-	-
C_2H_6	-	-	-	-	-	-	-	-	-
C_3H_8	-	-	-	-	-	-	-	-	-
H_2O	-	-	-	-	-	-	-	-	-
Exergy, MW	-98.9	-99.6	-96.0	-95.9	-111.3	-110.7	-110.7	-107.5	-107.5

Exergy = H-T_oS, where T_o =298 K, H, S: enthalpy and entropy of the stream

Stream	32	33	35	36	37	38	39	40	41
Temperature, °C	-25	42	43	-55	-55	-55	-55	42	-55
Pressure, bar	20.5	20.3	79.8	79.7	79.5	20.7	79.5	79.3	15.8
Vapor Fraction	1	1	1	0.133	0	0.038	1	1	1
Mole Flow, kmol/hr	932.2	932.2	932.2	932.2	808.4	808.4	123.8	123.8	123.8
Volume Flow, m^3/hr	797.07	1,126.98	226.83	61.23	32.38	56.77	28.94	43.10	143.11
Mole Flow, kmol/hr									
H_2	90.595	90.595	90.595	90.595	8.989	8.989	81.606	81.606	81.606
N_2	0	0	0	0	0	0	0	0	0
O_2	0	0	0	0	0	0	0	0	0
CO	58.985	58.985	58.985	58.985	30.049	30.049	28.936	28.936	28.936
CO_2	782.62	782.62	782.62	782.62	769.318	769.318	13.302	13.302	13.302
CH_4	0	0	0	0	0	0	0	0	0
C_2H_6	0	0	0	0	0	0	0	0	0
C_3H_8	0	0	0	0	0	0	0	0	0
H_2O	0	0	0	0	0	0	0	0	0
Exergy, MW	-86.5	-86.5	-85.8	-85.2	-83.0	-83.1	-2.2	-2.3	-2.4

Exergy = H-T_oS, where T_o =298 K, H, S: enthalpy and entropy of the stream

Table J.8
Material and energy balance for the delivery mode of the GM-C, see Figure J.2 for flowsheet (continue).

Stream	42	43	44	45	46	47	48	49	50
Temperature, °C	42	13	42	800	43	43	43	43	43
Pressure, bar	15.6	10.4	10.2	10.0	19.3	19.1	9.1	8.9	1.9
Vapor Fraction	1	1	1	1	0.005	0	0.003	0	0.002
Mole Flow, kmol/hr	123.8	123.8	123.8	122.6	2.4	7.9	7.9	4,058.4	4,058.4
Volume Flow, m^3/hr	210.56	285.23	319.66	1,096.70	0.07	0.19	0.25	98.62	222.10
Mole Flow, kmol/hr									
H_2	81.61	81.61	81.61	80.79	-	-	-	0.04	0.04
N_2	-	-	-	-	-	-	-	-	-
O_2	-	-	-	-	-	-	-	-	-
CO	28.94	28.94	28.94	28.65	-	-	-	0.01	0.01
CO_2	13.30	13.30	13.30	13.17	0.03	0.05	0.05	11.05	11.05
CH_4	-	-	-	-	-	-	-	-	-
C_2H_6	-	-	-	-	-	-	-	-	-
C_3H_8	-	-	-	-	-	-	-	-	-
H_2O	-	-	-	-	2.37	7.84	7.84	4,047.34	4,047.34
Exergy, MW	-2.4	-2.4	-2.4	-2.0	-0.2	-0.5	-0.5	-268.0	-268.0

Exergy = H-T_oS, where T_o =298 K, H, S: enthalpy and entropy of the stream

Stream	51	52	53	54	55	56	57	58	59
Temperature, °C	49	205	43	118	118	688	25	310	290
Pressure, bar	1.9	9.2	9.1	1.9	10.7	10.0	10.9	10.5	10.2
Vapor Fraction	1	1	0.945	0	0	1	1	1	1
Mole Flow, kmol/hr	11.9	11.9	11.9	1,808.9	2,237.7	2,237.7	3,675.6	153.9	157.6
Volume Flow, m^3/hr	167.87	51.09	31.33	34.49	42.65	17,826.56	8,204.71	712.03	725.56
Mole Flow, kmol/hr									
H_2	0.04	0.04	0.04	-	-	-	78.19	3.27	3.27
N_2	-	-	-	-	-	-	-	-	-
O_2	-	-	-	-	-	-	-	-	-
CO	0.01	0.01	0.01	-	-	-	0.24	0.01	0.01
CO_2	11.05	11.05	11.05	-	-	-	18.85	0.79	0.79
CH_4	-	-	-	-	-	-	3,578.27	149.84	149.84
C_2H_6	-	-	-	-	-	-	-	-	-
C_3H_8	-	-	-	-	-	-	-	-	-
H_2O	0.76	0.76	0.76	1,808.93	2,237.65	2,237.65	-	-	3.71
Exergy, MW	-1.3	-1.2	-1.2	-118.8	-147.0	-131.4	-47.0	-1.8	-2.1

Exergy = H-T_oS, where T_o =298 K, H, S: enthalpy and entropy of the stream

Table J.9
Material and energy balance for the delivery mode of the GM-C, see Figure J.2 for flowsheet (continue).

Stream	60	61	62	63	64	65	66	67	a
Temperature, °C	680	25	152	680	922	796	180	40	-60
Pressure, bar	10.0	1.0	10.2	10.0	9.7	5.7	5.5	1.1	20.0
Vapor Fraction	1	1	1	1	1	1	1	1	0.065
Mole Flow, kmol/hr	157.6	12,428.6	12,428.6	12,428.6	10,629.7	10,629.7	10,629.7	10,629.7	3,193.8
Volume Flow, m^3/hr	1,252.82	304,016.00	43,233.61	98,772.47	109,023.99	166,928.67	73,573.20	251,301.22	362.76
Mole Flow, kmol/hr									
H_2	3.27	-	-	-	-	-	-	-	-
N_2	-	9,637.65	9,637.65	9,637.65	9,637.65	9,637.65	9,637.65	9,637.65	-
O_2	-	2,557.69	2,557.69	2,557.69	758.80	758.80	758.80	758.80	-
CO	0.01	-	-	-	-	-	-	-	-
CO_2	0.79	37.07	37.07	37.07	37.07	37.07	37.07	37.07	-
CH_4	149.84	-	-	-	-	-	-	-	960.02
C_2H_6	-	-	-	-	-	-	-	-	558.25
C_3H_8	-	-	-	-	-	-	-	-	1,675.49
H_2O	3.71	196.20	196.20	196.20	196.20	196.20	196.20	196.20	-
Exergy, MW	-1.5	-21.7	0.2	31.5	42.9	29.7	-4.3	-18.6	-23.8

Exergy = H-T_oS, where T_o =298 K, H, S: enthalpy and entropy of the stream

Stream	b	c	d
Temperature, °C	42	43	-56
Pressure, bar	19.9	41.7	41.6
Vapor Fraction	1	0.655	0
Mole Flow, kmol/hr	3,193.8	3,193.8	3,193.8
Volume Flow, m^3/hr	3,526.67	1,050.58	215.41
Mole Flow, kmol/hr			
H_2	-	-	-
N_2	-	-	-
O_2	-	-	-
CO	-	-	-
CO_2	-	-	-
CH_4	960.02	960.02	960.02
C_2H_6	558.25	558.25	558.25
C_3H_8	1,675.49	1,675.49	1,675.49
H_2O	-	-	-
Exergy, MW	-25.6	-24.7	-23.6

Compressors power, MW		**Pumps power, kW**	
K-1	33.13	**P-1**	16.93
K-2	0.02		
K-3	1.54	**SOFC power, MW**	
K-4	0.84	153.49	
K-5	1.22		
K-6	1.84		
Turbines power, MW			
T-1	12.20		
T-2	11.82		
T-3	0.27		
T-4	0.10		
T-5	0.03		

Exergy = H-T_oS, where T_o =298 K, H, S: enthalpy and entropy of the stream

APPENDIX K. MATERIAL AND ENERGY BALANCE FOR THE MO-C

K.1 Storage mode

K.2 Delivery mode

For flowsheet, material balance, and energy balance, see appendix E.

Table K.1
Material and energy balance for the storage mode of the Mo-C, see Figure 4.13 for flowsheet.

Stream	1	2	3	4	5	6	7	8	9
Temperature, ° C	100	100	161	171	175	511	950	950	203
Pressure, bar	1.1	11.5	11.2	10.5	10.4	10.2	10.0	9.7	9.5
Vapor Fraction	0.00	0.00	0.00	0.44	0.73	1.00	1.00	1.00	1.00
Mole Flow, kmol/hr	10,850	10,906	10,906	12,149	12,149	12,149	12,149	12,149	12,149
Volume Flow, m^3/hr	203.9	277.7	297.1	18,232.2	30,296.3	77,172.4	123,685.3	127,622.1	50,855.4
Mole Flow, kmol/h									
H_2	-	0.01	0.01	1,229.42	1,229.42	1,229.42	1,229.42	11,962.26	11,962.26
N_2	-	-	-	-	-	-	-	-	-
O_2	-	-	-	-	-	-	-	-	-
CO	-	-	-	-	-	-	-	-	-
CO_2	-	-	-	-	-	-	-	-	-
CH_4	-	-	-	-	-	-	-	-	-
C_2H_6	-	-	-	-	-	-	-	-	-
C_3H_8	-	-	-	-	-	-	-	-	-
CH_3OH	3.43	3.59	3.59	3.98	3.98	3.98	3.98	3.98	3.98
H_2O	10,846.70	10,902.14	10,902.14	10,915.18	10,915.18	10,915.18	10,915.18	182.33	182.33
Exergy, MW	-713.5	-717.0	-713.3	-698.5	-686.3	-653.9	-612.1	57.8	10.1

Exergy = H-T_oS, where T_o =298 K, H, S: enthalpy and entropy of the stream

Stream	10	11	12	13	14	15	16	17	18
Temperature, ° C	170	163	43	43	42	194	250	278	189
Pressure, bar	9.3	9.1	9.0	8.8	8.6	80.2	80.0	79.0	78.8
Vapor Fraction	1.00	1.00	1.00	1.00	1.00	1.00	1.00	1.00	1.00
Mole Flow, kmol/hr	12,149	12,149	12,149	10,850	11,139	11,064	60,872	53,907	53,907
Volume Flow, m^3/hr	48,384.5	48,712.1	35,620.5	32,692.9	34,268.9	5,532.8	33,173.1	31,196.1	25,781.5
Mole Flow, kmol/h									
H_2	11,962.26	11,962.26	11,962.26	10,732.84	10,792.74	10,792.68	44,770.81	34,311.32	34,311.32
N_2	-	-	-	-	-	-	-	-	-
O_2	-	-	-	-	-	-	-	-	-
CO	-	-	-	-	3.39	3.39	1,709.69	1,720.66	1,720.66
CO_2	-	-	-	-	209.54	209.53	14,046.80	10,552.99	10,552.99
CH_4	-	-	-	-	-	-	-	-	-
C_2H_6	-	-	-	-	-	-	-	-	-
C_3H_8	-	-	-	-	-	-	-	-	-
CH_3OH	3.98	3.98	3.98	3.43	19.95	16.79	246.29	3,729.13	3,729.13
H_2O	182.33	182.33	182.33	113.86	113.30	41.68	98.88	3,592.69	3,592.69
Exergy, MW	8.7	8.3	5.8	8.4	-16.0	9.3	-1,438.2	-1,464.6	-1,484.9

Exergy = H-T_oS, where T_o =298 K, H, S: enthalpy and entropy of the stream

Table K.2
Material and energy balance for the storage mode of the Mo-C, see Figure 4.13 for flowsheet (continue).

Stream	19	20	21	22	23	24	25	26	27
Temperature, ° C	164	141	122	114	43	43	48	130	142
Pressure, bar	78.7	78.6	78.5	78.4	76.9	76.7	80.8	80.6	80.4
Vapor Fraction	1.00	0.99	0.94	0.92	0.86	1.00	1.00	1.00	1.00
Mole Flow, kmol/hr	53,907	53,907	53,907	53,907	53,907	46,229	46,229	46,229	46,229
Volume Flow, m^3/hr	24,187.0	48,545.2	20,881.7	20,267.0	16,361.1	15,989.9	15,414.0	19,170.6	19,768.9
Mole Flow, kmol/h									
H_2	34,311.32	34,311.32	34,311.32	34,311.32	34,311.32	33,977.58	33,977.58	33,977.58	33,977.58
N_2	-	-	-	-	-	-	-	-	-
O_2	-	-	-	-	-	-	-	-	-
CO	1,720.66	1,720.66	1,720.66	1,720.66	1,720.66	1,703.63	1,703.63	1,703.63	1,703.63
CO_2	10,552.99	10,552.99	10,552.99	10,552.99	10,552.99	10,261.51	10,261.51	10,261.51	10,261.51
CH_4	-	-	-	-	-	-	-	-	-
C_2H_6	-	-	-	-	-	-	-	-	-
C_3H_8	-	-	-	-	-	-	-	-	-
CH_3OH	3,729.13	3,729.13	3,729.13	3,729.13	3,729.13	229.51	229.51	229.51	229.51
H_2O	3,592.69	3,592.69	3,592.69	3,592.69	3,592.69	57.20	57.20	57.20	57.20
Exergy, MW	-1,489.7	-1,498.1	-1,502.7	-1,505.6	-1,517.3	-1,088.6	-1,086.8	-1,081.0	-1,079.8

Exergy = H-T_oS, where T_o =298 K, H, S: enthalpy and entropy of the stream

Stream	28	29	30	31	32	33	34	35	36
Temperature, ° C	162	43	44	43	74	142	43	43	43
Pressure, bar	80.2	25.9	8.8	8.8	11.4	11.2	8.8	11.5	76.7
Vapor Fraction	1.00	0.00	0.00	1.00	1.00	1.00	0.00	0.00	0.00
Mole Flow, kmol/hr	46,229	75	75	1,243	1,243	1,243	56	56	7,306
Volume Flow, m^3/hr	20,786.9	1.9	2.0	3,744.9	3,170.3	3,860.6	1.4	1.4	285.4
Mole Flow, kmol/h									
H_2	33,977.58	0.06	0.06	1,229.41	1,229.41	1,229.41	0.01	0.01	59.84
N_2	-	-	-	-	-	-	-	-	-
O_2	-	-	-	-	-	-	-	-	-
CO	1,703.63	-	-	-	-	-	-	-	3.39
CO_2	10,261.51	0.02	0.02	-	-	-	-	-	209.50
CH_4	-	-	-	-	-	-	-	-	-
C_2H_6	-	-	-	-	-	-	-	-	-
C_3H_8	-	-	-	-	-	-	-	-	-
CH_3OH	229.51	3.16	3.16	0.39	0.39	0.39	0.16	0.16	3,497.78
H_2O	57.20	71.62	71.62	13.04	13.04	13.04	55.44	55.44	3,535.03
Exergy, MW	-1,078.8	-4.9	-4.9	1.0	1.2	1.3	-3.7	-3.7	-420.1

Exergy = H-T_oS, where T_o =298 K, H, S: enthalpy and entropy of the stream

Table K.3
Material and energy balance for the storage mode of the Mo-C, see Figure 4.13 for flowsheet (continue).

Stream	37	38	39	40	41	42	43	44	45
Temperature, ° C	40	133	43	42	49	40	86	99	43
Pressure, bar	2.0	9.0	8.8	3.9	2.0	1.8	1.8	2.1	2.0
Vapor Fraction	0.04	1.00	0.96	0.00	0.00	0.00	1.00	1.00	0.07
Mole Flow, kmol/hr	7,306	296	296	82	103	7,398	306	306	306
Volume Flow, m^3/hr	3,993.1	1,093.9	827.9	2.1	4.6	290.3	4,981.9	4,399.0	304.6
Mole Flow, kmol/h									
H_2	59.84	59.85	59.85	0.01	0.01	0.35	0.35	0.35	0.35
N_2	-	-	-	-	-	-	-	-	-
O_2	-	-	-	-	-	-	-	-	-
CO	3.39	3.39	3.39	-	-	0.02	0.02	0.02	0.02
CO_2	209.50	209.52	209.52	0.01	0.23	19.58	19.58	19.58	19.58
CH_4	-	-	-	-	-	-	-	-	-
C_2H_6	-	-	-	-	-	-	-	-	-
C_3H_8	-	-	-	-	-	-	-	-	-
CH_3OH	3,497.78	14.75	14.75	1.40	22.93	3,710.24	225.82	225.82	225.82
H_2O	3,535.03	8.24	8.24	80.41	80.16	3,667.47	60.27	60.27	60.27
Exergy, MW	-421.0	-24.0	-24.0	-5.4	-6.4	-418.8	-16.2	-16.2	-16.7

Exergy = H-T_oS, where T_o =298 K, H, S: enthalpy and entropy of the stream

Stream	46	47	48	49	50	51	52	53	54
Temperature, ° C	89	74	43	114	25	152	922	950	949
Pressure, bar	1.8	1.5	1.2	1.6	1.0	10.4	10.2	10.0	9.7
Vapor Fraction	0.00	0.00	0.00	0.00	1.00	1.00	1.00	1.00	1.00
Mole Flow, kmol/hr	7,092	3,484	3,484	3,607	9,120	9,120	9,120	9,120	14,486
Volume Flow, m^3/hr	291.6	199.9	191.4	93.2	223,085.7	31,055.4	88,858.4	92,853.4	152,012.2
Mole Flow, kmol/h									
H_2	-	-	-	-	-	-	-	-	-
N_2	-	-	-	-	7,072.07	7,072.07	7,072.07	7,072.07	7,072.07
O_2	-	-	-	-	1,876.82	1,876.82	1,876.82	1,876.82	7,243.24
CO	-	-	-	-	-	-	-	-	-
CO_2	-	-	-	-	27.20	27.20	27.20	27.20	27.20
CH_4	-	-	-	-	-	-	-	-	-
C_2H_6	-	-	-	-	-	-	-	-	-
C_3H_8	-	-	-	-	-	-	-	-	-
CH_3OH	3,484.43	3,480.91	3,480.91	3.52	-	-	-	-	-
H_2O	3,607.20	3.48	3.48	3,603.79	143.97	143.97	143.97	143.97	143.97
Exergy, MW	-401.1	-161.4	-161.7	-236.9	-15.9	0.3	38.0	39.7	69.5

Exergy = H-T_oS, where T_o =298 K, H, S: enthalpy and entropy of the stream

Table K.4
Material and energy balance for the storage mode of the Mo-C, see Figure 4.13 for flowsheet (continue).

Stream	55	56	57	58	59	60	61	62	Purge
Temperature, ° C	489	198	158	12	-46	-44	24	136	43
Pressure, bar	9.5	9.3	9.1	1.5	9.8	80.7	80.3	80.2	76.7
Vapor Fraction	1.00	1.00	1.00	1.00	0.00	0.00	0.00	1.00	1.00
Mole Flow, kmol/hr	14,486	14,486	14,486	14,486	3,579	3,579	3,579	3,579	373
Volume Flow, m^3/hr	96,985.9	61,393.0	57,348.5	228,786.3	149.4	147.4	238.1	1,340.7	129.0
Mole Flow, kmol/h									
H_2	-	-	-	-	0.65	0.65	0.65	0.65	274.01
N_2	7,072.07	7,072.07	7,072.07	7,072.07	-	-	-	-	-
O_2	7,243.24	7,243.24	7,243.24	7,243.24	-	-	-	-	-
CO	-	-	-	-	2.68	2.68	2.68	2.68	13.74
CO_2	27.20	27.20	27.20	27.20	3,575.85	3,575.85	3,575.85	3,575.85	82.75
CH_4	-	-	-	-	-	-	-	-	-
C_2H_6	-	-	-	-	-	-	-	-	-
C_3H_8	-	-	-	-	-	-	-	-	-
CH_3OH	-	-	-	-	-	-	-	-	1.85
H_2O	143.97	143.97	143.97	143.97	-	-	-	-	0.46
Exergy, MW	25.8	6.9	5.0	-15.7	-381.7	-381.4	-382.7	-381.5	-8.8

Exergy = H-T_oS, where T_o =298 K, H, S: enthalpy and entropy of the stream

APPENDIX L. FLOWSHEET, MATERIAL BALANCE, AND ENERGY BALANCE FOR THE MOW-C

L.1 Storage mode

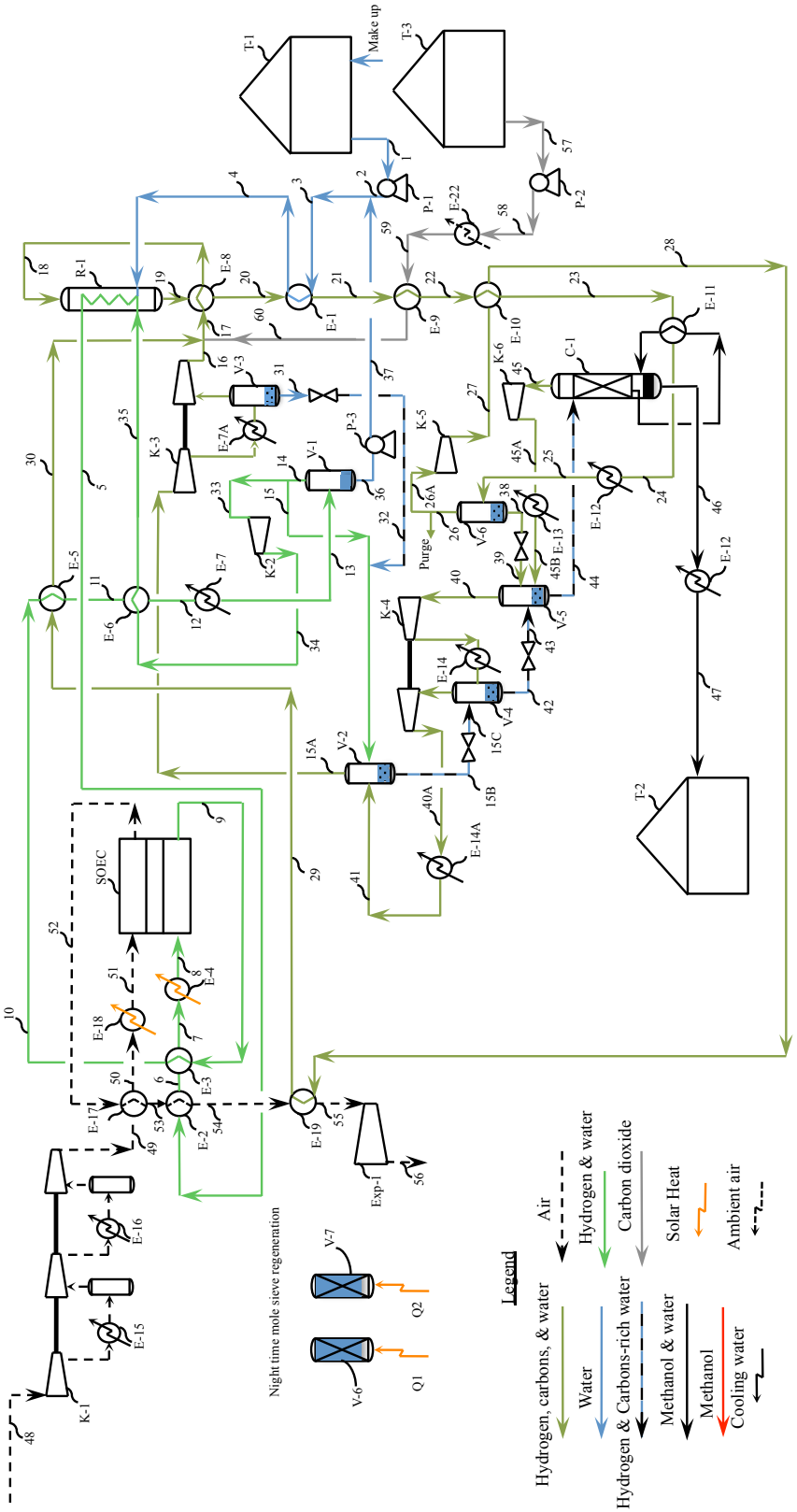

Figure L.1. Detailed flowsheet for the storage mode of the MoW-C.

Table L.1
Material and energy balance for the storage mode of the MoW-C, see Figure L.1 for flowsheet.

Stream	1	2	3	4	5	6	7	8	9
Temperature, ° C	100	100	100	161	171	175	511	950	950
Pressure, bar	1.1	11.5	11.5	11.2	10.5	10.4	10.2	10.0	9.7
Vapor Fraction	0.00	0.00	0.00	0.00	0.44	0.73	1.00	1.00	1.00
Mole Flow, kmol/hr	10,847	10,847	10,902	10,902	12,145	12,145	12,145	12,145	12,145
Volume Flow, m^3/hr	203.8	203.8	277.5	296.8	18,228.7	30,292.1	77,133.9	123,645.3	127,580.8
Mole Flow, kmol/h									
H_2	-	-	0.01	0.01	1,229.74	1,229.74	1,229.74	1,229.74	11,962.33
N_2	-	-	-	-	-	-	-	-	-
O_2	-	-	-	-	-	-	-	-	-
CO	-	-	-	-	-	-	-	-	-
CO_2	-	-	-	-	-	-	-	-	-
CH_4	-	-	-	-	-	-	-	-	-
C_2H_6	-	-	-	-	-	-	-	-	-
C_3H_8	-	-	-	-	-	-	-	-	-
CH_3OH	-	-	-	-	-	-	-	-	-
H_2O	10,846.70	10,846.70	10,901.84	10,901.84	10,914.92	10,914.92	10,914.92	10,914.92	182.33
Exergy, MW	-713.3	-713.3	-716.8	-713.1	-698.3	-686.1	-653.7	-611.9	58.0

Exergy = H-T_oS, where T_o =298 K, H, S: enthalpy and entropy of the stream

Stream	10	11	12	13	14	15	15A	15B	15C
Temperature, ° C	203	170	163	43	43	43	42	42	43
Pressure, bar	9.5	9.3	9.1	9.0	8.8	8.8	8.6	8.6	3.9
Vapor Fraction	1.00	1.00	1.00	1.00	1.00	1.00	1.00	0.00	0.00
Mole Flow, kmol/hr	12,145	12,145	12,145	12,145	12,090	10,847	11,134	82	82
Volume Flow, m^3/hr	50,840.5	48,369.6	48,696.9	35,610.6	36,427.6	32,682.8	34,256.1	2.0	2.1
Mole Flow, kmol/h									
H_2	11,962.33	11,962.33	11,962.33	11,962.33	11,962.32	10,732.59	10,792.50	0.01	0.01
N_2	-	-	-	-	-	-	-	-	-
O_2	-	-	-	-	-	-	-	-	-
CO	-	-	-	-	-	-	3.37	-	-
CO_2	-	-	-	-	-	-	208.07	0.01	0.01
CH_4	-	-	-	-	-	-	-	-	-
C_2H_6	-	-	-	-	-	-	-	-	-
C_3H_8	-	-	-	-	-	-	-	-	-
CH_3OH	-	-	-	-	-	-	15.98	1.10	1.10
H_2O	182.33	182.33	182.33	182.33	127.18	114.11	113.76	80.39	80.39
Exergy, MW	10.3	8.9	8.5	6.0	9.5	8.5	-15.7	-5.4	-5.4

Exergy = H-T_oS, where T_o =298 K, H, S: enthalpy and entropy of the stream

L.2 Delivery mode

Table L.2
Material and energy balance for the storage mode of the MoW-C, see Figure L.1 for flowsheet (continue).

Stream	16	17	18	19	20	21	22	23	24
Temperature, ° C	194	164	250	278	189	164	141	122	114
Pressure, bar	80.2	80.2	80.0	79.0	78.8	78.7	78.6	78.5	78.4
Vapor Fraction	1.00	1.00	1.00	1.00	1.00	1.00	0.99	0.94	0.92
Mole Flow, kmol/hr	11,059	60,846	60,846	53,881	53,881	53,881	53,881	53,881	53,881
Volume Flow, m^3/hr	5,530.9	27,438.9	33,163.1	31,186.0	25,771.4	24,173.6	48,505.0	20,877.7	20,262.9
Mole Flow, kmol/h									
H_2	10,792.45	44,818.63	44,818.63	34,359.80	34,359.80	34,359.80	34,359.80	34,359.80	34,359.80
N_2	-	-	-	-	-	-	-	-	-
O_2	-	-	-	-	-	-	-	-	-
CO	3.37	1,701.44	1,701.44	1,712.43	1,712.43	1,712.43	1,712.43	1,712.43	1,712.43
CO_2	208.06	13,983.99	13,983.99	10,490.39	10,490.39	10,490.39	10,490.39	10,490.39	10,490.39
CH_4	-	-	-	-	-	-	-	-	-
C_2H_6	-	-	-	-	-	-	-	-	-
C_3H_8	-	-	-	-	-	-	-	-	-
CH_3OH	13.51	242.60	242.60	3,725.22	3,725.22	3,725.22	3,725.22	3,725.22	3,725.22
H_2O	41.94	99.09	99.09	3,592.70	3,592.70	3,592.70	3,592.70	3,592.70	3,592.70
Exergy, MW	9.6	-1,449.4	-1,430.9	-1,457.3	-1,477.6	-1,482.4	-1,490.8	-1,495.4	-1,498.2

Exergy = H-T_oS, where T_o =298 K, H, S: enthalpy and entropy of the stream

Stream	25	26	26A	27	28	29	30	31	32
Temperature, ° C	43	43	43	48	130	142	162	43	44
Pressure, bar	76.9	76.7	76.7	80.8	80.6	80.4	80.2	25.9	8.8
Vapor Fraction	0.86	1.00	1.00	1.00	1.00	1.00	1.00	0.00	0.00
Mole Flow, kmol/hr	53,881	46,580	46,207	46,207	46,207	46,207	46,207	74	74
Volume Flow, m^3/hr	16,357.9	16115.5	15986.6	15411.3	19166.1	19765.4	20779.8	1.9	2.0
Mole Flow, kmol/h									
H_2	34,359.80	34,299.86	34,025.46	34,025.46	34,025.46	34,025.46	34,025.46	0.05	0.05
N_2	-	-	-	-	-	-	-	-	-
O_2	-	-	-	-	-	-	-	-	-
CO	1,712.43	1,709.07	1,695.40	1,695.40	1,695.40	1,695.40	1,695.40	-	-
CO_2	10,490.39	10,282.38	10,200.12	10,200.12	10,200.12	10,200.12	10,200.12	0.01	0.01
CH_4	-	-	-	-	-	-	-	-	-
C_2H_6	-	-	-	-	-	-	-	-	-
C_3H_8	-	-	-	-	-	-	-	-	-
CH_3OH	3,725.22	230.94	229.10	229.10	229.10	229.10	229.10	2.48	2.48
H_2O	3,592.70	57.61	57.15	57.15	57.15	57.15	57.15	71.82	71.82
Exergy, MW	-1,509.9	-1090.3	-1081.6	-1079.7	-1074.0	-1072.7	-1071.8	-4.9	-4.9

Exergy = H-T_oS, where T_o =298 K, H, S: enthalpy and entropy of the stream

Table L.3
Material and energy balance for the storage mode of the MoW-C, see Figure L.1 for flowsheet (continue).

Stream	33	34	35	36	37	38	39	40	40A
Temperature, ° C	43	74	142	43	43	43	40	40	133
Pressure, bar	8.8	11.4	11.2	8.8	11.5	76.7	2.0	1.8	9.0
Vapor Fraction	1.00	1.00	1.00	0.00	0.00	0.00	0.04	1.00	1.00
Mole Flow, kmol/hr	1243	1243	1243	55	55	7301	7301	316	294
Volume Flow, m^3/hr	3744.8	3170.3	3860.5	1.3	1.3	285.2	3,974.0	4,548.5	1,088.3
Mole Flow, kmol/h									
H_2	1,229.74	1,229.74	1,229.74	0.01	0.01	59.86	59.86	59.87	59.88
N_2	-	-	-	-	-	-	-	-	-
O_2	-	-	-	-	-	-	-	-	-
CO	-	-	-	-	-	3.37	3.37	3.37	3.37
CO_2	-	-	-	-	-	208.06	208.06	208.28	208.06
CH_4	-	-	-	-	-	-	-	-	-
C_2H_6	-	-	-	-	-	-	-	-	-
C_3H_8	-	-	-	-	-	-	-	-	-
CH_3OH	-	-	-	-	-	3,494.27	3,494.27	36.14	14.61
H_2O	13.07	13.07	13.07	55.15	55.15	3,535.09	3,535.09	7.96	8.23
Exergy, MW	1.0	1.2	1.4	-3.6	-3.6	-419.8	-420.7	-25.2	-23.8

Exergy = H-T_oS, where T_o =298 K, H, S: enthalpy and entropy of the stream

Stream	41	42	43	44	45	45A	45B	46	47
Temperature, ° C	43	50	50	40	86	99	43	89	43
Pressure, bar	8.8	3.7	2.0	1.8	1.8	2.1	2.0	1.8	1.5
Vapor Fraction	0.96	0.00	0.00	0.00	1.00	1.00	0.07	0.00	0.00
Mole Flow, kmol/hr	294	103	103	7,394	306	306	306	7,088	7,088
Volume Flow, m^3/hr	823.5	3.2	4.6	290.1	4,986.7	4,403.2	303.6	291.4	276.5
Mole Flow, kmol/h									
H_2	59.88	0.01	0.01	0.35	0.35	0.35	0.35	-	-
N_2	-	-	-	-	-	-	-	-	-
O_2	-	-	-	-	-	-	-	-	-
CO	3.37	-	-	0.02	0.02	0.02	0.02	-	-
CO_2	208.06	0.22	0.22	19.51	19.51	19.51	19.51	-	-
CH_4	-	-	-	-	-	-	-	-	-
C_2H_6	-	-	-	-	-	-	-	-	-
C_3H_8	-	-	-	-	-	-	-	-	-
CH_3OH	14.61	22.64	22.64	3,706.82	226.05	226.05	226.05	3,480.77	3,480.77
H_2O	8.23	80.12	80.12	3,667.63	60.38	60.38	60.38	3,607.25	3,607.25
Exergy, MW	-23.9	-6.4	-6.4	-418.6	-16.2	-16.2	-16.7	-400.9	-401.9

Exergy = H-T_oS, where T_o =298 K, H, S: enthalpy and entropy of the stream

Table L.4
Material and energy balance for the storage mode of the MoW-C, see Figure L.1 for flowsheet (continue).

Stream	48	49	50	51	52	53	54	55	56
Temperature, ° C	25	152	922	950	949	489	198	158	12
Pressure, bar	1.0	10.4	10.2	10.0	9.7	9.5	9.3	9.1	1.5
Vapor Fraction	1.00	1.00	1.00	1.00	1.00	1.00	1.00	1.00	1.00
Mole Flow, kmol/hr	9,120	9,120	9,120	9,120	14,486	14,486	14,486	14,486	14,486
Volume Flow, m^3/hr	223,080.3	31,054.7	88,856.3	92,851.2	152,008.6	96,983.6	61,394.5	57,344.9	228,775.1
Mole Flow, kmol/h									
H_2	-	-	-	-	-	-	-	-	-
N_2	7,071.90	7,071.90	7,071.90	7,071.90	7,071.90	7,071.90	7,071.90	7,071.90	7,071.90
O_2	1,876.77	1,876.77	1,876.77	1,876.77	7,243.07	7,243.07	7,243.07	7,243.07	7,243.07
CO	-	-	-	-	-	-	-	-	-
CO_2	27.20	27.20	27.20	27.20	27.20	27.20	27.20	27.20	27.20
CH_4	-	-	-	-	-	-	-	-	-
C_2H_6	-	-	-	-	-	-	-	-	-
C_3H_8	-	-	-	-	-	-	-	-	-
CH_3OH	-	-	-	-	-	-	-	-	-
H_2O	143.97	143.97	143.97	143.97	143.97	143.97	143.97	143.97	143.97
Exergy, MW	-15.9	0.3	38.0	39.7	69.5	25.8	6.9	5.0	-15.7

Exergy = H-T_oS, where T_o =298 K, H, S: enthalpy and entropy of the stream

Stream	57	58	59	60	Purge				
						Compressors power, MW		**Turbines power, MW**	
Temperature, ° C	-46	-44	24	136	43	**K-1**	24.2	**Exp-1**	16.9
Pressure, bar	9.8	80.7	80.3	80.2	76.7	**K-2**	0.3	**SOEC power, MW**	
Vapor Fraction	0.00	0.00	0.00	1.00	1.00	**K-3**	27.0	743.258	
Mole Flow, kmol/hr	3,579	3,579	3,579	3,579	373	**K-4**	0.5	**Pumps power, kW**	
Volume Flow, m^3/hr	149.4	147.4	238.1	1,340.0	128.9	**K-5**	2.2	**P-1**	77.4
Mole Flow, kmol/h						**K-6**	0.01	**P-2**	399.0
H_2	0.65	0.65	0.65	0.65	274.40	**External Heating, MW**		**P-3**	0.3
N_2	-	-	-	-	-	**E-4**	60.1		
O_2	-	-	-	-	-	**E-18**	2.5		
CO	2.68	2.68	2.68	2.68	13.67	**E-22**	8.8		
CO_2	3,575.85	3,575.85	3,575.85	3,575.85	82.26	**Q1 at 310 °C**	0.7		
CH_4	-	-	-	-	-				
C_2H_6	-	-	-	-	-				
C_3H_8	-	-	-	-	-				
CH_3OH	-	-	-	-	1.85				
H_2O	-	-	-	-	0.46				
Exergy, MW	-381.7	-381.4	-382.7	-381.5	-8.7				

Exergy=H-T_oS, where T_o =298 K, H, S: enthalpy and entropy of the stream

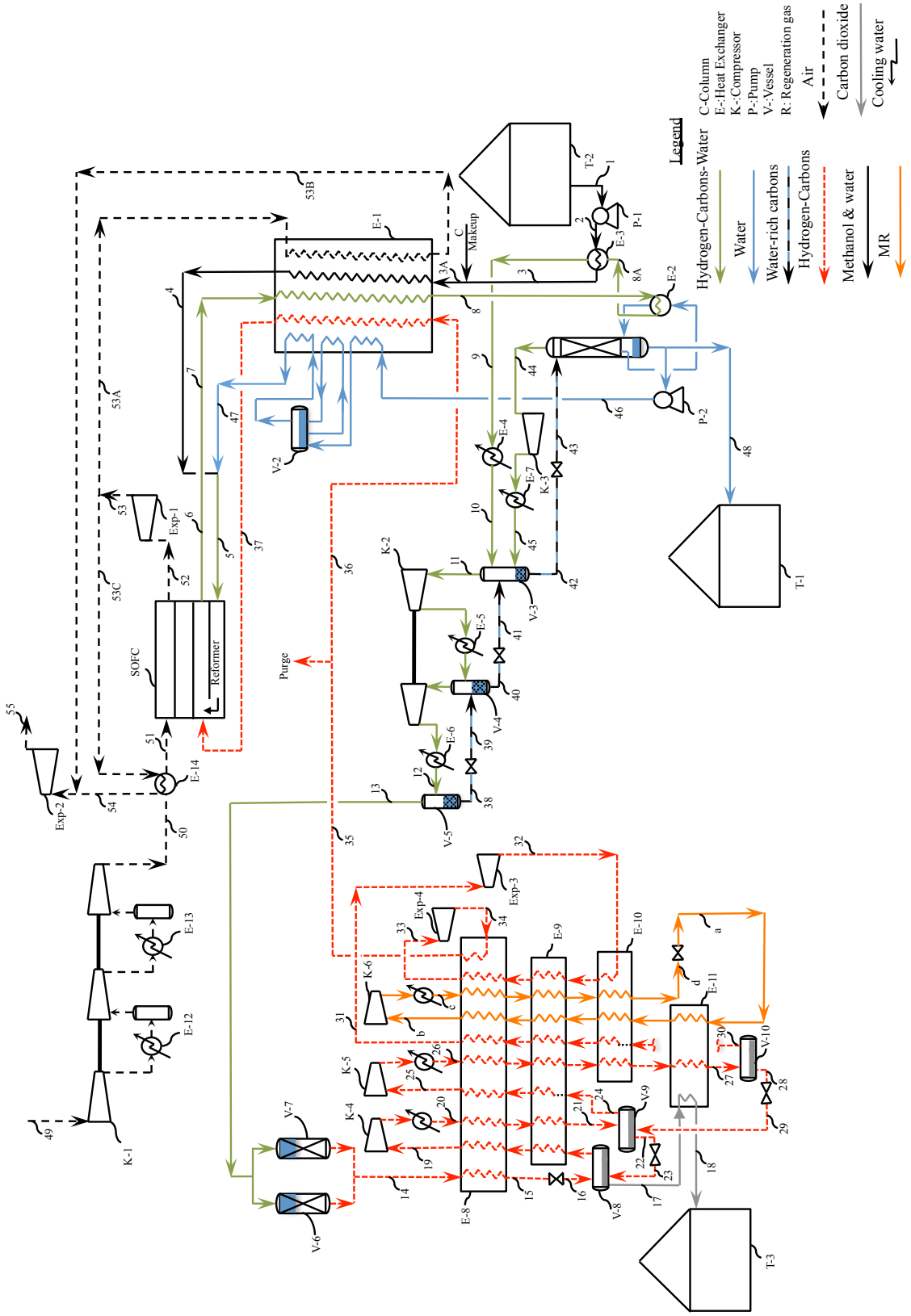

Figure L.2. Detailed flowsheet for the delivery mode of the MoW-C.

Table L.5
Material and energy balance for the delivery mode of the MoW-C, see Figure L.2 for flowsheet.

Stream	1	2	3	3A	4	5	6 and 7	8	8A
Temperature, ° C	43	44	134	133	680	680	950	165	163
Pressure, bar	1.5	11.0	10.7	10.7	10.0	10.0	9.7	9.5	9.4
Vapor Fraction	0.00	0.00	0.00	0.00	1.00	1.00	1.00	0.99	0.88
Mole Flow, kmol/hr	1,772	1,772	1,772	1,797	1,797	2,059	3,940	3,940	3,940
Volume Flow, m^3/hr	69.1	69.1	77.9	79.3	14,248.7	16,319.4	41,333.4	14,362.7	12,837.5
Mole Flow, kmol/h									
H_2	-	-	-	-	-	-	55.81	55.81	55.81
N_2	-	-	-	-	-	-	-	-	-
O_2	-	-	-	-	-	-	-	-	-
CO	-	-	-	-	-	-	27.19	27.19	27.19
CO_2	-	-	-	-	-	-	904.12	904.12	904.12
CH_4	-	-	-	-	-	-	-	-	-
C_2H_6	-	-	-	-	-	-	-	-	-
C_3H_8	-	-	-	-	-	-	-	-	-
CH_3OH	870.19	870.19	870.19	895.00	895.00	895.00	-	-	-
H_2O	901.81	901.81	901.81	901.81	901.81	1,163.50	2,952.78	2,952.78	2,952.78
Exergy, MW	-100.5	-100.5	-99.7	-100.9	-87.3	-102.8	-260.3	-282.9	-284.4

Exergy = H-T_oS, where T_o =298 K, H, S: enthalpy and entropy of the stream

Stream	9	10	11	12	13	14	15	16	17
Temperature, ° C	160	43	43	43	43	43	-1	-42	-42
Pressure, bar	9.3	9.2	9.0	43.7	43.5	43.0	42.9	10.0	9.8
Vapor Fraction	0.78	0.25	1.00	1.00	1.00	1.00	0.57	0.73	0.00
Mole Flow, kmol/hr	3,940	3,940	998	993	990	987	987	987	895
Volume Flow, m^3/hr	11,528.3	2,815.1	2,833.3	497.5	499.9	504.5	241.0	1,260.6	37.9
Mole Flow, kmol/h									
H_2	55.81	55.81	55.81	55.81	55.81	55.81	55.81	55.81	0.16
N_2	-	-	-	-	-	-	-	-	-
O_2	-	-	-	-	-	-	-	-	-
CO	27.19	27.19	27.19	27.19	27.19	27.19	27.19	27.19	0.67
CO_2	904.12	904.12	904.16	904.14	904.12	904.12	904.12	904.12	893.96
CH_4	-	-	-	-	-	-	-	-	-
C_2H_6	-	-	-	-	-	-	-	-	-
C_3H_8	-	-	-	-	-	-	-	-	-
CH_3OH	-	-	-	-	-	-	-	-	-
H_2O	2,952.78	2,952.78	10.67	5.46	3.18	-	-	-	-
Exergy, MW	-285.7	-293.5	-99.6	-98.3	-98.2	-98.0	-97.9	-98.4	-95.5

Exergy = H-T_oS, where T_o =298 K, H, S: enthalpy and entropy of the stream

Table L.6
Material and energy balance for the delivery mode of the MoW-C, see Figure L.2 for flowsheet (continue).

Stream	18	19	20	21	22	23	24	25	26
Temperature, ° C	-46	41	43	-12	-25	-40	-25	41	43
Pressure, bar	9.8	9.6	20.8	20.7	20.5	10.0	20.5	20.3	79.8
Vapor Fraction	0.00	1.00	1.00	1.00	0.00	0.15	1.00	1.00	1.00
Mole Flow, kmol/hr	895	847	847	847	754	754	703	703	703
Volume Flow, m^3/hr	37.4	2,225.3	993.9	762.5	34.7	216.0	600.6	847.0	171.8
Mole Flow, kmol/h									
H_2	0.16	56.25	56.25	56.25	0.60	0.60	61.99	61.99	61.99
N_2	-	-	-	-	-	-	-	-	-
O_2	-	-	-	-	-	-	-	-	-
CO	0.67	29.35	29.35	29.35	2.83	2.83	54.66	54.66	54.66
CO_2	893.96	761.08	761.08	761.08	750.93	750.93	586.81	586.81	586.81
CH_4	-	-	-	-	-	-	-	-	-
C_2H_6	-	-	-	-	-	-	-	-	-
C_3H_8	-	-	-	-	-	-	-	-	-
CH_3OH	-	-	-	-	-	-	-	-	-
H_2O	-	-	-	-	-	-	-	-	-
Exergy, MW	-95.4	-83.5	-83.1	-83.0	-80.4	-80.4	-65.2	-65.3	-64.7

Exergy = H-T_oS, where T_o =298 K, H, S: enthalpy and entropy of the stream

Stream	27	28	29	30	31	32	33	34	35
Temperature, ° C	-55	-55	-56	-55	41	-55	41	11	41
Pressure, bar	79.7	79.5	20.7	79.5	79.3	16.0	15.8	10.4	10.2
Vapor Fraction	0.13	0.00	0.05	1.00	1.00	1.00	1.00	1.00	1.00
Mole Flow, kmol/hr	703	611	611	92	92	92	92	92	92
Volume Flow, m^3/hr	45.9	24.5	46.7	21.4	32.1	104.8	154.0	211.1	237.4
Mole Flow, kmol/h									
H_2	61.99	6.35	6.35	55.64	55.64	55.64	55.64	55.64	55.64
N_2	-	-	-	-	-	-	-	-	-
O_2	-	-	-	-	-	-	-	-	-
CO	54.66	28.15	28.15	26.51	26.51	26.52	26.52	26.51	26.51
CO_2	586.81	576.66	576.66	10.15	10.15	10.15	10.15	10.15	10.15
CH_4	-	-	-	-	-	-	-	-	-
C_2H_6	-	-	-	-	-	-	-	-	-
C_3H_8	-	-	-	-	-	-	-	-	-
CH_3OH	-	-	-	-	-	-	-	-	-
H_2O	-	-	-	-	-	-	-	-	-
Exergy, MW	-64.3	-62.4	-62.5	-1.9	-1.9	-2.0	-2.0	-2.0	-2.0

Exergy = H-T_oS, where T_o =298 K, H, S: enthalpy and entropy of the stream

Table L.7
Material and energy balance for the delivery mode of the MoW-C, see Figure L.2 for flowsheet (continue).

Stream	36	37	38	39	40	41	42	43	44
Temperature, ° C	41	800	43	43	43	43	43	43	43
Pressure, bar	10.2	10.0	43.5	19.5	19.3	9.2	9.0	1.9	1.9
Vapor Fraction	1.00	1.00	0.00	0.01	0.00	0.00	0.00	0.00	1.00
Mole Flow, kmol/hr	91	91	2	2	8	8	2,958	2,958	9
Volume Flow, m^3/hr	235.1	817.6	0.1	0.1	0.2	0.2	71.9	166.3	122.2
Mole Flow, kmol/h									
H_2	55.09	55.09	-	-	-	-	0.02	0.02	0.02
N_2	-	-	-	-	-	-	-	-	-
O_2	-	-	-	-	-	-	-	-	-
CO	26.25	26.25	-	-	-	-	0.01	0.01	0.01
CO_2	10.05	10.05	0.03	0.03	0.05	0.05	8.38	8.38	8.38
CH_4	-	-	-	-	-	-	-	-	-
C_2H_6	-	-	-	-	-	-	-	-	-
C_3H_8	-	-	-	-	-	-	-	-	-
CH_3OH	-	-	-	-	-	-	-	-	-
H_2O	-	-	2.28	2.28	7.49	7.49	2,950.02	2,950.02	0.41
Exergy, MW	-2.0	-1.7	-0.2	-0.2	-0.5	-0.5	-195.4	-195.4	-0.9

Exergy = H-T_oS, where T_o =298 K, H, S: enthalpy and entropy of the stream

Stream	45	46	47	48	49	50	51	52	53
Temperature, ° C	43	118	680	118	25	152	680	922	778
Pressure, bar	9.2	10.7	10.0	1.9	1.0	10.2	10.0	9.7	5.3
Vapor Fraction	0.96	0.00	1.00	0.00	1.00	1.00	1.00	1.00	1.00
Mole Flow, kmol/hr	9	262	262	2,688	12,339	12,339	12,339	10,997	10,997
Volume Flow, m^3/hr	23.4	5.0	2,067.2	51.2	301,822.7	42,921.7	98,059.9	112,796.8	182,130.3
Mole Flow, kmol/h									
H_2	0.02	-	-	-	-	-	-	-	-
N_2	-	-	-	-	9,568.12	9,568.12	9,568.12	9,568.12	9,568.12
O_2	-	-	-	-	2,539.23	2,539.23	2,539.23	1,197.56	1,197.56
CO	0.01	-	-	-	-	-	-	-	-
CO_2	8.38	-	-	-	36.80	36.80	36.80	36.80	36.80
CH_4	-	-	-	-	-	-	-	-	-
C_2H_6	-	-	-	-	-	-	-	-	-
C_3H_8	-	-	-	-	-	-	-	-	-
CH_3OH	-	-	-	-	-	-	-	-	-
H_2O	0.41	261.69	261.69	2,687.92	194.78	194.78	194.78	194.78	194.78
Exergy, MW	-0.9	-17.2	-15.4	-176.5	-21.6	0.2	31.3	44.6	29.3

Exergy = H-T_oS, where T_o =298 K, H, S: enthalpy and entropy of the stream

Table L.8
Material and energy balance for the delivery mode of the MoW-C, see Figure L.2 for flowsheet (continue).

Stream	c	d				
			Turbines power, MW		**Pumps power, MW**	
Temperature, ° C	43	-53	**Exp-1**	14.15	**P-1**	27.5
Pressure, bar	34.3	34.2	**Exp-2**	11.78	**P-2**	3.9
Vapor Fraction	0.51	0.00	**Exp-3**	0.07		
Mole Flow, kmol/hr	2,300	2,300	**Exp-4**	0.02	**Compressor power, MW**	
Volume Flow, m^3/hr	782.7	162.0			**K-1**	32.89
Mole Flow, kmol/h			**SOFC power, MW**		**K-2**	1.50
H_2	-	-	124.0		**K-3**	0.02
N_2	-	-			**K-4**	0.62
O_2	-	-			**K-5**	0.92
CO	-	-			**K-6**	2.03
CO_2	-	-				
CH_4	526.37	526.37				
C_2H_6	293.50	293.50				
C_3H_8	1,480.13	1,480.13				
CH_3OH	-	-				
H_2O	-	-				
Exergy, MW	-16.4	-15.7				

Exergy = H-T_oS, where T_o =298 K, H, S: enthalpy and entropy of the stream

APPENDIX M. FLOWSHEET, MATERIAL BALANCE, AND ENERGY BALANCE FOR THE LM-C OXY-FUEL NGCC

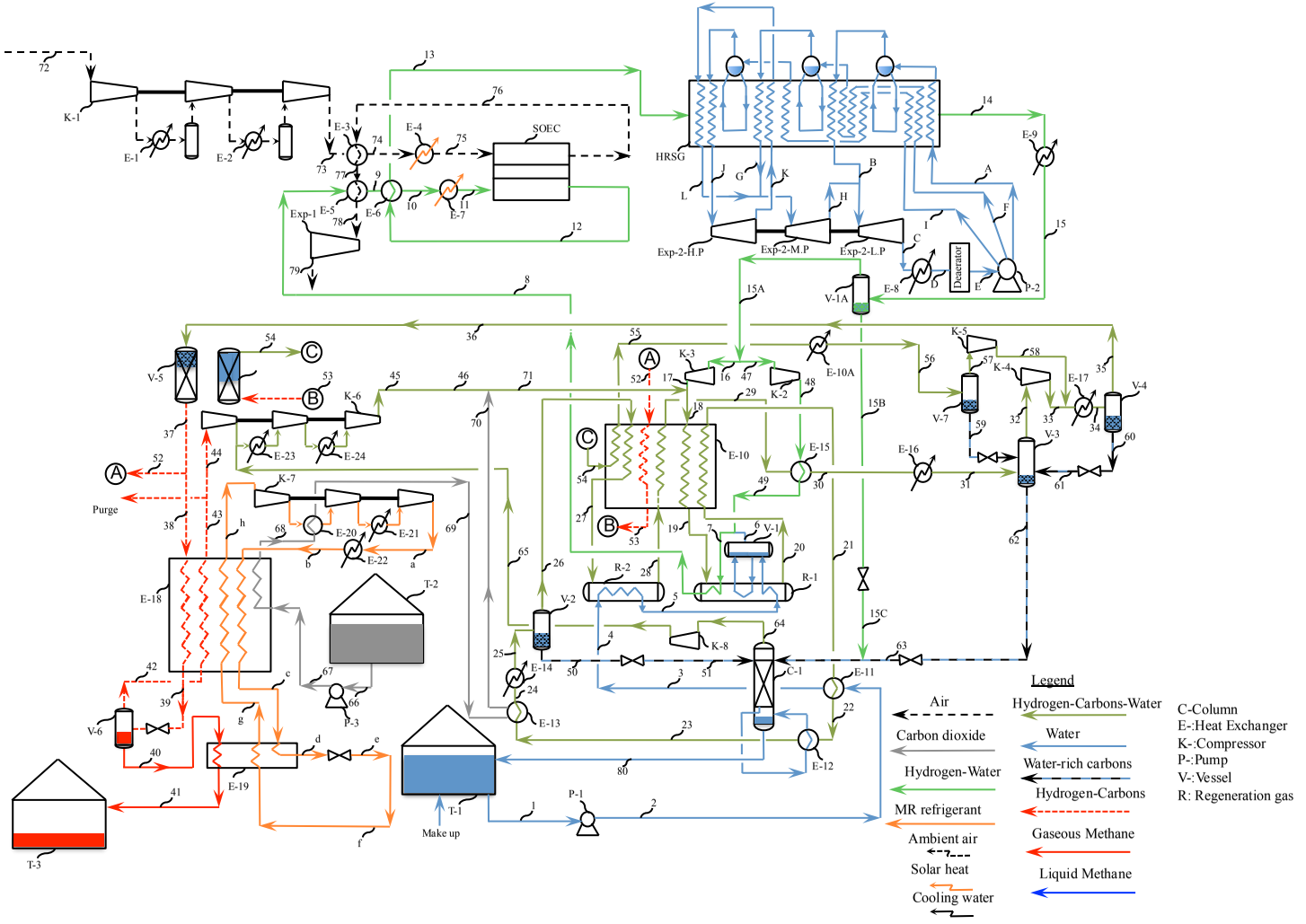

Figure M.1. Detailed flowsheet for the storage mode of LM-C with oxy-fuel NGCC for the delivery mode.

Table M.1
Material and energy balance for the storage mode of the LM-C with oxy-fuel NGCC for the delivery mode, see Figure M.1 for flowsheet.

Stream	1	2	3 and 4	5	8	9	10	11	12
Temperature, °C	85	85	178	185	304	461	818	950	950
Pressure, bar	1.9	12.0	11.6	11.3	10.6	10.4	10.2	10.0	9.7
Vapor Fraction	0.00	0.00	0.00	0.01	1.00	1.00	1.00	1.00	1.00
Mole Flow, kmol/hr	14,348	14,348	14,348	14,348	15,984	15,984	15,984	15,984	15,984
Volume Flow, m^3/hr	266.8	266.7	290.7	734.1	70,817.9	93,001.2	142,099.4	162,734.6	167,924.8
Mole Flow, kmol/hr									
H_2	-	-	-	-	1,616.48	1,616.48	1,616.48	1,616.48	15,639.73
N_2	-	-	-	-	-	-	-	-	-
AR	-	-	-	-	-	-	-	-	-
O_2	-	-	-	-	-	-	-	-	-
CO	-	-	-	-	-	-	-	-	-
CO_2	-	-	-	-	-	-	-	-	-
CH_4	-	-	-	-	-	-	-	-	-
C_2H_6	-	-	-	-	-	-	-	-	-
C_3H_8	-	-	-	-	-	-	-	-	-
nC_4H_{10}	-	-	-	-	-	-	-	-	-
nC_5H_{12}	-	-	-	-	-	-	-	-	-
H2O	14,348.14	14,348.14	14,348.14	14,348.14	14,367.34	14,367.34	14,367.34	14,367.34	344.10
Exergy, MW	-944.4	-944.3	-936.9	-935.6	-879.1	-865.4	-823.6	-805.5	69.5

Exergy = H-T_oS, where T_o =298 K, H, S: enthalpy and entropy of the stream

Stream	13	14	15	15A	15B	15C	16	17	18
Temperature, °C	489	124	43	43	43	43	43	180	170
Pressure, bar	9.5	8.1	8.0	7.8	7.8	1.9	7.8	22.1	22.1
Vapor Fraction	1.00	1.00	0.99	1.00	0.00	0.00	1.00	1.00	1.00
Mole Flow, kmol/hr	15,984	15,984	15,984	15,826	158	158	14,190	14,190	17,916
Volume Flow, m^3/hr	106,978.9	65,308.5	52,207.4	53,551.0	3.8	4.0	48,016.1	24,409.2	29,788.7
Mole Flow, kmol/hr									
H_2	15,639.73	15,639.73	15,639.73	15,639.71	0.02	0.02	14,023.23	14,023.23	14,177.77
N_2	-	-	-	-	-	-	-	-	2.07
AR	-	-	-	-	-	-	-	-	7.99
O_2	-	-	-	-	-	-	-	-	0.20
CO	-	-	-	-	-	-	-	-	0.01
CO_2	-	-	-	-	-	-	-	-	3,506.74
CH_4	-	-	-	-	-	-	-	-	53.88
C_2H_6	-	-	-	-	-	-	-	-	-
C_3H_8	-	-	-	-	-	-	-	-	-
nC_4H_{10}	-	-	-	-	-	-	-	-	-
nC_5H_{12}	-	-	-	-	-	-	-	-	-
H2O	344.10	344.10	344.10	185.80	158.30	158.30	166.60	166.60	167.48
Exergy, MW	25.8	1.7	-0.3	9.9	-10.4	-10.4	8.8	22.5	-360.7

Exergy = H-T_oS, where T_o =298 K, H, S: enthalpy and entropy of the stream

Table M.2
Material and energy balance for the storage mode of the LM-C with oxy-fuel NGCC for the delivery mode, see Figure M.1 for flowsheet (continue).

Stream	19	20	21	22	23	24	25	26	27
Temperature, °C	357	400	206	180	173	170	43	43	300
Pressure, bar	21.9	20.9	20.8	20.7	20.6	20.5	20.4	20.2	20.0
Vapor Fraction	1.00	1.00	1.00	0.77	0.68	0.65	0.38	1.00	1.00
Mole Flow, kmol/hr	17,916	11,167	11,167	11,167	11,167	11,167	11,167	4,268	4,268
Volume Flow, m^3/hr	42,837.4	29,598.2	20,413.3	15,139.5	13,301.2	12,707.7	5,592.1	5,480.8	10,247.4
Mole Flow, kmol/hr									
H_2	14,177.77	677.42	677.42	677.42	677.42	677.42	677.42	677.12	677.12
N_2	2.07	2.07	2.07	2.07	2.07	2.07	2.07	2.07	2.07
AR	7.99	7.99	7.99	7.99	7.99	7.99	7.99	7.98	7.98
O_2	0.20	-	-	-	-	-	-	-	-
CO	0.01	1.14	1.14	1.14	1.14	1.14	1.14	1.14	1.14
CO_2	3,506.74	130.90	130.90	130.90	130.90	130.90	130.90	129.49	129.49
CH_4	53.88	3,428.58	3,428.58	3,428.58	3,428.58	3,428.58	3,428.58	3,426.60	3,426.60
C_2H_6	-	-	-	-	-	-	-	-	-
C_3H_8	-	-	-	-	-	-	-	-	-
nC_4H_{10}	-	-	-	-	-	-	-	-	-
nC_5H_{12}	-	-	-	-	-	-	-	-	-
H2O	167.48	6,918.42	6,918.42	6,918.42	6,918.42	6,918.42	6,918.42	24.01	24.01
Exergy, MW	-347.5	-470.5	-482.7	-492.8	-496.7	-498.1	-511.8	-57.2	-53.2

Exergy = H-T_oS, where T_o =298 K, H, S: enthalpy and entropy of the stream

Stream	28	29	30	31	32	33	34	35-36	37
Temperature, °C	350	206	183	43	43	139	43	43	43
Pressure, bar	19.0	18.8	18.6	18.5	18.3	49.6	49.4	49.2	48.8
Vapor Fraction	1.00	1.00	1.00	0.94	1.00	1.00	1.00	1.00	1.00
Mole Flow, kmol/hr	4,009	4,009	4,009	4,009	3,750	3,750	14,322	14,312	4,309
Volume Flow, m^3/hr	11,007.0	8,510.3	8,168.2	5,244.2	5,296.7	2,593.8	6,541.9	6,569.0	2,226.1
Mole Flow, kmol/hr									
H_2	159.47	159.47	159.47	159.47	159.47	159.47	184.42	184.42	184.42
N_2	2.07	2.07	2.07	2.07	2.07	2.07	2.39	2.39	2.39
AR	7.98	7.98	7.98	7.98	7.98	7.98	9.23	9.23	9.23
O_2	-	-	-	-	-	-	-	-	-
CO	0.03	0.03	0.03	0.03	0.03	0.03	0.03	0.03	0.03
CO_2	0.91	0.91	0.91	0.91	1.19	1.19	9,957.08	9,956.98	-
CH_4	3,556.29	3,556.29	3,556.29	3,556.29	3,556.21	3,556.21	4,112.53	4,112.52	4,112.52
C_2H_6	-	-	-	-	-	-	-	-	-
C_3H_8	-	-	-	-	-	-	-	-	-
nC_4H_{10}	-	-	-	-	-	-	-	-	-
nC_5H_{12}	-	-	-	-	-	-	-	-	-
H2O	282.28	282.28	282.28	282.28	22.93	22.93	56.51	46.86	-
Exergy, MW	-56.1	-59.7	-60.1	-62.1	-45.0	-41.8	-1123.4	-1122.8	-47.4

Exergy = H-T_oS, where T_o =298 K, H, S: enthalpy and entropy of the stream

Table M.3
Material and energy balance for the storage mode of the LM-C with oxy-fuel NGCC for the delivery mode, see Figure M.1 for flowsheet (continue).

Stream	38	39	40	41	42	43	44	45-46	47
Temperature, °C	43	-170	-170	-172	-170	-4	-4	153	43
Pressure, bar	48.8	48.6	2.1	2.1	2.1	1.9	1.9	22.1	7.8
Vapor Fraction	1.00	0.01	0.00	0.00	1.00	1.00	1.00	1.00	1.00
Mole Flow, kmol/hr	3,726	3,726	3,516	3,516	210	210	208	213	1,636
Volume Flow, m^3/hr	1,925.0	141.6	130.2	129.1	855.9	2,499.7	2,474.7	343.8	5,534.9
Mole Flow, kmol/hr									
H_2	159.47	159.47	3.69	3.69	155.78	155.78	154.23	154.54	1,616.48
N_2	2.07	2.07	1.37	1.37	0.70	0.70	0.70	0.70	-
AR	7.98	7.98	6.88	6.88	1.11	1.11	1.09	1.10	-
O_2	-	-	-	-	-	-	-	-	-
CO	0.03	0.03	0.02	0.02	0.01	0.01	0.01	0.01	-
CO_2	-	-	-	-	-	-	-	1.41	-
CH_4	3,556.21	3,556.21	3,503.87	3,503.87	52.34	52.34	51.81	53.88	-
C_2H_6	-	-	-	-	-	-	-	-	-
C_3H_8	-	-	-	-	-	-	-	-	-
nC_4H_{10}	-	-	-	-	-	-	-	-	-
nC_5H_{12}	-	-	-	-	-	-	-	-	-
H2O	-	-	-	-	-	-	-	0.88	19.20
Exergy, MW	-41.0	-31.6	-31.9	-31.6	-0.5	-0.7	-0.7	-0.6	1.0

Exergy = H-T_oS, where T_o =298 K, H, S: enthalpy and entropy of the stream

Stream	48	49	50	51	52	53	54	55	56
Temperature, °C	90	178	43	44	43	310	290	206	43
Pressure, bar	11.5	11.3	20.2	1.9	48.8	48.5	48.0	47.8	47.6
Vapor Fraction	1.00	1.00	0.00	0.00	1.00	1.00	1.00	1.00	1.00
Mole Flow, kmol/hr	1,636	1,636	6,898	6,898	583	583	10,586	10,586	10,586
Volume Flow, m^3/hr	4,327.0	5,472.7	167.4	206.2	301.1	593.3	10,329.3	8,634.0	4,653.8
Mole Flow, kmol/hr									
H_2	1,616.48	1,616.48	0.29	0.29	24.95	24.95	24.95	24.95	24.95
N_2	-	-	0.00	0.00	0.32	0.32	0.32	0.32	0.32
AR	-	-	0.01	0.01	1.25	1.25	1.25	1.25	1.25
O_2	-	-	-	-	-	-	-	-	-
CO	-	-	-	-	0.00	0.00	0.00	0.00	0.00
CO_2	-	-	1.41	1.41	-	-	9,956.06	9,956.06	9,956.06
CH_4	-	-	1.98	1.98	556.32	556.32	556.32	556.32	556.32
C_2H_6	-	-	-	-	-	-	-	-	-
C_3H_8	-	-	-	-	-	-	-	-	-
nC_4H_{10}	-	-	-	-	-	-	-	-	-
nC_5H_{12}	-	-	-	-	-	-	-	-	-
H2O	19.20	19.20	6,894.41	6,894.41	-	-	46.86	46.86	46.86
Exergy, MW	1.5	1.8	-454.6	-454.7	-6.4	-5.8	-1067.0	-1072.1	-1077.7

Exergy = H-T_oS, where T_o =298 K, H, S: enthalpy and entropy of the stream

Table M.4
Material and energy balance for the storage mode of the LM-C with oxy-fuel NGCC for the delivery mode, see Figure M.1 for flowsheet (continue).

Stream	57	58	59	60	61	62	63	64	65
Temperature, °C	43	47	43	43	43	43	44	73	156
Pressure, bar	47.4	49.6	47.4	49.2	18.5	18.3	1.9	1.9	4.3
Vapor Fraction	1.00	1.00	0.00	0.00	0.01	0.00	0.00	1.00	1.00
Mole Flow, kmol/hr	10,572	10,572	13	10	10	282	282	5	5
Volume Flow, m^3/hr	4,673.9	4,539.1	0.3	0.2	0.3	6.9	8.0	71.1	38.8
Mole Flow, kmol/hr									
H_2	24.95	24.95	-	-	-	0.00	0.00	0.31	0.31
N_2	0.32	0.32	-	-	-	-	-	0.00	0.00
AR	1.25	1.25	-	-	-	-	-	0.01	0.01
O_2	-	-	-	-	-	-	-	-	-
CO	0.00	0.00	-	-	-	-	-	-	-
CO_2	9,955.88	9,955.88	0.18	0.10	0.10	0.00	0.00	1.41	1.41
CH_4	556.32	556.32	0.00	0.00	0.00	0.09	0.09	2.07	2.07
C_2H_6	-	-	-	-	-	-	-	-	-
C_3H_8	-	-	-	-	-	-	-	-	-
nC_4H_{10}	-	-	-	-	-	-	-	-	-
nC_5H_{12}	-	-	-	-	-	-	-	-	-
H2O	33.58	33.58	13.28	9.65	9.65	282.28	282.28	0.88	0.88
Exergy, MW	-1076.9	-1076.6	-0.9	-0.6	-0.6	-18.6	-18.6	-0.2	-0.2

Exergy = H-T_oS, where T_o =298 K, H, S: enthalpy and entropy of the stream

Stream	66	67	68	69	70	72	73	74	75
Temperature, °C	-44	-43	-4	51	146	25	152	922	950
Pressure, bar	9.8	22.7	22.6	22.3	22.1	1.0	10.4	10.2	10.0
Vapor Fraction	0.00	0.00	1.00	1.00	1.00	1.00	1.00	1.00	1.00
Mole Flow, kmol/hr	3,514	3,514	3,514	3,514	3,514	11,916	11,916	11,916	11,916
Volume Flow, m^3/hr	148.2	147.8	2,865.6	3,865.6	5,377.0	291,477.7	40,576.2	116,100.0	121,319.8
Mole Flow, kmol/hr									
H_2	-	-	-	-	-	-	-	-	-
N_2	1.37	1.37	1.37	1.37	1.37	9,240.18	9,240.18	9,240.18	9,240.18
AR	6.89	6.89	6.89	6.89	6.89	-	-	-	-
O_2	0.20	0.20	0.20	0.20	0.20	2,452.20	2,452.20	2,452.20	2,452.20
CO	-	-	-	-	-	-	-	-	-
CO_2	3,505.33	3,505.33	3,505.33	3,505.33	3,505.33	35.54	35.54	35.54	35.54
CH_4	-	-	-	-	-	-	-	-	-
C_2H_6	-	-	-	-	-	-	-	-	-
C_3H_8	-	-	-	-	-	-	-	-	-
nC_4H_{10}	-	-	-	-	-	-	-	-	-
nC_5H_{12}	-	-	-	-	-	-	-	-	-
H2O	-	-	-	-	-	188.11	188.11	188.11	188.11
Exergy, MW	-374.2	-374.1	-377.0	-377.1	-376.3	-20.8	0.4	49.7	51.9

Exergy = H-T_oS, where T_o =298 K, H, S: enthalpy and entropy of the stream

Table M.5
Material and energy balance for the storage mode of the LM-C with oxy-fuel NGCC for the delivery mode, see Figure M.1 for flowsheet (continue).

Stream	76	77	78	79	A	B	C	D	G
Temperature, °C	949	489	336	107	32	230	39	39	320
Pressure, bar	9.7	9.5	9.3	1.1	5.7	5.0	0.1	0.1	29.8
Vapor Fraction	1.00	1.00	1.00	1.00	0.00	1.00	0.90	0.00	1.00
Mole Flow, kmol/hr	18,928	18,928	18,928	18,928	536	536	2,943	2,943	656
Volume Flow, m^3/hr	198,615.0	126,719.2	103,553.3	543,855.7	9.7	4,386.5	975,101.8	53.4	1,011.7
Mole Flow, kmol/hr									
H_2	-	-	-	-	-	-	-	-	-
N_2	9,240.18	9,240.18	9,240.18	9,240.18	-	-	-	-	-
AR	-	-	-	-	-	-	-	-	-
O_2	9,463.82	9,463.82	9,463.82	9,463.82	-	-	-	-	-
CO	-	-	-	-	-	-	-	-	-
CO_2	35.54	35.54	35.54	35.54	-	-	-	-	-
CH_4	-	-	-	-	-	-	-	-	-
C_2H_6	-	-	-	-	-	-	-	-	-
C_3H_8	-	-	-	-	-	-	-	-	-
nC_4H_{10}	-	-	-	-	-	-	-	-	-
nC_5H_{12}	-	-	-	-	-	-	-	-	-
H2O	188.11	188.11	188.11	188.11	535.79	535.79	2,942.61	2,942.61	656.39
Exergy, MW	90.8	33.7	18.9	-23.1	-35.3	-33.2	-192.6	-194.0	-39.8

Exergy = H-T_oS, where T_o =298 K, H, S: enthalpy and entropy of the stream

Stream	H	I	J	K	L	MKUP	PURGE	a	b
Temperature, °C	218	32	460	278	460	32	-4	117	43
Pressure, bar	5.0	120.0	119.3	30.0	29.8	11.4	1.9	26.5	26.3
Vapor Fraction	1.00	0.00	1.00	1.00	1.00	0.00	1.00	1.00	1.00
Mole Flow, kmol/hr	2,407	1,750	1,750	1,750	1,750	5,223	2	5,627	5,627
Volume Flow, m^3/hr	19,189.2	31.5	782.6	2,419.6	3,477.5	94.5	25.0	6,547.4	4,975.3
Mole Flow, kmol/hr									
H_2	-	-	-	-	-	-	1.56	-	-
N_2	-	-	-	-	-	-	0.01	479.76	479.76
AR	-	-	-	-	-	-	0.01	-	-
O_2	-	-	-	-	-	-	-	-	-
CO	-	-	-	-	-	-	-	-	-
CO_2	-	-	-	-	-	-	-	-	-
CH_4	-	-	-	-	-	-	0.52	1,977.47	1,977.47
C_2H_6	-	-	-	-	-	-	-	2,025.73	2,025.73
C_3H_8	-	-	-	-	-	-	-	1,143.55	1,143.55
nC_4H_{10}	-	-	-	-	-	-	-	-	-
nC_5H_{12}	-	-	-	-	-	-	-	-	-
H2O	2,406.82	1,750.43	1,750.43	1,750.43	1,750.43	5,223.13	-	-	-
Exergy, MW	-149.4	-115.3	-103.6	-106.4	-104.5	-344.3	0.0	-45.7	-46.7

Exergy = H-T_oS, where T_o =298 K, H, S: enthalpy and entropy of the stream

Table M.6
Material and energy balance for the storage mode of the LM-C with oxy-fuel NGCC for the delivery mode, see Figure M.1 for flowsheet (continue).

Stream	d	e and f
Temperature, °C	-173	-176
Pressure, bar	26.2	1.2
Vapor Fraction	0.00	0.06
Mole Flow, kmol/hr	5,627	5,627
Volume Flow, m^3/hr	262.3	2,466.3
Mole Flow, kmol/hr		
H_2	-	-
N_2	479.76	479.76
AR	-	-
O_2	-	-
CO	-	-
CO_2	-	-
CH_4	1,977.47	1,977.47
C_2H_6	2,025.73	2,025.73
C_3H_8	1,143.55	1,143.55
nC_4H_{10}	-	-
nC_5H_{12}	-	-
H2O	-	-
Exergy, MW	-30.2	-30.9

Exergy = H-T_oS, where T_o =298 K, H, S: enthalpy and entropy of the stream

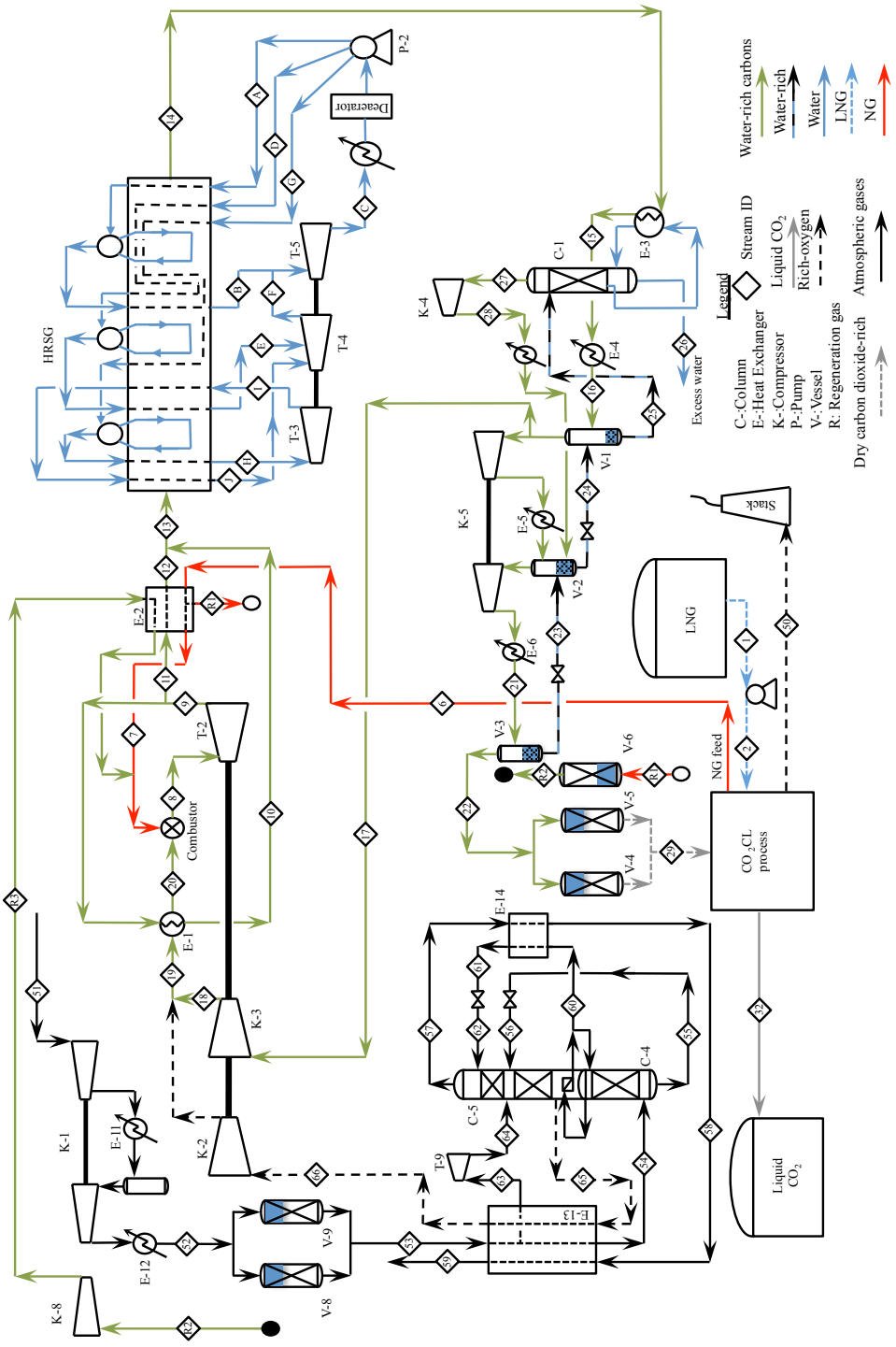

Figure M.2. Detailed flowsheet for the delivery mode oxy-fuel NGCC of LM-C.

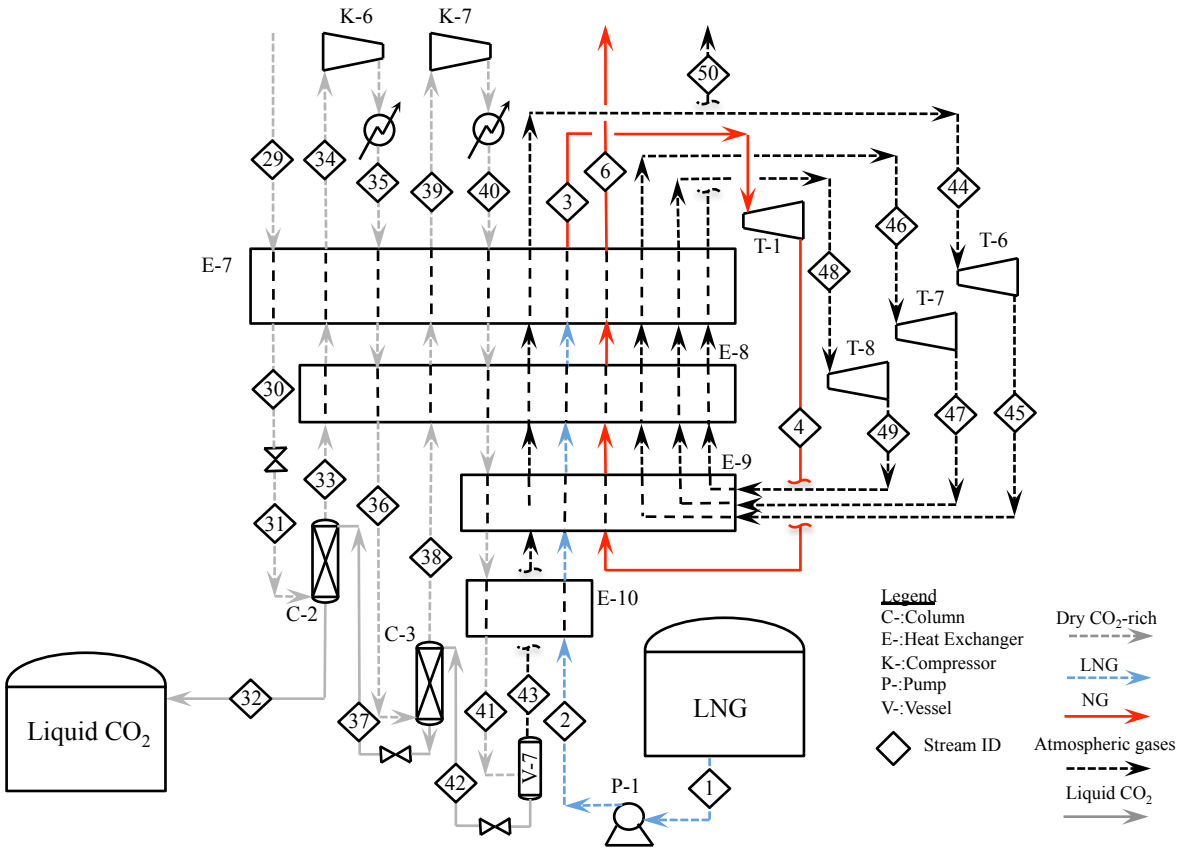

Figure M.3. Carbon dioxide capture and liquefaction section of the developed NGCC with oxygen based combustion shown in Figure M.2.

Table M.7
Material and energy balance for the delivery mode oxy-fuel NGCC of LM-C, see Figure M.2 and M.3 for flowsheets.

Stream	1	2	3	4	6	8	9	13
Temperature, °C	-172	-165	36	-59	36	1328	896	392
Pressure, bar	2.1	100.0	99.9	20.0	19.8	18.6	1.8	1.6
Vapor Fraction	0.00	0.00	1.00	1.00	1.00	1.00	1.00	1.00
Mole Flow, kmol/hr	879	879	879	879	879	28,779	28,779	28,779
Volume Flow, m^3/hr	32.3	32.3	205.3	697.3	1,112.6	206,709.5	1,517,370.0	971,489.6
Mole Flow, kmol/hr								
H_2	0.92	0.92	0.92	0.92	0.92	-	-	-
N_2	0.34	0.34	0.34	0.34	0.34	548.32	548.32	548.32
AR	1.72	1.72	1.72	1.72	1.72	1,845.86	1,845.86	1,845.86
O_2	-	-	-	-	-	46.18	46.18	46.18
CO	0.01	0.01	0.01	0.01	0.01	-	-	-
CO_2	-	-	-	-	-	22,586.17	22,586.17	22,586.17
CH_4	875.97	875.97	875.97	875.97	875.97	-	-	-
C_2H_6	-	-	-	-	-	-	-	-
C_3H_8	-	-	-	-	-	-	-	-
nC_4H_{10}	-	-	-	-	-	-	-	-
nC_5H_{12}	-	-	-	-	-	-	-	-
H_2O	-	-	-	-	-	3,752.87	3,752.87	3,752.87
Exergy, MW	-7.9	-7.9	-9.7	-10.5	-10.6	-2348.6	-2542.2	-2676.4

Exergy = H-T_oS, where T_o =298 K, H, S: enthalpy and entropy of the stream

Stream	14	15	16	17	18	19	20	21
Temperature, °C	142	135	43	40	370	376	869	43
Pressure, bar	1.4	1.3	1.2	1.0	19.8	19.8	19.6	15.0
Vapor Fraction	1.00	1.00	0.94	1.00	1.00	1.00	1.00	0.98
Mole Flow, kmol/hr	28,779	28,779	28,779	25,990	25,990	27,875	27,875	1,017
Volume Flow, m^3/hr	693,507.9	733,799.8	577,709.7	663,764.8	70,407.8	76,169.9	135,659.8	1,658.0
Mole Flow, kmol/hr								
H_2	-	-	-	-	-	-	-	-
N_2	548.32	548.32	548.32	526.60	526.60	547.98	547.98	21.72
AR	1,845.86	1,845.86	1,845.86	1,772.75	1,772.75	1,844.14	1,844.14	73.11
O_2	46.18	46.18	46.18	44.35	44.35	1,836.64	1,836.64	1.83
CO	-	-	-	-	-	-	-	-
CO_2	22,586.17	22,586.17	22,586.17	21,691.16	21,691.16	21,691.16	21,691.16	895.09
CH_4	-	-	-	-	-	-	-	-
C_2H_6	-	-	-	-	-	-	-	-
C_3H_8	-	-	-	-	-	-	-	-
nC_4H_{10}	-	-	-	-	-	-	-	-
nC_5H_{12}	-	-	-	-	-	-	-	-
H_2O	3,752.87	3,752.87	3,752.87	1,955.12	1,955.12	1,955.12	1,955.12	24.84
Exergy, MW	-2716.4	-2718.5	-2726.6	-2513.1	-2425.1	-2423.0	-2301.2	-98.2

Exergy = H-T_oS, where T_o =298 K, H, S: enthalpy and entropy of the stream

Table M.8
Material and energy balance for the delivery mode oxy-fuel NGCC of LM-C, see Figure M.2 and M.3 for flowsheets (continue).

Stream	22	23	24	25	26	27	28	29
Temperature, °C	43	43	43	40	101	98	273	43
Pressure, bar	14.8	3.8	1.2	1.0	1.0	1.0	3.9	14.8
Vapor Fraction	1.00	0.00	0.00	0.00	0.00	1.00	1.00	1.00
Mole Flow, kmol/hr	998	18	83	1,801	1,791	10	10	992
Volume Flow, m^3/hr	1,680.9	0.8	3.4	43.6	45.6	290.6	110.6	1,670.5
Mole Flow, kmol/hr								
H_2	-	-	-	-	-	-	-	-
N_2	21.72	-	-	-	-	-	-	21.72
AR	73.11	-	-	0.00	-	0.00	0.00	73.11
O_2	1.83	-	-	-	-	-	-	1.83
CO	-	-	-	-	-	-	-	-
CO_2	895.01	0.08	0.10	0.58	-	0.58	0.58	895.01
CH_4	-	-	-	-	-	-	-	-
C_2H_6	-	-	-	-	-	-	-	-
C_3H_8	-	-	-	-	-	-	-	-
nC_4H_{10}	-	-	-	-	-	-	-	-
nC_5H_{12}	-	-	-	-	-	-	-	-
H_2O	6.83	18.01	82.86	1,799.99	1,790.92	9.06	9.06	-
Exergy, MW	-97.0	-1.2	-5.5	-118.7	-117.8	-0.6	-0.6	-96.6

Exergy = H-T_oS, where T_o =298 K, H, S: enthalpy and entropy of the stream

Stream	30	31	32	33	34	35	36	37
Temperature, °C	-34	-43	-44	-44	36	43	1	-44
Pressure, bar	14.7	10.0	9.8	9.8	9.6	33.8	33.7	10.0
Vapor Fraction	0.64	0.68	0.00	1.00	1.00	1.00	1.00	0.19
Mole Flow, kmol/hr	992	992	878	808	808	808	808	695
Volume Flow, m^3/hr	765.1	1,173.1	37.0	1,420.5	2,089.9	557.6	433.0	253.3
Mole Flow, kmol/hr								
H_2	-	-	-	-	-	-	-	-
N_2	21.72	21.72	0.34	24.56	24.56	24.56	24.56	3.18
AR	73.11	73.11	1.72	92.05	92.05	92.05	92.05	20.66
O_2	1.83	1.83	0.05	2.23	2.23	2.23	2.23	0.45
CO	-	-	-	-	-	-	-	-
CO_2	895.01	895.01	876.33	688.95	688.95	688.95	688.95	670.28
CH_4	-	-	-	-	-	-	-	-
C_2H_6	-	-	-	-	-	-	-	-
C_3H_8	-	-	-	-	-	-	-	-
nC_4H_{10}	-	-	-	-	-	-	-	-
nC_5H_{12}	-	-	-	-	-	-	-	-
H_2O	-	-	-	-	-	-	-	-
Exergy, MW	-96.2	-96.3	-93.5	-74.5	-74.6	-73.9	-73.9	-71.7

Exergy = H-T_oS, where T_o =298 K, H, S: enthalpy and entropy of the stream

Table M.9
Material and energy balance for the delivery mode oxy-fuel NGCC of LM-C, see Figure M.2 and M.3 for flowsheets (continue).

Stream	38	39	40	41	42	43	44	45
Temperature, °C	-27	36	43	-53	-63	-53	36	-56
Pressure, bar	33.5	33.3	99.8	99.7	33.7	99.5	99.3	29.8
Vapor Fraction	1.00	1.00	1.00	0.12	0.38	1.00	1.00	1.00
Mole Flow, kmol/hr	967	967	967	967	854	113	113	113
Volume Flow, m^3/hr	484.7	695.0	211.7	51.9	168.1	14.2	27.9	61.5
Mole Flow, kmol/hr								
H_2	-	-	-	-	-	-	-	-
N_2	75.88	75.88	75.88	75.88	54.51	21.37	21.37	21.37
AR	356.73	356.73	356.73	356.73	285.35	71.39	71.39	71.39
O_2	7.49	7.49	7.49	7.49	5.72	1.78	1.78	1.78
CO	-	-	-	-	-	-	-	-
CO_2	526.74	526.74	526.74	526.74	508.07	18.67	18.67	18.67
CH_4	-	-	-	-	-	-	-	-
C_2H_6	-	-	-	-	-	-	-	-
C_3H_8	-	-	-	-	-	-	-	-
nC_4H_{10}	-	-	-	-	-	-	-	-
nC_5H_{12}	-	-	-	-	-	-	-	-
H_2O	-	-	-	-	-	-	-	-
Exergy, MW	-56.0	-56.1	-55.5	-54.9	-53.4	-1.8	-1.8	-1.8

Exergy = H-T_oS, where T_o =298 K, H, S: enthalpy and entropy of the stream

Stream	46	47	48	49	50	A	B	C
Temperature, °C	36	-55	36	-55	36	43	209	39
Pressure, bar	29.6	8.6	8.4	2.4	2.2	5.9	5.0	0.1
Vapor Fraction	1.00	1.00	1.00	1.00	1.00	0.00	1.00	0.88
Mole Flow, kmol/hr	113	113	113	113	113	1,153	1,153	5,683
Volume Flow, m^3/hr	96.3	230.6	342.5	849.7	1,324.7	21.0	9,015.6	1,847,520.0
Mole Flow, kmol/hr								
H_2	-	-	-	-	-	-	-	-
N_2	21.37	21.37	21.37	21.37	21.37	-	-	-
AR	71.39	71.39	71.39	71.39	71.39	-	-	-
O_2	1.78	1.78	1.78	1.78	1.78	-	-	-
CO	-	-	-	-	-	-	-	-
CO_2	18.67	18.67	18.67	18.67	18.67	-	-	-
CH_4	-	-	-	-	-	-	-	-
C_2H_6	-	-	-	-	-	-	-	-
C_3H_8	-	-	-	-	-	-	-	-
nC_4H_{10}	-	-	-	-	-	-	-	-
nC_5H_{12}	-	-	-	-	-	-	-	-
H_2O	-	-	-	-	-	1,152.78	1,152.78	5,683.37
Exergy, MW	-1.9	-1.9	-2.0	-2.0	-2.1	-76.0	-71.6	-372.0

Exergy = H-T_oS, where T_o =298 K, H, S: enthalpy and entropy of the stream

Table M.10
Material and energy balance for the delivery mode oxy-fuel NGCC of LM-C, see Figure M.2 and M.3 for flowsheets (continue).

Stream	D	E	F	G	H	R1	R2	R3
Temperature, °C	44	266	188	44	362	310	290	294
Pressure, bar	20.0	19.1	5.0	60.0	59.1	19.6	19.1	19.8
Vapor Fraction	0.00	1.00	1.00	0.00	1.00	1.00	1.00	1.00
Mole Flow, kmol/hr	1,487	1,487	4,531	3,043	3,043	336	343	343
Volume Flow, m^3/hr	27.0	3,258.5	33,719.7	55.2	2,428.9	838.4	845.2	822.9
Mole Flow, kmol/hr								
H_2	-	-	-	-	-	0.35	0.35	0.35
N_2	-	-	-	-	-	0.13	0.13	0.13
AR	-	-	-	-	-	0.64	0.64	0.64
O_2	-	-	-	-	-	-	-	-
CO	-	-	-	-	-	0.00	0.00	0.00
CO_2	-	-	-	-	-	-	-	-
CH_4	-	-	-	-	-	335.11	335.11	335.11
C_2H_6	-	-	-	-	-	-	-	-
C_3H_8	-	-	-	-	-	-	-	-
nC_4H_{10}	-	-	-	-	-	-	-	-
nC_5H_{12}	-	-	-	-	-	-	-	-
H_2O	1,487.14	1,487.14	4,530.60	3,043.46	3,043.46	-	6.83	6.83
Exergy, MW	-98.0	-90.8	-281.8	-200.5	-182.7	-3.7	-4.2	-4.2

Exergy = H-T_oS, where T_o =298 K, H, S: enthalpy and entropy of the stream

Compressors, MW		Turbines, MW		Pumps, kW	
K-1	17.82	**T-1**	-0.57	**P-1**	151.50
K-2	7.13	**T-2**	-182.92	**P-2**	172.22
K-3	97.45	**T-3**	-3.28		
K4	0.02	**T-4**	-5.76		
K-5	3.06	**T-5**	-15.41		
K-6	1.03	**T-6**	-0.06		
K-7	1.04	**T-7**	-0.07		
K-8	0.02	**T-8**	-0.07		

VITA

VITA

Easa I. Al-musleh was born on 23th June, 1984 in California, USA. Easa spent most of his school years in Doha-Qatar. In June 2000, Easa completed 12th grade from Omar Bin Al-Khattab Scientific School, Doha and then subsequently joined Qatar University, Doha to pursue a Bachelors degree in Chemical Engineering. At the completion of his undergraduate education in July 2007, Easa was awarded a scholarship from Qatar University to pursue his higher education. Through his undergraduate education and the internship experience at Qatar Gas and Qatar Petroleum, Easa developed a strong passion for process design and cryogenics engineering which motivated him to join Prof. Rakesh Agrawal research group. Thus, he joined the School of Chemical Engineering at Purdue University in May 2008, where he pursued a master research in the area of Liquefied Natural Gas process design and optimization flowed by a PhD research on design and optimization of power generation and energy storage processes, both guided by Prof. Rakesh Agrawal. While at Purdue, Easa received an Excellence for Undergraduate Teaching Assistant award which motivated him to accept a Faculty position offer from Qatar University, Doha. Prior to joining Qatar University, Easa will be joining Prof.Sigurd skogestad process control group in Norwegian University of Science and Technology, Trondheim, Norway.